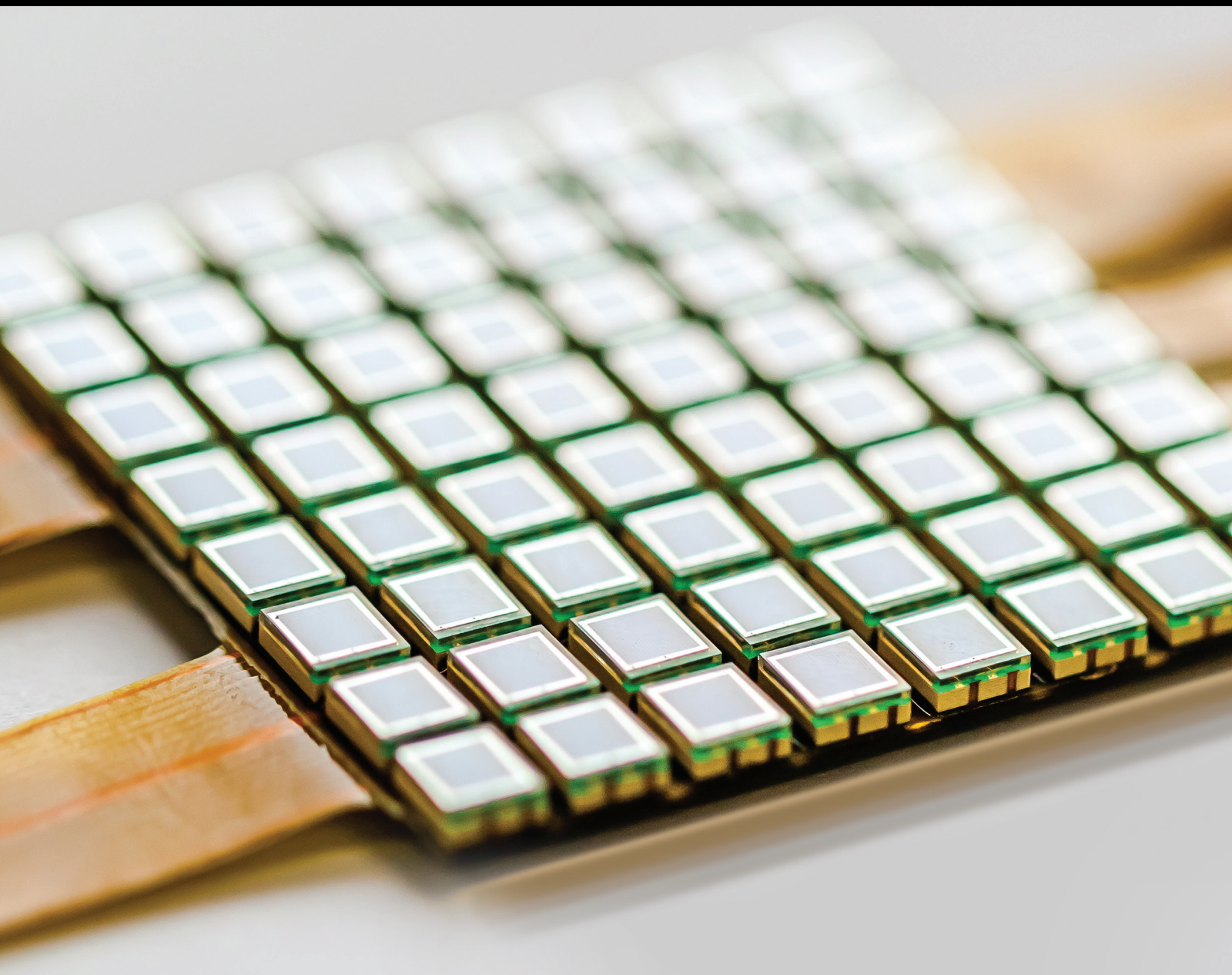# Bioimpedance Sensors: Instrumentation, Models, and Applications

Lead Guest Editor: David Naranjo-Hernández
Guest Editors: Javier Reina-Tosina, Ruben Buendia, and Mart Min

Bioimpedance Sensors: Instrumentation, Models, and Applications

Bioimpedance Sensors:
Instrumentation, Models, and Applications

Lead Guest Editor: David Naranjo-Hernández
Guest Editors: Javier Reina-Tosina, Ruben Buendia, and Mart Min

Editorial Board

Contents

Editorial

Bioimpedance Sensors: Instrumentation, Models, and Applications

David Naranjo-Hernández ,[1] **Javier Reina-Tosina** ,[1]
Rubén Buendía ,[2] **and Mart Min** [3]

[1]*University of Seville, Seville, Spain*
[2]*University of Borås, Borås, Sweden*
[3]*Tallinn University of Technology, Tallinn, Estonia*

Correspondence should be addressed to David Naranjo-Hernández; dnaranjo@us.es

Population aging and the consequent increase in chronic patients are driving research and development of multiple biomedical sensor technologies. These allow for better monitoring of people's health status as well as improved diagnosis, which anticipate a more personalized, preventive, and proactive healthcare. Bioimpedance technology offers valuable information about tissue/cell physiology and pathology. This way bioimpedance sensors technology is becoming the basis of novel and noninvasive medical diagnostic devices.

Considering the frequency response of bioimpedance and the dielectric/conductive properties of the different tissues it is possible to estimate the diverse compartments of the human body, i.e., intracellular and extracellular water, lean mass, fat mass, etc. The clinical usefulness of body composition analysis by bioimpedance techniques (BIA) has been demonstrated in multiple clinical areas: nephrology, for the optimal management of renal patient excess fluid; nutrition, for a better control of the patient's nutritional status; also during pregnancy and lactation, as a marker or direct cause of diseases; during the decision-making process about a disease, as a complement to the diagnosis and monitoring of conditions related to the cardiovascular system or in oncology, among others. Body composition analysis is also useful in chronic diseases, such as chronic obstructive pulmonary disease, where the loss of body weight and the decrease in muscle mass are risk factors associated with

increased morbidity and mortality and deterioration in the quality of life.

Changes in fluids and volumes in the thoracic cavity as result of cardiac hemodynamics also produce changes in the thoracic impedance which allow estimating parameters related to the mechanical function of the heart such as cardiac output, stroke volume, systolic time ratio, and the time of ejection of the left ventricle or the preejection period. The application of bioimpedance technology in the monitoring of cardiac parameters is called impedance cardiography (ICG), which has been proven very useful in the diagnosis of cardiovascular diseases as well as in trauma emergencies.

Bioimpedance measurements allow for the characterization of biological media and organic tissues and have been used for detection of edema, diagnosis of skin-related diseases, detection of cancerous tissues, and monitoring of ischemia during the transplant process and even as a noninvasive and nonobstructive estimation of blood pressure and blood glucose level. Bioimpedance techniques are also the basis of some laboratory devices for the monitoring of cell cultures and the study of the mechanical properties of cells (population, motility, viability, etc.).

The application of bioimpedance to obtain medical images of the inside of the human body using the technique known as electrical impedance tomography (EIT) is as well noteworthy. Despite the low resolution of the images

obtained, EIT has other advantages. It is particularly useful for monitoring lung function because lung tissue resistivity is five times higher than most other soft tissues in the thorax.

Despite the enormous potential of bioimpedance technology, its application to the clinical practice is still limited and a significant research effort is required to address the future challenges: electrodes for continuous monitoring, miniaturization of bioimpedance devices, reduction of energy consumption, improvement of sensitivity and specificity, detection and correction of artifacts, and application in implants, biosensors, and Lab-on-Chip technologies. This special issue is aimed at surveying recent advances in bioimpedance sensors, devices, and applications. Out of sixteen submissions, five articles were accepted after a thorough and rigorous peer-review process. A brief introduction of the published articles follows.

The paper "Orthogonal Multitone Electrical Impedance Spectroscopy (OMEIS) for the Study of Fibrosis Induced by Active Cardiac Implants" by E. De Roux et al. is devoted to the development and implementation of the simultaneous multitone impedance spectroscopy for detection as well as characterization of tissue modifications (fibrosis) around the implanted electrodes. Such electrodes are in use for both, stimulation and sensing, in implantable cardiac rhythm management devices (pacemakers and defibrillators), including also the data acquisition in implantable cardiac monitors. Because the fibrosis reduces susceptibility to stimulation (pacing) and sensibility for sensing, the methods for early detection of fibrosis are of great importance.

The paper "Electrical Impedance-Based Methodology for Locating Carcinoma Emulators on Breast Models" by M. Gutierrez-Lopez et al. describes the *Anomaly Tracking Circle algorithm*. This is a novel method to estimate the presence and location of breast carcinoma based on bioimpedance measurements through eight Ag/AgCl electrodes uniformly distributed in a ring configuration. Whereas all different technologies for breast tumor diagnosis have pros and cons, bioimpedance promises a painless, minimally invasive diagnosis at a low cost. Despite the method being in an early stage (it was evaluated on experimental agar breast models), results show great promise.

A key issue for bioimpedance-based measurement systems is the electrode configuration and material. In the paper "The Influence of Blood Glucose Meter Resistance Variation on the Performance of a Biosensor with a Gold-Coated Circuit Board" by K.-Y. Kim et al. the authors present a novel test strip for blood glucose measurement. Their contribution is based on the analysis of the effects of glucose oxidase in the reaction zone of gold-coated test strips, which provides a way of tuning the anodic and reductive peaks, thereby adjusting the resistance of the electrochemical reaction. To validate their approach, an experimental study was conducted in which glucose oxidase was combined with standard solutions with different concentrations and the corresponding current changes were measured. Results reveal that the accuracy of blood glucose measurement can be influenced by adjusting the resistance of the electrode test strip.

The work entitled "Simultaneous Recording of ICG and ECG Using Z-RPI Device with Minimum Number of Electrodes" by A. Hadif et al. describes a device and a procedure to monitor ICG and electrocardiogram (ECG) signals simultaneously using the same electrodes for both measurements, as opposed to the common methodology that uses separate electrode configurations. The results presented show the viability of the proposed scheme, constituting a step forward to the development of portable biomedical sensor technologies.

Last but not least, the paper titled "Fundamentals, Recent Advances, and Future Challenges in Bioimpedance Devices for Healthcare Applications" by D. Naranjo-Hernández et al. performs a complete review of bioimpedance technology and its applications in biomedical sensors. A strength of this study is that it provides the reader with a complete view of the technology, from the physical and physiological basis of bioimpedance, through the different mathematical models proposed in the literature, to the main instrumentation schemes. The main problems of bioimpedance measurements are also analyzed, such as the electrode issues or the noise and artifacts. Since bioimpedance is a very broad and heterogeneous concept, the fundamentals and results of the main applications of bioimpedance are shown in a structured way in separate sections: BIA, ICG, IET, transthoracic impedance pneumography, skin conductance, and biosensors. A final section analyzes recent advances and challenges and future applications of bioimpedance.

It is exciting to present this special issue on recent advances in bioimpedance technology and we hope that the articles published will promote discussions and inspire new innovations towards the improvement of people's health and quality of life.

Conflicts of Interest

The editors declare that they have no conflicts of interest regarding the publication of this special issue.

Acknowledgments

David Naranjo-Hernández
Javier Reina-Tosina
Rubén Buendía
Mart Min

Review Article

Fundamentals, Recent Advances, and Future Challenges in Bioimpedance Devices for Healthcare Applications

David Naranjo-Hernández (ID),[1] **Javier Reina-Tosina** (ID),[1] **and Mart Min** (ID)[2]

[1]*Biomedical Engineering Group, University of Seville, Seville, Spain*
[2]*Tallinn University of Technology, Tallinn, Estonia*

Correspondence should be addressed to David Naranjo-Hernández; dnaranjo@us.es

This work develops a thorough review of bioimpedance systems for healthcare applications. The basis and fundamentals of bioimpedance measurements are described covering issues ranging from the hardware diagrams to the configurations and designs of the electrodes and from the mathematical models that describe the frequency behavior of the bioimpedance to the sources of noise and artifacts. Bioimpedance applications such as body composition assessment, impedance cardiography (ICG), transthoracic impedance pneumography, electrical impedance tomography (EIT), and skin conductance are described and analyzed. A breakdown of recent advances and future challenges of bioimpedance is also performed, addressing topics such as transducers for biosensors and Lab-on-Chip technology, measurements in implantable systems, characterization of new parameters and substances, and novel bioimpedance applications.

1. Introduction

The continuous increase in life expectancy is contributing to an aging population and an increase in the prevalence of chronic diseases [1, 2]. The consequence is an impact on the socioeconomic structure of society in terms of increased medical expenses and health and social welfare needs. This problem has driven new technological advances (sensing devices, low power electronics, wearable systems, communication technologies, etc.) to improve current healthcare systems and citizens quality of life [3]. Multiple sensorization technologies are being investigated and developed towards their application to the monitoring of the health condition, either in a clinical environment or in wearable devices for remote monitoring at the user's home [4, 5]: heart rate variability [6], glucose level in the blood [7], blood pressure [4], temperature [8], physical activity [2], pulse oximetry [9], etc. Among these technologies, bioimpedance takes a prominent place, since it allows providing an insight about the internal processes of the body in a noninvasive way [10, 11].

Bioimpedance techniques are based on the injection into a biological medium (human body, tissue, or cell culture) of an alternating electric current of very low intensity. The electric current produces a voltage drop, the higher, the greater the electrical impedance of the tissue [12]. Bioimpedance measurements are based on the fact that biological mediums behave as conductors, dielectrics, or insulators of electrical current, depending on their composition. The result of this phenomenon is a dependence of bioimpedance values with frequency, which can provide information on the physiology and pathology of tissues and cells.

One of the most outstanding applications of bioimpedance in healthcare is the estimation of body composition, which is normally applied to assess the nutritional and hydration status and useful in multiple clinical areas: obstetrics [13], postoperative monitoring [14], critical care [15], pregnancy and lactation [16], gastroenterology [17], nutrition [18], chronic inflammation [19], obesity [20], or sports science [21]. An area of great interest is nephrology since it has been shown that bioimpedance methods can help in the dialysis process to achieve the desired euvolemic state [12].

Impedance cardiography (ICG) is another bioimpedance application of great clinical interest related to the noninvasive monitoring of cardiac dynamics. The analysis of ICG signals

is used in the diagnosis of patients with cardiovascular diseases [22, 23]. From ICG it is possible to obtain a series of parameters related to the mechanical function of the heart such as stroke volume, cardiac output, preejection period, left-ventricular ejection time, or systolic time ratio [22]. From bioimpedance measurements and more specifically by the analysis of pulse wave velocity (PWV), arterial stiffness can also be estimated, which is a parameter of interest in the diagnosis of hypertension situations or arrhythmia and stroke events [24]. Moreover, it can be used to find blood pressure indirectly [25].

The application of bioimpedance to obtain medical images of the inside of the human body should also be highlighted, which is known as electrical impedance tomography (EIT). In this method, harmless electric currents are applied on the subject skin and the resulting electric potentials are recorded with an electrode array [26, 27]. From these boundary voltage measurements, it is possible to reconstruct the internal volumetric conductivity distribution and images related to the impedance distribution inside a body, of great clinical interest despite its low resolution [28–30].

Bioimpedance methods are also the basis for clinical laboratory tools such as hematocrit meters, coulter counters, and cell culture monitoring systems, including Lab-on-Chip applications [31]. The bioimpedance spectrum reveals the electrical and mechanical properties of the cells such as growth, motility, activity, and viability [32, 33]. In cell cultures, bioimpedance has been used for the detection of interactions with drugs [34], the analysis of cell regulation [35], and its kinetics or the in vivo investigation of cancer models [36, 37].

Given their characteristics, bioimpedance measurements allow the characterization of biological media and organic tissues, including the human body, but also inorganic media [38]. In this sense, bioimpedance methods have been employed in skin monitoring (diagnosis of diseases and evaluation of a treatment progress) [38], cancerous tissue characterization and detection [31], sleep apnea detection through bioimpedance measurements [39], as a means of precisely controlling the energy delivered to the heart during defibrillation [40], as a predictor of intradialytic hypotension [41], for precise bone cement milling during revision of total hip replacement [42], for longitudinal knee joint health assessment [43, 44], for the evaluation of high-resolution temporal information corresponding to pharyngeal swallowing [45], to monitor the ischemia and viability of transplanted organs [46, 47], edema determination [48], brain and pulmonary function monitoring [49, 50], and even as a method for the noninvasive measurement of glucose level [51].

Bioimpedance devices are noninvasive, low-cost, portable, and user-friendly, practical advantages that have led to their rapid development. However, research in the field of bioimpedance is a very active area as more efficient and miniaturized instrumentation, novel models and algorithms, new parameters, and substance characterizations are required. It is important to optimize the sensors for sensitivity and power consumption, especially when used in Lab-on-Chip devices and implantable systems such as cardiac and other monitors and pacemakers. Repeatability

and reproducibility are often limitations of this technology; thus, novel sensing techniques are necessary. Moreover, high frequency measurements require in-depth circuit design techniques to overcome challenges.

The purpose of this paper is to provide a review of bioimpedance fundamentals and applications and an updated record of state-of-the-art in bioimpedance technology for healthcare applications. The content of the review is organized in the following sections and subsections:

(i) Section 2: Measurement methods and devices

    (a) Bioimpedance definition

    (b) Bioelectrical basis of bioelectrical impedance

    (c) Bioimpedance models

    (d) Electrode designs and configurations

    (e) Design and implementation of bioimpedance instrumentation

    (f) Sources of artifacts and noise in bioimpedance measurements

(ii) Section 3: Bioimpedance for body composition assessment

(iii) Section 4: Impedance cardiography

(iv) Section 5: Transthoracic impedance pneumography

(v) Section 6: Electrical impedance tomography

(vi) Section 7: Skin conductance applications

(vii) Section 8: Impedance detection in biosensors

(viii) Section 9: Future challenges of bioimpedance

2. Measurement Methods and Devices

This section reviews the fundamentals of bioimpedance measurements, from the instrumentation and hardware used in the devices to the bioimpedance models that support the measurement algorithms. Given the importance of the electrodes in this type of systems, a section is included that covers the most outstanding aspects found in the bibliography related to this term. A final part reviews noise problems and artifacts that affect bioimpedance measurements.

2.1. Bioimpedance Definition. The impedance (Z), or bioimpedance when it comes to a biological medium, is defined as the ratio of a voltage over the electric current that it generates (Z = V/I), and it represents the opposition of a conductor to the circulation of an electric current [12]. This property depends on the characteristics of the biological medium through which current flows, but also on frequency. Generically, bioimpedance is a complex number with electric resistance (R) as real part and reactance (X_C) as imaginary part, both expressed in Ω.

$$Z = R + jX_C \tag{1}$$

R is described as the opposition of the medium to the flow of electric current and is inversely proportional to the

conductance [52]. The other component, X_C, can be defined as the opposition of the medium to a change in electric current and is inversely proportional to the capacitance (biological mediums can be considered capacitive) [53].

2.2. Bioelectrical Basis of Bioelectrical Impedance.

Electricity and chemistry are intimately related in biological media. As the electric current is transported by ions dissolved in the medium, it is not possible to explain the flow of electric current without taking into account the electrolytic theory [54]. Conductivity defines the amount of electricity that can flow and is directly proportional to the concentration of dissolved ions in the biological medium. The electric resistance R increases if the concentration of ions decreases [52, 55, 56]. The viscosity of the medium, an increase in the concentration of nonconductive substances or in the distance between the measuring electrodes, or a decrease in the effective area of the medium are also factors that contribute to the increase of R. Other factors such as temperature or composition of the medium also influence the value of R.

There is another property related to bioimpedance in a biological medium, the permittivity, which describes the ability of the medium to be polarized by an electric field [55–57]. In dielectric media such as biological ones, a decrease in permittivity occurs as a consequence of the absorption of electromagnetic energy by the relaxation effects associated with the dipoles of the medium. At low frequencies, the changes produced in the electromagnetic field are slow enough to allow the dipoles to reach equilibrium before the field has reversed its polarity. From a certain frequency, the dipoles cannot follow the variations of the electric field due to the viscosity of the medium and a time delay is caused in the response of the medium, leading to the dissipation of energy in the form of heat. In biological media, three main dispersion regions can be distinguished in the frequency spectrum [55, 57–59]:

(i) α *dispersion*, normally in the frequency range between 10 Hz to 10 kHz. It is not fully understood yet but has been related to the phenomena of ionic diffusion of the cell membrane and the counterion effects [59, 60].

(ii) β *dispersion*, in the frequency range between 10 kHz and 100 MHz. It is mainly caused by the polarization phenomenon of cell membranes, whose behavior is similar to that of a capacitance [52, 58, 59]. The polarization phenomena of proteins and other organic macromolecules also contribute to this dispersion [58, 59].

(iii) γ *dispersion*, in the range of gigahertz, caused mainly by the polarization of water molecules [59, 60].

The dielectric spectrum can then be modeled as the sum of five dispersions, giving rise to the following expression for the complex relative permittivity (ε^*) depending on the angular frequency ($\omega = 2 \cdot \pi \cdot$ frequency) [61, 62]:

$$\varepsilon^* = \varepsilon_\infty + \sum_{n=1}^{5} \frac{\Delta\varepsilon_n}{1 + j\omega\tau_n} + \frac{\sigma}{j\omega\varepsilon_0} \tag{2}$$
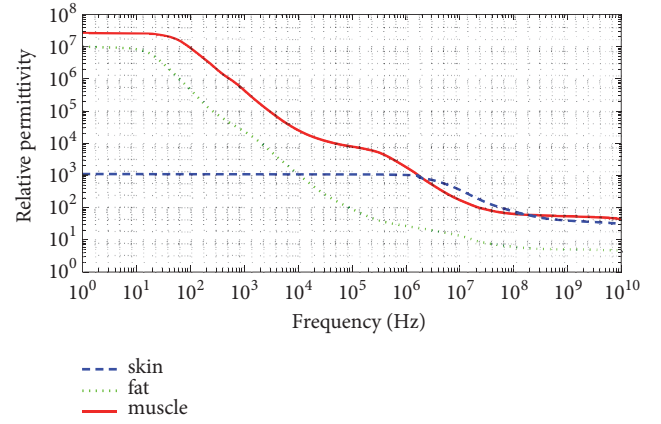
Figure 1: Relative permittivity of skin, fat and muscle [61].

where (ε_∞) is the permittivity at an infinite frequency, $\Delta\varepsilon_n$ and τ_n are the magnitudes and the time constants that characterize each dispersion (n=1,2,3 for α, β and γ dispersions, respectively) [63], and σ is the static ionic conductivity of the biological material. Figure 1 shows the dependence of the relative permittivity as a function of frequency for three body tissues (skin, fat, and muscle) according to the parameters defined in [61].

A more realistic model takes into account the complexity of biological materials, both in terms of composition and structure, through the inclusion of distribution parameters for of the time constants ($0 < \alpha_n \leq 1$), according to the Cole-Cole model [55, 62]:

$$\varepsilon^* = \varepsilon_\infty + \sum_{n=1}^{3} \frac{\Delta\varepsilon_n}{1 + (j\omega\tau_n)^{\alpha_n}} + \frac{\sigma}{j\omega\varepsilon_0} \tag{3}$$

The analysis of biological materials by bioimpedance is based on the study of the conductive or dielectric properties of the medium [58, 59, 64]. As the conductivity is directly proportional to the concentration of ions in the fluids of the medium, the electrolyte solutions of the body fluids (interstitial fluid, blood, lymph, etc.) and the soft tissues (muscles, organs, etc.) are good electrical conductors. The bone, the adipose tissue, and the air present in the lungs behave like a bad conductor (insulators). The frequency dependence in the bioimpedance differs from one tissue to another but also depends on the physiological state of the tissue (normal or pathological, alive or dead, dry or hydrated, etc.), so the impedance analysis is a suitable tool for the characterization of the state of the tissues [65].

2.3. Bioimpedance Models.

Biological media are characterized by the presence of cells. In them, the intracellular medium, formed by intracellular water (ICW), and the extracellular medium, composed of extracellular water (ECW), can be distinguished [66]. Both media are conductive, as a consequence of the dissolved ions, and separated from each other by the cell membrane that acts as a dielectric [12]. This context affects the conduction of the electric current, and its behavior resembles that of a capacitance in which ECW and
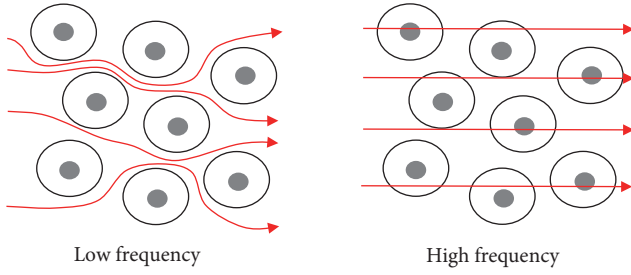
FIGURE 2: Current flow in a biological medium at low and high frequency.

ICW are the plates of the capacitor and the membrane is the dielectric material [52]. For this reason, at low frequencies the current mainly flows through the space between the cells (see Figure 2). As frequency increases, a greater amount of current also penetrates in the intracellular medium, the more the greater the frequency.

Throughout the literature, a set of models have been proposed to respond to this behavior, which is directly related to bioimpedance.

(i) *Single-dispersion RC model:* the simplest model of this behavior is a resistance R_E that exemplifies the extracellular path of the current in parallel to a series disposition of a resistance R_I and a capacitor C to incorporate the frequency behavior of the intracellular path, with C representing the cell membrane and R_I being the intracellular medium [66] (see (a) in Figure 3).

The bioimpedance in the s-domain can be expressed in terms of R_0 (resistance at zero frequency) and R_∞ (resistance at infinite frequency) as follows:

$$Z(s) = R_\infty + \frac{R_0 - R_\infty}{1 + \tau s} \tag{4}$$

where

$$R_0 = R_E \tag{5}$$

$$R_\infty = \frac{R_I \cdot R_E}{R_I + R_E} \tag{6}$$

s = jω, ω is the angular frequency, corresponding to 2πf, f is frequency in Hz, and τ represents the time constant of the dispersion due to the capacitive component. For the single-dispersion RC model, the time constant τ is calculated by the following expression:

$$\tau = (R_I + R_E) \cdot C \tag{7}$$

If the bioimpedance values, from a zero frequency to an infinite frequency, are represented in the complex plane, a circular impedance curve is obtained (see Figure 4). The imaginary part of the bioimpedance is commonly represented with the opposite sign

on the vertical axis, to avoid a representation in the fourth quadrant corresponding to a capacitive effect. The zero-frequency bioimpedance is purely resistive (R_0). As frequency increases, the position of the bioimpedance moves counterclockwise along the semicircle from R_0 to R_∞.

(ii) *Single-dispersion Cole model:* according to fractional calculus [67], a general fractional component with impedance in the s-domain proportional to s^α can be defined. The traditional components of the circuits would be special cases of this component with a value of α equal to 1, 0 and -1 for an inductor, resistor, and capacitor, respectively. A special case of the general fractional component is the constant phase element (CPE), whose impedance is $Z_{CPE} = 1/(s^\alpha C)$ in the s-domain, where C is the value of the capacitance and α is its order. Its name refers to its phase angle φ_{CPE}, which is constant at all frequencies and depends only on the α value ($\varphi_{CPE} = \alpha\pi/2$). Typical values of α are in the range of $0 \le \alpha \le 1$ [68].

The Cole model is composed of three components (see (b) in Figure 3): a resistor at infinite frequency R_∞, a resistor R_1, and a CPE. The bioimpedance is given by the following equation:

$$Z(s) = R_\infty + \frac{R_1}{1 + s^{\alpha_1} R_1 C_1} \tag{8}$$

The bioimpedance plot is also circular, but the circle center is located below the real axis of the impedance [12]. As it is shown in Figure 5, $\Theta = \alpha(\pi/2)$ is the angle in which the center of the circle is displaced below the real axis. The cause of this effect comes from a distribution of relaxation times caused by the heterogeneity of cell sizes and shapes, the inaccuracy of the membrane behavior as an ideal capacitor, or physiological processes like the Warburg diffusion [54]. This model is very used because of its simplicity and good fit with bioimpedance measurements.

The single-dispersion Cole model and its parameters have been employed in various medical applications, since each parameter of the model has its own physical meaning [12, 69]: body composition analysis [70], measurement of the concentration of urea in the dialysate [71], tissue characterization [72–74] or analysis of blood samples [75, 76], ischemia monitoring [72, 77], hydration status evaluation [78], or cancer detection [68, 79]. This model has also shown its utility in biology applications, fundamentally in plant physiology [80, 81] or the early detection of bacteria [69].

(iii) *Extended single-dispersion Cole model:* single-dispersion Cole model can be extended by introducing a time delay invariant with frequency (T_D), which exemplifies the delays caused by the electronics and the measurement cables [82]. This effect is modeled by a
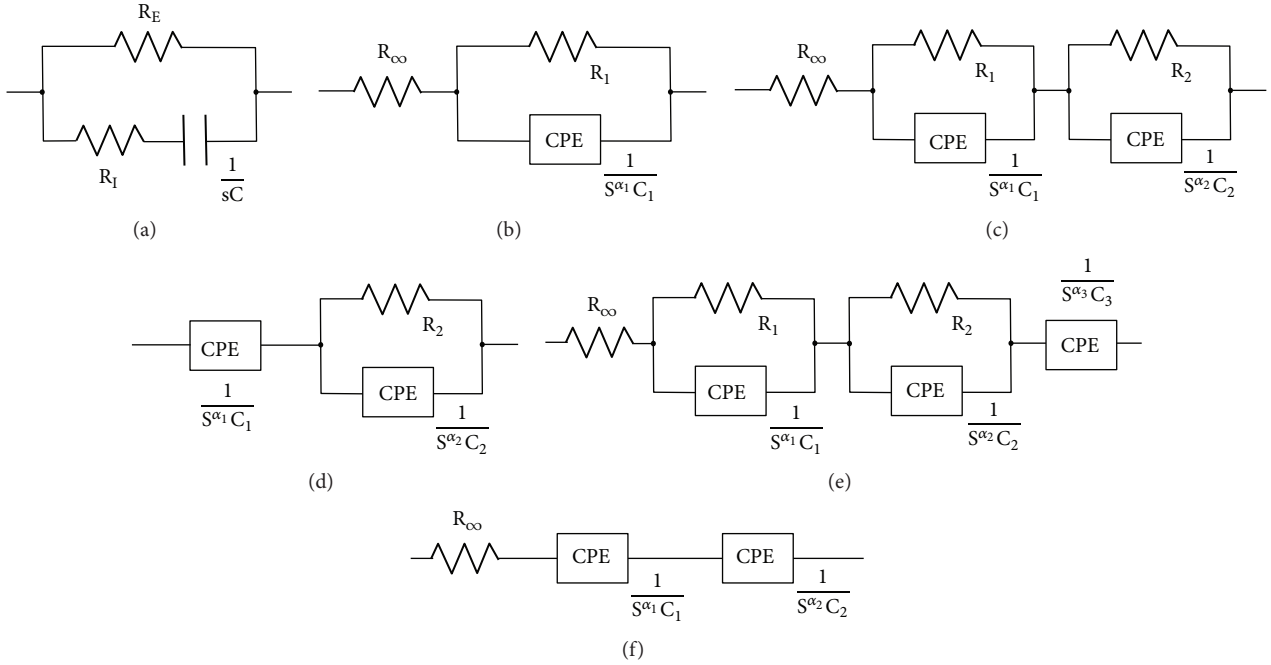
FIGURE 3: Bioimpedance models: (a) single-dispersion RC model, (b) single-dispersion Cole model, (c) double dispersion Cole model, (d) one resistor and two CPEs, (e) three resistors and three CPEs, and (f) one resistor and two CPEs, in series. R_E and R_I are the extracellular and intracellular resistances, respectively; C is the membrane capacitance; s is the complex variable in the Laplace domain; R_∞ is the resistance at infinite frequency; CPE symbolizes a constant phase element; R_1, R_2 are the resistance increase due to the first and second dispersions, respectively; α_1, α_2, and α_3 are the order of the fractional components associated with the first, second, and third dispersions, respectively; and C_1, C_2, and C_3 are capacitances related to the first, second, and third dispersions, respectively.
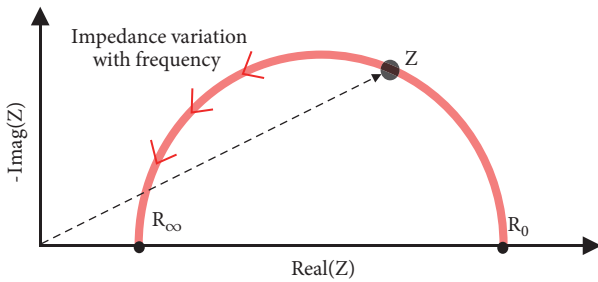
FIGURE 4: Typical bioimpedance plot.
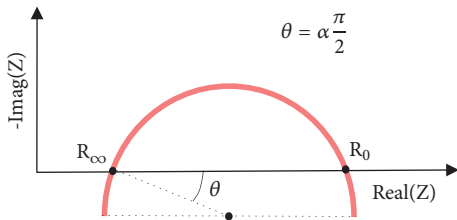
FIGURE 5: Bioimpedance plot of the single-dispersion Cole model.

linear phase increase with frequency as shown in the following expression:

$$Z(s) = \left(R_\infty + \frac{R_1}{1 + s^{\alpha_1} R_1 C_1} \right) e^{sT_D} \tag{9}$$

(iv) *Double dispersion Cole model:* this model allows representing the values of bioimpedance over a wider range of frequencies, where more than one dispersion can take place, or for more complex biomaterials [83]. This model is formed with a single-dispersion Cole model in series with a resistance and a CPE (see (c) in Figure 3) and the bioimpedance value responds to the following equation:

$$Z(s) = R_\infty + \frac{R_1}{1 + s^{\alpha_1} R_1 C_1} + \frac{R_2}{1 + s^{\alpha_2} R_2 C_2} \tag{10}$$

(v) *Other fractional models:* the model (d) in Figure 3 is formed by a resistance and two CPEs. This model has been used in the estimation of the internal moisture in wood [84], with a bioimpedance value given by

$$Z(s) = \frac{1}{s^{\alpha_1} C_1} + \frac{R_2}{1 + s^{\alpha_2} R_2 C_2} \tag{11}$$

The model (e) in Figure 3 has been used in the monitoring of root growth [85], which is formed by three CPEs and three resistors, with the following bioimpedance:

$$Z(s) = R_\infty + \frac{R_1}{1 + s^{\alpha_1} R_1 C_1} + \frac{R_2}{1 + s^{\alpha_2} R_2 C_2} + \frac{1}{s^{\alpha_3} C_3} \tag{12}$$

A resistor in series with two CPEs according to the model (f) in Figure 3 has been used in the modeling
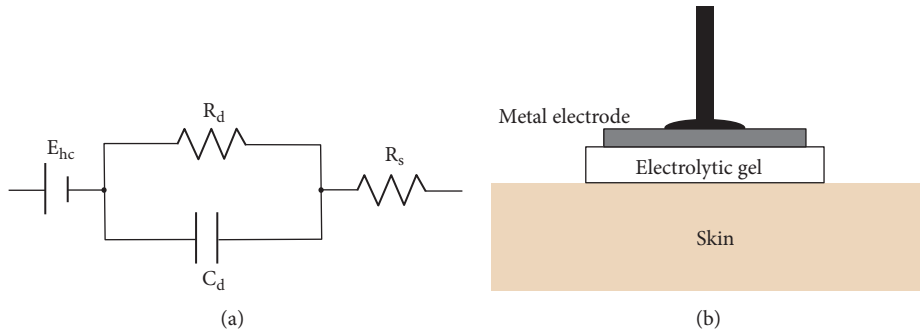
FIGURE 6: (a) Generic electrode model. (b) Electrode elements.

of the electrode-skin interface [86], with the following expression:

$$Z(s) = R_\infty + \frac{1}{s^\alpha C_1} + \frac{1}{s^\beta C_2} \tag{13}$$

(vi) *Multiscale models:* multiscale models have been proposed for modeling the dispersions of liver tissue. This model is built on a basic unit formed by resistors and capacitors [87], and through a hierarchical repetition of individual elements, from less to more, the different scales of the model are obtained: blood, liver cells, liver lobules, and liver tissue.

2.4. Electrode Designs and Configurations. A fundamental, but at the same time critical, aspect of a bioimpedance measurement system is the electrodes. They are the electrochemical interface necessary to put the biological medium in contact with the measuring equipment, both for the injection of current and for the detection of voltage. However, they are a major source of errors in bioimpedance measurements due to the stray capacitance and electrode polarization, the high contact impedance, the noise of the interface, and the artifacts due to movements, fluctuations, and contact problems [32, 88]. The impedance of the electrodes can be from hundreds of Ω to several MΩ, depending on frequency, but also on the characteristics of the electrodes [89]. One way to reduce the adverse effects is by maximizing the surface of the electrodes [32].

The design of a bioimpedance device starts from a good understanding of the behavior of the electrode-medium interface, thus the modeling of the electrodes has received a considerable interest [88, 90]. Figure 6 shows a generalized electrode model with a single time constant [12]. In this model, E_{hc} represents the double layer potential between the electrode and the electrolyte, when it exists, and between the electrolyte and the medium. R_d is associated with the conduction currents due to the double layer and C_d is associated with the displacement currents. R_s represents the conduction losses in the electrolyte. More precise models employ two time constants, the first to model the skin, and the second for the behavior of the electrode itself [89].

For bioimpedance measurements on the human body, the electrode-skin contact usually consists of a metal electrode,

an electrolytic gel, and the skin (see Figure 6). In these applications, the most common type of electrode is the Ag-AgCl electrode, with an electrolyte based on Cl$^-$ [22]. Current injection and voltage measurement electrodes are usually located on the hand and on the foot of the same side of the body (global lateral position (a) in Figure 7), although other positions are possible, also with the electrodes on the hands and feet because of their better accessibility: (b), (c), (d), (e), and (f) in Figure 7 for bioimpedance measurements of one arm, trunk, left leg, right leg, or two arms, respectively.

For ICG measurements, Ag-AgCl electrodes are usually used in the Sramek configuration [91], in which two electrodes are located on the right lateral side of the neck, and two other electrodes on the left side of the thorax [22] (see (g) in Figure 7). In contrast, electrical impedance tomography typically uses an array of multiple electrodes uniformly distributed over the measurement area [26] (see (a) in Figure 8).

Apart from the Ag-AgCl electrodes, other types of electrodes have also been used, such as the gold paste electrodes in the form of two concentric spirals presented in [38] to measure sweat on the skin. As an alternative to gel electrodes, capacitive electrodes have also been proposed as a measurement way that avoids direct contact with the user [92]. However, the results were not as accurate as in the traditional bioimpedance method because the impedance provided by the capacitive electrodes is much higher, in several orders of magnitude, than the impedance provided by the common direct contact electrodes and more susceptible to movement artifacts. Another example is the active electrodes based on a very low noise amplifier, with very high input impedance, and low output impedance, arranged directly on the electrodes [93].

Recently, textile electrodes have greatly increased their use in medical applications, including bioimpedance measurements, because they provide greater comfort to users, and to the extent that gel electrodes are not suitable for continuous use, they are disposable and can cause skin irritation [89, 94]. An example is the custom-made electrode garment described in [95], which is based on a biocompatible silver-based conductive fabric [95] for tetrapolar bioimpedance measurements between the wrist and the ankle.

In the case of microfluidic electrochemical sensors, coplanar electrode design is the most used configuration due to
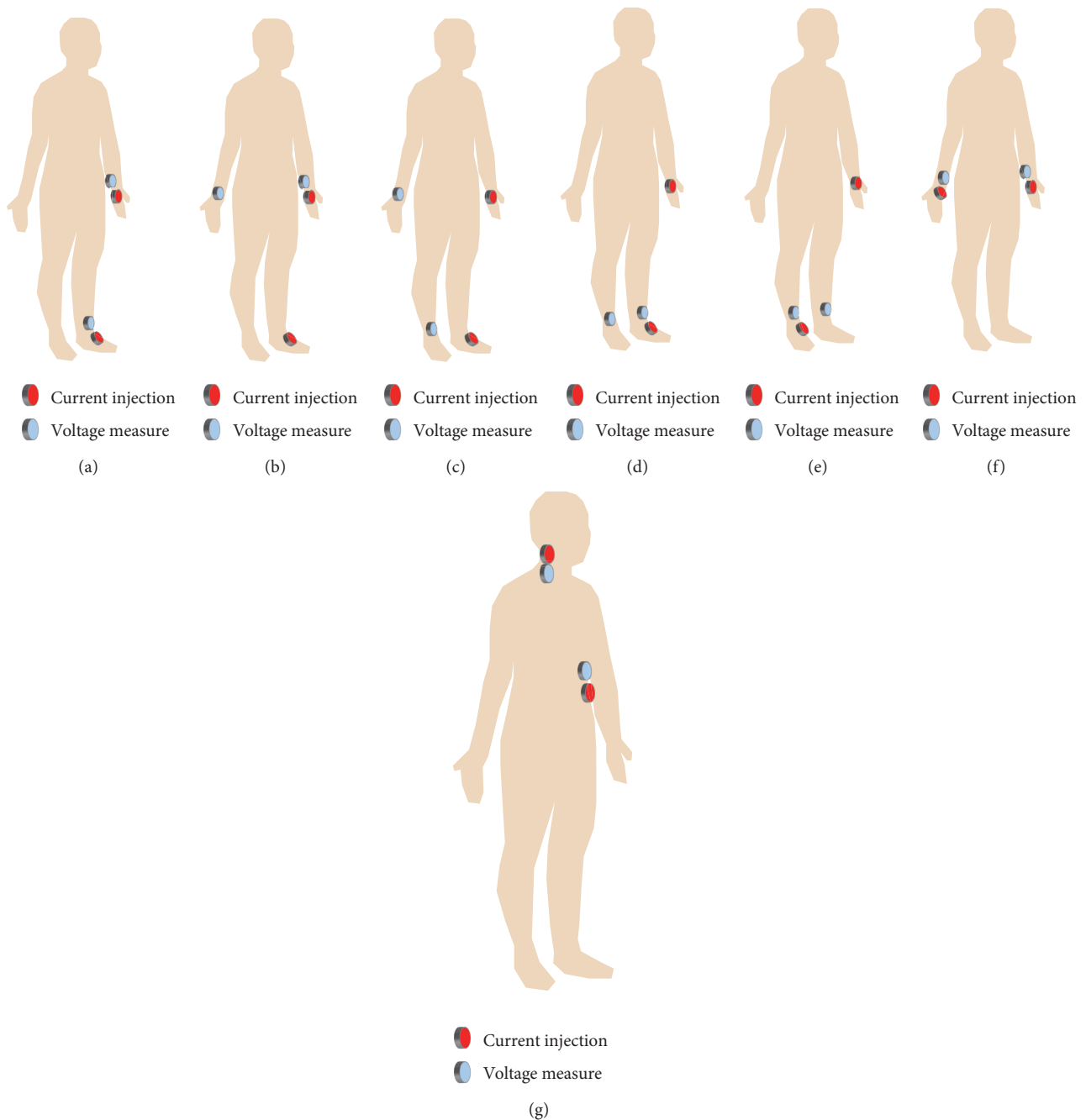
FIGURE 7: Typical electrode configurations for human body bioimpedance measurement: (a) global lateral, (b) one arm, (c) trunk, (d) left leg, (e) right leg, (f) two arms, and (g) example of electrode configuration for ICG measurement.

its easy manufacture. Nevertheless, the sensitivity of coplanar electrodes is limited as a result of the nonuniform field lines [32]. The incorporation of carbon nanofibers to the electrodes improves the sensitivity of these systems [96]. Another possibility is an arrangement of the electrodes in parallel plates [32].

For the characterization of biological media, the tetrapolar configuration is the most used because it minimizes the influence of the electrodes in the measurement process. This is the basis of the cylindrical chamber employed in [97] for

the analysis of breast cancer cells, with circular electrodes at the ends as current electrodes and needle electrodes inside as voltage sensing electrodes [97]. In [68], the tetrapolar configuration was used on the same plane to study samples of breast tissue.

However, the tetrapolar electrode configuration can be affected by the anisotropy of the tissue such as nerve fibers and muscle or blood vessels. Measurement schemes that include multiple orientations have been proposed in the literature, as the case shown in [98], in which sixteen

(a)   (b)
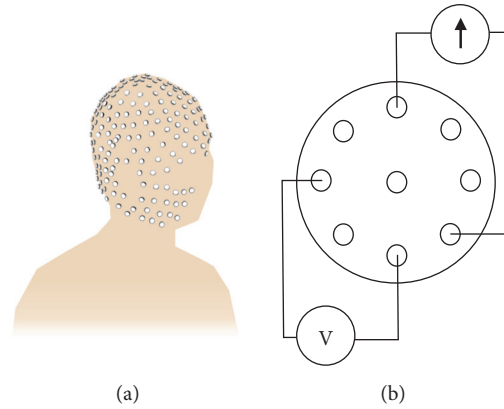
FIGURE 8: (a) Example of electrodes placement for electrical impedance tomography. Electrical impedance tomography of human head. (b) Example of electrode configuration for the simultaneous measurement in different orientations [37].

miniature electrodes perform sequential tetrapolar measurements to recover anisotropic conductivity tensors [98]. Another example is shown in [37], in which a nine-electrode microendoscopic probe was used (see (b) in Figure 8). In both cases, current injection and voltage measurement were carried out sequentially in different electrodes following a preconfigured pattern [37]. In [98, 99], new methods for measuring the anisotropy of tissues using bioimpedance have been proposed by modeling the anisotropy in both the resistivity and reactivity in three or more different directions. The anisotropy measurement has the potential to provide new insights in medical evaluation and diagnosis. In [100] a 16-electrode probe was used to reconstruct the anisotropic impedance spectrum allowing discriminating neurogenic and myopathic diseases. In other cases, however, a spiral structure has been employed in the electrodes to eliminate the anisotropic properties of the skin and measure the impedance independently of the direction in which the sensing device is located [38].

The polarity of the electrodes has also been analyzed in an application that uses bioimpedance as a guidance method during the craniotomy [101]. According to these results, a bipolar scheme, in which two opposite currents are injected into the medium at the same time in two different positions, is more sensitive than a monopolar scheme, with a single injection point.

2.5. Design and Implementation of Bioimpedance Instrumentation. The basis of a bioimpedance device is the injection of a current into a biological medium, at one or more frequencies, and the measurement of the voltage produced by the circulation of that current [102]. If the biological medium is the human body, in order to avoid any possible harmful effect, the international safety standards specified in standard IEC 60601 must be strictly complied [31, 95, 103]. For this reason, most devices inject a current less than 1 mA [45, 103].

The standard measurement frequency of bioimpedance devices is 50 kHz [31, 104]. However, due to the interest of the frequency behavior of bioimpedance [31, 33], some

devices analyze multiple frequencies by means of a more complex instrumentation. The frequency of the injected current can be generated by an oscillator [43, 105], but it can also be generated digitally by means of a digital-to-analog converter (DAC) [106, 107]. A voltage-controlled current source (VCCS) transforms this oscillating signal into a suitable current for its injection into the biological medium [43, 105, 106].

The injected current can be monitored to avoid exceeding the established limits [44], but the most common method is the injection of a fixed amplitude current [108]. Although multiple current source topologies have been employed for the VCSS, most are based on the improved Howland current pump [102, 106], implemented by discrete designs based on operational amplifiers (OPAM). However, this topology is not practical for integrated circuits (IC) due to the need for high-value precision resistors [109]. In this case, designs based on transconductors [110] and integrated current drivers fabricated in complementary metal-oxide-semiconductor (CMOS) technology have been proposed [111]. The desirable characteristics for the design of the VCCS are a constant current for variable loads and a high output impedance, especially in the case of EIT [112].

Bioimpedance measurements are mainly performed in two different configurations, depending on the number of electrodes [33, 45, 68, 107, 113]: two and four electrodes. When only two electrodes are used, the voltage is measured at the same current injection electrodes. This configuration is typical in the monitoring of cell cultures by electrochemical impedance spectroscopy (EIS), where the presence of a particle perturbs the electric field lines, and therefore the impedance, between two coplanar electrodes [96].

As the impedance of the electrode-medium interface is in series with the bioimpedance to be measured, important errors may arise. To solve this problem, the four-electrode configuration (tetrapolar) is usually employed [107, 108]. In this scheme, the current is injected by the external electrodes (distal electrodes) and the voltage is measured in the internal electrodes (proximal electrodes) (see Figure 9) by means of an instrumentation amplifier. Since the input impedance of
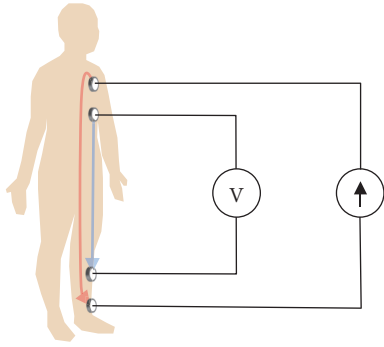
FIGURE 9: Four electrodes configuration.

the instrumentation amplifier is very high, the voltage drop at the sensing electrode can be considered negligible [36].

Bioimpedance can be evaluated in multiple ways by the measurement instrumentation. Below, some of the most relevant bioimpedance measurement schemes are presented:

(i) *Modulus measurement:* when only the temporal variation of the impedance modulus is of interest, it is common to perform an amplitude demodulation (bioimpedance variations can be seen as the modulation of a carrier signal in this case). The magnitude can be evaluated by peak detection [31, 114] or by rectification (half-wave or full-wave) with subsequent low-pass filtering [45].

(ii) *Phase measurement:* if a square current signal is generated, the comparison of the original signal and the measured signal can be used to detect the phase of bioimpedance [115]. XOR or SR latch schemes have also been employed to generate clock signals with pulse width dependent on the phase shift [116].

(iii) *Quadrature demodulation:* this method is based on two multiplications of the measured voltage signal, one by an in-phase signal (0°) and another by a quadrature signal (90°) [43, 44]. The output of each multiplier is filtered to obtain the DC components, and from them, the modulus and the phase of the impedance are estimated. The scheme of a bioimpedance meter based on quadrature demodulation is shown in Figure 10. The order and the cutoff frequency of the filter are established by the bioimpedance signal to be monitored [117]. If the bioimpedance changes slowly, a single multiplication can be used by alternating the phase between 0° and 90° [31].

(iv) *Intermediate frequency approach:* the high bandwidth required by the signal sensing channel has a negative effect on power consumption. To reduce this effect, the bioimpedance frequency can be transferred to a lower intermediate frequency before amplification. This procedure is generally carried out in two phases: first, the signal is transferred to baseband, and next the signal is modulated at an intermediate frequency. In [31] an alternative method composed

of a single phase was proposed. Finally, the signal is demodulated in amplitude or quadrature to obtain bioimpedance information.

(v) *Synchronous sampling:* since the amplitude, phase and frequency of the signal are known parameters, it is possible to obtain the complex bioimpedance value by sampling the signal at the instants in which the acquired signal reaches the peak values and zero-crossings [118]. This procedure requires a very precise synchronization and makes the measurement rather challenging at high frequencies [31].

(vi) *Oscillation-based method:* this method converts the medium under test into an oscillator. Any variation in the bioimpedance produces a variation in the oscillation frequency, which is easily measurable with minor hardware resources [33, 119]. In addition, the need to generate a stimulation signal is avoided. To maintain the oscillation condition, a nonlinear element (a simple comparator) is included in the feedback loop. LC oscillators have also been used in the monitoring of bioimpedance changes by displacements of the resonance frequency [119].

(vii) *Impedance bridge method:* in this method, an impedance bridge topology is used to estimate the bioimpedance of the biological medium, represented in Figure 11 as Z_B [12, 120]. Its value can be estimated by the following expression:

$$Z_B = \frac{Z_1 Z_3}{Z_2} \tag{14}$$

where Z_2 and Z_3 have known values and Z_1 is tuned until no current flows through M.

Current implementations of this method employ a simplified scheme known as self-balancing method [121]. A typical implementation is shown in Figure 12, where two voltage sources are used (V_1 and V_2), Z_1 is the impedance to calculate, and R_2 is a resistance of known value [121]. The signals V_1 and V_2 respond to the following expressions:

$$V_1 = A_1 \cdot \sin(2\pi f t) \tag{15}$$

$$V_2 = A_2 \cdot \sin(2\pi f t + \varphi_2) \tag{16}$$

The value of A_1 is known and fixed and the values of A_2 and φ_2 are modified until a balanced voltage is obtained in the G terminal. Then, the bioimpedance value can be calculated with the following equation:

$$Z = R_2 \frac{A_1}{A_2} \angle \varphi_2 \tag{17}$$

Variants of the self-balancing method have employed an instrumentation amplifier and a DAC to get the balance by feedback [122] or a scheme based on an adjustable digital potentiometer as reference and instrumentation amplifiers for measuring voltage values in a four-electrode configuration [123].
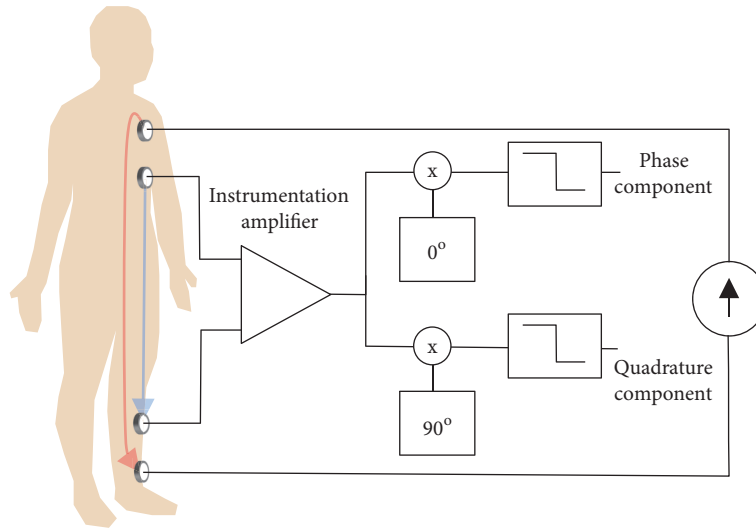
FIGURE 10: Quadrature demodulation method.
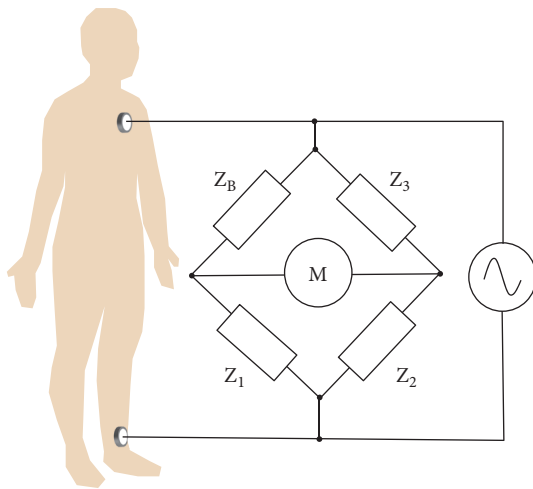
FIGURE 11: Impedance bridge method.
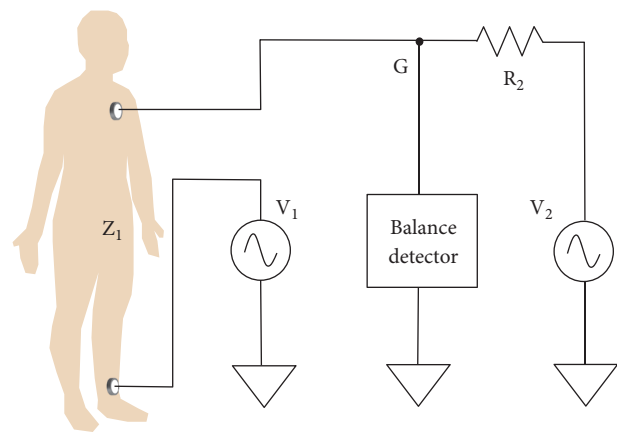
FIGURE 12: Self-balancing method bridge method according to [121].

(viii) *Amplitude-to-time conversion*: this method has been used in the evaluation of the gain/attenuation with respect to the reference voltage applied in EIT measurement systems [124]. It is based on the fact that sinusoidal signals of different amplitudes intercept each other with a fixed delay with respect to the reference signal, as shown by (18).

$$A \cdot \sin\left(2\pi f t\right) = \sin\left(2\pi f t + \varphi\right) \quad (18)$$

Figure 13 shows the scheme proposed in [124], in which a reference sinusoidal signal is generated as an offset copy of the excitation signal. Comparator A generates a square signal whose active value represents the condition that occurs when the delayed reference signal takes a negative value (see Figure 14). The square signal resulting from comparator B reflects

the intersections of the reference signal with the measured signal. The time duration of the period in which the signals from comparator A and comparator B are active at the same time is related to the gain of the measured signal. The relationship between this time measurement and the gain also depends on the phase shift applied by the phase-delay unit, and a calibration can be performed to adjust this parameter [124].

(ix) *Fast Fourier Transform (FFT)*: FFT has also been used to obtain the bioimpedance spectrum using a multisine excitation [125], chirp signals [126, 127], or white noise [128].

(x) *Orthogonal sequential digital demodulation method*: in this method, two or more frequencies are employed, and subsequently, a digital demodulation based on the orthogonal property of the triangle function is performed [129, 130].

FIGURE 13: Amplitude-to-time conversion method proposed in [124].

(a) Gain = 0.2

(b) Gain = 0.8

FIGURE 14: Example of signals obtained according to amplitude-to-time conversion method for two gain conditions: (a) 0.2; (b) 0.8.

In a complementary way, bioimpedance measurements in multiple locations of the biological medium can be combined to improve the sensitivity and specificity, as in EIT [26]. In this case, frequency- or time-division multiplexing can be used to avoid superposition in the excitation signals [131].

Some commercial chips have also been developed to perform bioimpedance measurements. AD5933 impedance

network analyzer of Analog Devices performs impedance measurements between two terminals within the frequency range of 1 kHz to 100 kHz [22, 95, 108]. For this, it uses a 12-bit ADC and a processing based on FFT. To allow the use of AD5933 in humans in a four-electrode configuration, analog-front-end (AFE) designs have been proposed [108, 132]. AFE4300 of Texas Instruments is another example of

a chip for bioimpedance measurements. Its design is based on a 6-bit pattern generator, a VCCS that generates a current signal between two terminals and a 16-bit ADC. However, the 150 kHz limit of the system makes it unsuitable for bioimpedance spectroscopy applications [133]. AD8302 of Analog Devices is a phase and gain detector that has also been used in bioimpedance estimations [105]. These advances and the important research effort carried out in this field have allowed the development of wearable bioimpedance devices, some of which include wireless communication capabilities [22, 95, 108, 134].

2.6. Sources of Artifacts and Noise in Bioimpedance Measurements. A bioimpedance measurement system is more robust and stable against noise and motion artifacts than other biopotential measurement systems such as the ECG as a consequence of the injection of a reference current in one or more well-determined frequencies, which generates a voltage easily measurable in most cases [135]. However, bioimpedance measurements can be affected by multiple sources of error that can affect the signal-to-noise ratio (SNR) [22].

The first challenge faced by a bioimpedance device is the design of the current generator, which ideally must be precise and stable, both in modulus and phase, independently of the measured bioimpedance value [31]. This avoids the need for constant measurement of the injected current and minimizes its effect as a possible source of noise. A precise generation of a sine wave may require a high-precision DAC, which affects the power consumption and cost of the device [136]. In this case, a square signal can be used instead of a sinusoidal source. The harmonics generated by the square wave produce an error in the demodulation of the signal, but correction algorithms can be used to improve the precision of the estimations [136]. Another way to generate a precise sine signal is through a stable oscillator, as the case of the diode-stabilized Wien-Bridge oscillator described in [43]. To maintain the accuracy, the sinusoidal signal must be converted into current by means of a VCCS with a high output impedance and a high bandwidth, in order to support the bioimpedance variations without any distortion [43]. In the case of very small impedance, the gain of the VCCS can be controlled by increasing its value to improve the SNR [43], always within the safety limits established in IEC 60601 [95].

Another challenge is the design of a voltage measurement stage, sufficiently precise and robust against noise. It is common to use an instrumentation amplifier with a high input impedance, high common-mode rejection ratio (CMRR), typically greater than 80 dB, and sufficient bandwidth to support the measurement frequencies without distortion [136–138]. However, the sensitivity requirements in the EIT applications are even stricter and any improvements provided in the accuracy of the measurements will result in a decrease in errors and an increase in the accuracy of the images. For this purpose, structures based on dual instrumentation amplifiers have been proposed to reduce the input noise, decrease energy consumption and improve the gain [107, 139, 140].

In a system based on bioimpedance spectroscopy, the error in the estimates decreases if the number of measurement frequencies [133] increases and/or an exhaustive timing control of the signals is performed, as it can be done in a field-programmable gate array (FPGA) device [106]. The sources of noise are also reduced by a suitable calibration of the bioimpedance device, incorporating the capacitive effects in the frequency response [141] and the effect of the electrodes [103]. This calibration is usually done manually, although it can be convenient to carry out automatically [22].

Some authors have shown the effect of the parasitic capacitance of the body to the earth C_B as a major source of errors in bioimpedance measurements above 100 kHz [142]. This capacitance can be from 11 pF to 3.9 nF for a standing person [143]. It produces gain and nonlinear errors whose main effects are the following [142, 143]:

(i) A gain error that increases with the frequency, behaving like an inductive effect proportional to the value of C_B and the sum of all the resistances (measured and parasitic). This effect can even lead to positive phase angles in the bioimpedance measurement.

(ii) A gain error independent of the frequency and proportional to the ratio between C_B/C_C, where C_C is the capacitance of the electrode. This effect translates into an offset in the magnitude of the bioimpedance.

(iii) A resonance effect that may be below 1 MHz, generated by the input capacitance of the instrumentation amplifier C_{in} and the inductive effect of C_B. If C_{in} is kept below 10 pF, it is possible to keep the resonance frequency above 10 MHz.

In bioimpedance systems based on spectroscopy, a key point is a correct identification of the single-dispersion Cole model parameters, since important errors can be made if this process is not carried out in a convenient way. As already mentioned in Section 2.3, the bioimpedance plot has a circular shape (see Figure 5). From the circular arc, the theoretical R_0 and R_∞ can be approximated by projecting the curve that best fits the bioimpedance values [67]. The parameter α can be estimated taking into account the angle formed by the center of the circle with the real axis of the bioimpedance ($\varphi_{CPE} = \alpha\pi/2$). The frequency at which the maximum of the absolute value of the bioimpedance imaginary part is produced corresponds to $f_C = 1/\tau$, where τ is the time constant of the dispersion. The value of this frequency allows the calculation of the parameter C, since $\tau = [(R_0 - R_\infty)C]^{1/\alpha}$.

Cole model parameter identification is normally obtained by means of Nonlinear Least Squares (NLLS) methods, which aims at obtaining the best coefficients for the Cole model that fits the curve minimizing the summed squared of the error between the measured data and the modeled values [73, 144–146]. Some authors use only the impedance modulus when performing parameter identification [145, 147, 148], others only use the real or imaginary part [67]. However, the techniques that achieve a smaller error use both the real and the imaginary parts of the impedance [145] and recursive algorithms for parameter search, using NLLS methods [144].
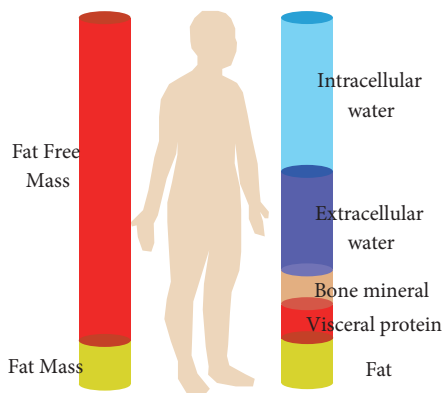
FIGURE 15: Compartmental model of the human body.

These methods do not often solve analytically the problem of parameter identification but use complex algorithms of successive approximations that can only be executed off-line on personal computers.

A major research effort has been made to reduce the amount of hardware needed and the cost of bioimpedance measurement instruments so that they can be used in portable applications [149, 150]. Part of this effort has focused on reducing the processing costs so that it can be performed in portable devices [67].

3. Bioimpedance for Body Composition Assessment

The human body can be considered as a multicompartmental system, in which in a first instance each cell can be considered as a compartment [12]. In a generalized model, two compartments could be considered: the intracellular compartment, which contains the ICW, and the extracellular compartment, which integrates the ECW. The border between both media is the cell membrane [151]. The total body water (TBW) is the sum of ICW and ECW. The distribution of water content is nonuniform throughout the body and can be considered another model composed of a fat mass (FM) compartment, which includes water-free body lipids, and another compartment formed by the rest, called fat free mass (FFM) [151] (see Figure 15).

Bioelectrical impedance analysis (BIA) is a set of methods applied in the estimation of body composition through the measurement of bioimpedance [12]. The basis is the determination of the electrical impedance of an electric current that passes through the body that can be estimated in one or multiple frequencies. The BIA analysis has become a standardized technique in the estimation of body composition since it does not present the restrictions of the dissolution methods [152–154] and provides more accurate estimations than the anthropometric methods [154]. In addition, it is a simple, safe and noninvasive technique. Thanks to the BIA analysis it is possible to obtain an estimation of body fluid volumes and body composition in both normal and pathological states. The bioimpedance methods also have many practical advantages that have guided its rapid development

[152, 153]: the instrumentation is portable, relatively low-cost, and the measurements can be carried out quickly with minimal operator training; bioimpedance methods require little maintenance and the measurements are safe and easy to perform; it is a noninvasive technique, requiring only the placement of electrodes in the body; the results are obtained immediately, and the measurements can be repeated as often as desired, with great interobserver reproducibility.

The clinical usefulness of BIA techniques has been demonstrated in numerous studies: in nephrology [12, 155] (identification of dry weight in renal patients, improvement of cardiovascular management, monitoring of fluid transfer during ultrafiltration, estimation of the volume of distribution of urea in the calculation of the Kt/V parameter, or nutritional assessment), in nutrition (chronic malnutrition [156], obesity [157, 158], cachexia [159], sarcopenia [160], etc.), during pregnancy [161] and lactation [162], for the risk assessment of various pathologies [163], as a marker or direct cause of diseases [164], during the process of decision making in a disease, during aging or a rehabilitation process [165], as a complement in the diagnosis and monitoring of conditions related to the cardiovascular system (fluid accumulation after cardiac surgery [155], hyponatremia [166], etc.), in issues related to the immune system (patients with AIDS, dengue, hemorrhagic fever, and chronic inflammation [167]), in the evaluation of nutritional status in nervous system-related conditions (Alzheimer [155], anorexia nervosa [168], and mental disability [169]), in pediatrics [170], in oncology (evaluation of the patient's condition [155, 171], early diagnosis [172], etc.), in the postoperative period [171], for patients in critical care (follow-up of physiological trends in intensive care [173], sepsis [174], hemodynamic resuscitation [175], acute respiratory distress syndrome [176], patients bedridden [177], and patients with liver cirrhosis [178]), in gerontology [179, 180], and even in sports science (evaluation of the effectiveness of a training program [21], detection of anomalies in the distribution of liquids [181], etc.).

BIA analysis is also useful in chronic respiratory diseases, where the loss of body weight and the decrease in muscle mass have been recognized as risk factors associated with increased morbidity (inflammation, cachexia, anorexia, skeletal muscle dysfunction, increase of dyspnea, worsening of health status, increased risk of exacerbations, and decreased exercise capacity) [182], mortality [183], and a deterioration in the quality of life [184]. But fundamentally, BIA has a special relevance in patients with chronic or acute kidney disease, where fluid excess is also a condition related to increased morbidity and mortality [185].

The common basis of all BIA analysis systems is a measurement of the human body bioimpedance. To provide greater accuracy in estimations it is common to keep the human body in supine position for a time before the measurements, typically 15 minutes, to favor the balance of body fluids [186]. The electrodes are usually arranged according to the global lateral position shown in Figure 7, although many other configurations are possible [187]. Finally, the estimation of body composition is made from the analysis of bioimpedance measurements, which can be performed from

TABLE 1: Examples of SFBIA equations.

Compartment	Equation	Reference
TBW	*Men:* 1.02 + 0.449·Height(cm)^2/R$_{50kHz}$ (ohm) + 0.176·Weight(kg) *Women:* 3.747 + 0.45·Height(cm)^2/R$_{50kHz}$ (ohm) + 0.113·Weight(kg)	[188]
ECW	*Men:* -5.22 + 0.2·Height(cm)^2 /R$_{50kHz}$ (ohm) + 0.005·Height(cm)^2/X$_{50kHz}$ (ohm) + 0.08·Weight(kg) + 1.9 *Women:* ECW (Men) + 1.86	[190]
FFM	*Women:* -12.44 + 0.34·Height(cm)^2/R$_{50kHz}$ (ohm) + 0.1534·Height(cm) + 0.273·Weight(kg) - 0.127·Age(years) *Men:* FFM (Women) + 4.56	[191]
Body fat % of the Weight	*Women:* 14.94 - 0.079·Height(cm)^2 /R$_{50kHz}$ (ohm) + 0.818·Weight(kg) - 0.231·Height(cm) + 0.077·Age(years) *Men:* Body Fat (Men) - 0.064·Weight(kg)	[189]

multiple approaches. The most representative methods are shown below.

(1) Single Frequency Bioimpedance Analysis (SFBIA). In order to simplify the analysis of bioimpedance, the human body can be modeled as a cylinder whose length is the height [66]. The electrical resistance of this model responds to the following generic expression, where σ is the cylinder conductivity:

$$R = \frac{Height}{\sigma \cdot Area} = \frac{Height^2}{\sigma \cdot Volume} \qquad (19)$$

Multiplying the numerator and denominator by the height, it is possible to obtain a generic expression of the volume depending on the height and resistance of the virtual cylinder that models the human body [52]:

$$Volume = \frac{Height^2}{\sigma \cdot R} \qquad (20)$$

This relationship is the basis of SFBIA for the estimation of body compartment volumes. Numerous equations have been proposed in the literature for the approximation to the body parameters using the SFBIA technique [188–191]. These equations are usually defined from a regression analysis on a study population using the parameter Height^2/R as one of the independent variables. To take into account the anthropometric characteristics of the subject, other variables such as weight or sex can also be incorporated as independent variables. The dependent variable is the body parameter to be estimated, which can be the volume of water (ICW, ECW, or TBW), but also the corresponding weight of fat or lean mass. The reference of this parameter is obtained from the standard gold estimation method, usually dissolution methods [133]. The resulting equations usually respond to the following expression [66, 192]:

$$Volume = K_0 + K_1 \cdot Weight + K_2 \cdot \frac{Height^2}{R} \qquad (21)$$

in which the coefficients K_i are determined by the multivariate linear regression analysis in the study population [133]. Normally, SFBIA equations use the resistance value at the frequency of 50 kHz [193], since this is the standardized frequency. The Table 1 shows some examples of equations based on the SFBIA method for different body compartments.

These equations have been selected for their widespread use and a minor error obtained in the evaluation studies [194]. The estimation of body parameters can be performed for a body segment (leg, arm, trunk, etc.) [195], modeling this segment as a cylinder, or for the whole body, in which case the different sections are approximated by different cylinders [52], although it could be considered a single cylinder that weighs the influence of the different body sections [196].

If the equations use the impedance obtained in two or more frequencies, the method is then called Multifrequency Bioimpedance Analysis (MFBIA). The main disadvantage of SFBIA and MFBIA methods is that the parameters of the equations are obtained empirically by means of a regression analysis. If these equations are applied in a different population group from which they were established, in altered states of composition or in people with anatomical particularities, important errors may occur in the estimations.

(2) Bioimpedance Spectroscopy (BIS). The BIS method removes the apparent population specificity of the SFBIA methods. This method is based on the fact that low-frequency currents only flow through the extracellular compartment, while high frequency currents circulate through both compartments. This assumption, together with the theory of mixtures of Hanai, has resulted in a set of equations for the estimation of the body compartments [63]. The ECW is obtained from the resistance $R_{ECW} = R_0$ according to the following expression [12, 63, 103, 106, 133]:

$$ECW = \frac{1}{100} \cdot \left(\frac{K_B \cdot \rho_{ECW} \cdot Height^2 \cdot \sqrt{Weight}}{D_B^{1/2} \cdot R_{ECW}} \right)^{2/3} \qquad (22)$$

in which K_B is a dimensionless form factor with a typical value of 4.3 that incorporates the geometry of arms and trunk in the virtual cylindrical model of the human body [196], ρ_{ECW} is the resistivity of the extracellular medium, height is in cm, Weight is in kg, and D_B is the body density in kg/L.

Similarly, TBW can be estimated from R_∞ by the following equation [12, 133, 192, 197, 198]:

$$TBW = \frac{1}{100} \cdot \left(\frac{K_B \cdot \rho_\infty \cdot Height^2 \cdot \sqrt{Weight}}{D_B^{1/2} \cdot R_\infty} \right)^{2/3} \qquad (23)$$

where ρ_∞ is the expected resistivity of the human body at an infinite frequency.
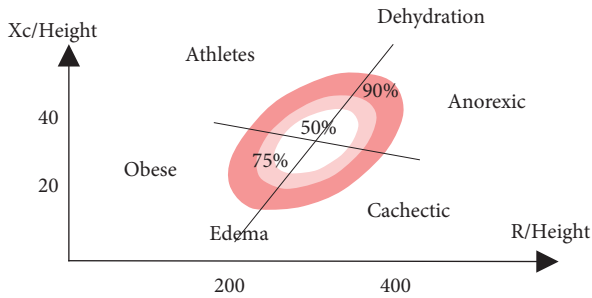
Figure 16: BIVA graph.

From TBW it is possible to calculate ICW, since ICW=TBW-ECW, and FFM, taking into account the fact that the water proportion of FFM in normal states is 73.2% [199]. In addition, the FM and its percentage can be established from FFM, since according to its own definition, FM=W-FFM.

4. Impedance Cardiography

(3) Bioelectrical Impedance Vector Analysis (BIVA). The BIVA method does not require assumptions about geometry, as in the case of the BIS method, and it does not depend on approximations obtained by regression, as in the SFBIA method [12, 108, 200]. BIVA is based on a vector representation of the resistance and the reactance of the bioimpedance, normally at the frequency of 50 kHz, in absolute and normalized values with respect to the height of the subject. R/height is plotted on the abscissa axis and X_C/Height on the ordinate axis [201]. Due to the correlation that exists between R and X_C, the distribution of bioimpedances on the BIVA graph takes an elliptical form as shown in Figure 16. In this figure we can see the tolerance or reference ellipses that represent 50%, 75% and 95% of the reference population. Given their dependence on the study population, multiple reference ellipses have been proposed for different ethnic groups based on sex, age, and even body mass index (BMI) [108, 202, 203]. The bioimpedance values that fall outside the reference ellipse of 75% indicate an abnormal physiological situation, and depending on its location, the following analysis can be performed [12, 203]:

(i) Variations along the major axis of the ellipse are related to the state of hydration. Situations below the lower vertex indicate a state of overhydration or edema, or a state of dehydration above the opposite vertex.

(ii) Variations along the minor axis are associated with nutritional status, with excess of soft tissue or cells in situations that surpass the left vertex and deficit of cell mass with respect to the opposite vertex.

(4) Clinical Results in Body Composition Assessment. The estimations performed by bioimpedance devices have been compared with the results obtained by the methods considered gold standard in the measurement of the body composition (deuterium oxide dilution (D_2O) or tritium dilution (TrD)

for TBW measurement, bromide dilution (BrD) for ECW assessment, total body potassium (TBK) for ICW determination and dual-energy X-ray absorptiometry (DEXA) for measurements of fat mass and lean mass). Tables 2 and 3 show some comparisons of the results obtained in several recent clinical studies. Table 2 shows the correlation coefficient r and the p-value of statistical significance obtained in different correlation studies between the bioimpedance methods and the reference methods. Table 3 indicates the results of Bland Altman's analysis in relation to the mean value of the differences (reference value-BIA value) between the two estimations and the 95% confidence interval (CoIn) of the differences.

The comparative results of BIA methods show a good correlation and concordance with the reference methods, indicating an adequate accuracy. The BIS method is more accurate than the SFBIA method if the mean error is taken into account, although both ones are comparable. Usually, FFM is overestimated in BIA with respect to BIS. In contrast, fat mass is underestimated. Fluid excess can reduce the accuracy of DEXA, so bioimpedance may be a better option for patients in altered states of hydration. Moreover, DEXA which possibly underestimates FFM, which agrees with the estimates made by bioimpedance [204], does not allow evaluating the distribution of TBW between ECW and ICW so as to estimate body cell mass [205] and BIA has the advantage over DEXA of avoiding radiation exposure. As the BIA method is simpler, less invasive, and less expensive, its routine clinical use is reasonable [206]. Most studies on BIA also show its usefulness in the evaluation of changes in body composition [207].

Impedance cardiography (ICG) comprises a set of methods that provide an assessment of the transthoracic electrical bioimpedance and its time dependence on blood volume, circulation, and cardiac function [215]. It is also known as transthoracic electrical impedance plethysmography and provides a noninvasive approach to the measurement of the cardiac output [216]. Transthoracic impedance is modulated by cardiorespiratory activity, such that a decrease in impedance can be related to an increase of blood flow. The derivative of impedance (dZ/dt) contains a set of seven points (A, B, E, X, Y, O, Z, see Figure 17) related to cardiodynamic events [217]. Hence, cardiovascular condition and diverse hemodynamic parameters such as heart rate, cardiac volume, stroke volume, cardiac output, vascular resistance, velocity index, or thoracic fluid content, among others, can be noninvasively monitored against time by extracting characteristic points and periods of the dZ/dt signal through ICG [218]. Stroke volume (SV) can be estimated in milliliters per beat from Kubicek formula:

$$SV = \rho_b \left(\frac{L}{Z_0} \right)^2 \cdot LVET \cdot \left. \frac{dZ}{dt} \right|_{max} \tag{24}$$

where ρ_b is the resistivity of blood, L is the transthoracic length, Z_0 is the impedance baseline, LVET is the left-ventricular ejection time (i.e., X-B segment), and $(dZ/dt)|_{max}$ is the maximum slope of the impedance signal on a given beat. Cardiac output (CO) is computed in milliliters per

TABLE 2: Comparison of correlation analysis results in studies of body composition.

Study	Sample size	Measurement	Reference method	Bioimpedance method	Bioimpedance device	Correlation coefficient r	p-value
[193]	94 patients on growth hormone replacement therapy	TBW (L)	TrD	SFBIA [208] SFBIA [189] SFBIA [209] SFBIA [188] BIS [154] BIS [63]	Body Scout, Fresenius Medical Care, Germany	0.9 0.91 0.97 0.97 0.97 0.96	p < 0.001
[207]	122 adult hemodialysis patients	TBW (L)	DEXA	BIS	Body Composition Monitor, Fresenius Medical Care, Germany	0.87	p < 0.001
[204]	84 postmenopausal women	Fat mass (kg) Fat mass (%)	DEXA	MFBIA	BIA-ACC, BIOTEKNA, Italy	0.95 0.76	p < 0.001
[205]	11 hemodialysis patients 25 healthy subjects	Fat mass (kg)	DEXA	BIS	Impedimed IMP SFB7, Impedimed, USA	0.96 0.92	p < 0.001
[210]	30 healthy adults	FFM (kg) Fat mass (kg)	DEXA	SFBIA	RJL Systems Quantum IV, RJL Systems, USA	0.96 0.92	p < 0.001
[206]	53 adult hemodialysis patients	Bone mineral (kg) Fat mass (kg) FFM (kg)	DEXA	SFBIA	InBody S10, InBody, Korea	0.67 0.93 0.96	p < 0.001

minute as stroke volume times the heart rate. Cardiac index (CI) is obtained from CO normalizing with respect to body surface area.

Research works about ICG started in the 1940s and technology development in the 1960s. ICG bioimpedance is performed by using a constant current injection approach using a four-electrode (tetrapolar) arrangement. Usually, currents in the frequency range of 20-100 kHz are used for excitation at the driving electrodes and voltage is measured at the sensing electrodes. The common configuration places the driving electrodes around the abdomen and the upper part of the neck, respectively, while the sensing electrodes are fixed around the thorax and the lower part of the neck [219]. Both band and spot electrodes have been reported for the use of ICG [220].

The advances in microprocessor technology and wireless communications have accelerated the design and development of wearable multifunction sensors providing the joint electrical (ECG) and mechanical (ICG) ambulatory monitoring of heart function using high-resolution analog-to-digital converters [221, 222], embedded design with LabView [223], Raspberry PI platform [22], or off-the-shelf impedance converters [224]. The imperative of portability is a usual requirement for recent ICG monitors [225, 226]. The use of textile electrodes has improved the portability of ICG systems through its seamless introduction in shirts [227], vests [228], the use of necklace-shaped electrode arrangements [229], or the adoption of contactless approaches [230, 231]. In other works, ICG and ECG are complemented with transmission and reflection photoplethysmography (PPG) to reduce the
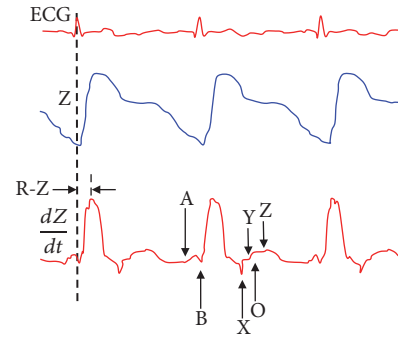
FIGURE 17: Transthoracic bioimpedance signal, its derivative, and relevant points (adapted from [220]).

sensibility of ICG to noise interference [232]. This interference has also been studied in [233] in the context of simultaneous functional magnetic resonance imaging and ICG acquisition, showing that changes in impedance (dZ/dt) are not affected.

In the context of processing the ICG signal, efforts are placed on improving the accuracy of slope change for the impedance derivative's (dZ/dt), which is related to the opening of the aortic valve [234]. The same issue has been addressed in [235] by considering the computation of the second and third derivatives, revealing the importance of the latter. The removal of ICG artifacts (both physiological and nonphysiological) has also been addressed by using adaptive filtering techniques [236] and wavelet analysis [237, 238].

TABLE 3: Comparison of bland Altman analysis results in studies of body composition.

Study	Sample size	Measurement	Reference method	Bioimpedance method	Bioimpedance device	Differences Mean value	95% CoIn
[211]	49 hemodialysis patients	TBW (L)	D_2O	SFBIA	Xitron 4200, Xitron Technologies, USA	-2.1	-5.3 to 1.1
		ICW (L)	TBK			0.5	-1.5 to 2.4
		ECW (L)	BrD			-4.4	-6.2 to -2.6
		TBW (L)	D_2O	BIS		1.9	-1.3 to 5.1
		ICW (L)	TBK			0.3	-1.7 to 2.2
		ECW (L)	BrD			-0.2	-1.9 to 1.6
[193]	94 patients on growth hormone replacement therapy	TBW (L)	TrD	SFBIA [208]	Body Scout, Fresenius Medical Care, Germany	2.3	-5.8 to 10.4
				SFBIA [189]		-0.9	-9.3 to 7.5
				SFBIA [209]		-2.7	-7.5 to 2.1
				SFBIA [188]		-2.1	-7.2 to 3
				BIS [154]		0.6	-4.2 to 5.4
				BIS [63]		0.9	-4.1 to 5.8
[212]	130 women with a normal weight to the third degree of obesity	Fat mass (kg)	DEXA	SFBIA	Bodystat 1500, Bodystat, Isle of Man	-0.7	-9.4 to 8
					Omron BF 300, Omron, Japan	-0.6	-7.2 to 6
					Tanita TBF 410 GS, Tanita, Japan	0.6	-7.3 to 8.5
[213]	120 pre-dialysis patients	Body fat (kg)	DEXA	BIS	Body Composition Monitor, Fresenius Medical Care, Germany	3.1	-6.8 to 13
		FFM (kg)				-2.8	-12 to 6.5
[204]	84 postmenopausal women	Fat mass (kg)	DEXA	MFBIA	BIA-ACC, BIOTEKNA, Italy	3.5	1.5 to 8.6
		Fat mass (%)				5.3	-2.3 to 12.8
		FFM (kg)				-2.9	-11.1 to 5.4
		FFM (%)				-5.2	-12.5 to 2.1
[207]	122 adult hemodialysis patients	Fat mass (kg)	DEXA	BIS	Body Composition Monitor, Fresenius Medical Care, Germany	0.3	-5.5 to 6.2
[210]	30 healthy adults	FFM (kg)	DEXA	SFBIA	RJL Systems Quantum IV, RJL Systems, USA	-3.1	-9.3 to 2.6
		Fat mass (kg)				4.2	-5 to 12.7
[214]	31 healthy women	Fat mass (%)	DEXA	SFBIA	BIA 101, Akern, Italy	0.5	-1.2 to 1.7
[206]	53 adult hemodialysis patients	Bone mineral (kg)	DEXA	SFBIA	InBody S10, InBody, Korea	1.9	0.9 to 2.9
		Fat mass (kg)				-6.5	-15 to 2
		FFM (kg)				4.2	-3 to 11.5

TABLE 4: Comparison of bland Altman analysis results in studies of ICG-based cardiovascular parameters.

Study	Sample size	Measurement	Reference method	ICG device	Differences Mean value	95% CoIn
[242]	42 patients (newborn - 16 yr)	CI (L/min/m^2)	Doppler echocardiography	NiCaS, NI Medical, Israel	0.05	-0.77 to 0.87
[243]	25 healthy adults	CI (L/min/m^2)	Magnetic resonance imaging (MRI)	FhysioFlow, Manatec Biomedical, France	0.1	-1.1 to 1.3
	32 patients with chronic anemia				1.5	-0.6 to 3.6
[244]	11 healthy adults	SV (mL)	MRI	Cardiotronic, Osypka Medical, Germany	~ 0	-64 to 64
[245]	17 patients under hemodialysis	SV (mL)	Doppler echocardiography	NiCaS, NI Medical, Israel	1.3	-11.6 to 14.1
[246]	32 healthy adults	SV (mL)	Doppler echocardiography	non-commercial	-1.53	-26.7 to 23.64
		CO (L/min)			0.32	-1.19 to 0.18
[247]	53 pregnant women	SV (mL)	Doppler echocardiography	ICG, Philips Medical Systems, USA	2.5	-15.7 to 20.7
		CO (L/min)			0.2	-1.3 to 1.7

The use of artificial neural networks has been proposed to improve the calculation of stroke volume from ensemble averages of ICG signals [239]. Finally, kernel methods have been used to analyze the time-frequency content of the ICG signal in [240, 241].

While some studies have warned against the accuracy of ICG-based measurements compared with gold standards for cardiovascular condition (Table 4 summarizes recent studies for diverse health conditions), its low-cost and ease of use make this technique appropriate for clinical use.

5. Transthoracic Impedance Pneumography

Transthoracic impedance pneumography (TIP) is a noninvasive method that evaluates the thoracic impedance and changes related to respiratory activity, becoming an alternative to spirometry or pneumotachometry for ambulatory and outside hospital settings [248]. It offers a simple way for the characterization of respiration rate together with other vital pulmonary signs, such as respiration cycle length and tidal volume. Hence, it provides essential indicators for the respiratory condition. Breathing activity changes the thoracic volume, geometry, and conductivity, thus modulating the impedance that can be recorded between two surface electrodes placed on the chest [249]. While it can be acquired from the same electrodes as ECG [250], TIP uses 50-500 kHz low amplitude currents. Tetrapolar electrode configuration is also popular to reduce skin-electrode effects [251]. Due to the conductivity of lung tissue, most of the impedance changes are due to the current passing through the chest and back. Upon respiration activity, voltage increase and drop are associated with lung air filling (inspiration) and emptying (expiration), respectively, with a linear correlation between impedance changes and the volume of ventilated air [252]. In [253], such relation is expressed similarly to (24) as

$$\Delta V_L = \rho \cdot \left(\frac{L}{Z_0} \right)^2 \cdot \Delta Z \tag{25}$$

where V_L and ΔZ are the respiration volume change and magnitude of the impedance change, respectively. L is the length of the conducting volume, Z_0 the impedance baseline, and ρ a resistivity parameter. Flow can be expressed as

$$\Phi = \frac{dV_L}{dt} \tag{26}$$

However, the respiratory airflow monitored by TIP is sensitive to movement artifacts [254].

TIP has been used to measure lung volume changes [255], to evaluate respiratory condition during normal and deep breathing [256], the assessment of asthma risk from tidal flow variability [257], sleep disorders [258], energy expenditure estimation [259], or even the detection of body posture changes [260]. Another application of TIP is the gating of positron-emission tomography (PET) and single-photon emission computed tomography (SPECT) images. Respiratory movement is an important source of error in studies using PET images of the thoracic region. Due to the long period of time necessary for taking a PET image, usually minutes, the respiratory movement can deteriorate the image quality [261], leading to an incorrect diagnosis or inadequate treatment [262]. TIP has been used to compensate for the adverse effects of movement in oncological PET images [261]. It has also been applied to reduce the effects of respiratory movements in the analysis of myocardial perfusion SPECT images [263].

Like ICG, the e-health paradigm has fostered the design of wearable sensors supported by signal processing algorithms. Among the former, textile electrodes have been designed in [264] to provide joint ECG and TIP monitoring. The careful design of the electrodes has stimulated research, with the adoption of textile multimaterial fibers for contactless TIP sensing [265], compound electrodes [266], and graphene electrodes for a long-term measurement life [267]. Signal processing methods for TIP are focused on the derivation of respiratory rate through autoregressive models [250] or power spectral density estimation [268], the decomposition of the cardiac and respiratory components [269],

TABLE 5: Bland Altman analysis results obtained in TIP.

Study	Sample size	Measurement	Reference method	TIP device	Differences Mean value	95% CoIn
[271]	20 adult patients in postoperative care	Respiratory rate (breaths/min)	Capnography	Datex Ohmeda Compact S3 (e-PRESTN), Datex Ohmeda, Finland	-1.9	-13.1 to 9.2
[272]	98 patients scheduled for upper gastrointestinal endoscopy	Respiratory rate (breaths/min)	Acoustic respiratory rate monitoring	AG-920RA bedside monitor, Nihon Koden, Japan	0.4	-11.1 to 11.9

the improvement of respiratory parameters using nonlinear corrections with neural networks [270], and the removal of motion artifacts based on correlation measurements [251].

Given the characteristics of the signal, TIP has been evaluated as an alternative in the study of the respiratory rate [271, 272]. Table 5 shows the results obtained in two recent clinical studies. Another application of TIP is the gating of positron-emission tomography (PET) and single-photon emission computed tomography (SPECT) images. Respiratory movement is an important source of error in studies using PET images of the thoracic region. Due to the long period of time necessary for taking a PET image, usually minutes, the respiratory movement can deteriorate the image quality [261], leading to an incorrect diagnosis or inadequate treatment [262]. TIP has been used to compensate for the adverse effects of movement in oncological PET images [261]. It has also been applied to reduce the effects of respiratory movements in the analysis of myocardial perfusion SPECT images [263].

6. Electrical Impedance Tomography

Introduced by Barber and Brown in the 1980s [273], electrical impedance tomography (EIT) is a medical imaging modality that provides the spatial distribution of bioimpedance inside the body [274], relying on a set of 16-32 electrodes [275] placed on the surface confining the volume of interest. Current excitation in the typical frequency range of 20-250 kHz causes an electromagnetic field that interacts with volume tissues yielding electric potential maps that can be measured [276]. However, different operating frequencies have been proposed for EIT systems. For instance, the KHU Mark 2.5 EIT system, designed for imaging brain function, operates within 11-500 kHz [277], and broadband EIT systems for breast imaging span from 10 kHz to 12.5 MHz [278]. A high output impedance current source is required for broadband EIT applications [279].

Two complementary problems may be distinguished in the context of EIT. The forward problem assumes a known conductivity distribution within volume tissues and involves the numerical computation of voltages on the surface electrodes [280]. The inverse problem addresses the prediction of conductivity distribution from the electric potential measurements through a reconstruction algorithm [281], from which bioimpedance images are derived. Among the advantages, EIT outstands as a low-cost, harmless, simple, and noninvasive technique yielding high-speed imaging and high temporal resolution. It can be very fast, able to generate thousands of images per second. Compared to nuclear imaging, EIT does not use ionizing radiations and thus harmful side effects are avoided. Its drawbacks are associated with the limited spatial resolution it provides [282] due to physical constraints for electrode separation and the numerical issues for impedance image reconstruction due to the ill-posed nature of the inverse problem. However, compared to other imaging modalities EIT is regarded as a high-resolution technique in terms of the functional parameters that it provides.

In the biomedical field, EIT has been applied to the examination of chest [283], to manage patients with acute respiratory distress syndrome (ARDS) in the intensive care unit (ICU) by estimating regional lung ventilation at the bedside [284]. Other areas of application include stroke imaging [285], the characterization of brain tissues [26, 286], the monitoring of regional cerebral edema during clinical dehydration treatment [287], the early warning of brain injury during aortic arch replacement operation [288], gesture recognition [289], cancer detection [290–292], pediatric intensive care [293], tissue engineering [294], thermal management of hyperthermia [295], or laparoscopic surgery [296]. Another application of EIT is the gating of positron-emission tomography (PET) and single-photon emission computed tomography (SPECT) images. Respiratory movement is an important source of error in studies using PET images of the thoracic region. Due to the long period of time necessary for taking a PET image, usually minutes, the respiratory movement can deteriorate the image quality [261], leading to an incorrect diagnosis or inadequate treatment [262]. EIT has been used to compensate for the adverse effects of movement in oncological PET images [261]. It has also been applied to reduce the effects of respiratory movements in the analysis of myocardial perfusion SPECT images [263]. Other applications have been reviewed in [297].

The EIT forward problem usually relies on the finite-element (FE) method. The dimensionality of the forward problem has been regarded as the most critical factor limiting the quality of image reconstruction [298]. The analysis of convergence of the FE approximation for EIT has been analyzed in [299], showing that the estimated voltages on the

TABLE 6: Bland Altman analysis results obtained in EIT studies.

Study	Sample size	Measurement	Reference method	EIT device	Differences Mean value	95% CoIn
[339]	14 patients with severe respiratory failure	Regional expiratory time constant (s)	Anemometry (V-Meter, EKU, Germany)	Swisstom BB2, Swisstom, Switzerland)	0.14	0.37 to 0.65
[340]	15 ventilated intensive care patients	Positive end-expiratory pressure (PEEP) (mbar)	PEEP trial	Pulmovista 500, Draguer, Germany	1	2 to 1
[341]	9 healthy piglets	Ventilation (ml)	Vibration response imaging	Goe-MFII, CareFusion, Germany	-1	-49 to 47

electrodes converge to the true values as the underlying mesh is more refined. Regarding the inverse problem, different linearization methods have been proposed to address the linear inverse in an iterative algorithm [300]. Among the regularization approaches for the nonlinear inverse problem, the "D-bar method" [301] and the "Calderón method" [302] are proven strategies which have been extended in [303] with a convolutional neural network to prevent image blurring. Deep learning approaches applied to image reconstruction for EIT have also been addressed in [304, 305]. The incorporation of structural information has been applied in [306] to reduce the dimensionality and sensitivity to regularization parameters. Another way of compensating the ill-posedness of the inverse problem is the enforcement of monotonicity constraints about the reconstructed conductivity [307–309]. In other papers, regularization incorporates a priori knowledge yielding sparse solutions [306]. Other works combine level set function, shape and topological derivatives to avoid local minima in the optimization algorithm [310]. The consideration of alternate solution spaces, such as the logarithmic conductivity, has proven to be more robust to the initial guess and yield faster convergence [311]. With regard to EIT image resolution, resampling-based methods [312] and sparse Bayesian learning [313] have been suggested to improve the quality of EIT image reconstruction. In other words, multiple information fusion methods are approached to address the limitations of EIT. Careful considerations of a priori information, measurement error, and the model parameters are required, together with close collaboration between mathematicians and experimentalists.

During the last couple of years, EIT sensors and systems have been customized for real-time operation and portability. A wearable EIT system has been proposed in [314] based on system-on-chip technology. It integrates 48 channels in a flexible printed circuit board belt with wireless communications to an external imaging device. Another belt design with 32 electrodes is reported in [294], which uses active electrode ASIC (Application-Specific Integrated Circuit) technology. The electronic sensing architecture proposed in [315] uses dry electrodes integrated in a vest for the simultaneous EIT and multilead ECG data acquisition through frequency division multiplexing. The prototype described in [316] uses an arrangement of 16 microelectrodes placed around the base of a circular chamber for 3D cultivation imaging. The system in [317] integrates multifrequency operation with 32 electrodes for 2D and 3D imaging. Alternative methods to sequential electrode excitation have also been tested in [318], which uses mixed excitation patterns yielding a simultaneous linear combination of single excitations. The reconfigurability and control of the variables involved in the experimental operation is another highly demanded requirement [319] for EIT systems.

As it has been previously mentioned, the medical images provided by EIT are of great clinical utility. These images have also been used to derive clinical parameters from the analysis of their evolution. Table 6 summarizes some examples of recent studies that compare estimates against reference standards.

7. Skin Conductance Applications

The sympathetic skin conductance response (SCR) is one index of autonomic arousal [320]. Electrodermal activity (EDA) measures the electrical activity on the surface of the skin or originating from the skin [321]. It can be characterized as a tonic level through skin conductance or as a transient response through galvanic skin response. EDA measurement systems are based on the injection of a signal—usually an electric current—into the body using surface electrodes attached to the skin, and the electric voltage developed as a consequence of the injection of the current is usually recorded. Sweat gland permeability is the main responsible for skin conductance changes [322]. As sweat gland activity is neurally mediated through sympathetic activity, EDA is highly appreciated in psychophysiology and behavioral medicine [323]. However, EDA is also influenced by factors such as external temperature, and requires reference measurements and calibration [324].

EDA processing is focused on activity modeling and the removal of artifacts. While exponential smoothing [325] and low-pass filtering [326] are common approaches to signal denoising, wavelet transform has been used in [327] for motion artifact reduction in drivers and machine learning algorithms have been suggested in [328] to distinguish artifacts in an EDA signal from normal physiological responses. Sparse recovery based on the orthogonal matching pursuit algorithm has been applied in [329] to separate skin conductance response from artifacts with a high accuracy. For

TABLE 7: Bland Altman analysis results obtained in skin conductance studies.

Study	Sample size	Measurement	Reference method	SCR device	Differences Mean value	95% CoIn
[337]	49 healthy elderly	Resting energy expenditure (kcal/24h) in the morning	Indirect calorimetry	Sensewear armband, Body- Media, USA	-166	-438 to 105
		Resting energy expenditure (kcal/24h) at night			-187	-427 to 53
[338]	133 type 2 diabetic patients and 41 control subjects	Sudomotor function (%) on hands	Quantitative sudomotor axon reflex test	EZSCAN, Impeto Medical, France	-4.3	-23.5 to 15
		Sudomotor function (%) on foots			-1	-14 to 12

the analysis of EDA signals and identification of arousals, the methods range from power spectral density analysis [330, 331], machine learning [332], compressed sensing [333], to nonlinear analysis based on chaotic characterization and complexity assessment [334].

EDA sensors can be based on Ag/AgCl disc electrodes attached to the palm sides of index and middle fingers, such as the prototype reported in [335], or multilayered sensor disc for use as a dry electrode [336]. The use of spiral geometry for the electrodes has been suggested in [38] to make measurement results independent of skin anisotropy.

An example of application of skin conductance measurement is the evaluation of the metabolic condition of a person. Table 7 shows the results obtained in a comparative study of the skin conductance with the measurement of the resting energy expenditure [337]. Another example is the evaluation of sudomotor function [338].

8. Impedance Detection in Biosensors

Impedance biosensors are in use for the detection and characterization of different bioparticles as bacteria, viruses, cells, and biomolecular structures by the aid of measurement of their electrical impedance in microfluidic environment. The rise of impedance-based biosensors was initiated by the following two enabling factors.

(1) *Impedance sensing in electrochemistry*: first, the impedance-based electrochemical sensors for the detection and concentration determination of chemical have been known for many decades already [342]. Electrochemical sensors have used the impedance measurement for a long time already [342], e.g., for determination the concentration of ionic reagents in solutions and for monitoring reduction-oxidation (redox) reactions. Emergence of electrical current as the product of chemical reactions is known as the Faradaic process. The level of evoked current depends on intensity of chemical reactions. Sensing methods are potentiometry, amperometry, and voltammetry using either direct current or slowly changing alternating current. Such the sensing method is called Faradaic, which are widely used in electrochemistry, but preferably not in biosensors. Electrochemistry gave impetus to the use of impedance sensing in biosensors, but the biosensors use mostly non-Faradaic formation of electrical current, which depends on the rate of presence (concentration) certain biological particles-cells and biomolecules as DNA, but mostly the pathogens as bacteria and viruses-causing changes in the impedance to alternating electrical current in kHz and MHz frequency range.

(2) *Bioimpedance sensing in microfluidics*: another boost to the rise of impedance methods gave an expansion of microfluidic technology, enabling to create miniature lab-on-a-chip (LoC) devices [343]. First of all, the bioparticles were discovered and characterized by labeling-introducing certain chemicals for visual detection through the changing of label colour. Unfortunately, the labeling chemicals are not fully passive; they change the properties of fluids and can change also the bioparticles to be detected. Moreover, the labeling chemicals are not always available and can be expensive. Using of impedance methods enables the label-free detection of bioparticles. Besides, the label-free impedance detection is the fastest method known.

Both the above described reasons have worked as accelerators for introducing the methods for bioimpedance detection and analysis. Two types of impedance biosensors are known:

(1) *Sensors of floating/flowing bioparticles*: the task is to detect the floating or fast flowing bioparticles in a narrow submillimeter or micrometer range channel, only a slightly larger than detectable bioparticles. Such the devices are, for example, impedance cytometers intended for the counting and selection of single cells, e.g., for making difference between bigger and smaller cells or for separating the living and dead cells. Bare or coated (electrically insulated) metal electrodes are in use. Capturing of particles to electrodes is not requested, on the contrary, it should be avoided. Fast flow of fluids containing particles is needed [344].

(2) *Affinity biosensors*: the affinity biosensors selectively detect the bound (immobilized) bioparticles. At least one of the electrodes is covered by a selectively acting layer (antibody or aptamer layer), which binds to itself
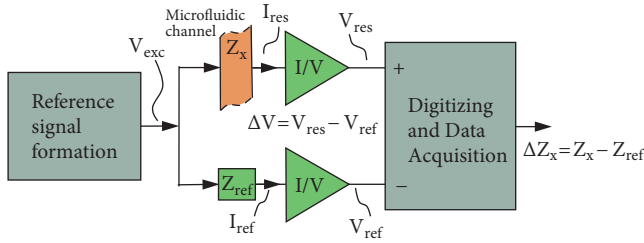
FIGURE 18: A generalized measurement scheme for differential measurement of changes ΔZ_x of the impedance to be measured Z_x. The current responses (I_{res} and I_{ref}) to voltage excitation V_{exc} are converted into response voltages (V_{res} and V_{ref}); the difference of which is amplified, acquired, and digitized by the aid of differential input analog-to-digital converter giving the digital output ΔZ_x.

the specific bioparticles (bacteria and viruses, also big protein molecules), existing in the surrounding fluid. Antibodies exist in human and animal organisms as the guarantors of immunity or are formed there if the pathogens attack. As already told, the antibodies are selective, they bind only these pathogens (named as antigens, in general), which called them up. Producing of natural antibodies can be complicated and costly. Artificially synthesized aptamers have the same binding effect, but are cheaper and more flexible to modify, only their production technologies are still in development stage.

8.1. Impedance Measurement Principles in Biosensors. Important is to underline that it is extremely hard to measure tiny impedance deviations ΔZ_x around 0.05 to 0.5% from its basic value Z_x. Therefore, differential measurements are needed. In Figure 18, there is given a 2-channel measurement scheme to determine, how much the impedance to be measured Z_x (impedance of the microfluidic channel in Figure 18) differs from the reference value Z_{ref}, which is introduced as an electrical equivalent circuit mimicking the measurement channel (microfluidic channel) physically. As a result, the resolution of measurement enhances at least tens and hundreds of times. In microscale biosensors, mostly the voltage excitation V_{exc} and current response I_{res} are used for impedance measurement.

8.2. Biosensor Electrodes. The measurement of impedance Z_x requires electrodes made from conductive material, frequently metallic ones or carbon based. In microfluidic channels, mostly golden electrodes are used for bioimpedance measurement, bare or covered by thin electrically insulating layer. Electrodes for affinity sensors use multilayer structure on gold (see Figure 21).

Though mostly quadrupole electrodes (4-electrode system, one pair for excitation current and the other one for voltage pick-up) are used for bioimpedance measurement, only two electrodes are predominantly applied both for the voltage excitation and current response. The reason is that it is complicated to take advantage of 4-electrode system in miniature non-Faradaic biosensors. It is important to remember that there is no current due to chemical reactions

but solely due to the voltage excitation. The electrical current through the sensing part between electrodes is ionic (charge carriers are ions), but outside of this the charge carriers are electrons. As a result, a thin interfacial double layer appears at electrodes, which behaves like a modified capacitance and is modeled as CPE (see (27)). The impedance of CPE can be expressed through the frequency dependent magnitude $Z_{CPE}(\omega)$ and constant phase φ, where n can be set from n = 0 (ideal resistor R) through n = 0.5 (ideal Warburg impedance) to n = 1 (ideal capacitor C, valid in case of electrically insulated electrode):

$$Z_{CPE}(\omega) = \frac{Z_0}{\omega^n} \qquad (27)$$

and

$$\phi = -n\frac{\pi}{2} \qquad (28)$$

The frequency response plot of the CPE at different values of n is given in Figure 19(b) in logarithmic scale.

Configurations of the most commonly used electrodes for miniature impedance biosensors are depicted in Figure 20 [345, 346]. The simplest one in Figure 20(a) represents linearly placed quadrupole electrodes. A similar arrangement of concentric configuration is given in Figure 20(b). A linear configuration of 2-pole interdigitated electrodes covering a wider sensing area is given in Figure 20(c). Analogous interdigitated sensor with concentric arrangement of electrodes is given in Figure 20(d).

8.3. Affinity Biosensor. A typical affinity based biosensor for the bioimpedance detection of pathogen in a biological solutions which uses gold electrodes on substrate is depicted in Figure 21. To connect antibody (or aptamer) layer strongly onto gold electrode, a thin nanometer range self-assembling monolayer (SAM) is required for interfacing inorganic electrode from one side and the biological material (biomolecules, cells, liquid). Thiol and dithiol SAMs on metals, and particularly on gold, have attracted attention due to their easy preparation from gas phase or from solution, and their relatively high stability mediated by the strength of the SAu (sulfur-gold) bond and by van der Waals forces from molecular interactions [347]. If there exist appropriate bioparticles (named also as antigens) in saline solution, then the selective antibody layer selects these antigens (bacteria, viruses) and antigen-antibody layer will be formed. Antigens (pathogens) change the impedance of antibody layers. This change ΔZ_x informs us on the presence of corresponding pathogens and enables also to estimate their concentrations.

The multilayer coating on gold electrode can be divided into two parts. First, the complex impedance $Z_e(j\omega)$ takes in only the double layer and the accompanying phenomena (Figure 19(a)). The other part of impedance, $Z_x(j\omega)$, contains the impedance of SAM, antigen-antibody layer and saline solution with floating bioparticles (R_1, R_2, and C_1 together with a parasitic stray capacitor C_p); see Figure 19(a). Resistor R_1 brings together the resistive components of saline solution, SAM, and antigen-antibody layer, changing the last of which
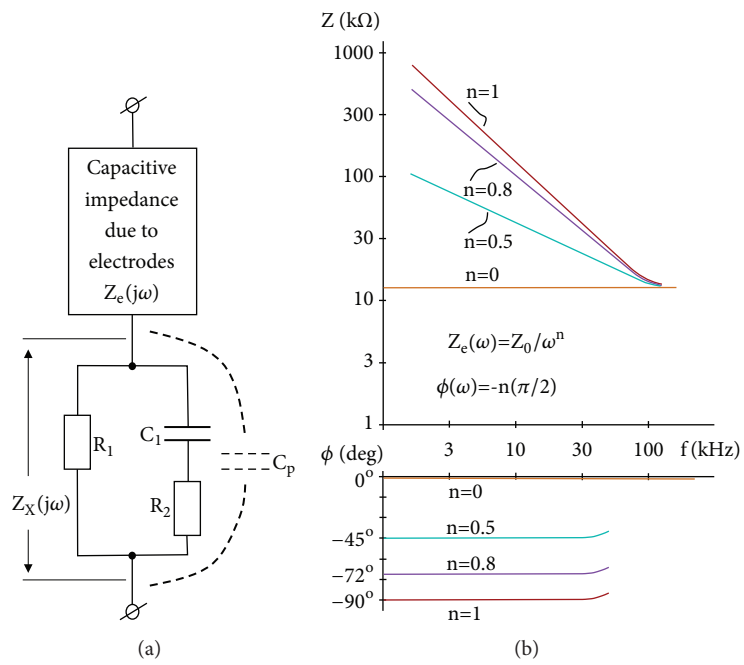
(a) (b)

FIGURE 19: Characterization of non-Faradaic affinity based impedance biosensors: (a) an equivalent electrical circuit; (b) the frequency response of its impedance magnitude $Z(f)$ and constant phase φ.
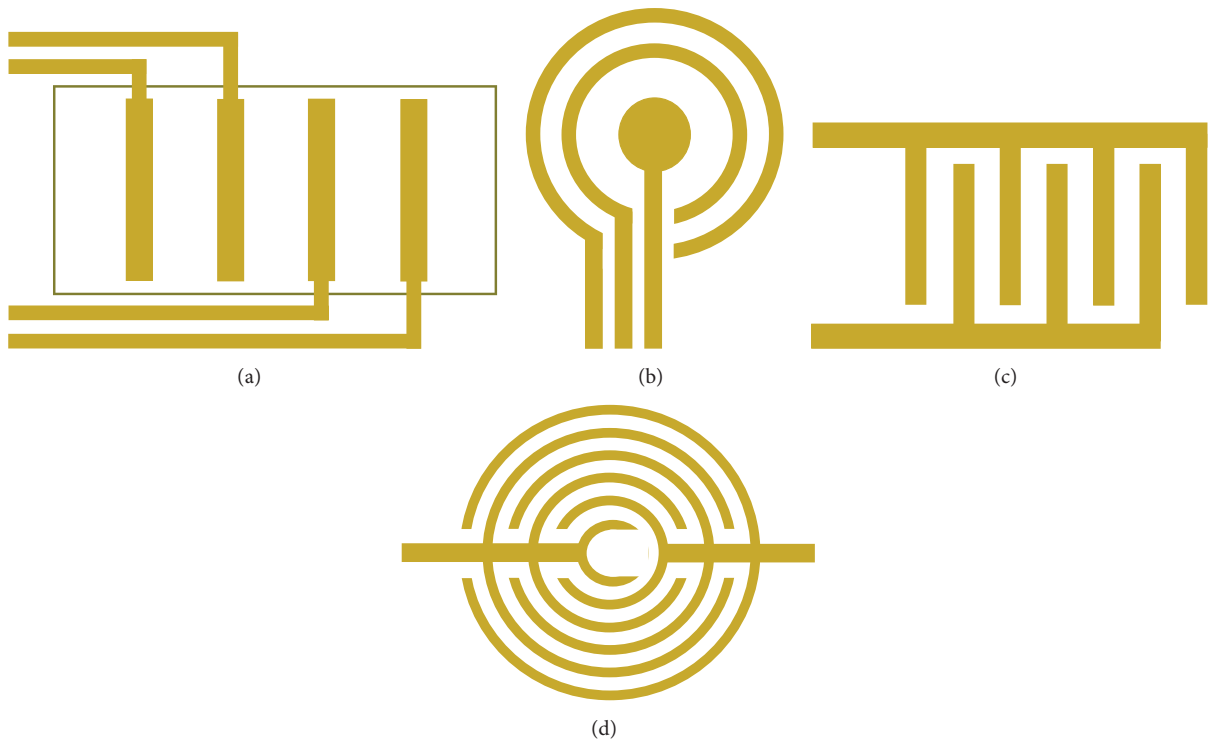

(a) (b) (c)

(d)

FIGURE 20: Configurations of electrodes: (a) linear 4-pole; (b) concentric; (c) interdigitated 2-pole, linear; (d) interdigitated 2-pole, concentric.
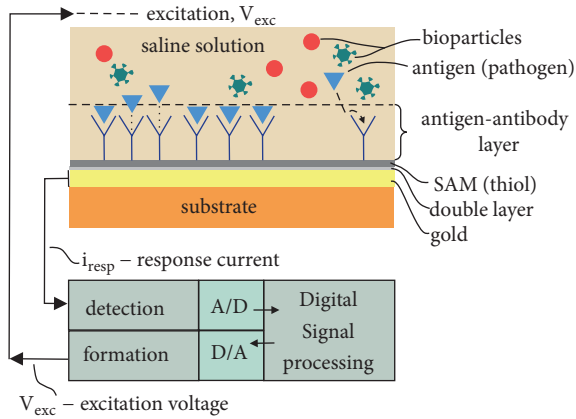
FIGURE 21: Affinity biosensor for bioimpedance detection of pathogens in biological solution.
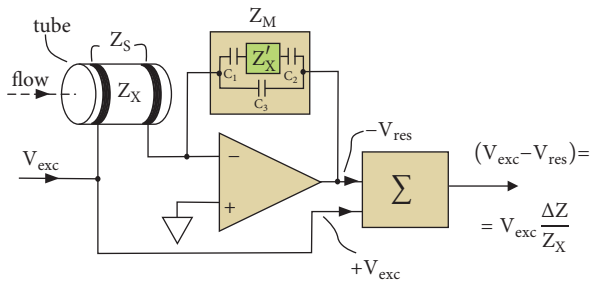

FIGURE 22: Biosensor with insulated electrodes on the tube form channel.

FIGURE 23: Frequency dependence of magnitude $Z_S(\omega)$ and phase $\varphi_S(\omega)$ of sensor impedance $Z_S(j\omega)$ at different values of concentration expressed through the resistive impedance Z in the graph. Informative value is measured at such frequencies, at which the phase curves obtain their maximal value about -25°.

ΔR_1 is caused by binding of antigens to antibodies (formation of the antigen-antibody layer). Presence of capacitance C_1 brings us the reason of arising capacitive current through SAM and antigen-antibody layer, also between the bioparticles in the saline solution. This current is limited by the resistor R_2 at higher frequencies, but overall capacitive current continues flowing through the parasitic stray capacitance C_p. Despite the fact that only changing resistive component, ΔR_1, is expected to be an informative factor, this change reflects in both, in real and imaginary parts $\text{Re}[Z_x(j\omega)]$ and $\text{Im}[Z_x(j\omega)]$ of the complex impedance $Z_x(j\omega)$. Extraction of ΔR_1 requires spectral measurements at least over the range of medium frequencies.

In Figure 22, there is given a case of measurement with electrodes fully insulated from biological material. A glass microtube (100 μm inner diameter, 50 μm thick wall) is used for the measurement of impedance of biosolution flowing through [344]. Because of absence of contact between ionic solution and surrounding metallic ring electrodes, also the double layer is absent. Instead of, nearly ideal capacitances C_1 and C_2 exist between the electrodes and solution, which is characterized now by n = 1 in (27) and in Figure 19, $C_e(j\omega)$ transforms to the impedance of capacitor $Z_c(j\omega) = 1/(j\omega C)$.

The measurement configuration in Figure 22 is based on the structure of inverting operational amplifier with electrical model (impedance Z_M) in the feedback circuit and physical sensors with impedance Z_S at the input. Complex impedance

of the model $Z_M(j\omega)$ and of the real sensor $Z_S(j\omega)$ must be as similar as possible in the wide range of frequency $\omega = 2\pi f$. As a result, the output signal of electronic summation Σ is proportional to the relative change $\Delta Z_x/Z_x$ of the impedance to be measured; in more detail, please read [344].

How to extract the value of resistance R_1, and its changing component ΔR_1, which carries primary information? The most reasonable way is to measure the impedance at the frequency, at which the phase shift φ obtains its minimal value (Figure 23). At this frequency the impedance turns to its real value. For finding that frequency we have to measure in some range of frequencies, that is, to put through impedance spectroscopy around the expected frequency.

An experimental device for impedance-based counter of cells (cytometer) together with impedance-based characterization and sorting of cells and/or droplets is given in Figure 24 [348]. This device uses 4-electrode system having two pairs of electrodes, one pair for current excitation i_{exc} outside the channel, and the other one for pick-up the voltage response V_{res} inside the channel. Spectral analysis of cell impedance enables to differentiate the cells and count them separately using automatic decision maker operating on the bases of measurement results.

In Figures 25 and 26 there are described two practical versions of differential impedance measurement without using of some electronic reference circuits as designed for the device in Figure 22; see impedance Z_M [344]. The both are for detecting and comparative analyzing of cells, i.e., the both are specific cytometers. In the first version
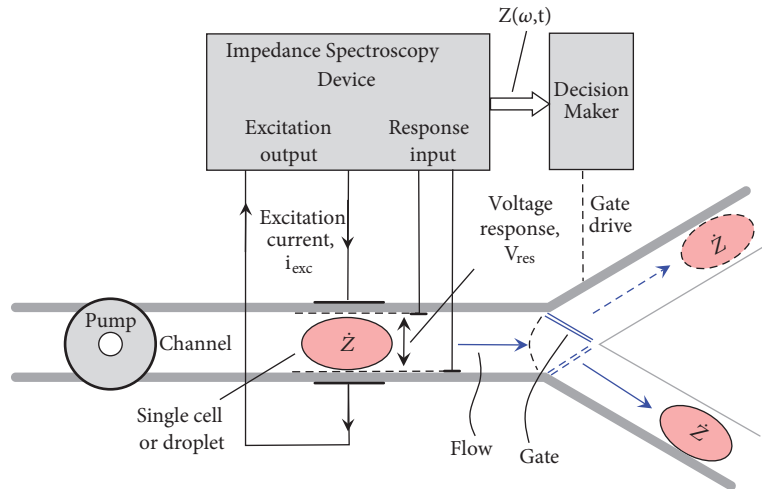
FIGURE 24: A cell or droplet sorter based on time dependent impedance spectroscopy (adapted from [348]).
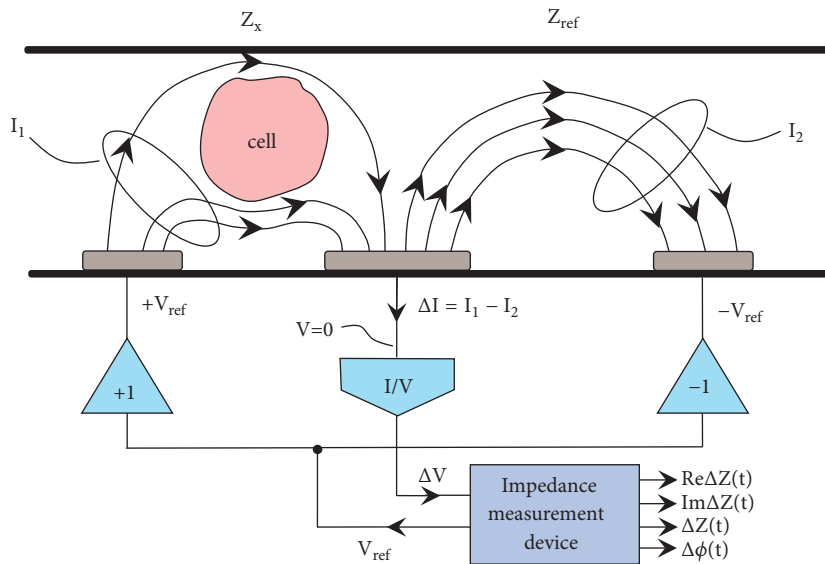
FIGURE 25: Three electrode system for the differential cell counting and characterizing.

(Figure 25), the opposite phase excitation signal as references $+V_{ref}$ and $-V_{ref}$ are generated. If the reference impedance Z_x and impedance Z_{ref} are equal (no cells in the channel), then the response current ΔI is absent. But if the cell is present in channel, then Z_x becomes higher than V_{ref} at lower frequencies (cell membrane does not conduct low-frequency currents). This phenomenon is the bases for the detecting and characterization of cells.

Similar principle is in use in Figure 26, where only a single excitation voltage V_{exc} is applied to the both impedance Z_x and impedance Z_{ref}. Separate output currents, I_{res} and I_{ref}, which will be subtracted from each other for yielding the difference ΔI. Significant difference between these currents ($\Delta I > 0$) produces the voltage difference ΔV at the output of current-to-voltage converter I/V. The voltage difference ΔV signal indicates the presence of a cell in the channel.

9. Future Challenges of Bioimpedance

Despite all the advances made in bioimpedance for healthcare applications, there are still many challenges and open study fields for future research.

The development of wearable technologies has had a spectacular growth in recent years (heart rate, body temperature, physical activity, etc.). Important research efforts are carried out so that the information provided by these biomedical sensors can be really useful (remote monitoring of patients, early detection of anomalies, promotion of self-care, etc.) towards an improvement in health and quality of life. There has been a paradigm shift in healthcare, moving from a curative medicine to a personalized, preventive, and proactive medicine [134, 349]. This evolution is supported by the development of wearable biomedical devices for the management of personal health, which allow users to monitor
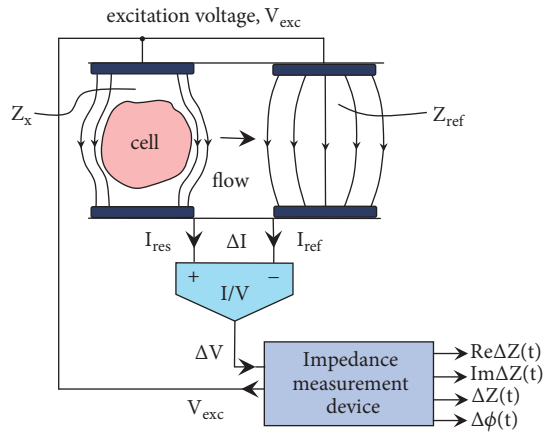
FIGURE 26: Four-electrode system for the differential cell counting and characterizing.

their physiological parameters continuously throughout the day. This functionality increases people's awareness of their current state of health and allows them to make adjustments in their lifestyle or seek early medical attention when the prognosis of the disease may be more favorable [134, 349]. As mentioned in previous sections, bioimpedance devices can provide multiple physiological parameters, and a huge interest is represented by the continuous monitoring of them. This circumstance poses the challenge of portability in bioimpedance systems, since the typical applications of bioimpedance measurement on the human body (BIA, ICG, TIP, EIT, and EDA) use electrodes on the skin. An obstacle for the development of portable bioimpedance devices is that a suitable electrode system is yet an open issue for wearable applications. These electrodes should be comfortable, easy to place by the user and should provide reliable measurements [95]. Aspects such as the material, size, shape, and disposition of the electrodes are a still open study area in contact electrodes for a nonobstructive use. As the contact electrodes like Ag/AgCl are not suitable for continuous use, new methods based on conductive textiles and other noncontact coupling methods are being investigated. The use of noncontact electrodes can solve this problem, but it raises others as a greater sensitivity to the artifacts of movement and the electrical conditions of the environment and the human body [350]. Although the specific placement of the electrodes for BIA, ICG, EIT, and TIP applications has been widely discussed in the literature, there is a lack of information on the performances and issues about their application in a compact configuration more suitable for a portable environment, such as a patch or a textile garment [351]. The understanding of the current and voltage distribution mechanisms inside the body will be essential to optimize the sensitivity of bioimpedance devices in portable applications [351].

The standard methods of bioimpedance usually require the interaction of the doctor/nurse with the patient (placement of cables, electrodes, device management, etc.), so that these measurement systems are only adequate in a clinical setting. However, in an ideal healthcare application, the patient must forget that he/she is being monitored,

for a realistic evaluation under conditions of daily life. Bioimpedance devices must be seamless to the user and carers. To that aim, important challenges are related to the miniaturization and contact-free and unobtrusive use of bioimpedance systems, which must also have processing and wireless communication capabilities for its integration into an e-Health system. The bioimpedance acts as an additional source of data, with the ability to integrate information into the electronic medical record and the consequent interoperability needs. It is necessary to establish a trade-off between the comfort of the user, the capacity for long-term use and the wireless communications of reliable data. The complexity of the bioimpedance systems is usually quite high (current injection, voltage measurement, demodulation, processing, etc.) [351] and the use of high frequency signals (from tens to hundreds of kHz) generally requires a high energy consumption [351], so this new horizon involves a hardware optimization in size, robustness, and precision, but also in energy consumption, to maximize the autonomy of the devices, fundamental in the case of implants [116, 352]. A key point of bioimpedance systems is the improvement of the current source. A research effort must be made to increase the bandwidth and the output impedance of the current source to improve the accuracy of the measurements and make the devices robust against load bioimpedance variations [112]. As the digital signal processing and wireless communications are the main sources of energy consumption in sensor devices, any progress in both the hardware and the processing algorithms will have a positive impact on increasing energy efficiency [140, 353]. An alternative may be the use of comparators and timers instead of ADC to reduce the energy consumption associated with processing [354].

The improvement of sensitivity is highlighted as a study objective in bioimpedance equipment development, since the biological process to be monitored can lead to very small signal variations [355]. An adaptive preconditioning can be convenient for this purpose. The application of new approaches like nanotechnologies can improve the sensitivity of bioimpedance systems, as already it has been demonstrated in the case of the incorporation of carbon nanofibers on the electrodes of electrochemical sensors [96] or graphene electrodes for body measurements [267]. Due to the characteristics of an EIT system, with multiple electrodes and the need for processing algorithms, portability and real-time monitoring is an open challenge in the case of EIT.

Since the bioimpedance measurements are affected by multiple factors at the same time and it is very complicated to isolate the influence of the parameter to be measured, another challenge is the investigation of new models, equations, and methods to improve the specificity [356]. The problem of specificity is common to all bioimpedance methods. In BIA applications, the dependence of SFBIA method on a population regression study implies a loss of specificity in situations different from that of the study. Although BIS method is more robust in this sense, more extensive investigations must still be carried out. In bioimpedance measurements of biological samples, the concentration of the metabolite or substance to be detected can be masked by the presence of another element that affects electrically in the same way. An EIT image is

naturally fuzzy because the electric currents diffuse inside a volume. However, new EIT models, measurement schemes and electrode configurations can provide a higher spatial resolution. The application of new processing algorithms, more complex and taking into account a greater number of factors, can also allow an improvement in specificity.

As mentioned in Section 2.6, multiple sources of noise and artifacts can affect bioimpedance measurements. High frequency measurement devices suffer from significant distortions in the phase [357]. Research that minimizes these effects must be done at the hardware level, but also at the processing level to detect and correct its effects. The phenomena that introduce errors in bioimpedance measurement should be investigated in greater depth to incorporate these parameters in the processing algorithms [358]. In addition, the context of continuous monitoring imposes an even greater challenge, since artifacts due to movement and parasitic capacitances can be even greater. To reduce errors, bioimpedance systems use calibrations; however, there is no standard calibration protocol for the different bioimpedance applications. Standardized protocols should also be established when carrying out studies with bioimpedance, to allow evaluating the results of different authors on the same conditions and with the electrodes in the same positions.

The anisotropic properties of the skin and tissues must be taken into account, since the flow of the electric current inside the human body is modified by the composition and orientation of the cells in the tissues [88, 359]. Since the tetrapolar configuration of electrodes, which is commonly used in bioimpedance measurements, is affected by the anisotropic properties of blood vessels, muscle and nerve fibers [98], new electrode configurations and methods must be investigated to mitigate their effects [38] or allow their measurement as a diagnostic parameter of diseases [98, 99, 360]. Moreover, the anisotropy is of special relevance in EIT and its incorporation to image reconstruction models using tensors of anisotropic conductivity can provide a higher resolution [361].

Advances in miniaturization of IC technologies, biocompatible materials and wireless communication technologies have made implants more and more feasible for clinical use. To the extent, bioimpedance technology can provide a characterization of a tissue, and taking into account the fact that it is safe, simple and of low-cost, this technology has been investigated for its incorporation in implants such as cardiac pacemakers for the objective evaluation of the cardiac and respiratory process [140], in stimulation intracranial electrodes or cochlear implants to assess the state of the implant [362], to help in the process of placement of an implant [363] or in the detection of prostate cancer with microendoscopic probes [37]. Future advances in the field of implants will give rise to new challenges in the application of bioimpedance, to serve as a complement of the implant, but also serve as a basis in innovative implantable devices for in situ monitoring of a physiological process.

Biosensors and Lab-on-Chip technologies based on bioimpedance are of great interest in biological, medical, and industrial fields, mainly due to their low-cost and speed in the measurement, and because they can be used in continuous monitoring processes. The development of novel implants could also benefit from these technologies. However, the problems of precision and sensitivity are a major challenge in this type of applications. In-depth investigations must be carried out to accurately model the behavior of the biological impedance of these systems. As previously discussed, specificity is a major problem that can be solved by antibodies or artificially synthesized aptamers, still in the process of development. Implementation of bioimpedance sensing in Lab-on-Chip based technology for point-of-care (PoC) and need-of-care (NoC) devices [364] opens new perspectives to prevent of epidemic spread of infectious diseases in developing countries, and environmental and social disasters, everywhere. New implantable sensors can be designed as well on the bases of bioimpedance sensing [365]. The biosensors can detect cell nutrients such as glucose, metabolites such as lactate, cell density and pH in biological processes, but the field of research is open to new parameters and substances. Besides, the sample preparation process imposes important portability restrictions in some applications, hindering the development of this technology.

In this work, a review of the most recent applications of bioimpedance has been carried out, but in all of them there are some challenges that must be addressed. Although the estimation of body composition by bioimpedance has multiple advantages (noninvasive, painless, safe, simple and nonionizing-radiation-based method [103]) and exhibits a strong correlation with reference methods [210], this technique has not yet been accepted in routine clinical practice, possibly due to artifacts, systematic errors and estimation errors that occur in the measurements [366]. The algorithms used in commercial devices are usually unknown and there is little information about their validation in a clinical setting [103]. Clinical studies in which these devices have been used are limited by the small sample size [151] and additional research is needed with larger and more heterogeneous population samples, especially in obese individuals, subjects with low weight and in population groups with unique anthropometric characteristics or in altered states of composition [210]. To improve the error, innovative and individualized approaches must be developed to improve the accuracy of the bioimpedance methods [193].

In a typical bioimpedance body estimation, the electrodes are usually placed on the hand and the foot due to the multiple benefits that this configuration provides (reduction of the variability of the position, simply and easy measurement, the user does not need to undress, possibility of patient evaluation in bed, etc.) [210]. However, this location may not be optimal for assessing the specific composition in a corporal segment, especially in those patients who suffer extreme changes in body composition, such as patients on hemodialysis or patients with spinal cord injury [367]. The measurement of segmental and localized bioimpedance is an area of study that requires additional research [210, 367].

Despite the maturity of ICG, there are still doubts about whether this technique can really reflect the cardiac function and the filling pressures in the heart [368], especially under unnormal health conditions. The data provided in most of the studies are small and often are not controlled. More extensive

studies must be conducted to test the clinical utility of this technology and extend its application beyond the scope of the research. A disadvantage of ICG is that the distances between the measuring electrodes are high, and thus inaccuracies may arise in the estimation of parameters due to the own cardiorespiratory dynamics [369]. New methods based on ensemble averaging, wavelet transform, or signal filtering can address this inaccuracy [369, 370].

Despite the low resolution of the EIT technology for its application in medical images, which results in a smoothing effect, this technology stands out because functional information related to the internal body bioimpedance compartments is generated. In this way, EIT provides added value when it is applied in combination with other diagnostic methods. EIT is a very active study area as represents a low-cost and harmless method that can be used to obtain images of organs, tumors and blood vessels, although with low spatial resolution [371]. This method is very sensitive to modeling and measurement errors, and a small difference can lead to a large error in the reconstruction [372]. Advances in more accurate body models and in technology to provide increased stability and SNR will lead to an improvement in image resolution [26, 373]. Many researchers use phantoms that mimic body tissues to calibrate and test EIT systems [374]. As the intracellular compartment can only be observed at high frequencies, EIT usually needs a high bandwidth that is affected by the parasitic capacitance of the cables and switches. One way to solve the inherent inaccuracy of this technology can be the fusion of different sources of information, but also the parallel use of diverse technologies. Some research groups are investigating new schemes to improve the bandwidth by using multiple current injectors and voltmeters in parallel [372]. Other approaches employ active electrodes to mitigate the effects of parasitic capacitances [375, 376]. The collaboration of technical experts, mathematicians, and clinicians will be necessary to make a trade-off between the hardware and software complexity and the precision performance.

Bioimpedance based sensing methods have found an established usage in some types of biosensors (e.g., for single cell counting and sorting), but their implementation in biotechnology and medicine is still a topic of future developments. Excellent perspectives are opening in detection of pathogens for preventing epidemic spread of infectious diseases in developing countries, and environmental and social disasters, everywhere. Implementation of bioimpedance sensing in Lab-on-Chip based technology for point-of-care (PoC) and need-of-care (NoC) devices [364] opens new perspectives for prevention of the above-mentioned threats.

Although bioimpedance measurement technology is a mature method, a major research effort must be made in conjunction with experts in clinical diagnosis to improve the sensitivity, the specificity, and the confidence in the use of technology in routine clinical practice. Another challenge faced by bioimpedance is the research and development of new applications, in which the detection of cancer will have a prominent position [31, 37, 65, 68], but other new applications are feasible such as lymphoedema evaluation [43, 48], vital sign monitoring in automotive environments [377], noninvasive cuffless blood pressure estimation [378–381], electrical impedance myography [382], glucose concentration assessment [383, 384], noninvasive detection of physiological processes [385], diagnosis of diseases of peripheral vascular system [43, 386], evaluation of elbow joint motion [387], detection of bacteria populations in water solutions [388], evaluation of the status of wound healing [389], infiltration detection during intravenous therapy [390], blood flow assessment [43], and characterization of an implantable neurostimulator [391], as a surgical aid tool [101, 392] or in the evaluation of transplanted organs [46].

Acronyms

ADC:	Analog-to-digital converter
AFE:	Analog-front-end
ASIC:	Application-specific integrated circuit
BIA:	Bioelectrical impedance analysis
BIS:	Bioimpedance spectroscopy
BIVA:	Bioelectrical impedance vector analysis
BMI:	Body mass index
BrD:	Bromide dilution
CI:	Cardiac index
CMOS:	Complementary metal-oxide-semiconductor
CMRR:	Common-mode rejection ratio
CO:	Cardiac output
CoIn:	Confidence interval
CPE:	Constant phase element
D_2O:	Deuterium oxide dilution
DAC:	Digital-to-analog converter
DEXA:	Dual-energy X-ray absorptiometry
ECG:	Electrocardiogram
ECW:	Extracellular water
EDA:	Electrodermal activity
EIS:	Electrochemical impedance spectroscopy
EIT:	Electrical impedance tomography
FFM:	Fat free mass
FE:	Finite-element
FFT:	Fast Fourier Transform
FM:	Fat mass
FPGA:	Field-programmable gate array
IC:	Integrated circuit
ICG:	Impedance cardiography
ICW:	Intracellular water
LoC:	Lab-on-a-chip
LVET:	Left-ventricular ejection time
MFBIA:	Multifrequency Bioimpedance Analysis
MRI:	Magnetic resonance imaging
NLLS:	Nonlinear least squares
NoC:	Need-of-care
OPAM:	Operational amplifier
PEEP:	Positive end-expiratory pressure
PET:	Positron-emission tomography
PoC:	Point-of-care
PPG:	Photoplethysmography
PWV:	Pulse wave velocity
SAM:	Self-assembling monolayer
SCR:	Skin conductance response

SFBIA: Single frequency bioimpedance analysis
SPECT: Single-photon emission computed tomography
SNR: Signal-to-noise ratio
SV: Stroke volume
TBK: Total body potassium
TBW: Total body water
TIP: Transthoracic impedance pneumography
TrD: Tritium dilution
VCCS: Voltage-controlled current source.

Conflicts of Interest

The authors declare that there are no conflicts of interest with any company or organization regarding the material discussed in this paper.

Acknowledgments

References

[1] E. Borelli, G. Paolini, F. Antoniazzi et al., "Habitat: an IoT solution for independent elderly," *Sensors*, vol. 19, no. 5, 2019.

[2] S. Majumder, T. Mondal, and M. J. Deen, "A simple, low-cost and efficient gait analyzer for wearable healthcare applications," *IEEE Sensors Journal*, vol. 19, no. 6, pp. 2320–2329, 2019.

[3] R. Punj and R. Kumar, "Technological aspects of WBANs for health monitoring: a comprehensive review," *Wireless Networks*, vol. 25, no. 3, pp. 1125–1157, 2019.

[4] F. Riaz, M. A. Azad, J. Arshad, M. Imran, A. Hassan, and S. Rehman, "Pervasive blood pressure monitoring using Photoplethysmogram (PPG) sensor," *Future Generation Computer Systems*, vol. 98, pp. 120–130, 2019.

[5] L. Haoyu, L. Jianxing, N. Arunkumar, A. F. Hussein, and M. M. Jaber, "An IoMT cloud-based real time sleep apnea detection scheme by using the SpO2 estimation supported by heart rate variability," *Future Generation Computer Systems*, vol. 98, pp. 69–77, 2019.

[6] M. S. Mahmud, H. Fang, and H. Wang, "An integrated wearable sensor for unobtrusive continuous measurement of autonomic nervous system," *IEEE Internet of Things Journal*, vol. 6, no. 1, pp. 1104–1113, 2019.

[7] Y. Li, S. Li, H. Song, B. Shao, X. Yang, and N. Deng, "Noninvasive blood pressure estimation with peak delay of different pulse waves," *International Journal of Distributed Sensor Networks*, vol. 15, no. 3, 2019.

[8] K. Xu, Y. Lu, and K. Takei, "Multifunctional skin-inspired flexible sensor systems for wearable electronics," *Advanced Materials Technologies*, vol. 4, no. 3, 2019.

[9] J. Harvey, S. Salehizadeh, Y. Mendelson, and K. Chon, "OxiMA: a frequency-domain approach to address motion artifacts in photoplethysmograms for improved estimation of arterial oxygen saturation and pulse rates," *IEEE Transactions on Biomedical Engineering*, vol. 66, no. 2, pp. 311–318, 2019.

[10] M. Rapin, F. Braun, A. Adler et al., "Wearable sensors for frequency-multiplexed EIT and multilead ECG data acquisition," *IEEE Transactions on Biomedical Engineering*, vol. 66, no. 3, pp. 810–820, 2019.

[11] E. Piuzzi, S. Pisa, E. Pittella, L. Podesta, and S. Sangiovanni, "Low-cost and portable impedance plethysmography system for the simultaneous detection of respiratory and heart activities," *IEEE Sensors Journal*, vol. 19, no. 7, pp. 2735–2746, 2019.

[12] L. M. Roa, D. Naranjo, J. Reina-Tosina et al., "Applications of bioimpedance to end stage renal disease (ESRD)," *Studies in Computational Intelligence*, vol. 404, pp. 689–769, 2013.

[13] S. Kugananthan, Z. Gridneva, C. T. Lai et al., "Associations between maternal body composition and appetite hormones and macronutrients in human milk," *Nutrients*, vol. 9, no. 3, 2017.

[14] L. Mullie, A. Obrand, M. Bendayan et al., "Phase angle as a biomarker for frailty and postoperative mortality: the BICS study," *Journal of the American Heart Association*, vol. 7, no. 17, Article ID e008721, 2018.

[15] M. S. Mundi, J. J. Patel, and R. Martindale, "Body composition technology: implications for the ICU," *Nutrition in Clinical Practice*, vol. 34, no. 1, pp. 48–58, 2019.

[16] E. M. Widen, I. Tsai, S. M. Collins et al., "HIV infection and increased food insecurity are associated with adverse body composition changes among pregnant and lactating Kenyan women," *European Journal of Clinical Nutrition*, vol. 73, no. 3, pp. 474–482, 2019.

[17] A. Ruiz-Vargas, J. W. Arkwright, and A. Ivorra, "A portable bioimpedance measurement system based on red pitaya for monitoring and detecting abnormalities in the gastrointestinal tract," in *Proceedings of the 2016 IEEE-EMBS Conference on Biomedical Engineering and Sciences, IECBES 2016*, pp. 150–154, December 2016.

[18] M. V. Fedewa, B. S. Nickerson, and M. R. Esco, "Associations of body adiposity index, waist circumference, and body mass index in young adults," *Clinical Nutrition*, vol. 38, no. 2, pp. 715–720, 2019.

[19] S. Lai, M. Muscaritoli, P. Andreozzi et al., "Sarcopenia and cardiovascular risk indices in patients with chronic kidney disease on conservative and replacement therapy," *Nutrition Journal*, vol. 62, pp. 108–114, 2019.

[20] X. Zhang, J. Zheng, L. Zhang et al., "Systemic inflammation mediates the detrimental effects of obesity on asthma control," *Allergy and Asthma Proceedings*, vol. 39, no. 1, pp. 43–50, 2018.

[21] T. R. Ackland, T. G. Lohman, J. Sundgot-Borgen et al., "Current status of body composition assessment in sport: review and position statement on behalf of the Ad Hoc research working group on body composition health and performance, under the auspices of the I.O.C. medical commission," *Sports Medicine*, vol. 42, no. 3, pp. 227–249, 2012.

[22] A. Hafid, S. Benouar, M. Kedir-Talha, F. Abtahi, M. Attari, and F. Seoane, "Full impedance cardiography measurement device using raspberry PI3 and system-on-chip biomedical instrumentation solutions," *IEEE Journal of Biomedical and Health Informatics*, vol. 22, no. 6, pp. 1883–1894, 2018.

[23] S. Said and G. T. Hernandez, "The link between chronic kidney disease and cardiovascular disease," *Journal of Nephropathology*, vol. 3, no. 3, pp. 99–104, 2014.

[24] W. Lee and S. Cho, "Integrated all electrical pulse wave velocity and respiration sensors using bio-impedance," *IEEE Journal of Solid-State Circuits*, vol. 50, no. 3, pp. 776–785, 2015.

[25] W. Lee and S. H. Cho, "An integrated pulse wave velocity sensor using Bio-impedance and noise-shaped body channel communication," in *Proceedings of the 2013 Symposium on VLSI Circuits, VLSIC 2013*, pp. C218–C219, June 2013.

[26] M. Fernández-Corazza, S. Turovets, P. Luu, N. Price, C. H. Muravchik, and D. Tucker, "Skull modeling effects in conductivity estimates using parametric electrical impedance tomography," *IEEE Transactions on Biomedical Engineering*, vol. 65, no. 8, pp. 1785–1797, 2018.

[27] G. Boverman, D. Isaacson, J. C. Newell et al., "Efficient simultaneous reconstruction of time-varying images and electrode contact impedances in electrical impedance tomography," *IEEE Transactions on Biomedical Engineering*, vol. 64, no. 4, pp. 795–806, 2017.

[28] Z. Zhao, M. Chang, M. Chang et al., "Positive end-expiratory pressure titration with electrical impedance tomography and pressure–volume curve in severe acute respiratory distress syndrome," *Annals of Intensive Care*, vol. 9, no. 1, 2019.

[29] B. Sun, S. Yue, Z. Hao, Z. Cui, and H. Wang, "An improved tikhonov regularization method for lung cancer monitoring using electrical impedance tomography," *IEEE Sensors Journal*, vol. 19, no. 8, pp. 3049–3057, 2019.

[30] M. Takhti and K. Odame, "Structured design methodology to achieve a high SNR electrical impedance tomography," *IEEE Transactions on Biomedical Circuits and Systems*, vol. 13, no. 2, pp. 364–375, 2019.

[31] P. Kassanos, L. Constantinou, I. F. Triantis, and A. Demosthenous, "An integrated analog readout for multi-frequency bioimpedance measurements," *IEEE Sensors Journal*, vol. 14, no. 8, pp. 2792–2800, 2014.

[32] R. E. Fernandez, E. Lebiga, A. Koklu, A. C. Sabuncu, and A. Beskok, "Flexible bioimpedance sensor for label-free detection of cell viability and biomass," *IEEE Transactions on NanoBioscience*, vol. 14, no. 7, pp. 700–706, 2015.

[33] G. Huertas, A. Maldonado, A. Yufera, A. Rueda, and J. L. Huertas, "The bio-oscillator: a circuit for cell-culture assays," *IEEE Transactions on Circuits and Systems II: Express Briefs*, vol. 62, no. 2, pp. 164–168, 2015.

[34] F. A. Alexander, D. T. Price, and S. Bhansali, "From cellular cultures to cellular spheroids: is impedance spectroscopy a viable tool for monitoring multicellular spheroid (MCS) drug models?" *IEEE Reviews in Biomedical Engineering*, vol. 6, pp. 63–76, 2013.

[35] R. Kraya, A. Komin, and P. Searson, "On chip bioelectric impedance spectroscopy reveals the effect of P-glycoprotein efflux pumps on the paracellular impedance of tight junctions at the blood–brain barrier," *IEEE Transactions on NanoBioscience*, vol. 15, no. 7, pp. 697–703, 2016.

[36] K. Yu, Q. Shao, S. Ashkenazi, J. C. Bischof, and B. He, "In vivo electrical conductivity contrast imaging in a mouse model of cancer using high-frequency magnetoacoustic tomography with magnetic induction (hfMAT-MI)," *IEEE Transactions on Medical Imaging*, vol. 35, no. 10, pp. 2301–2311, 2016.

[37] S. Khan, A. Mahara, E. S. Hyams, A. R. Schned, and R. J. Halter, "Prostate cancer detection using composite impedance metric," *IEEE Transactions on Medical Imaging*, vol. 35, no. 12, pp. 2513–2523, 2016.

[38] K. Dudzinski, M. Dawgul, K. D. Pluta, B. Wawro, W. Torbicz, and D. G. Pijanowska, "Spiral concentric two electrode sensor fabricated by direct writing for skin impedance measurements," *IEEE Sensors Journal*, vol. 17, no. 16, pp. 5306–5314, 2017.

[39] S. Ahmad, I. Batkin, O. Kelly, H. R. Dajani, M. Bolic, and V. Groza, "Multiparameter physiological analysis in obstructive sleep apnea simulated with mueller maneuver," *IEEE Transactions on Instrumentation and Measurement*, vol. 62, no. 10, pp. 2751–2762, 2013.

[40] P. Walsh, O. Escalona, J. Velasquez, N. Waterman, and P. Rodrigues, "Impedance compensated passive implantable atrial defibrillator," *IEEE Electronics Letters*, vol. 50, no. 17, pp. 1192-1193, 2014.

[41] L. Sornmo, F. Sandberg, E. Gil, and K. Solem, "Noninvasive techniques for prevention of intradialytic hypotension," *IEEE Reviews in Biomedical Engineering*, vol. 5, pp. 45–59, 2012.

[42] C. Brendle, B. Rein, A. Niesche et al., "Electrical bioimpedance-controlled surgical instrumentation," *IEEE Transactions on Biomedical Circuits and Systems*, vol. 9, no. 5, pp. 743–750, 2015.

[43] S. Hersek, H. Toreyin, and O. T. Inan, "A robust system for longitudinal knee joint edema and blood flow assessment based on vector bioimpedance measurements," *IEEE Transactions on Biomedical Circuits and Systems*, vol. 10, no. 3, pp. 545–555, 2016.

[44] S. Hersek, H. Toreyin, C. N. Teague et al., "Wearable vector electrical bioimpedance system to assess knee joint health," *IEEE Transactions on Biomedical Engineering*, vol. 64, no. 10, pp. 2353–2360, 2017.

[45] C. J. Chester, P. T. Gaynor, R. D. Jones, and M. Huckabee, "Electrical bioimpedance measurement as a tool for dysphagia visualisation," *Healthcare Technology Letters*, vol. 1, no. 3, pp. 115–118, 2014.

[46] O. I. Al-Surkhi and R. Y. Naser, "Detection of cell morphological changes of ischemic rabbit liver tissue using bioimpedance spectroscopy," *IEEE Transactions on NanoBioscience*, vol. 17, no. 4, pp. 402–408, 2018.

[47] H. Wang, Y. He, Q. Yan et al., "Correlation between the dielectric properties and biological activities of human ex vivo hepatic tissue," *Physics in Medicine and Biology*, vol. 60, no. 6, pp. 2603–2617, 2015.

[48] M. Asklöf, P. Kjølhede, N. B. Wodlin, and L. Nilsson, "Bioelectrical impedance analysis; a new method to evaluate lymphoedema, fluid status, and tissue damage after gynaecological surgery - A systematic review," *European Journal of Obstetrics & Gynecology and Reproductive Biology*, vol. 228, pp. 111–119, 2018.

[49] C. Hawthorne, M. Shaw, I. Piper, L. Moss, and J. Kinsella, "Transcranial bioimpedance measurement as a non-invasive estimate of intracranial pressure," *Acta Neurochirurgica, Supplementum*, vol. 126, pp. 89–92, 2018.

[50] P. Langer, P. Jurák, V. Vondra et al., "Respiratory-induced hemodynamic changes measured by whole-body multichannel impedance plethysmography," *Physiological Research*, vol. 67, no. 4, pp. 571–581, 2018.

[51] M.-H. Jun, S. Kim, B. Ku et al., "Glucose-independent segmental phase angles from multi-frequency bioimpedance analysis to discriminate diabetes mellitus," *Scientific Reports*, vol. 8, no. 1, 2018.

[52] A. C. Buchholz, C. Bartok, and D. A. Schoeller, "The validity of bioelectrical impedance models in clinical populations," *Nutrition in Clinical Practice*, vol. 19, no. 5, pp. 433–446, 2004.

[53] J. Castizo-Olier, A. Irurtia, M. Jemni, M. Carrasco-Marginet, R. Fernández-García, and F. A. Rodríguez, "Bioelectrical impedance vector analysis (BIVA) in sport and exercise: Systematic review and future perspectives," *PLoS ONE*, vol. 13, no. 6, 2018.

[54] S. Grimnes and Ø. Martinsen, *Bioimpedance and Bioelectricity Basics*, Academic Press, London, UK, 3rd edition, 2014.

[55] V. S. Teixeira, W. Krautschneider, and J. J. Montero-Rodriguez, "Bioimpedance spectroscopy for characterization of healthy and cancerous tissues," in *Proceedings of the 2018 IEEE International Conference on Electrical Engineering and Photonics (EExPolytech)*, pp. 147–151, October 2018.

[56] D. Križaj, "Basics of numerical simulations of bioimpedance phenomena," in *Bioimpedance in Biomedical Applications and Research*, pp. 101–116, Springer International Publishing, 2018.

[57] C. Gabriel, S. Gabriel, and E. Corthout, "The dielectric properties of biological tissues: I. Literature survey," *Physics in Medicine and Biology*, vol. 41, no. 11, pp. 2231–2249, 1996.

[58] M. Lin, D. Hu, M. Marmor, S. Herfat, C. Bahney, and M. Maharbiz, "Smart bone plates can monitor fracture healing," *Scientific Reports*, vol. 9, no. 1, 2019.

[59] P. Bhardwaj, D. V. Rai, M. L. Garg, and B. P. Mohanty, "Potential of electrical impedance spectroscopy to differentiate between healthy and osteopenic bone," *Clinical Biomechanics*, vol. 57, pp. 81–88, 2018.

[60] M. Amini, J. Hisdal, and H. Kalvøy, "Applications of bioimpedance measurement techniques in tissue engineering," *Journal of Electrical Bioimpedance (JEB)*, vol. 9, no. 1, pp. 142–158, 2018.

[61] S. Gabriel, R. W. Lau, and C. Gabriel, "The dielectric properties of biological tissues: III. Parametric models for the dielectric spectrum of tissues," *Physics in Medicine and Biology*, vol. 41, no. 11, pp. 2271–2293, 1996.

[62] M. D. O'Toole, L. A. Marsh, J. L. Davidson, Y. M. Tan, D. W. Armitage, and A. J. Peyton, "Non-contact multi-frequency magnetic induction spectroscopy system for industrial-scale bio-impedance measurement," *Measurement Science and Technology*, vol. 26, no. 3, 2015.

[63] A. De Lorenzo, A. Andreoli, J. Matthie, and P. Withers, "Predicting body cell mass with bioimpedance by using theoretical methods: a technological review," *Journal of Applied Physiology*, vol. 82, no. 5, pp. 1542–1558, 1997.

[64] A. Piccoli, L. D. Nescolarde, and J. Rosell, "Conventional and vectorial analysis of bioimpedance in clinical practice," *Nefrología*, vol. 22, no. 3, pp. 228–238, 2002.

[65] C. Carpano Maglioli, D. G. Caldwell, and L. S. Mattos, "A bioimpedance sensing system for in-vivo cancer tissue identification: Design and preliminary evaluation," in *Proceedings of the 39th Annual International Conference of the IEEE Engineering in Medicine and Biology Society, EMBC 2017*, pp. 4235–4238, July 2017.

[66] U. G. Kyle, I. Bosaeus, A. D. De Lorenzo et al., "Bioelectrical impedance analysis—part I: review of principles and methods," *Clinical Nutrition*, vol. 23, no. 5, pp. 1226–1243, 2004.

[67] T. J. Freeborn, "A survey of fractional-order circuit models for biology and biomedicine," *IEEE Journal on Emerging and Selected Topics in Circuits and Systems*, vol. 3, no. 3, pp. 416–424, 2013.

[68] J. Shell and W. D. Gregory, "Efficient cancer detection using multiple neural networks," *IEEE Journal of Translational Engineering in Health and Medicine*, vol. 5, pp. 1–7, 2017.

[69] H. Wu, Y. Zuo, F. Wei et al., "Study on complex Td correction and Cole-Cole parameters for the impedance of immuno-biosensor," in *Proceedings of the 2011 International Conference on New Technology of Agricultural Engineering, ICAE 2011*, pp. 806–809, May 2011.

[70] R. Buendia, F. Seoane, I. Bosaeus et al., "Robustness study of the different immittance spectra and frequency ranges in bioimpedance spectroscopy analysis for assessment of total body composition," *Physiological Measurement*, vol. 35, no. 7, pp. 1373–1395, 2014.

[71] P. D. Jensen, P. M. Meaney, N. R. Epstien, and K. D. Paulsen, "Cole–cole parameter characterization of urea and potassium for improving dialysis treatment assessment," *IEEE Antennas and Wireless Propagation Letters*, vol. 11, pp. 1598–1601, 2012.

[72] M. Guermazi, O. Kanoun, and N. Derbel, "Investigation of long time beef and veal meat behavior by bioimpedance spectroscopy for meat monitoring," *IEEE Sensors Journal*, vol. 14, no. 10, pp. 3624–3630, 2014.

[73] K. Sasaki, K. Wake, and S. Watanabe, "A dosimetric study using best-fit Cole-Cole parameters of biological tissues and organs in radio frequency band," in *Proceedings of the 2013 21st International Symposium on Electromagnetic Theory, EMTS 2013*, pp. 630–633, May 2013.

[74] B. Rigaud, L. Hamzaoui, M. R. Frikha, N. Chauveau, and J.-P. Morucci, "In vitro tissue characterization and modelling using electrical impedance measurements in the 100 Hz-10 MHz frequency range," *Physiological Measurement*, vol. 16, no. 3A, pp. A15–A28, 1995.

[75] M. Sezdi, M. Bayik, and Y. Ulgen, "Storage effects on the Cole-Cole parameters of erythrocyte suspensions," *Physiological Measurement*, vol. 27, no. 7, pp. 623–635, 2006.

[76] T. Dai and A. Adler, "In vivo blood characterization from bioimpedance spectroscopy of blood pooling," *IEEE Transactions on Instrumentation and Measurement*, vol. 58, no. 11, pp. 3831–3838, 2009.

[77] S. Kun, B. Ristic, R. Peura, and R. Dunn, "Algorithm for tissue ischemia estimation based on electrical impedance spectroscopy," *IEEE Transactions on Biomedical Engineering*, vol. 50, no. 12, pp. 1352–1359, 2003.

[78] O. I. Al-Surkhi, P. J. Riu, F. F. Vazquez, and J. Ibeas, "Monitoring Cole-Cole parameters during haemodialysis (HD)," in *Proceedings of the 2007 29th Annual International Conference of the IEEE Engineering in Medicine and Biology Society*, pp. 2238–2241, August 2007.

[79] C. Wang, M. Li, and M. Yao, "Impedance feature extraction of breast cancer and the surrounding tissues," in *Proceedings of the 3rd International Conference on BioMedical Engineering and Informatics, BMEI 2010*, vol. 3, pp. 922–926, October 2010.

[80] B. Maundy and A. S. Elwakil, "Extracting single dispersion Cole–Cole impedance model parameters using an integrator setup," *Analog Integrated Circuits and Signal Processing*, vol. 71, no. 1, pp. 107–110, 2012.

[81] I. Jesus and J. T. MacHado, "Application of Integer and Fractional Models in Electrochemical Systems," *Mathematical Problems in Engineering*, vol. 2012, Article ID 248175, 17 pages, 2012.

[82] A. De Lorenzo, N. Candeloro, A. Andreoli, and P. Deurenberg, "Determination of intracellular water by multifrequency bioelectrical impedance," *Annals of Nutrition and Metabolism*, vol. 39, no. 3, pp. 164–176, 1995.

[83] A. H. Eldarrat, A. S. High, and G. M. Kale, "Age-related changes in ac-impedance spectroscopy studies of normal human dentine: further investigations," *Journal of Materials Science: Materials in Medicine*, vol. 21, no. 1, pp. 45–51, 2010.

[84] M. Tiitta and H. Olkkonen, "Electrical impedance spectroscopy device for measurement of moisture gradients in wood," *Review of Scientific Instruments*, vol. 73, no. 8, pp. 3093–3100, 2002.

[85] T. Repo, J. Laukkanen, and R. Silvennoinen, "Measurement of the tree root growth using electrical impedance spectroscopy," *Silva Fennica*, vol. 39, no. 2, pp. 159–166, 2005.

[86] R. L. Magin and M. Ovadia, "Modeling the cardiac tissue electrode interface using fractional calculus," *Journal of Vibration and Control*, vol. 14, no. 9-10, pp. 1431–1442, 2008.

[87] W. H. Huang, C. K. Chui, S. H. Teoh, and S. K. Chang, "A multiscale model for bioimpedance dispersion of liver tissue," *IEEE Transactions on Biomedical Engineering*, vol. 59, no. 6, pp. 1593–1597, 2012.

[88] M. A. Callejón, P. del Campo, J. Reina-Tosina, and L. M. Roa, "A parametric computational analysis into galvanic coupling intrabody communication," *IEEE Journal of Biomedical and Health Informatics*, vol. 22, no. 4, pp. 1087–1096, 2018.

[89] B. Taji, S. Shirmohammadi, V. Groza, and I. Batkin, "Impact of skin-electrode interface on electrocardiogram measurements using conductive textile electrodes," *IEEE Transactions on Instrumentation and Measurement*, vol. 63, no. 6, pp. 1412–1422, 2014.

[90] M. H. Jones and J. Scott, "Scaling of electrode-electrolyte interface model parameters in phosphate buffered saline," *IEEE Transactions on Biomedical Circuits and Systems*, vol. 9, no. 3, pp. 441–448, 2015.

[91] H. H. Woltjer, B. J. M. van der Meer, H. J. Bogaard, and P. M. J. M. de Vries, "Comparison between spot and band electrodes and between two equations for calculations of stroke volume by means of impedance cardiography," *Medical & Biological Engineering & Computing*, vol. 33, no. 3, pp. 330–334, 1995.

[92] B. Eilebrecht, J. Willkomm, A. Pohl, T. Wartzek, and S. Leonhardt, "Impedance measurement system for determination of capacitive electrode coupling," *IEEE Transactions on Biomedical Circuits and Systems*, vol. 7, no. 5, pp. 682–689, 2013.

[93] M. Guermandi, R. Cardu, E. F. Scarselli, and R. Guerrieri, "Active electrode IC for EEG and electrical impedance tomography with continuous monitoring of contact impedance," *IEEE Transactions on Biomedical Circuits and Systems*, vol. 9, no. 1, pp. 21–33, 2015.

[94] B. W. Lee, C. Lee, J. Kim, and M. Lee, "Comparison of conductive fabric electrode with electromyography to evaluate knee joint movement," *IEEE Sensors Journal*, vol. 12, no. 2, pp. 410-411, 2012.

[95] J. Ferreira, I. Pau, K. Lindecrantz, and F. Seoane, "A handheld and textile-enabled bioimpedance system for ubiquitous body composition analysis. an initial functional validation," *IEEE Journal of Biomedical and Health Informatics*, vol. 21, no. 5, pp. 1224–1232, 2017.

[96] Y. Yu, K. A. Al Mamun, A. S. Shanta, S. K. Islam, and N. McFarlane, "Vertically aligned carbon nanofibers as a cell impedance sensor," *IEEE Transactions on Nanotechnology*, vol. 15, no. 6, pp. 856–861, 2016.

[97] G. Qiao, W. Wang, W. Duan, F. Zheng, A. J. Sinclair, and C. R. Chatwin, "Bioimpedance analysis for the characterization of breast cancer cells in suspension," *IEEE Transactions on Biomedical Engineering*, vol. 59, no. 8, pp. 2321–2329, 2012.

[98] H. Kwon, H. Wi, B. Karki et al., "Bioimpedance spectroscopy tensor probe for anisotropic measurements," *IEEE Electronics Letters*, vol. 48, no. 20, pp. 1253–1255, 2012.

[99] H. Kwon, M. Guasch, J. A. Nagy, S. B. Rutkove, and B. Sanchez, "New electrical impedance methods for the in situ measurement of the complex permittivity of anisotropic skeletal muscle using multipolar needles," *Scientific Reports*, vol. 9, no. 1, 2019.

[100] B. Karki, H. Wi, A. McEwan et al., "Evaluation of a multi-electrode bioimpedance spectroscopy tensor probe to detect the anisotropic conductivity spectra of biological tissues," *Measurement Science and Technology*, vol. 25, no. 7, 2014.

[101] D. Teichmann, L. Rohe, A. Niesche, M. Mueller, K. Radermacher, and S. Leonhardt, "Estimation of penetrated bone layers during craniotomy via bioimpedance measurement," *IEEE Transactions on Biomedical Engineering*, vol. 64, no. 4, pp. 765–774, 2017.

[102] A. S. Tucker, R. M. Fox, and R. J. Sadleir, "Biocompatible, high precision, wideband, improved howland current source with lead-lag compensation," *IEEE Transactions on Biomedical Circuits and Systems*, vol. 7, no. 1, pp. 63–70, 2013.

[103] A. S. Anusha, S. P. Preejith, J. Joseph, and M. Sivaprakasam, "Design and implementation of a hand-to-hand multifrequency bioimpedance measurement scheme for Total Body Water estimation," in *Proceedings of the 2017 IEEE International Instrumentation and Measurement Technology Conference, I2MTC 2017*, May 2017.

[104] H. Ko, T. Lee, J. Kim, J. Park, and J. P. Kim, "Ultralow-power bioimpedance IC with intermediate frequency shifting chopper," *IEEE Transactions on Circuits and Systems II: Express Briefs*, vol. 63, no. 3, pp. 259–263, 2016.

[105] M. Etemadi, P. Chung, J. A. Heller, J. A. Liu, L. Rand, and S. Roy, "Towards birthalert—a clinical device intended for early preterm birth detection," *IEEE Transactions on Biomedical Engineering*, vol. 60, no. 12, pp. 3484–3493, 2013.

[106] J. E. Sanders, M. A. Moehring, T. M. Rothlisberger et al., "A bioimpedance analysis platform for amputee residual limb assessment," *IEEE Transactions on Biomedical Engineering*, vol. 63, no. 8, pp. 1760–1770, 2016.

[107] L. Yan, J. Pettine, S. Mitra et al., "A 13 murmA analog signal processing IC for accurate recognition of multiple intra-cardiac signals," *IEEE Transactions on Biomedical Circuits and Systems*, vol. 7, no. 6, pp. 785–795, 2013.

[108] R. Harder, A. Diedrich, J. S. Whitfield, M. S. Buchowski, J. B. Pietsch, and F. J. Baudenbacher, "Smart multi-frequency bioelectrical impedance spectrometer for BIA and BIVA applications," *IEEE Transactions on Biomedical Circuits and Systems*, vol. 10, no. 4, pp. 912–919, 2016.

[109] L. Constantinou, I. F. Triantis, R. Bayford, and A. Demosthenous, "High-power CMOS current driver with accurate transconductance for electrical impedance tomography," *IEEE Transactions on Biomedical Circuits and Systems*, vol. 8, no. 4, pp. 575–583, 2014.

[110] P. J. Langlois, N. Neshatvar, and A. Demosthenous, "A sinusoidal current driver with an extended frequency range and multifrequency operation for bioimpedance applications," *IEEE Transactions on Biomedical Circuits and Systems*, vol. 9, no. 3, pp. 401–411, 2015.

[111] L. Constantinou, R. Bayford, and A. Demosthenous, "A wideband low-distortion CMOS current driver for tissue impedance analysis," *IEEE Transactions on Circuits and Systems II: Express Briefs*, vol. 62, no. 2, pp. 154–158, 2015.

[112] V. Chitturi and N. Farrukh, "An alternate voltage-controlled current source for electrical impedance tomography applications," *Lecture Notes in Networks and Systems*, vol. 43, pp. 93–102, 2019.

[113] Ø. G. Martinsen, B. Nordbotten, S. Grimnes, H. Fossan, and J. Eilevstjønn, "Bioimpedance-based respiration monitoring with a defibrillator," *IEEE Transactions on Biomedical Engineering*, vol. 61, no. 6, pp. 1858–1862, 2014.

[114] A. Yúfera and A. Rueda, "Design of a CMOS closed-loop system with applications to bio-impedance measurements," *Microelectronics Journal*, vol. 41, no. 4, pp. 231–239, 2010.

[115] P. Kassanos, I. F. Triantis, and A. Demosthenous, "A CMOS magnitude/phase measurement chip for impedance spectroscopy," *IEEE Sensors Journal*, vol. 13, no. 6, pp. 2229–2236, 2013.

[116] S.-J. Kweon, J.-H. Park, S. Shin, S.-S. Yoo, and H.-J. Yoo, "A reconfigurable time-to-digital converter based on time stretcher and chain-delay-line for electrical bioimpedance spectroscopy," in *Proceedings of the 60th IEEE International Midwest Symposium on Circuits and Systems, MWSCAS 2017*, vol. 2017, pp. 1037–1040, August 2017.

[117] B. Sanchez, G. Vandersteen, R. Bragos, and J. Schoukens, "Basics of broadband impedance spectroscopy measurements using periodic excitations," *Measurement Science and Technology*, vol. 23, no. 10, 2012.

[118] M. Min, T. Parve, A. Ronk, P. Annus, and T. Paavle, "Synchronous sampling and demodulation in an instrument for multifrequency bioimpedance measurement," *IEEE Transactions on Instrumentation and Measurement*, vol. 56, no. 4, pp. 1365–1372, 2007.

[119] S. K. Oruganti, S. H. Heo, H. Ma, and F. Bien, "Wireless energy transfer: Touch/Proximity/Hover sensing for large contoured displays and industrial applications," *IEEE Sensors Journal*, vol. 15, no. 4, pp. 2062–2068, 2015.

[120] F. R. Parente, S. Di Giovanni, G. Ferri, V. Stornelli, G. Pennazza, and M. Santonico, "An analog bootstrapped biosignal read-out circuit with common-mode impedance two-electrode compensation," *IEEE Sensors Journal*, vol. 18, no. 7, pp. 2861–2869, 2018.

[121] N. Li, H. Xu, W. Wang, Z. Zhou, G. Qiao, and D. D.-U. Li, "A high-speed bioelectrical impedance spectroscopy system based on the digital auto-balancing bridge method," *Measurement Science and Technology*, vol. 24, no. 6, 2013.

[122] J. He, M. Wang, X. Li, G. Li, and L. Lin, "Pulse wave detection method based on the bio-impedance of the wrist," *Review of Scientific Instruments*, vol. 87, no. 5, 2016.

[123] Y. Liu, X. Qiao, G. Li, and L. Lin, "An improved device for bioimpedance deviation measurements based on 4-electrode half bridge," *Review of Scientific Instruments*, vol. 87, no. 10, 2016.

[124] J. C. Bæg, H. Wi, T. I. Oh, A. L. McEwan, and E. J. Woo, "An amplitude-to-time conversion technique suitable for multichannel data acquisition and bioimpedance imaging," *IEEE Transactions on Biomedical Circuits and Systems*, vol. 7, no. 3, pp. 349–354, 2013.

[125] B. Sanchez, G. Vandersteen, R. Bragos, and J. Schoukens, "Optimal multisine excitation design for broadband electrical impedance spectroscopy," *Measurement Science and Technology*, vol. 22, no. 11, 2011.

[126] M. Min and T. Paavle, "Broadband discrete-level excitations for improved extraction of information in bioimpedance measurements," *Physiological Measurement*, vol. 35, no. 6, pp. 997–1010, 2014.

[127] T. Paavle, M. Min, and T. Parve, "Using of chirp excitation for bioimpedance estimation: Theoretical aspects and modeling," in *Proceedings of the 11th Biennial Baltic Electronics Conference, BEC 2008*, pp. 325–328, October 2008.

[128] B. Sanchez, J. Schoukens, R. Bragos, and G. Vandersteen, "Novel estimation of the electrical bioimpedance using the local polynomial method. application to in vivo real-time myocardium tissue impedance characterization during the cardiac cycle," *IEEE Transactions on Biomedical Engineering*, vol. 58, no. 12, part 1, pp. 3376–3385, 2011.

[129] X. Shi, F. You, Z. Ji, F. Fu, R. Liu, and X. Dong, "Digital Demodulation in data acquisition system for multi-frequency electrical impedance tomography," in *Proceedings of the 4th International Conference on Bioinformatics and Biomedical Engineering, iCBBE 2010*, June 2010.

[130] X. Shi, F. You, C. Xu et al., "Design and implementation of a high-precision electrical impedance tomography data acquisition system for brain imaging," in *Proceedings of the 12th IEEE Biomedical Circuits and Systems Conference, BioCAS 2016*, pp. 9–13, China, October 2016.

[131] J. Gracia, V. P. Seppa, J. Viik, and J. Hyttinen, "Multilead measurement system for the time-domain analysis of bioimpedance magnitude," *IEEE Transactions on Biomedical Engineering*, vol. 59, no. 8, pp. 2273–2280, 2012.

[132] F. Seoane, J. Ferreira, J. J. Sanchéz, and R. Bragós, "An analog front-end enables electrical impedance spectroscopy system on-chip for biomedical applications," *Physiological Measurement*, vol. 29, no. 6, pp. S267–S278, 2008.

[133] B. Sanchez, A. L. Aroul, E. Bartolome, K. Soundarapandian, and R. Bragos, "Propagation of measurement errors through body composition equations for body impedance analysis," *IEEE Transactions on Instrumentation and Measurement*, vol. 63, no. 6, pp. 1535–1544, 2014.

[134] M. Konijnenburg, S. Stanzione, L. Yan et al., "A Multi(bio)sensor Acquisition System with Integrated Processor, Power Management, 8×8 LED Drivers, and Simultaneously Synchronized ECG, BIO-Z, GSR, and Two PPG Readouts," *IEEE Journal of Solid-State Circuits*, vol. 51, no. 11, pp. 2584–2595, 2016.

[135] E. M. Bartels, E. R. Sørensen, and A. P. Harrison, "Multifrequency bioimpedance in human muscle assessment," *Physiological Reports*, vol. 3, no. 4, 2015.

[136] R. Kubendran, S. Lee, S. Mitra, and R. F. Yazicioglu, "Error correction algorithm for high accuracy bio-impedance measurement in wearable healthcare applications," *IEEE Transactions on Biomedical Circuits and Systems*, vol. 8, no. 2, pp. 196–205, 2014.

[137] A. A. Silverio, W.-Y. Chung, and V. F. S. Tsai, "A low power high CMRR CMOS instrumentation amplifier for Bio-impedance Spectroscopy," in *Proceedings of the 2014 IEEE International Symposium on Bioelectronics and Bioinformatics, IEEE ISBB 2014*, April 2014.

[138] E. H. Sanabria, J. A. Palacio, H. H. Herrera, and W. Van Noije, "A design methodology for an integrated CMOS instrumentation amplifier for bioespectroscopy applications," in *Proceedings of the 2017 CHILEAN Conference on Electrical, Electronics Engineering, Information and Communication Technologies, CHILECON 2017*, pp. 1–7, October 2017.

[139] K. Kim, K. Song, K. Bong et al., "A 24 μW 38.51 mΩrms resolution bio-impedance sensor with dual path instrumentation amplifier," in *Proceedings of the 43rd IEEE European Solid State Circuits Conference, ESSCIRC 2017*, pp. 223–226, September 2017.

[140] M. Zamani, Y. Rezaeiyan, O. Shoaei, and W. A. Serdijn, "A 1.55 μw bio-impedance measurement system for implantable cardiac pacemakers in 0.18 μm CMOS," *IEEE Transactions on Biomedical Circuits and Systems*, vol. 12, no. 1, pp. 211–221, 2018.

[141] M. Ulbrich, J. Muhlsteff, D. Teichmann, S. Leonhardt, and M. Walter, "A thorax simulator for complex dynamic bioimpedance measurements with textile electrodes," *IEEE Transactions on Biomedical Circuits and Systems*, vol. 9, no. 3, pp. 412–420, 2015.

[142] C. Aliau-Bonet and R. Pallas-Areny, "A novel method to estimate body capacitance to ground at mid frequencies," *IEEE Transactions on Instrumentation and Measurement*, vol. 62, no. 9, pp. 2519–2525, 2013.

[143] C. Aliau-Bonet and R. Pallas-Areny, "On the effect of body capacitance to ground in tetrapolar bioimpedance measurements," *IEEE Transactions on Biomedical Engineering*, vol. 59, no. 12, pp. 3405–3411, 2012.

[144] Y. Yang, W. Ni, Q. Sun, H. Wen, and Z. Teng, "Improved Cole parameter extraction based on the least absolute deviation method," *Physiological Measurement*, vol. 34, no. 10, pp. 1239–1252, 2013.

[145] R. Buendia, R. Gil-Pita, and F. Seoane, "Cole parameter estimation from total right side electrical bioimpedance spectroscopy measurements—influence of the number of frequencies and the upper limit," in *Proceedings of the 33rd Annual International Conference of the IEEE Engineering in Medicine and Biology Society (EMBS '11)*, pp. 1843–1846, IEEE, Boston, Mass, USA, September 2011.

[146] T. J. Freeborn, B. Maundy, and A. Elwakil, "Improved Cole-Cole parameter extraction from frequency response using least squares fitting," in *Proceedings of the 2012 IEEE International Symposium on Circuits and Systems, ISCAS 2012*, pp. 337–340, Republic of Korea, May 2012.

[147] L. C. Ward, T. Essex, and B. H. Cornish, "Determination of Cole parameters in multiple frequency bioelectrical impedance analysis using only the measurement of impedances," *Physiological Measurement*, vol. 27, no. 9, pp. 839–850, 2006.

[148] B. J. Nordbotten, C. Tronstad, Ø. G. Martinsen, and S. Grimnes, "Evaluation of algorithms for calculating bioimpedance phase angle values from measured whole-body impedance modulus," *Physiological Measurement*, vol. 32, no. 7, pp. 755–765, 2011.

[149] A. Keshtkar, Z. Salehnia, A. Keshtkar, and B. Shokouhi, "Bladder cancer detection using electrical impedance technique (Tabriz Mark 1)," *Pathology Research International*, vol. 2012, Article ID 470101, 5 pages, 2012.

[150] F. Villa, A. Magnani, G. Merati, and P. Castiglioni, "Feasibility of long-term monitoring of multifrequency and multisegment body impedance by portable devices," *IEEE Transactions on Biomedical Engineering*, vol. 61, no. 6, pp. 1877–1886, 2014.

[151] S. L. Yoon, O. Grundmann, J. J. Williams, L. Gordan, and T. J. George, "Body composition changes differ by gender in stomach, colorectal, and biliary cancer patients with cachexia: Results from a pilot study," *Cancer Medicine*, vol. 7, no. 8, pp. 3695–3703, 2018.

[152] C. Earthman, D. Traughber, J. Dobratz, and W. Howell, "Bioimpedance spectroscopy for clinical assessment of fluid distribution and body cell mass," *Nutrition in Clinical Practice*, vol. 22, no. 4, pp. 389–405, 2007.

[153] S. Sipahi, E. Hur, S. Demirtas et al., "Body composition monitor measurement technique for the detection of volume status in peritoneal dialysis patients: the effect of abdominal fullness," *International Urology and Nephrology*, vol. 43, no. 4, pp. 1195–1199, 2011.

[154] U. M. Moissl, P. Wabel, P. W. Chamney et al., "Body fluid volume determination via body composition spectroscopy in health and disease," *Physiological Measurement*, vol. 27, no. 9, pp. 921–933, 2006.

[155] S. Khalil, M. Mohktar, and F. Ibrahim, "The theory and fundamentals of bioimpedance analysis in clinical status monitoring and diagnosis of diseases," *Sensors*, vol. 14, no. 6, pp. 10895–10928, 2014.

[156] R. Thibault and C. Pichard, "The evaluation of body composition: a useful tool for clinical practice," *Annals of Nutrition and Metabolism*, vol. 60, no. 1, pp. 6–16, 2012.

[157] P. P. Gupta, G. C. Fonarow, and T. B. Horwich, "Obesity and the obesity paradox in heart failure," *Canadian Journal of Cardiology*, vol. 31, no. 2, pp. 195–202, 2015.

[158] S. Hocking, D. Samocha-Bonet, K.-L. Milner, J. R. Greenfield, and D. J. Chisholm, "Adiposity and insulin resistance in humans: the role of the different tissue and cellular lipid depots," *Endocrine Reviews*, vol. 34, no. 4, pp. 463–500, 2013.

[159] M. Kovarik, M. Hronek, and Z. Zadak, "Clinically relevant determinants of body composition, function and nutritional status as mortality predictors in lung cancer patients," *Lung Cancer*, vol. 84, no. 1, pp. 1–6, 2014.

[160] E. De Rosa, L. Santarpia, M. Marra et al., "Preliminary evaluation of the prevalence of sarcopenia in obese patients from Southern Italy," *Nutrition Journal* , vol. 31, no. 1, pp. 79–83, 2015.

[161] E. M. Widen and D. Gallagher, "Body composition changes in pregnancy: measurement, predictors and outcomes," *European Journal of Clinical Nutrition*, vol. 68, no. 6, pp. 643–652, 2014.

[162] M. L. Giannì, P. Roggero, A. Orsi et al., "Body composition changes in the first 6 months of life according to method of feeding," *Journal of Human Lactation*, vol. 30, no. 2, pp. 148–155, 2014.

[163] A. Shuster, M. Patlas, J. H. Pinthus, and M. Mourtzakis, "The clinical importance of visceral adiposity: a critical review of methods for visceral adipose tissue analysis," *British Journal of Radiology*, vol. 85, no. 1009, pp. 1–10, 2012.

[164] A. A. Jackson, M. Johnson, K. Durkin, and S. Wootton, "Body composition assessment in nutrition research: value of BIA technology," *European Journal of Clinical Nutrition*, vol. 67, no. S1, pp. S71–S78, 2013.

[165] C. M. Toomey, A. Cremona, K. Hughes, C. Norton, and P. Jakeman, "A review of body composition measurement in the assessment of health," *Topics in Clinical Nutrition*, vol. 30, no. 1, pp. 16–32, 2015.

[166] K. Cumming, G. E. Hoyle, J. D. Hutchison, and R. L. Soiza, "Bioelectrical impedance analysis is more accurate than clinical examination in determining the volaemic status of elderly patients with fragility fracture and hyponatraemia," *The Journal of Nutrition, Health & Aging*, vol. 18, no. 8, pp. 744–750, 2014.

[167] C. Tsigos, C. Stefanaki, G. I. Lambrou, D. Boschiero, and G. P. Chrousos, "Stress and inflammatory biomarkers and symptoms are associated with bioimpedance measures," *European Journal of Clinical Investigation*, vol. 45, no. 2, pp. 126–134, 2015.

[168] L. Mattar, N. Godart, J. C. Melchior, and C. Pichard, "Anorexia nervosa and nutritional assessment: contribution of body composition measurements," *Nutrition Research Reviews*, vol. 24, no. 1, pp. 39–45, 2011.

[169] A. F. Casey, "Measuring body composition in individuals with intellectual disability: A scoping review," *Journal of Obesity*, vol. 2013, Article ID 628428, 6 pages, 2013.

[170] D. Thangarajah, M. J. Hyde, V. K. S. Konteti, S. Santhakumaran, G. Frost, and J. M. E. Fell, "Systematic review: Body composition in children with inflammatory bowel disease," *Alimentary Pharmacology & Therapeutics*, vol. 42, no. 2, pp. 142–157, 2015.

[171] E. Haverkort, P. Reijven, J. Binnekade et al., "Bioelectrical impedance analysis to estimate body composition in surgical and oncological patients: a systematic review," *European Journal of Clinical Nutrition*, vol. 69, pp. 3–13, 2015.

[172] Z. Erdogan Iyigun, D. Selamoglu, G. Alco et al., "Bioelectrical impedance for detecting and monitoring lymphedema in patients with breast cancer. Preliminary results of the florence nightingale breast study group," *Lymphatic Research and Biology*, vol. 13, no. 1, pp. 40–45, 2015.

[173] B. E. Lingwood, "Bioelectrical impedance analysis for assessment of fluid status and body composition in neonates—the good, the bad and the unknown," *European Journal of Clinical Nutrition*, vol. 67, no. S1, pp. S28–S33, 2013.

[174] E. Rivers, B. Nguyen, S. Havstad et al., "Early goal-directed therapy in the treatment of severe sepsis and septic shock," *The New England Journal of Medicine*, vol. 345, no. 19, pp. 1368–1377, 2001.

[175] J. H. Boyd, J. Forbes, T. Nakada, K. R. Walley, and J. A. Russell, "Fluid resuscitation in septic shock: a positive fluid balance and elevated central venous pressure are associated with increased mortality," *Critical Care Medicine*, vol. 39, no. 2, pp. 259–265, 2011.

[176] H. P. Wiedemann, A. P. Wheeler, G. R. Bernard et al., "Comparison of two fluid-management strategies in acute lung injury," *The New England Journal of Medicine*, vol. 354, no. 24, pp. 2564–2575, 2006.

[177] U. Mulasi, A. J. Kuchnia, A. J. Cole, and C. P. Earthman, "Bioimpedance at the bedside: current applications, limitations, and opportunities," *Nutrition in Clinical Practice*, vol. 30, no. 2, pp. 180–193, 2015.

[178] C. Moctezuma-Velázquez, I. García-Juárez, R. Soto-Solís, J. Hernández-Cortés, and A. Torre, "Nutritional assessment and treatment of patients with liver cirrhosis," *Nutrition Journal*, vol. 29, no. 11-12, pp. 1279–1285, 2013.

[179] M. Siervo, C. Prado, L. Hooper et al., "Serum osmolarity and haematocrit do not modify the association between the impedance index (Ht2/Z) and total body water in the very old: The Newcastle 85+ Study," *Archives of Gerontology and Geriatrics*, vol. 60, no. 1, pp. 227–232, 2015.

[180] S. M. Ribeiro and J. J. Kehayias, "Sarcopenia and the analysis of body composition," *Advances in Nutrition*, vol. 5, no. 3, pp. 260–267, 2014.

[181] G. Mascherini, C. Petri, and G. Galanti, "Integrated total body composition and localized fat-free mass assessment," *Sport Sciences for Health*, vol. 11, no. 2, pp. 217–225, 2015.

[182] A. Walter-Kroker, A. Kroker, M. Mattiucci-Guehlke, and T. Glaab, "A practical guide to bioelectrical impedance analysis using the example of chronic obstructive pulmonary disease," *Nutrition Journal*, vol. 10, no. 1, 2011.

[183] A. M. Abbatecola, A. Fumagalli, L. Spazzafumo et al., "Body composition markers in older persons with COPD," *Age and Ageing*, vol. 43, no. 4, pp. 548–553, 2014.

[184] J. Bauer, E. Egan, and A. Clavarino, "The scored patient-generated subjective global assessment is an effective nutrition assessment tool in subjects with chronic obstructive pulmonary disease," *e-SPEN Journal*, vol. 6, no. 1, pp. e27–e30, 2011.

[185] S. Mitra, "Extracellular hydration, cardiovascular risk, and the interstitium: a three-dimensional view," *Kidney International*, vol. 85, no. 3, pp. 510–512, 2014.

[186] R. Hussain, F. Kappel, F. Zhu, N. W. Levin, and P. Kotanko, "Body composition and solute kinetics in hemodialysis patients: a mathematical model," *IET Communications*, vol. 6, no. 18, pp. 3301–3308, 2012.

[187] R. Patterson, "Body fluid determinations using multiple impedance measurements," *IEEE Engineering in Medicine and Biology Magazine*, vol. 8, no. 1, pp. 16–18, 1989.

[188] S. S. Sun, W. C. Chumlea, S. B. Heymsfield et al., "Development of bioelectrical impedance analysis prediction equations for body composition with the use of a multicomponent model for use in epidemiologic surveys," *American Journal of Clinical Nutrition*, vol. 77, no. 2, pp. 331–340, 2003.

[189] B. L. Heitmann, "Prediction of body water and fat in adult Danes from measurement of electrical impedance. A validation study," *International Journal of Obesity*, vol. 14, no. 9, pp. 789–802, 1990.

[190] G. Sergi, M. Bussolotto, P. Perini et al., "Accuracy of bioelectrical impedance analysis in estimation of extracellular space in healthy subjects and in fluid retention states," *Annals of Nutrition and Metabolism*, vol. 38, no. 3, pp. 158–165, 1994.

[191] P. Deurenberg, K. Van Der Kooy, R. Leenen, J. A. Weststrate, and J. C. Seidell, "Sex and age specific prediction formulas for estimating body composition from bioelectrical impedance: A cross-validation study," *International Journal of Obesity*, vol. 15, no. 1, pp. 17–25, 1991.

[192] M. Ring, C. Lohmueller, M. Rauh, J. Mester, and B. M. Eskofier, "A temperature-based bioimpedance correction for water loss estimation during sports," *IEEE Journal of Biomedical and Health Informatics*, vol. 20, no. 6, pp. 1477–1484, 2016.

[193] F. Seoane, S. Abtahi, F. Abtahi et al., "Mean expected error in prediction of total body water: A true accuracy comparison between bioimpedance spectroscopy and single frequency regression equations," *BioMed Research International*, vol. 2015, Article ID 656323, 11 pages, 2015.

[194] U. G. Kyle, I. Bosaeus, A. D. De Lorenzo et al., "Bioelectrical impedance analysis—part II: utilization in clinical practice," *Clinical Nutrition*, vol. 23, no. 6, pp. 1430–1453, 2004.

[195] L. Nescolarde, T. Doñate, A. Piccoli, and J. Rosell, "Comparison of segmental with whole-body impedance measurements in peritoneal dialysis patients," *Medical Engineering & Physics*, vol. 30, no. 7, pp. 817–824, 2008.

[196] M. D. Van Loan, P. Withers, J. Matthie, and P. L. Mayclin, "Use of bioimpedance spectroscopy to determine extracellular fluid, intracellular fluid, total body water, and fat-free mass," *Basic Life Sciences*, vol. 60, pp. 67–70, 1993.

[197] M. Y. Jaffrin and M. V. Moreno, "Measurements of total body water with a foot-to-foot impedancemeter," *Medical Engineering & Physics*, vol. 30, no. 4, pp. 483–489, 2008.

[198] M. Y. Jaffrin and H. Morel, "Body fluid volumes measurements by impedance: a review of bioimpedance spectroscopy (BIS) and bioimpedance analysis (BIA) methods," *Medical Engineering & Physics*, vol. 30, no. 10, pp. 1257–1269, 2008.

[199] J. Eisenkölbl, M. Kartasurya, and K. Widhalm, "Underestimation of percentage fat mass measured by bioelectrical impedance analysis compared to dual energy X-ray absorptiometry method in obese children," *European Journal of Clinical Nutrition*, vol. 55, no. 6, pp. 423–429, 2001.

[200] A. Piccoli, B. Rossi, L. Pillon, and G. Bucciante, "A new method for monitoring body fluid variation by bioimpedance analysis:

the RXc graph," *Kidney International*, vol. 46, no. 2, pp. 534–539, 1994.

[201] L. Nescolarde, A. Piccoli, A. Román et al., "Bioelectrical impedance vector analysis in haemodialysis patients: relation between oedema and mortality," *Physiological Measurement*, vol. 25, no. 5, pp. 1271–1280, 2004.

[202] M. D. L. Á. Espinosa-Cuevas, L. Rivas-Rodríguez, E. C. González-Medina, X. Atilano-Carsi, P. Miranda-Alatriste, and R. Correa-Rotter, "Bioimpedance vector analysis for body composition in Mexican population," *Revista de Investigación Clínica*, vol. 59, no. 1, pp. 15–24, 2007.

[203] A. Piccoli, L. Pillon, and F. Dumler, "Impedance vector distribution by sex, race, body mass index, and age in the United States: standard reference intervals as bivariate Z scores," *Nutrition Journal* , vol. 18, no. 2, pp. 153–167, 2002.

[204] M. Peppa, C. Stefanaki, A. Papaefstathiou, D. Boschiero, G. Dimitriadis, and G. P. Chrousos, "Bioimpedance analysis vs. DEXA as a screening tool for osteosarcopenia in lean, overweight and obese caucasian postmenopausal females," *Hormones*, vol. 16, no. 2, pp. 181–193, 2017.

[205] A. Molfino, B. R. Don, and G. A. Kaysen, "Comparison of bioimpedance and dual-energy X-ray absorptiometry for measurement of fat mass in hemodialysis patients," *Nephron Clinical Practice*, vol. 122, no. 3-4, pp. 127–133, 2012.

[206] M. T. Najafi, O. Nasiri, A. Alamdari et al., "Comparison of body composition assessed by multi-frequency segmental bioelectrical impedance analysis and dual energy X-ray absorptiometry in hemodialysis patients," *Nephro-Urology Monthly*, vol. 10, no. 6, 2018.

[207] P. S. Lim, C. H. Chen, F. Zhu et al., "Validating body fat assessment by bioelectric impedance spectroscopy in taiwanese hemodialysis patients," *Journal of Renal Nutrition*, vol. 27, no. 1, pp. 37–44, 2017.

[208] P. Deurenberg, A. Tagliabue, and F. J. M. Schouten, "Multifrequency impedance for the prediction of extracellular water and total body water," *British Journal of Nutrition*, vol. 73, no. 3, pp. 349–358, 1995.

[209] R. F. Kushner and D. A. Schoeller, "Estimation of total body water by bioelectrical impedance analysis," *American Journal of Clinical Nutrition*, vol. 44, no. 3, pp. 417–424, 1986.

[210] B. C. Wingo, V. G. Barry, A. C. Ellis, and B. A. Gower, "Comparison of segmental body composition estimated by bioelectrical impedance analysis and dual-energy X-ray absorptiometry," *Clinical Nutrition ESPEN*, vol. 28, pp. 141–147, 2018.

[211] J. G. Raimann, F. Zhu, J. Wang et al., "Comparison of fluid volume estimates in chronic hemodialysis patients by bioimpedance, direct isotopic, and dilution methods," *Kidney International*, vol. 85, no. 4, pp. 898–908, 2014.

[212] R. Větrovská, Z. Vilikus, J. Klaschka et al., "Does impedance measure a functional state of the body fat?" *Physiological Research*, vol. 63, no. 2, pp. S309–S320, 2014.

[213] Y. Zhou, P. Höglund, and N. Clyne, "Comparison of DEXA and bioimpedance for body composition measurements in nondialysis patients with ckd," *Journal of Renal Nutrition*, vol. 29, no. 1, pp. 33–38, 2019.

[214] M. Krzykała, J. Konarski, R. Malina, K. Rachwalski, P. Leszczyński, and E. Ziółkowska-Łajp, "Fatness of female field hockey players: Comparison of estimates with different methods," *Homo: Journal of Comparative Human Biology*, vol. 67, no. 3, pp. 245–257, 2016.

[215] R. Patterson, "Fundamentals of impedance cardiography," *IEEE Engineering in Medicine and Biology Magazine*, vol. 8, no. 1, pp. 35–38, 1989.

[216] A. Sherwood(Chair), M. T. Allen, J. Fahrenberg, R. M. Kelsey, W. R. Lovallo, and L. J. Doornen, "Methodological guidelines for impedance cardiography," *Psychophysiology*, vol. 27, no. 1, pp. 1–23, 1990.

[217] S. Benouar, A. Hafid, M. Attari, M. Kedir-Talha, and F. Seoane, "Systematic variability in ICG recordings results in ICG complex subtypes – steps towards the enhancement of ICG characterization," *Journal of Electrical Bioimpedance (JEB)*, vol. 9, no. 1, pp. 72–82, 2018.

[218] G. Singh, S. Anand, B. Lall, A. Srivastava, and V. Singh, "A technical review of various bioelectric impedance methods for health monitoring," in *Proceedings of the 2018 IEEE Long Island Systems, Applications and Technology Conference, LISAT 2018*, pp. 1–6, 2018.

[219] T. K. Bera, "Bioelectrical impedance methods for noninvasive health monitoring: A review," *Journal of Medical Engineering*, vol. 2014, Article ID 381251, 28 pages, 2014.

[220] J. Malmivuo and R. Plonsey, *Bioelectromagnetism: Principles and Applications of Bioelectric and Biomagnetic Fields*, Oxford University Press, New York, NY, USA, 1995.

[221] X. Chen, X. Hu, R. Ren et al., "Noninvasive ambulatory monitoring of the electric and mechanical function of heart with a multifunction wearable sensor," in *Proceedings of the 2014 IEEE 38th International Computer Software and Applications Conference Workshops*, pp. 662–667, Vasteras, Sweden, July 2014.

[222] J. Xu, P. Harpe, and C. V. Hoof, "An energy-efficient and reconfigurable sensor IC for bio-impedance spectroscopy and ECG recording," *IEEE Journal on Emerging and Selected Topics in Circuits and Systems*, vol. 8, no. 3, pp. 616–626, 2018.

[223] X. Chen, J. Xie, Z. Fang, and S. Xia, "Low power electrocardiography and impedance cardiography detection system based on LabVIEW and Bluetooth Low Energy," in *Proceedings of the 2015 IET International Conference on Biomedical Image and Signal Processing, ICBISP 2015*, 2015.

[224] M. Snajdarova, S. Borik, and I. Cap, "Features extraction from impedance cardiography signal," in *Proceedings of the 11th International Conference on Measurement*, pp. 225–228, May 2017.

[225] X. Hu, X. Chen, and R. Ren, "Noninvasive ambulatory hemodynamic monitoring based on electrocardiogram and impedance cardiography," *Journal of Fiber Bioengineering and Informatics*, vol. 8, no. 4, pp. 741–749, 2015.

[226] H. Yazdanian, A. Mahnam, M. Edrisi, and M. Esfahani, "Design and implementation of a portable impedance cardiography system for noninvasive stroke volume monitoring," *Journal of Medical Signals and Sensors*, vol. 6, no. 1, pp. 47–56, 2016.

[227] M. Ulbrich, J. Mühlsteff, A. Sipilä et al., "The IMPACT shirt: textile integrated and portable impedance cardiography," *Physiological Measurement*, vol. 35, no. 6, pp. 1181–1196, 2014.

[228] A. Szczesna, A. Nowak, P. Grabiec, P. Rozentryt, and M. Wojciechowska, "Innovations in biomedical engineering. advances in intelligent systems and computing," in *Wearable sensor vest design study for vital parameters measurement system, Advances in Intelligent Systems and Computing*, vol. 526, pp. 330–337, Springer, Cham, Switzerland, 2017.

[229] M. Banet, S. Pede, M. Dhillon, and R. Hunt, *Body Worn Sensor for Characterizing Patients with Heart Failure*, Perminova Inc., 2014, Patent US 2014/0187990 A1.

[230] E. Pinheiro, O. Postolache, and P. Girão, "Contactless impedance cardiography using embedded sensors," *Measurement Science Review*, vol. 13, no. 3, pp. 157–164, 2013.

[231] D. B. Jain, J. Weeks, D. Nadezhdin, and J.-F. Asselin, "Contactless electric cardiogram system," *Patent WO 2016/044933 Al*, Article ID 044933, 2016.

[232] S.-H. Liu, J.-J. Wang, S. Chun-Hung, and D.-C. Cheng, "Improvement of left ventricular ejection time measurement in the impedance cardiography combined with the reflection photoplethysmography," *Sensors*, vol. 18, no. 9, 2018.

[233] M. Cieslak, W. S. Ryan, A. Macy et al., "Simultaneous acquisition of functional magnetic resonance images and impedance cardiography," *Psychophysiology*, vol. 52, no. 4, pp. 481–488, 2015.

[234] M. Forouzanfar, F. C. Baker, M. de Zambotti, C. McCall, L. Giovangrandi, and G. T. A. Kovacs, "Toward a better noninvasive assessment of preejection period: A novel automatic algorithm for B-point detection and correction on thoracic impedance cardiogram," *Psychophysiology*, vol. 55, no. 8, Article ID e13072, 2018.

[235] J. R. Árbol, P. Perakakis, A. Garrido, J. L. Mata, M. C. Fernández-Santaella, and J. Vila, "Mathematical detection of aortic valve opening (B point) in impedance cardiography: A comparison of three popular algorithms," *Psychophysiology*, vol. 54, no. 3, pp. 350–357, 2017.

[236] S. S. Mirza and M. Z. U. Rahman, "Efficient adaptive filtering techniques for thoracic electrical bio-impedance analysis in health care systems," *Journal of Medical Imaging and Health Informatics*, vol. 7, no. 6, pp. 1126–1138, 2017.

[237] S. Liu, K. Yue, H. Yang, L. Liu, X. Duan, and T. Guo, "Study on cardiac impedance signal feature point extraction," in *Proceedings of the 3rd IEEE Information Technology and Mechatronics Engineering Conference, ITOEC 2017*, pp. 790–793, October 2017.

[238] R. Stepanov, A. Dumler, S. Podtaev, and P. Frick, "Wavelet analysis in impedance rheocardiography," in *Bioimpedance in Biomedical Applications and Research*, pp. 257–269, Springer International Publishing, Cham, Switzerland, 2018.

[239] S. M. M. Naidu, U. R. Bagal, P. C. Pandey, S. Hardas, and N. D. Khambete, "Monitoring of stroke volume through impedance cardiography using an artificial neural network," in *Proceedings of the 2015 21st National Conference on Communications, NCC 2015*, pp. 1–6, March 2015.

[240] J. Muñoz, P. Gambús, E. W. Jensen, and M. Vallverdú, "Time-frequency features for impedance cardiography signals during anesthesia using different distribution kernels," *Methods of Information in Medicine*, vol. 57, no. S01, pp. e1–e9, 2018.

[241] J. Escrivá Muñoz, Y. Pan, S. Ge, E. W. Jensen, and M. Vallverdú, "Novel characterization method of impedance cardiography signals using time-frequency distributions," *Medical & Biological Engineering & Computing*, vol. 56, no. 10, pp. 1757–1770, 2018.

[242] R. Beck, L. Milella, and C. Labellarte, "Continuous non-invasive measurement of stroke volume and cardiac index in infants and children: comparison of Impedance Cardiography NICaSOR vs CardioQOR method," *La Clinica Terapeutica*, vol. 169, no. 3, pp. e110–e113, 2018.

[243] P. Bogui, E. Balayssac-Siransy, P. Connes et al., "The physioflow thoracic impedancemeter is not valid for the measurements of cardiac hemodynamic parameters in chronic anemic patients," *PLoS ONE*, vol. 8, no. 10, 2013.

[244] M. Borzage, K. Heidari, T. Chavez et al., "Measuring stroke volume: Impedance cardiography vs phasecontrast magnetic resonance imaging," *American Journal of Critical Care*, vol. 26, no. 5, pp. 408–415, 2017.

[245] M. J. Germain, J. Joubert, D. O'Grady, B. H. Nathanson, Y. Chait, and N. W. Levin, "Comparison of stroke volume measurements during hemodialysis using bioimpedance cardiography and echocardiography," *Hemodialysis International*, vol. 22, no. 2, pp. 201–208, 2018.

[246] D. P. Bernstein, I. C. Henry, H. J. Lemmens et al., "Validation of stroke volume and cardiac output by electrical interrogation of the brachial artery in normals: assessment of strengths, limitations, and sources of error," *Journal of Clinical Monitoring and Computing*, vol. 29, no. 6, pp. 789–800, 2015.

[247] H. Liang, Å. Vårtun, and G. Acharya, "Agreement between preload reserve measured by impedance cardiography and echocardiography during pregnancy," *Archives of Gynecology and Obstetrics*, vol. 298, no. 1, pp. 59–66, 2018.

[248] J. M. van De Water, B. E. Mount, J. R. Barela, R. Schuster, and F. S. Leacock, "Monitoring the chest with impedance," *Chest*, vol. 64, no. 5, pp. 597–603, 1973.

[249] A. F. Pacela, "Impedance pneumography—A survey of instrumentation techniques," *Medical & Biological Engineering*, vol. 4, no. 1, pp. 1–15, 1966.

[250] V. Jeyhani, T. Vuorinen, M. Mäntysalo, and A. Vehkaoja, "Comparison of simple algorithms for estimating respiration rate from electrical impedance pneumography signals in wearable devices," *Health and Technology*, vol. 7, no. 1, pp. 21–31, 2017.

[251] L. D'Alvia, E. Scalona, E. Palermo et al., "Tetrapolar low-cost systems for thoracic impedance plethysmography," in *Proceedings of the 13th IEEE International Symposium on Medical Measurements and Applications, MeMeA 2018*, pp. 1–6, June 2018.

[252] M. Młyńczak and G. Cybulski, "Impedance pneumography: Is it possible?" in *Photonics Applications in Astronomy, Communications, Industry, and High-Energy Physics Experiments*, vol. 8454, p. 84, 2012.

[253] M. H. Sim, M. Y. Kim, I. C. Jeong et al., "Development and evaluation of an improved technique for pulmonary function testing using electrical impedance pneumography intended for the diagnosis of chronic obstructive pulmonary disease patients," *Sensors*, vol. 13, no. 11, pp. 15846–15860, 2013.

[254] J. N. Wilkinson and V. U. Thanawala, "Thoracic impedance monitoring of respiratory rate during sedation - is it safe?" *Anaesthesia*, vol. 64, no. 4, pp. 455-456, 2009.

[255] V.-P. Seppä and J. Viik, *Measuring Lung Volume Changes by Impedance Pneumography*, Tampereen Teknillinen Yliopisto, 2015, Patent US 2015-0051469 A1.

[256] M. Młyńczak, W. Niewiadomski, M. Żyliński, and G. Cybulski, "Verification of the respiratory parameters derived from impedance pneumography during normal and deep breathing in three body postures," in *6th European Conference of the International Federation for Medical and Biological Engineering*, I. Lacković and D. Vasic, Eds., vol. 45, pp. 881–884, Springer International Publishing, Cham, Switzerland, 2015.

[257] V. Seppä, A. S. Pelkonen, A. Kotaniemi-Syrjänen, J. Viik, M. J. Mäkelä, and L. P. Malmberg, "Tidal flow variability measured by impedance pneumography relates to childhood asthma risk," *European Respiratory Journal*, vol. 47, no. 6, pp. 1687–1696, 2016.

[258] T. Das, T. K. Dawn, P. Das, and P. Basak, "Design of low cost apnea detector by modifying a simple pulse delay circuit interfacing with computer with audio input by freely available

audio software," in *Proceedings of the 1st International Conference on Electronics, Materials Engineering and Nano-Technology, IEMENTech 2017*, pp. 1–4, April 2017.

[259] K. Lu, L. Yang, F. Seoane, F. Abtahi, M. Forsman, and K. Lindecrantz, "Fusion of heart rate, respiration and motion measurements from a wearable sensor system to enhance energy expenditure estimation," *Sensors*, vol. 18, no. 9, 2018.

[260] Młyńczak M. and G. Cybulski, "Improvement of body posture changes detection during ambulatory respiratory measurements using impedance pneumography signals," in *Proceedings of the 14 Mediterranean Conference on Medical and Biological Engineering and Computing*, E. Kyriacou, S. Christofides, and C. S. Pattichis, Eds., pp. 167–171, Springer International Publishing, Cham, Switzerland, 2016.

[261] T. Koivumäki, J. Teuho, M. Teräs, M. Vauhkonen, and M. A. Hakulinen, "A novel respiratory gating method for oncologic positron emission tomography based on bioimpedance approach," *Annals of Nuclear Medicine*, vol. 29, no. 4, pp. 351–358, 2015.

[262] T. Koivumäki, M. Vauhkonen, J. T. Kuikka, and M. A. Hakulinen, "Optimizing bioimpedance measurement configuration for dual-gated nuclear medicine imaging: A sensitivity study," *Medical & Biological Engineering & Computing*, vol. 49, no. 7, pp. 783–791, 2011.

[263] M. J. Kortelainen, T. M. Koivumäki, M. J. Vauhkonen et al., "Respiratory motion reduction with a dual gating approach in myocardial perfusion SPECT: Effect on left ventricular functional parameters," *Journal of Nuclear Cardiology*, vol. 25, no. 5, pp. 1633–1641, 2018.

[264] K. Tuohimäki, S. Mahdiani, V. Jeyhani et al., "Electrode comparison for textile-integrated electrocardiogram and impedance pneumography measurement," in *Proceedings of the European Medical and Biological Engineering Confernce, Nordic-Baltic Conference on Biomedical Engineering and Medical Physics*, H. Eskola, O. Väisänen, J. Viik, and J. Hyttinen, Eds., pp. 302–305, Springer Singapore, Singapore, June 2018.

[265] P. Guay, S. Gorgutsa, S. Larochelle, and Y. Messaddeq, "Wearable contactless respiration sensor based on multi-material fibers integrated into textile," *Sensors*, vol. 17, no. 5, 2017.

[266] H. Li, H. Xu, Y. Ma et al., "Thoracic impedance measurement for lung function evaluation," in *Proceedings of the 2017 IEEE International Conference on Imaging Systems and Techniques, IST 2017*, pp. 1–5, China, October 2017.

[267] M. Młyńczak, M. Zyliński, D. Janczak, M. Jakubowska, W. Niewiadomski, and G. Cybulski, "Graphene electrodes for long-term impedance pneumography - A feasibility study," in *Proceedings of the European Medical and Biological Engineering Confernce, Nordic-Baltic Conference on Biomedical Engineering and Medical Physics*, H. Eskola, O. Väisänen, J. Viik, and J. Hyttinen, Eds., pp. 514–517, Springer Singapore, Singapore, 2018.

[268] S. Genc, *Respiration Rate Determination in Impedance Pneumography*, General Electric Company, 2017, Patent US 9-706-945 B2.

[269] M. Młyńczak and G. Cybulski, "Decomposition of the cardiac and respiratory components from impedance pneumography signals," in *Proceedings of the 10th International Joint Conference on Biomedical Engineering Systems and Technologies*, vol. 4, pp. 16–23, Porto, Portugal, Feburary 2017.

[270] M. Młyńczak and G. Cybulski, "Flow parameters derived from impedance pneumography after nonlinear calibration based on neural networks," in *Proceedings of the 10th International Joint Conference on Biomedical Engineering Systems and Technologies*, vol. 4, pp. 70–77, Porto, Portugal, Feburary 2017.

[271] K. van Loon, L. M. Peelen, E. C. van de Vlasakker, C. J. Kalkman, L. van Wolfswinkel, and B. van Zaane, "Accuracy of remote continuous respiratory rate monitoring technologies intended for low care clinical settings: a prospective observational study," *Canadian Journal of Anesthesia*, vol. 65, no. 12, pp. 1324–1332, 2018.

[272] B. G. Goudra, L. C. Penugonda, R. M. Speck, and A. C. Sinha, "Comparison of acoustic respiration rate, impedance pneumography and capnometry monitors for respiration rate accuracy and apnea detection during gi endoscopy anesthesia," *Open Journal of Anesthesiology*, vol. 3, no. 2, pp. 74–79, 2013.

[273] D. C. Barber and B. H. Brown, "Applied potential tomography," *Journal of Physics E: Scientific Instruments*, vol. 17, no. 9, pp. 723–733, 1984.

[274] N. Li, H. Xu, Z. Zhou, J. Xin, Z. Sun, and X. Xu, "Reconfigurable bioimpedance emulation system for electrical impedance tomography system validation," *IEEE Transactions on Biomedical Circuits and Systems*, vol. 7, no. 4, pp. 460–468, 2013.

[275] T. Mauri, A. Mercat, and G. Grasselli, "What's new in electrical impedance tomography," *Intensive Care Medicine*, 2018.

[276] S. Zhang, G. Xu, X. Zhang et al., "Computation of a 3-D model for lung imaging with electrical impedance tomography," *IEEE Transactions on Magnetics*, vol. 48, no. 2, pp. 651–654, 2012.

[277] T. I. Oh, E. J. Woo, and D. Holder, "Multi-frequency EIT system with radially symmetric architecture: KHU Mark1," *Physiological Measurement*, vol. 28, no. 7, pp. S183–S196, 2007.

[278] R. Halter, A. Hartov, and K. Paulsen, "A broadband high-frequency electrical impedance tomography system for breast imaging," *IEEE Transactions on Biomedical Engineering*, vol. 55, no. 2, pp. 650–659, 2008.

[279] C. W. Denyer, F. J. Lidgey, Q. S. Zhu, and C. N. McLeod, "A high output impedance current source," *Physiological Measurement*, vol. 15, no. 2A, pp. A79–A82, 1994.

[280] X. Zhang, G. Xu, S. Zhang et al., "A numerical computation forward problem model of electrical impedance tomography based on generalized finite element method," *IEEE Transactions on Magnetics*, vol. 50, no. 2, pp. 1045–1048, 2014.

[281] X. Zhang, J. Liu, and B. He, "Magnetic-resonance-based electrical properties tomography: a review," *IEEE Reviews in Biomedical Engineering*, vol. 7, pp. 87–96, 2014.

[282] G. Singh, S. Anand, B. Lall, A. Srivastava, and V. Singh, "Development of a microcontroller based electrical impedance tomography system," in *Proceedings of the 2015 IEEE Long Island Systems, Applications and Technology Conference, LISAT 2015*, 2015.

[283] I. Frerichs, M. Amato, A. H. van Kaam et al., "Chest electrical impedance tomography examination, data analysis, terminology, clinical use and recommendations: consensus statement of the translational EIT development study group," *Thorax*, vol. 72, no. 1, pp. 83–93, 2017.

[284] J. C. Richard, C. Pouzot, A. Gros et al., "Electrical impedance tomography compared to positron emission tomography for the measurement of regional lung ventilation: An experimental study," *Critical Care*, vol. 13, no. 3, 2009.

[285] T. Dowrick, C. Blochet, and D. Holder, "In vivo bioimpedance measurement of healthy and ischaemic rat brain: Implications for stroke imaging using electrical impedance tomography," *Physiological Measurement*, vol. 36, no. 6, article no. 1273, pp. 1273–1282, 2015.

[286] J. Zhang, B. Yang, H. Li et al., "A novel 3D-printed head phantom with anatomically realistic geometry and continuously varying skull resistivity distribution for electrical impedance tomography," *Scientific Reports*, vol. 7, no. 1, article no. 4608, 2017.

[287] F. Fu, B. Li, M. Dai et al., "Use of electrical impedance tomography to monitor regional cerebral edema during clinical dehydration treatment," *PLoS ONE*, vol. 9, no. 12, Article ID e113202, 2014.

[288] Y. Li, D. Zhang, B. Liu et al., "Noninvasive cerebral imaging and monitoring using electrical impedance tomography during total aortic arch replacement," *Journal of Cardiothoracic and Vascular Anesthesia*, vol. 32, no. 6, pp. 2469–2476, 2018.

[289] Y. Zhang, R. Xiao, and C. Harrison, "Advancing hand gesture recognition with high resolution electrical impedance tomography," in *Proceedings of the 29th Annual Symposium on User Interface Software and Technology (UIST '16)*, pp. 843–850, ACM, New York, NY, USA, October 2016.

[290] S. Hong, K. Lee, U. Ha et al., "A 4.9 mΩ-sensitivity mobile electrical impedance tomography IC for early breast-cancer detection system," *IEEE Journal of Solid-State Circuits*, vol. 50, no. 1, pp. 245–257, 2015.

[291] E. K. Murphy, A. Mahara, and R. J. Halter, "Absolute reconstructions using rotational electrical impedance tomography for breast cancer imaging," *IEEE Transactions on Medical Imaging*, vol. 36, no. 4, pp. 892–903, 2017.

[292] K. Ain, R. A. Wibowo, and S. Soelistiono, "Modeling of electrical impedance tomography to detect breast cancer by finite volume methods," *Journal of Physics: Conference Series*, vol. 853, no. 1, Article ID 012001, 2017.

[293] P. Davies, S. Gates, D. Bird, and C. Silvestre, "Impedance tomography in paediatric intensive care patients," *Pediatric Critical Care Medicine*, vol. 19, no. 6S, p. 46, 2018.

[294] Y. Wu, D. Jiang, A. Bardill, S. de Gelidi, R. Bayford, and A. Demosthenous, "A high frame rate wearable EIT system using active electrode ASICs for lung respiration and heart rate monitoring," *IEEE Transactions on Circuits and Systems I: Regular Papers*, vol. 65, no. 11, pp. 3810–3820, 2018.

[295] M. Ma, Y. Zhang, and N. Gu, "Estimation the tumor temperature in magnetic nanoparticle hyperthermia by infrared thermography: Phantom and numerical studies," *Journal of Thermal Biology*, vol. 76, pp. 89–94, 2018.

[296] A. Mahara, S. Khan, E. K. Murphy, A. R. Schned, E. S. Hyams, and R. J. Halter, "3D microendoscopic electrical impedance tomography for margin assessment during robot-assisted laparoscopic prostatectomy," *IEEE Transactions on Medical Imaging*, vol. 34, no. 7, pp. 1590–1601, 2015.

[297] T. K. Bera, "Applications of electrical impedance tomography (EIT): a short review," *IOP Conference Series: Materials Science and Engineering*, vol. 331, no. 1, Article ID 012004, 2018.

[298] K. Zhang, M. Li, F. Yang, S. Xu, and A. Abubakar, "Study on the accuracy of forward modeling in electrical impedance tomography for thorax imaging," in *Proceedings of the 32nd General Assembly and Scientific Symposium of the International Union of Radio Science, URSI GASS 2017*, pp. 1–4, August 2017.

[299] E. Ma, "Convergence of finite element approximation for electrical impedance tomography with the complete electrode model," *Journal of Physics Communications*, vol. 2, no. 8, Article ID 085024, 2018.

[300] N. Hyvönen and L. Mustonen, "Generalized linearization techniques in electrical impedance tomography," *Numerische Mathematik*, vol. 140, no. 1, pp. 95–120, 2018.

[301] K. Knudsen, M. Lassas, J. Mueller, and S. Siltanen, "Regularized D-bar method for the inverse conductivity problem," *Inverse Problems and Imaging*, vol. 35, no. 4, pp. 599–624, 2009.

[302] A. P. Calderón, "On an inverse boundary value problem," *Computational & Applied Mathematics*, vol. 25, no. 2-3, pp. 133–138, 2006.

[303] S. J. Hamilton and A. Hauptmann, "Deep D-bar: real-time electrical impedance tomography imaging with deep neural networks," *IEEE Transactions on Medical Imaging*, vol. 37, no. 10, pp. 2367–2377, 2018.

[304] X. Li, Y. Lu, J. Wang et al., "An image reconstruction framework based on deep neural network for electrical impedance tomography," in *Proceedings of the 24th IEEE International Conference on Image Processing, ICIP 2017*, pp. 3585–3589, September 2017.

[305] G. Kłosowski and T. T. Rymarczyk, "Using neural networks and deep learning algorithms in electrical impedance tomography," *Informatyka, Automatyka, Pomiary w Gospodarce i Ochronie Środowiska*, 2017.

[306] A. Samore, M. Guermandi, S. Placati, and R. Guerrieri, "Parametric detection and classification of compact conductivity contrasts with electrical impedance tomography," *IEEE Transactions on Instrumentation and Measurement*, vol. 66, no. 10, pp. 2666–2679, 2017.

[307] L. Zhou, B. Harrach, and J. K. Seo, "Monotonicity-based electrical impedance tomography for lung imaging," *Inverse Problems*, vol. 34, no. 4, Article ID 045005, 2018.

[308] B. Harrach and M. N. Minh, "Monotonicity-based regularization for phantom experiment data in electrical impedance tomography," in *New Trends in Parameter Identification for Mathematical Models*, pp. 107–120, Springer International Publishing, 2018.

[309] H. Garde and S. Staboulis, "Convergence and regularization for monotonicity-based shape reconstruction in electrical impedance tomography," *Numerische Mathematik*, vol. 135, no. 4, pp. 1221–1251, 2017.

[310] T. Rymarczyk and K. Szulc, "Solving inverse problem for electrical impedance tomography using topological derivative and level set method," in *Proceedings of the 2018 International Interdisciplinary PhD Workshop, IIPhDW 2018*, pp. 191–195, May 2018.

[311] S. P. Pellegrini, F. C. Trigo, and R. G. Lima, "Solving the electrical impedance tomography inverse problem for logarithmic conductivity: Numerical sensitivity," *COMPEL - The International Journal for Computation and Mathematics in Electrical and Electronic Engineering*, vol. 37, no. 2, pp. 681–690, 2018.

[312] R. A. Borsoi, J. C. C. Aya, G. H. Costa, and J. C. M. Bermudez, "Super-resolution reconstruction of electrical impedance tomography images," *Computers and Electrical Engineering*, vol. 69, pp. 1–13, 2018.

[313] S. Liu, J. Jia, Y. D. Zhang, and Y. Yang, "Image reconstruction in electrical impedance tomography based on structure-aware sparse bayesian learning," *IEEE Transactions on Medical Imaging*, vol. 37, no. 9, pp. 2090–2102, 2018.

[314] M. Kim, J. Jang, H. Kim et al., "A 1.4-m Ω-Sensitivity 94-dB dynamic-range electrical impedance tomography SoC and 48-channel Hub-SoC for 3-D lung ventilation monitoring system," *IEEE Journal of Solid-State Circuits*, vol. 52, no. 11, pp. 2829–2842, 2017.

[315] M. Rapin, F. Braun, A. Adler et al., "Wearable sensors for frequency-multiplexed EIT and multilead ECG data acquisition," *IEEE Transactions on Biomedical Engineering*, 2018.

[316] Y. Yang, J. Jia, S. Smith, N. Jamil, W. Gamal, and P. Bagnaninchi, "A miniature electrical impedance tomography sensor and 3-D image reconstruction for cell imaging," *IEEE Sensors Journal*, vol. 17, no. 2, pp. 514–523, 2017.

[317] Y. Yang and J. Jia, "A multi-frequency electrical impedance tomography system for real-time 2D and 3D imaging," *Review of Scientific Instruments*, vol. 88, no. 8, Article ID 085110, 2017.

[318] A. Dupré and S. Mylvaganam, "A simultaneous and continuous excitation method for high-speed electrical impedance tomography with reduced transients and noise sensitivity," *Sensors*, vol. 18, no. 4, 2018.

[319] J. Avery, T. Dowrick, M. Faulkner, N. Goren, and D. Holder, "A versatile and reproducible multi-frequency electrical impedance tomography system," *Sensors*, vol. 17, no. 2, 2017.

[320] H. D. Critchley, R. Elliott, C. J. Mathias, and R. J. Dolan, "Neural activity relating to generation and representation of galvanic skin conductance responses: a functional magnetic resonance imaging study," *The Journal of Neuroscience*, vol. 20, no. 8, pp. 3033–3040, 2000.

[321] R. L. Bailey, "Electrodermal activity (EDA)," in *The International Encyclopedia of Communication Research Methods, American Cancer Society*, pp. 1–15, 2017.

[322] M. Velana, S. Gruss, G. Layher et al., "The senseemotion database: a multimodal database for the development and systematic validation of an automatic pain- and emotion-recognition system," in *Multimodal Pattern Recognition of Social Signals in Human-Computer-Interaction*, F. Schwenker and S. Scherer, Eds., pp. 127–139, Springer International Publishing, Cham, Switzerland, 2017.

[323] H. Critchley and Y. Nagai, "Electrodermal activity (EDA)," in *Encyclopedia of Behavioral Medicine*, pp. 666–669, Springer, 2013.

[324] S. Walter, S. Gruss, H. Ehleiter et al., "The biovid heat pain database data for the advancement and systematic validation of an automated pain recognition system," in *Proceedings of the 2013 IEEE International Conference on Cybernetics (CYBCO)*, pp. 128–131, June 2013.

[325] J. Hernandez, R. R. Morris, and R. W. Picard, "Call center stress recognition with person-specific models," in *Affective Computing and Intelligent Interaction*, S. D'Mello, A. Graesser, B. Schuller, and J.-C. Martin, Eds., pp. 125–134, Springer, Berlin, Germany, 2011.

[326] R. Kocielnik, N. Sidorova, F. M. Maggi, M. Ouwerkerk, and J. H. D. M. Westerink, "Smart technologies for long-term stress monitoring at work," in *Proceedings of the 26th IEEE International Symposium on Computer-Based Medical Systems, CBMS 2013*, pp. 53–58, Portugal, June 2013.

[327] J. Shukla, M. Barreda-Ángeles, J. Oliver, and D. Puig, "Efficient wavelet-based artifact removal for electrodermal activity in real-world applications," *Biomedical Signal Processing and Control*, vol. 42, pp. 45–52, 2018.

[328] S. Taylor, N. Jaques, W. Chen, S. Fedor, A. Sano, and R. Picard, "Automatic identification of artifacts in electrodermal activity data," in *Proceedings of the 37th Annual International Conference of the IEEE Engineering in Medicine and Biology Society, EMBC 2015*, pp. 1934–1937, August 2015.

[329] M. Kelsey, M. Akcakaya, I. R. Kleckner et al., "Applications of sparse recovery and dictionary learning to enhance analysis of ambulatory electrodermal activity data," *Biomedical Signal Processing and Control*, vol. 40, pp. 58–70, 2018.

[330] H. F. Posada-Quintero, N. Reljin, C. Mills et al., "Time-varying analysis of electrodermal activity during exercise," *PLoS ONE*, vol. 13, no. 6, pp. 1–12, 2018.

[331] H. F. Posada-Quintero and K. H. Chon, "Exploring electrodermal activity in water-immersed subjects," in *Proceedings of the 15th IEEE International Conference on Wearable and Implantable Body Sensor Networks, BSN 2018*, pp. 90–93, March 2018.

[332] A. Greco, G. Valenza, L. Citi, and E. P. Scilingo, "Arousal and valence recognition of affective sounds based on electrodermal activity," *IEEE Sensors Journal*, vol. 17, no. 3, pp. 716–725, 2017.

[333] S. Jain, U. Oswal, K. S. Xu, B. Eriksson, and J. Haupt, "A compressed sensing based decomposition of electrodermal activity signals," *IEEE Transactions on Biomedical Engineering*, vol. 64, no. 9, pp. 2142–2151, 2017.

[334] S. G. Caliskan, M. D. Bilgin, and M. Polatli, "Nonlinear analysis of electrodermal activity signals for healthy subjects and patients with chronic obstructive pulmonary disease," *Australasian Physical & Engineering Sciences in Medicine*, vol. 41, no. 2, pp. 487–494, 2018.

[335] R. Zangróniz, A. Martínez-Rodrigo, J. M. Pastor, M. T. López, and A. Fernández-Caballero, "Electrodermal activity sensor for classification of calm/distress condition," *Sensors*, vol. 17, no. 10, 2017.

[336] D. McDonnell, *Electrodermal Activity Sensor*, Galvanic Ltd., 2017, Patent US 2017-0014043 A1.

[337] S. Heiermann, K. Khalaj Hedayati, M. J. Müller, and M. Dittmar, "Accuracy of a portable multisensor body monitor for predicting resting energy expenditure in older people: a comparison with indirect calorimetry," *Gerontology*, vol. 57, no. 5, pp. 473–479, 2011.

[338] H. Mayaudon, P. Miloche, and B. Bauduceau, "A new simple method for assessing sudomotor function: Relevance in type 2 diabetes," *Diabetes & Metabolism*, vol. 36, no. 6, pp. 450–454, 2010.

[339] C. Karagiannidis, A. D. Waldmann, P. L. Róka et al., "Regional expiratory time constants in severe respiratory failure estimated by electrical impedance tomography: A feasibility study," *Critical Care*, vol. 22, no. 1, 2018.

[340] J. Karsten, N. Voigt, H.-J. Gillmann, and T. Stueber, "Determination of optimal positive end-expiratory pressure based on respiratory compliance and electrical impedance tomography: A pilot clinical comparative trial," *Biomedizinische Technik. Biomedical Engineering*, 2018.

[341] C. Shi, S. Boehme, A. H. Bentley et al., "Assessment of regional ventilation distribution: comparison of vibration response imaging (VRI) with electrical impedance tomography (EIT)," *PLoS ONE*, vol. 9, no. 1, 2014.

[342] E. Barsoukov and J. Macdonald, *Impedance Spectroscopy: Theory, Experiment, and Applications*, Wiley-Interscience, Hoboken, NJ, USA, 3rd edition, 2018.

[343] S. Sang, Y. Wang, Q. Feng, Y. Wei, J. Ji, and W. Zhang, "Progress of new label-free techniques for biosensors: A review," *Critical Reviews in Biotechnology*, vol. 36, no. 3, pp. 465–481, 2016.

[344] M. Min, T. Parve, and U. Pliquett, "Impedance detection," in *Encyclopedia of Microfluidics and Nanofluidics*, pp. 1338–1361, Springer, New York, NY, USA, 2nd edition, 2015.

[345] A. De Ninno, V. Errico, F. R. Bertani, L. Businaro, P. Bisegna, and F. Caselli, "Coplanar electrode microfluidic chip enabling accurate sheathless impedance cytometry," *Lab on a Chip*, vol. 17, no. 6, pp. 1158–1166, 2017.

[346] M. Varshney and Y. Li, "Interdigitated array microelectrodes based impedance biosensors for detection of bacterial cells," *Biosensors and Bioelectronics*, vol. 24, no. 10, pp. 2951–2960, 2009.

[347] C. Vericat, M. E. Vela, G. Benitez, P. Carro, and R. C. Salvarezza, "Self-assembled monolayers of thiols and dithiols on gold: new challenges for a well-known system," *Chemical Society Reviews*, vol. 39, no. 5, pp. 1805–1834, 2010.

[348] M. Min, R. Land, T. Paavle, T. Parve, P. Annus, and D. Trebbels, "Broadband spectroscopy of dynamic impedances with short chirp pulses," *Physiological Measurement*, vol. 32, no. 7, pp. 945–958, 2011.

[349] M. Chua, "Design and development of an integrated health (i-health) monitoring watch," in *Proceedings of the 2016 IEEE/SICE International Symposium on System Integration*, pp. 296–300, 2017.

[350] M. Metshein and R. Gordon, "On the possibility of detecting the electrical bioimpedance of human body by using non-contact electrodes in capacitive connection," in *Proceedings of the 15th Biennial Baltic Electronics Conference, BEC 2016*, vol. 2016, pp. 171–174, October 2016.

[351] S. Rossi, C. Mancarella, C. Mocenni, and L. Della Torre, "Bioimpedance sensing in wearable systems: From hardware integration to model development," in *Proceedings of the 3rd IEEE International Forum on Research and Technologies for Society and Industry, RTSI 2017*, September 2017.

[352] P. De Carvalho, J. Palacio, and W. Van Noije, *Area Optimized CORDIC-Based Numerically Controlled Oscillator for Electrical Bioimpedance Spectroscopy*, 2016.

[353] I. Kim, Y. A. Bhagat, J. Homer, and R. Lobo, "Multimodal analog front end for wearable bio-sensors," *IEEE Sensors Journal*, vol. 16, no. 24, pp. 8784–8791, 2016.

[354] I. Kukharenko and V. Kotovskyi, "Low power bioimpedance tracking system for stress and activity monitoring," in *Proceedings of the 37th IEEE International Conference on Electronics and Nanotechnology, ELNANO 2017*, pp. 288–291, April 2017.

[355] D. Allegri, D. Vaca, D. Ferreira, M. Rogantini, and D. Barrettino, "Real-time monitoring of the hydration level by multifrequency bioimpedance spectroscopy," in *Proceedings of the 2017 IEEE International Instrumentation and Measurement Technology Conference, I2MTC 2017*, May 2017.

[356] R. Kumar, S. Perumalla, J. Vista, and A. Ranjan, "Realization of single and double cole tissue models using higher order approximation," in *Proceedings of the 1st International Conference on Electronics, Materials Engineering and Nano-Technology, IEMENTech 2017*, April 2017.

[357] P. Kassanos and G.-Z. Yang, "A CMOS programmable phase shifter for compensating synchronous detection bioimpedance systems," in *Proceedings of the 24th IEEE International Conference on Electronics, Circuits and Systems, ICECS 2017*, vol. 2018, pp. 218–221, 2018.

[358] D. Naranjo, L. M. Roa, L. J. Reina et al., "Analysis of anomalies in bioimpedance models for the estimation of body composition," in *Proceedings of the 13th Mediterranean Conference on Medical and Biological Engineering and Computing 2013 IFMBE*, vol. 41, pp. 1563–1566, 2013.

[359] C. A. Shiffman, "Adverse effects of near current-electrode placement in non-invasive bio-impedance measurements," *Physiological Measurement*, vol. 34, no. 11, pp. 1513–1529, 2013.

[360] H. Kwon, J. A. Nagy, R. Taylor, S. B. Rutkove, and B. Sanchez, "New electrical impedance methods for the in situ measurement of the complex permittivity of anisotropic biological tissues," *Physics in Medicine and Biology*, vol. 62, no. 22, pp. 8616–8633, 2017.

[361] Z. Wu, Y. Liu, M. Hong, and X. Yu, "A review of anisotropic conductivity models of brain white matter based on diffusion tensor imaging," *Medical & Biological Engineering & Computing*, vol. 56, no. 8, pp. 1325–1332, 2018.

[362] K. Badstuebner, M. Stubbe, T. Kroeger, E. Mix, and J. Gimsa, "Impedance detection of the electrical resistivity of the wound tissue around deep brain stimulation electrodes permits registration of the encapsulation process in a rat model," *Journal of Electrical Bioimpedance (JEB)*, vol. 8, no. 1, pp. 11–24, 2017.

[363] J. Anso, T. Wyss-Balmer, Y. Jegge et al., "Electrical impedance to assess facial nerve proximity during robotic cochlear implantation," *IEEE Transactions on Biomedical Engineering*, 2018.

[364] C.-H. Chuang and M. Shaikh, "Label-free impedance biosensors for Point-of-Care diagnostics," in *Point-of-Care Diagnostics - New Progresses and Perspectives*, pp. 171–201, IAPC Publishing, Zagreb, Croatia, 2017.

[365] P. Kassanos, S. Anastasova, and G.-Z. Yang, "Electrical and physical sensors for biomedical implants," in *Implantable Sensors and Systems: From Theory to Practice*, pp. 99–195, 2018.

[366] A. S. Anusha, S. P. Preejith, J. Joseph, and M. Sivaprakasam, "Design and preliminary analysis of a multifrequency bioimpedance measurement scheme," in *Proceedings of the 11th IEEE International Symposium on Medical Measurements and Applications, MeMeA 2016*, May 2016.

[367] A. Montalibet, W. Arkouche, P. B. Franco et al., "Localised impedance monitoring device for the remote clinical assessment of home-based dialysis patients," in *Proceedings of the 38th Annual International Conference of the IEEE Engineering in Medicine and Biology Society, EMBC 2016*, pp. 4427–4430, USA, August 2016.

[368] D. J. Wang and S. S. Gottlieb, "Impedance cardiography: More questions than answers," *Current Cardiology Reports*, vol. 8, no. 3, pp. 180–186, 2006.

[369] D. Buxi, E. Hermeling, M. Mercuri et al., "Systolic time interval estimation using continuous wave radar with on-body antennas," *IEEE Journal of Biomedical and Health Informatics*, vol. 22, no. 1, pp. 129–139, 2018.

[370] A. Ayadi, R. Ben Salah, K. Ouni, and W. Sahtout, "Determination of cardiovascular parameters from bioimpedance signal," in *Proceedings of the 2nd International Conference on Advanced Technologies for Signal and Image Processing, ATSIP 2016*, pp. 403–407, March 2016.

[371] R. Z. Rusho and M. A. Kadir, "Reconstruction algorithm for Pigeon Hole Imaging (PHI)," in *Proceedings of the 3rd International Conference on Electrical Information and Communication Technology, EICT 2017*, vol. 2018, pp. 1–6, 2018.

[372] L. Miao, Y. Ma, X. Chen et al., "A new symmetric semi-parallel electrical impedance tomography (EIT) system - II: The performance," in *Proceedings of the 2016 IEEE International Conference on Imaging Systems and Techniques, IST 2016*, pp. 283–288, October 2016.

[373] N. Jamil, Y. Yang, A. Tsiamis, J. Jia, and S. Smith, "Comparison of regularisation methods in image reconstruction for micro-bioimpedance tomography," in *Proceedings of the 16th IEEE SENSORS Conference, ICSENS 2017*, vol. 2017, pp. 1–3, UK, November 2017.

[374] V. G. Sirtoli, K. Morcelles, and P. Bertemes-Filho, "Electrical properties of phantoms for mimicking breast tissue," in *Proceedings of the 39th Annual International Conference of the IEEE*

Engineering in Medicine and Biology Society, EMBC 2017, pp. 157–160, July 2017.

[375] J. Jang, M. Kim, J. Bae, and H. Yoo, "A 2.79-mW 0.5%-THD CMOS current driver IC for portable electrical impedance tomography system," in *Proceedings of the 2017 IEEE Asian Solid-State Circuits Conference (A-SSCC)*, vol. 2017, pp. 145–148, November 2017.

[376] Z. Xu, J. Yao, Z. Wang et al., "Development of a portable electrical impedance tomography system for biomedical applications," *IEEE Sensors Journal*, vol. 18, no. 19, pp. 8117–8124, 2018.

[377] S. Leonhardt, L. Leicht, and D. Teichmann, "Unobtrusive vital sign monitoring in automotive environments—A review," *Sensors*, vol. 18, no. 9, 2018.

[378] T. H. Huynh, R. Jafari, and W.-Y. Chung, "A robust bioimpedance structure for smartwatch-based blood pressure monitoring," *Sensors*, vol. 18, no. 7, 2018.

[379] D. Buxi, J. Redout, and M. R. Yuce, "Blood pressure estimation using pulse transit time from bioimpedance and continuous wave radar," *IEEE Transactions on Biomedical Engineering*, vol. 64, no. 4, pp. 917–927, 2017.

[380] B. Ibrahim, V. Nathan, and R. Jafari, "Exploration and validation of alternate sensing methods for wearable continuous pulse transit time measurement using optical and bioimpedance modalities," in *Proceedings of the 39th Annual International Conference of the IEEE Engineering in Medicine and Biology Society, EMBC 2017*, pp. 2051–2055, July 2017.

[381] M. Min, P. Annus, H. Koiv, A. Krivosei, T. Uuetoa, and J. Lamp, "Bioimpedance sensing - A viable alternative for tonometry in non-invasive assessment of central aortic pressure," in *Proceedings of the 12th IEEE International Symposium on Medical Measurements and Applications, MeMeA 2017*, pp. 373–378, May 2017.

[382] B. Sanchez and S. B. Rutkove, "Electrical impedance myography and its applications in neuromuscular disorders," *Neurotherapeutics*, vol. 14, no. 1, pp. 107–118, 2017.

[383] J. Li, T. Igbe, Y. Liu et al., "An approach for noninvasive blood glucose monitoring based on bioimpedance difference considering blood volume pulsation," *IEEE Access*, vol. 6, pp. 51119–51129, 2018.

[384] T. Das, A. Ghosh, S. Guha, and P. Basak, "Early detection of diabetes based on skin impedance spectrogram and heart rate variability noninvasively," in *Proceedings of the 1st International Conference on Electronics, Materials Engineering and Nano-Technology, IEMENTech 2017*, April 2017.

[385] Q. Wang, H. Wang, H. Xu, W. Zhou, and G. Liu, "Non-invasive urination-desire sensing method based on bladder bioimpedance spectrum analysis," *Journal of Medical and Biological Engineering*, vol. 36, no. 2, pp. 191–196, 2016.

[386] E. Pittella, S. Pisa, E. Piuzzi, E. Rizzuto, and Z. Del Prete, "Combined impedance plethysmography and spectroscopy for the diagnosis of diseases of peripheral vascular system," in *Proceedings of the 12th IEEE International Symposium on Medical Measurements and Applications, MeMeA 2017*, pp. 367–372, May 2017.

[387] L. RenHe and B. Wongkittisuksa, "The evaluation of elbow joint motion using bio-impedance signal," in *Proceedings of the 14th International Conference on Electrical Engineering/Electronics, Computer, Telecommunications and Information Technology, ECTI-CON 2017*, pp. 262–265, June 2017.

[388] K. Kikkeri and M. Agah, "A monolithic dielectrophoretic chip for real-time low-abundance bacteria detection," in *Proceedings*

of the 30th IEEE International Conference on Micro Electro Mechanical Systems, MEMS 2017, pp. 358–361, January 2017.

[389] A. Kekonen, M. Bergelin, J.-E. Eriksson, H. Ylanen, S. Kielosto, and J. Viik, "Bioimpedance measurement system for evaluation of the status of wound healing," in *Proceedings of the 15th Biennial Baltic Electronics Conference, BEC 2016*, vol. 2016, pp. 175–178, October 2016.

[390] J. A. Jambulingam, R. McCrory, L. West, and O. T. Inan, "Non-invasive, multi-modal sensing of skin stretch and bioimpedance for detecting infiltration during intravenous therapy," in *Proceedings of the 38th Annual International Conference of the IEEE Engineering in Medicine and Biology Society, EMBC 2016*, vol. 2016, pp. 4755–4758, August 2016.

[391] D. Celinskis and B. C. Towe, "Characterization of the implantable neurostimulator-based wireless bioimpedance measurement technique," in *Proceedings of the 2016 IEEE EMBS International Student Conference, ISC 2016*, May 2016.

[392] H. Kalvoy, C. Tronstad, K. Ullensvang, T. Steinfeldt, and A. R. Sauter, "Detection of needle to nerve contact based on electric bioimpedance and machine learning methods," in *Proceedings of the 39th Annual International Conference of the IEEE Engineering in Medicine and Biology Society, EMBC 2017*, pp. 9–12, July 2017.

Research Article

Orthogonal Multitone Electrical Impedance Spectroscopy (OMEIS) for the Study of Fibrosis Induced by Active Cardiac Implants

Edwin De Roux [iD],[1,2] **Amelie Degache,**[3] **Mehdi Terosiet,**[1] **Florian Kölbl,**[1] **Michel Boissière,**[4] **Emmanuel Pauthe,**[4] **Aymeric Histace** [iD],[1] **Olivier Bernus,**[5] **Noëlle Lewis,**[3] **and Olivier Romain** [iD][1]

[1]*Laboratoire ETIS, Université Paris Seine, Université de Cergy-Pontoise, ENSEA, CNRS, UMR8051, France*
[2]*SENACYT and Universidad Tecnológica de Panamá, Panama*
[3]*IMS Bordeaux, Université Bordeaux, UMR5218, France*
[4]*Laboratoire ERRMECe, Université Paris Seine, Université de Cergy-Pontoise, EA1391, France*
[5]*IHU LIRYC, Université de Bordeaux, Inserm CRCTB U1045, F-33600 Pessac, France*

Correspondence should be addressed to Edwin De Roux; edwin.de-roux@ensea.fr

Fibrosis represents an open issue for mid- to long-term active implants, like pacemakers, given that this biological tissue surrounds the stimulation electrodes and can impact or modify the performances of the system. For this reason, we present a strategy for the continuous sensing of fibrosis induced by cardiac implants, based on the use of the same set of electrodes involved in the implant stimulation process and whose implementation can be integrated into the pacing and sensing circuitry of pacemakers. To do this, the proposed measurement system complies with certain requirements for its integration, such as rapid measurement time, flexibility, low power consumption, and low use of resources. This was achieved through the use of an orthogonal multitone stimulation signal and the design of an Orthogonal Frequency Division Multiplexing (OFDM) architecture that are the bases of the system. As a proof of concept, we implemented this technique within a FPGA. Initial tests of this system have been performed through *in vitro* measurements of cell cultures related to fibrosis, which, once validated, have allowed us to advance to ex vivo measurements of inhibited and perfused cardiac tissue; these are the conditions that offer a first view of *in vivo* measurements. This article describes the measurement system implemented and also discusses the results of its validation and of the *in vitro* and ex vivo measurements, comparing them with results obtained by a reference instrument.

1. Introduction

Over the last fifty years, electrotherapy has shown a very rapid development with many innovators contributing to a whole series of devices. Electrotherapy uses an external source of electricity to stimulate human tissue in ways that produce a beneficial therapeutic effect. The best known electrotherapy devices are the active implantable medical devices, among them are cardiac defibrillators (1949), pacemakers (PCM) (1957), and cochlear (1971) and deep brain (2000) stimulators.

These systems use the latest micro- and nanoelectronic technologies, with electrodes that stimulate and sense the surrounding biological environment. Such implanted devices induce an immediate and sustained inflammatory response from the body. This chronic and unresolved inflammation induces fibrosis, which is a complex biological process involving multiscale phenomena. At the cellular scale, fibroblasts are activated and differentiate to myofibroblasts; at the tissular scale, excessive secretion of extracellular matrix components, like collagen, finally produces a dense fibrous capsule around the implants, especially the electrodes [1].
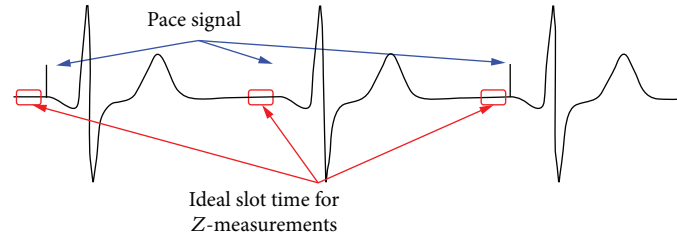
Figure 1: Strategy for measuring cardiac tissue impedance while using the PCM structure. The ECG signal is in black together with the PCM pulse.

In the case of PCM, fibrosis reduces both the functionality and the efficacy of the implant to target the desired tissue, diverting even the stimulating current to unforeseen regions and altering the impedance of the tissue around electrodes. Furthermore, it could change the shape and magnitude of the electric field generated [2] and forces the increase of the PCM stimulation threshold and the reduction of battery lifespan [3].

The fibrosis can be treated medically to reduce its consequences, but the effectiveness of the treatment depends on an accurate diagnosis. The standard method for determining the degree of tissue reaction surrounding implanted electrodes is histology. Immunohistochemical methods enable the visualization of specific markers like collagen, fibronectin, or smooth muscle actin [4]. The disadvantage of these methods is an inability to follow the tissue reaction in real time *in vivo* [5]. Optical methods such as late gadolinium-enhanced Cardiac Magnetic Resonance (CMR) are used to detect fibrosis in cardiac tissues even if it is scattered and in low concentration [6]. However, their effectiveness decreases when the patient carries a PCM because it could alter the quality of the image. In addition, due to risk factors, it is contraindicated to apply CMR in patients with PCM, and even if this is done, it is recommended to carry it out weeks after postimplant surgery, which allows a considerable accumulation of fibrous tissue on the electrodes [7]. Chronic monitoring of tissue alteration around implanted electrodes could be a first step to understand this long-term biological process. This advance could be used to ascertain the treatment effectiveness or to test new biocompatibility strategies of materials.

Electrical Impedance Spectroscopy (EIS) is a well-known technique for characterizing living tissues. Preliminary studies conclude that there is a correlation between the measured resistance and the morphology of the tissue next to the electrode [8]. Amorós-Figueras et al. [9] show that in situ impedance measurements in myocardium or epicardium allowed discriminating healthy and infarcted tissue. These results suggest that the tissue remodeling occurring in fibrosis has an EIS signature. Hence, we propose to apply local EIS, taking benefit of the electrodes and the electronic circuitry already existing in PCM, for the continuous and "low-cost" monitoring of electrode-induced fibrosis. This system should be capable of performing the measurements under the severe condition imposed by the dynamics of the heart, such as the heartbeat movement. Here, the impedance must be sensed over the desired frequency range during the short time slot between two consecutive muscle contractions, in order to avoid distorting the measurements, as shown in Figure 1. Therefore, the selected method must meet the following requirements: high measurement speed, flexibility in spectrum manipulation (bandwidth and frequency resolution), and feasibility of digital implementation.

Based on this strategy, we have devised a new EIS measurement approach which is fast and flexible, easy to synchronize with PCM pulses, and not affected by heart dynamics. The innovation is an original application of the Orthogonal Frequency Division Multiplexing (OFDM) technique, which is well known and successfully used in the field of digital communication. This technique, here adapted to embedded EIS, exhibits competitive performances, compared to traditional EIS methods, and meets all the previous requirements. This new approach is hereafter called the Orthogonal Multitone Electrical Impedance Spectroscopy (OMEIS).

This article is structured as follows: firstly, the EIS measurement principle and its traditional implementations are presented. Then, the original OMEIS method is described in Section 2. The following section describes the design and the validation of a prototype for the OMEIS method. Subsequently, preliminary experiments are conducted in both *in vitro* and ex vivo samples, with living cells and cardiac tissues, respectively. Finally, the results obtained in the impedance measurements are discussed.

2. EIS Overview

The EIS applied to the analysis of a biological material consists of injecting an alternating current or voltage into the tissue under study and then measuring the resultant (voltage or current, respectively) that appears through the stimulation electrodes. There are several alternating signal generation methods for EIS used for this purpose, with their advantages and disadvantages. These will be discussed next.

2.1. Classic Methods for EIS. The most common signal found in almost all commercial available EIS instruments, due to its implementation simplicity, is the fixed-frequency sinusoidal signal. Here, the measurements are carried out at a specific frequency, as is the case for these full-custom designs [10, 11], or in a small set of frequencies such as those found in the commercial instrument xCELLigence [12], which measures the impedance at three discrete frequencies.

TABLE 1: Memory requirement for the multisine and OFDM approaches for the generation of a $N/2$ frequency point broadband signal with a length of $N \cdot M$.

Approach	Multisine worst case	Multisine precalculated	OFDM	OFDM optimized
Memory words	$M \cdot N^2$	$M \cdot N$	$2N$	$5/4N + 1$

When the frequency sweep technique is used, spectroscopy could be performed within a larger set of determined frequencies. The impedance analysis on a large frequency range provides more insights regarding the tissue features. Gabriel et al. measured the impedance of various organs of the human body in different conditions. The obtained frequency responses are specific signatures for each tissue [13]. This technique presents some limitations in the estimation of time-variable systems or when the impedance estimation of multiple electrodes or samples are needed in a short time frame by the same device. Due to these restrictions, this method does not meet the requirements of the proposed strategy.

2.2. Broadband EIS. Different methods for the generation of broadband signals have been investigated to overcome the limitation of classic approaches. The first approach is dated back to 1975 where pseudorandom binary signals were used for the measurement of an electrode impedance in a wide frequency band [14]. The impedance is estimated by correlating the Sample Under Test (SUT) response with the pseudorandom stimulus signal, which results in the impulse response, followed by a Fourier transform. In the case of Maximum Length Sequence (MLS), a more efficient method than correlation has been proposed in [15] based on the Fast Hadamard transform. This kind of signals contains a large range of frequencies and for this reason allows a rapid impedance spectrum measurement. In addition, pseudorandom signals or MLS are preferred instead of the Dirac pulse, whose high amplitude peak is not desirable for the stimulation of biological samples [16, 17]. The main drawback of this method is the signal amplitude variation at each frequency. The spectrum of a MLS signal is also random, and it is possible that the energy at a desired frequency could be too low or equal in amplitude to the noise, which would induce errors in the measurement.

2.3. Multisine Approach. Multisine signals for impedance spectrum measurement of biological samples, reported for instance in [18–20], also provide a fast estimation with the following advantages: the Signal-to-Noise Ratio (SNR) can be improved when using random phases and the frequencies can be selected as required, i.e., linear or logarithmic [21]. Such approach is simple; however, it does not scale easily with higher numbers of frequencies. The memory required for the generation of the multisine increases with the number of tones, as it is shown in Table 1 and in [22]. Furthermore, the detection and impedance estimation at the receiver side could impede the implementation of this method. It could be verified, in the mentioned references, that the stimulation part could be implemented in digital form by storing in memory the externally created multisine signal. However, the receiving part requires a more complex hardware for the demodulation of the signal, usually implemented by the use of a data acquisition board or system, such as an oscilloscope and a personal computer (PC), for impedance computation.

2.4. OFDM for Our Application. Finally, orthogonal multitone signals also offer a wide spectrum for a rapid impedance estimation in the frequency bandwidth of interest. The generation of this kind of signals could be efficiently implemented by using the OFDM method [23]. This OFDM technique is successfully used in the field of digital communication; however, the application for impedance measurement is a novelty and requires of modifications, such as those presented in Section 4. The OFDM method allows controlling the spectrum of the multitone signal with great flexibility by defining the values of the OFDM symbols with the use of an appropriate modulation scheme and/or the manipulation of the system parameters, such as sampling frequency.

Compared to the multisine technique mentioned above, the OFDM method requires less memory for the implementation of the signal generator, as depicted by Table 1. Here, the memory required for the multisine and the OFDM approaches for the generation of a broadband signal of length $N \cdot M$ is calculated, where $N/2$ is the quantity of frequencies of the broadband signal and M is the number of multisine periods or OFDM symbol blocks needed to reduce noise by averaging.

As it can be noticed, the precalculated (stored in memory) multisine requires $N \cdot M$ memory words because it is advisable to apply different random phases on each period of the multisine signal for the improvement of the SNR. However, the normal OFDM approach requires only $2N$ memory words because during each cycle only one symbol of N samples is generated and sequentially exit to the Digital-to-Analog Converter (DAC). This continues, synchronously, until reaching M symbols. For these reasons, the OFDM approach is finally the solution that we have retained.

3. OFDM Considerations

The OFDM model starts by creating a code composed of M blocks of N symbols, $X(k, m)$, $k = 1, 2, \ldots, N$ and $m = 1, 2, \ldots, M$, with each symbol modulating one of a set of N subcarriers for the generation of the multitone signal. The subcarriers are orthogonal, and a cost-effective approach is achieved when the Inverse Fast Fourier Transformation (IFFT) algorithm is used, giving the following:

$$x(n, m) = \frac{1}{N} \sum_{k=0}^{N-1} X(k, m) \cdot e^{j(2\pi k n/N)}. \tag{1}$$

In our application, a low Crest Factor (CF) of the multitone signal is desirable to avoid intermodulation due to the nonlinearities of the analog parts (such as the saturation of
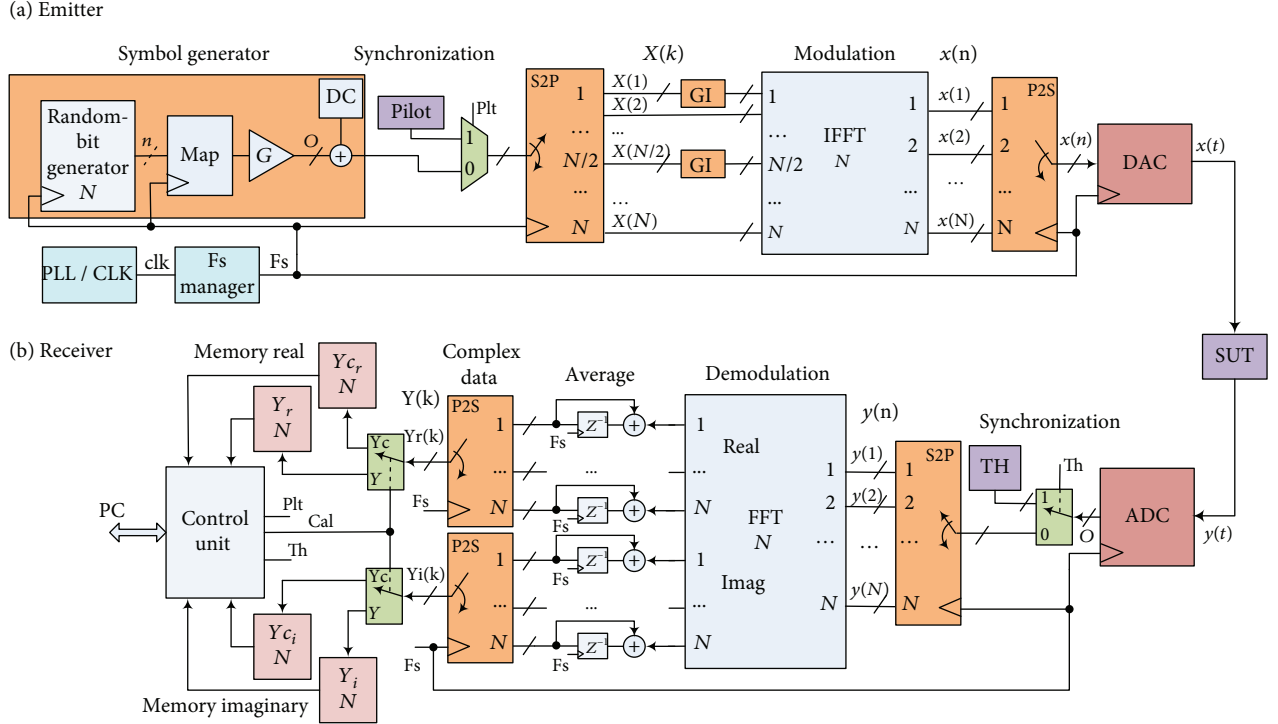
FIGURE 2: OMEIS emitter and receiver structures.

the operational amplifiers). We use a simple technique to reduce the CF that consists of generating multiple sets of N random complex values by controlling the seed and the output delay parameters of a random-bit generator, a block that will be detailed in Section 4.1. Then, each set of values is applied to the OFDM emitter and the CF is calculated. The seed and delay yielding the best CF are retained. The CF is calculated as follows:

$$ \text{CF} = \frac{|x|_{\text{peak}}}{x_{\text{rms}}}. \tag{2} $$

The output of the IFFT is a sequence of complex values as a function of time. For the sake of simplicity, real-valued signals are assumed hereafter which converts equation (1) into the following:

$$ \text{Re}\,\{x(n,m)\} = \frac{1}{N}\sum_{k=0}^{N-1}|X(k,m)|\cdot\cos\left(\frac{2\pi kn}{N} - \theta_X(k,m)\right), \tag{3} $$

where $n = 0, \dots, N-1$ is the discrete time index, and $m = 1, \dots, M$ is the symbol index, with $N \in \mathbf{Z}$ and $M \in \mathbf{Z}$ being the IFFT size and the quantity of symbol blocks, respectively, and θ_X is the random phase.

One step found in a telecommunication OFDM model is the addition of a Cyclic Prefix (CP) to reduce intersymbol interference caused by a multipath fading channel. This CP consists of taking a copy of N_{cp} elements from the end of the symbol block and concatenating them in front of it.

However, EIS measurements do not suffer from multipath propagation; therefore, instead of a CP, a small Guard Interval (GI) with zeros at the extremes of the frequency band (at 0 and $Fs/2$ Hz) will be used to reduce the energy applied on these not useful frequencies.

4. OMEIS System Design, Implementation, and Validation

The proposed OMEIS technique is based on the OFDM model explained above; however, some additional modifications are necessary for the implementation of the EIS measuring system. Firstly, the shape and quantity of symbols should be generated taking into consideration the properties that a stimulation signal should have for fast EIS: low voltage, short duration, and the desired spectrum. Secondly, it should be assured that the energy is propagated at the frequency tones under test. Furthermore, because a perfect synchronization is required in the implementation, a pilot signal should be used. Both additions will be explained in Section 4.1.

In Sections 4.1 and 4.2, the system will be analyzed according to its two parts, first the emitting part and then the receiving part.

4.1. The OMEIS Emitter. The purpose of the emitter is to generate the stimulation signal with the desired spectrum. The structure of the emitter is shown in Figure 2(a). It consists mainly of symbol generation, synchronization, inverse Fourier transformation, and digital-to-analog conversion stages.

In the symbol generator, the code that gives shape to the multitone signal spectrum is created in a synchronized

manner. There are several codes that offer a spectrum with specific differences. For example, a code with a constant amplitude generates a spectrum with tones of similar values at the IFFT subcarrier frequencies, that is, in $\text{Fp}(n) = n \cdot \text{Fs}/N$, where Fs is the sampling frequency, N is the size of IFFT, and $n = 0, 1, \ldots, (N/2) - 1$. The SUT output to a signal with this spectrum could have impulse responses that may require rapid sampling to capture the transients. Another example is a sinusoidal code, with constant frequency Fd, which when applied is sparsed throughout the whole OFDM bandwidth, locating Fd above and below each subcarrier frequency, resulting in tones with amplitudes at frequencies $\text{Fp}(n) -$ Fd and $\text{Fp}(n) + $ Fd, this signal being a type of multisine. However, although this code does not inject much energy into the IFFT subcarrier frequencies, it could be used in case of nonlinearity analysis. Finally, a random code generates a random spectrum within the frequency bandwidth between 0 and $\text{Fs}/2 - \text{Fs}/N$. However, as mentioned above, there is the possibility of a low amplitude in the frequencies of interest resulting in their corruption by noise.

Therefore, one solution is to combine a random code with a constant offset, other than zero, large enough to ensure good amplitude at the carrier frequencies. The latter is provided by a random-bit generator whose output values are mapped with a QPSK modulator and then amplified and shifted with a DC offset. The amplification (G) is selected based on the maximum signal amplitude required, and the complex QPSK mapping is used because it introduces a random phase information to the IFFT subcarriers, as shown in equation (3), that better improves the CF compared to real value mapping such as BPSK [24]. The mathematical backgrounds concerning the performances (BER vs. SNR) of digital modulations show that OFDM-BPSK and OFDM-QPSK are very similar; however, QPSK is better for CF [25]. The symbols are generated at a rate of one sample every $1/\text{Fs}$ seconds, with a total of N samples per measurement cycle.

Following the symbol generator is the synchronization section. This is a critical step during the calibration stage because it measures the system delay. This information is used for the correct synchronization between the transmitter and the receiver. Perfect synchronization between both systems is essential to ensure that the selected N input samples of the FFT correspond to the IFFT transmitted symbol.

The method for synchronization is as follows: before calibration, a pilot signal is used which generates voltage peaks at known intervals. The generated peaks can be detected using an appropriate threshold. This method allows the recording of, in one hand, the delay of the transmitter output signal and, on the other, the joint delay of the analog-digital-analog conversions and the AFE stages.

Next is the modulation stage. Here, as explained above, a GI is used before the IFFT. The size of the IFFT (N) gives the quantity of frequency points for the impedance spectrum. The minimum frequency is at Fs/N, and the maximum is at $\text{Fs}/2 - \text{Fs}/N$ with a frequency separation of Fs/N. Serial-to-Parallel (S2P) and Parallel-to-Serial (P2S) blocks are required before and after the IFFT.

Finally, the real output of the IFFT is selected and converted into an analog signal by the DAC.

4.2. The OMEIS Receiver.
Once the signal coming from the AFE is encoded by the ADC, the Control Unit multiplexes it, depending on whether it is the pilot signal, which is sent during the synchronization, or the multitone one, which is sent to the threshold detector (TH) and the OFDM demodulation, respectively. At the end of the synchronization, when performing calibration or measurement, the response of the SUT is first demodulated using the FFT, then accumulated with values of previous measurement cycles, and finally stored in the corresponding memories: Ycr and Yci in calibration and Yr and Yi in measurement, where r stands for real and i for imaginary.

As it is shown in Figure 2(b), the demodulation produces complex values which are averaged, stored, and transmitted independently. The accumulation can increase the number of bits of the samples but reduces the amount of data to be transmitted. The impedance is then estimated as follows:

$$Z(k) = H_{\text{CAL}}(k, m) \frac{Y_C(k, m)}{Y(k, m)}, \tag{4}$$

where H_{CAL} is the known calibration SUT which may slightly vary in frequency k but is assumed constant in each cycle m of multitone generation; Y is the measurement data; and Y_c is the calibration data received, $k = 1, 2, \ldots, N$ and $m = 1, 2, \ldots, M$.

At the end of the measurement, after all the computation cycles have been performed, the resulting calibration and measurement data are sent to a PC for the final treatment and display.

4.3. The OMEIS Implementation.
The modified OFDM structure, detailed in the preceding sections, is suitable for embedded systems. The implementation takes advantage of the computing power and parallel features of FPGAs, performing both as emitter and receiver in a Cyclone IV FPGA device programmed in VHDL language.

Figure 3 shows the OMEIS system implementation. The emitter part of the OMEIS system is implemented by using the IFFT and the PLL clock generator Megacore IP. The remaining blocks, for instance the Cell Automata (CA), the Fs Manager, the Pilot, and the QPSK blocks, were coded in VHDL.

The values of the emitter's parameters, such as IFFT size or sampling frequency, can be adjusted as required. The default value used for the IFFT size is 1024. The Fs Manager allows changing the sampling frequency Fs of the system to 1 MHz, 500 kHz, and 250 kHz.

The symbol generator is the combination of the CA and the QPSK blocks. First, the CA uses a Cellular Automata algorithm for the creation of two (2) random bits that are next mapped in the following way: the QPSK output for bits "11" is $(G + jG) + \text{DC}$, for "10" it is $(G - jG) + \text{DC}$, for "01" it is $(-G + jG) + \text{DC}$, and finally for "00" it is $(-G - jG) + \text{DC}$, where G is 1023 and DC is equal to 80 in our implementation; both values were selected taking into consideration the output voltage amplitude and frequency spectrum shape.
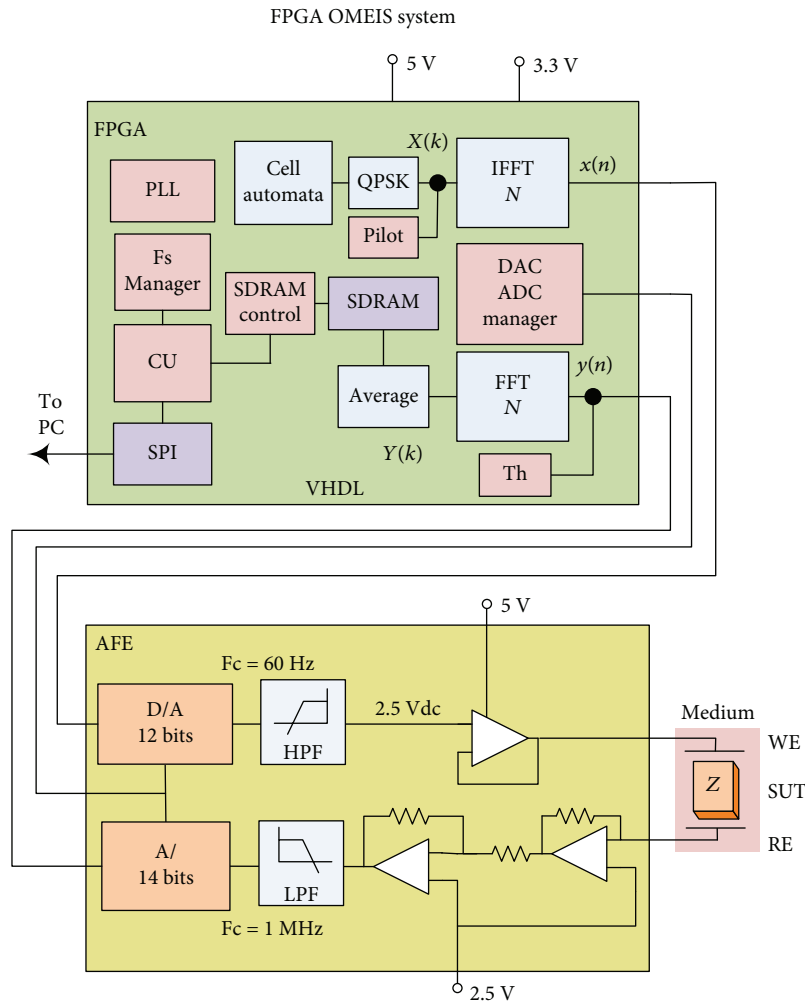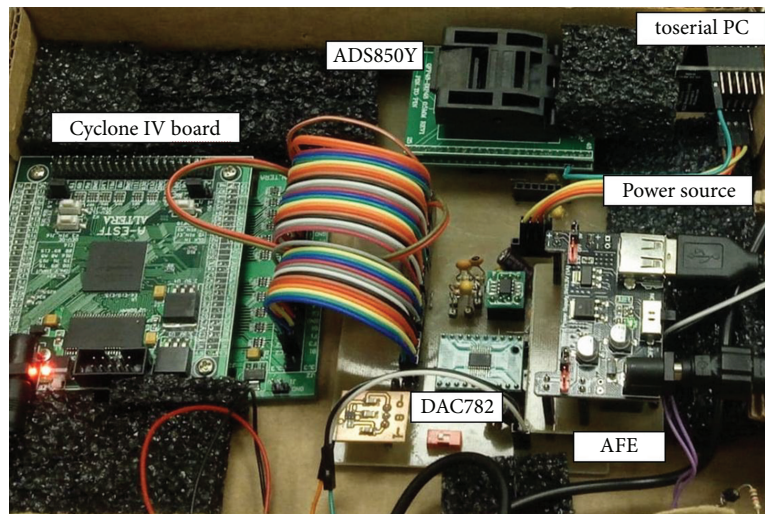
Figure 3: The OMEIS system schematic.

Figure 4: The OMEIS system board.

A synchronous state machine, which operates as a Control Unit (CU), manages the overall behavior of the system. Both the CU and the DAC/ADC manager are coded in VHDL as well.

An analog custom board has been developed in order to perform EIS in biological samples. It has a parallel input 12-bit DAC converter (DAC7821), a parallel output 14-bit
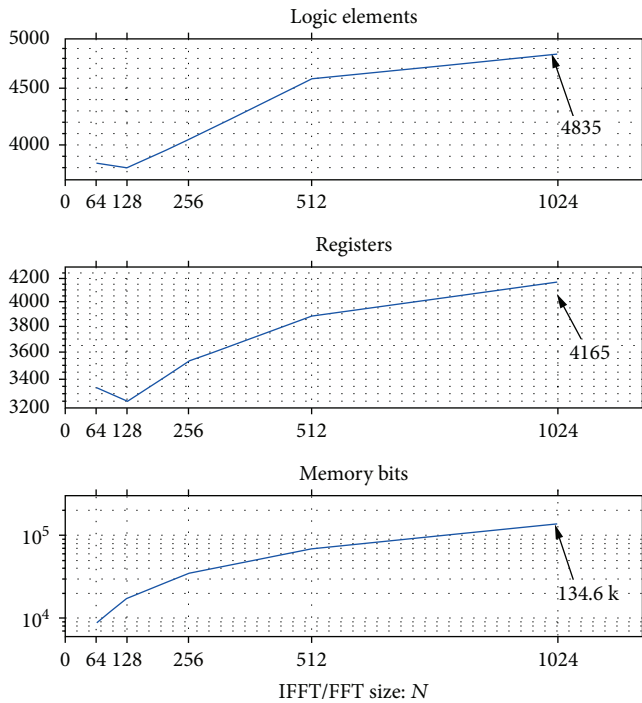
FIGURE 5: Hardware resource utilization of the OMEIS emitter implemented in a Cyclone IV FPGA.

ADC (ADS850Y), and an Analog Front End (AFE) board, as depicted in Figure 4. This AFE board has a maximum stimulation voltage amplitude of 200 mV, low output impedance, and a very low voltage offset between the Working Electrode (WE) and Counter Electrode (CE), which are required for biological measurements. Additionally, the AFE filters nondesired DC and 50/60 Hz components from the multitone signal. The stimulation signal is voltage, and the resulting current is captured and converted into voltage via a Transimpedance Amplifier (TIA) in which the values of a feedback resistor are set during calibration.

At the receiver side, the demodulator is implemented using the FFT Megacores of Altera. The size of the FFT is the same as that of the IFFT. Both the calibration and SUT data, coming from the average block, are stored in a 256 Mb SDRAM (W9825G6EH). Then, they are sent via SPI to a PC. The PC runs a Human-Machine Interface (HMI), coded in MATLAB, for the control of the system as well as for the analysis of the data received running equation (4) for the final impedance estimation. The OFDM TH block, coded in VHDL, employs a threshold algorithm to detect the pilot signals and compute the transmitted signal output delay and the system response delay to send them to the CU.

Figure 5 shows the cost in hardware resources of the OMEIS emitter as a function of the IFFT size N. The values of the resources for $N = 1024$ are depicted on the plots. The number of multipliers is 24 for all N. Notice that N is double the quantity of frequencies of the multitone signal.

4.4. The Orthogonal Multitone Spectrum. The orthogonal multitone signal was analyzed by using the OMEIS

implementation configured with a sampling frequency of Fs = 1 MHz, 32 symbols, and an IFFT size of $N = 1024$ giving a multitone subcarrier frequency separation of 976.5 Hz. Also, a guard interval of 10 frequency points at the end of the spectrum is applied giving a maximum frequency of 488.28 kHz. Furthermore, to test the frequency selection capabilities of the system, the subcarriers were also eliminated in the range from $n = 100$ to $n = 150$, which corresponds to a bandwidth of 97.65 kHz to 146.48 kHz $(F(n) = n \cdot \text{Fs}/N)$. A digital oscilloscope (Tektronix DPO500B) with FFT function capabilities was used to measure the spectrum of the signal during this test.

Figure 6 shows the spectrum of the stimulation multitone voltage signal (upper part) and the voltage signal spectrum of a resistance Rn = 671.8Ω (lower part) that is connected in series with the test impedance (Rs + Rp$\|$C, Rs = 265.4Ω, Rp = 4.62 kΩ, and C = 1.1 nF). The second signal was intentionally displaced 20 dB downward in Figure 6, for better visibility.

As shown in the upper part of Figure 6, the spectrum of the multitone signal has a flat shape between 0 Hz and 488.281 kHz, with the exception of the removed bandwidth measured between 97.65 kHz and 146.5 kHz.

When the voltage spectrum of the resistance Rn is measured (Figure 6, lower part), the amplitude of the spectrum changes as expected: at the frequency of 488.28 kHz, where the test impedance "Z" is about 410 Ω, the amplitude is about -23.57 dB, that is -4.2 dB less than the multitone signal amplitude of -19.37 dB. This very closely corresponds to the theoretical difference of 20 log (671.8/(410 + 671.8)) = −4.13 dB. At low frequency (19.5 kHz, Z = 4.2 kΩ), the delta marker shows -16.2 dB that is also very similar to the theoretical 20 log (671.8/(4.2 k + 671.8)) = −17 dB.

4.5. The OMEIS System Performance. For the validation of the OMEIS system, the size of the IFFT and the FFT is 1024 and Fs = 1 MHz. Therefore, there are 511 available frequency points for the impedance estimation with a spectrum resolution and first frequency point of 976.5 Hz (DC frequency is not calculated). The stimulation time depends on Fs, the size of the IFFT/FFT ($N = 1024$), and the symbol quantity ($M = 32$ in this case), resulting in 32.76 ms. M also corresponds to the number of measurement cycles used for averaging. This test was performed by using a test circuit (Rs = 750 Ω, Rp = 30 kΩ, Cp = 2 nF), as shown in Figure 7. The result shows a good accuracy in the impedance estimation with a 1.39% mean error.

5. Experiments

After having characterized the performances of our system in terms of hardware resources, signal spectrum, and impedance estimation, we proceed to the presentation of preliminary results of *in vitro* and ex vivo experiments performed under conditions related to fibrosis. First, we describe experiments with cell cultures, in which the correlation between the impedance and the cell population is observed. OMEIS's spectrum management and frequency resolution flexibility is
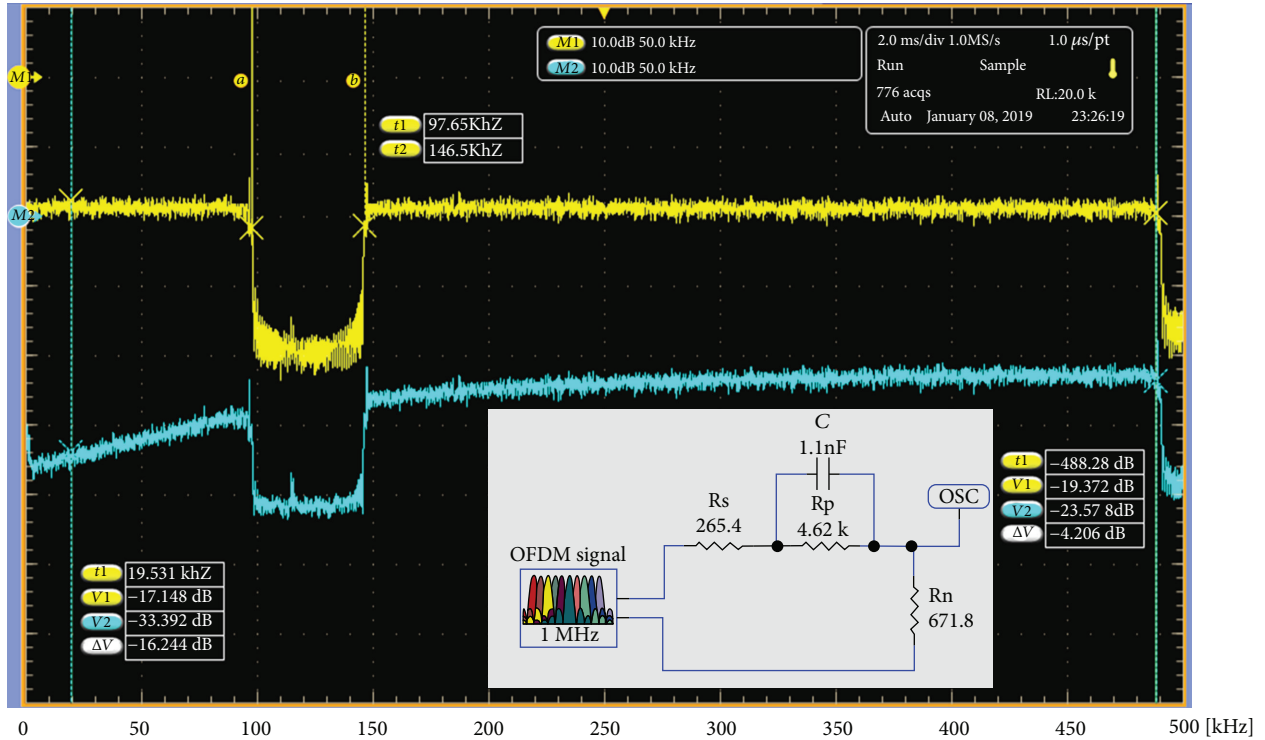
FIGURE 6: Spectrum of a resistance Rn voltage signal (spectrum in lower part) form a voltage divider circuit between Rn and the test impedance powered by the multitone signal (spectrum in upper part). The values of the test impedance are shown. The markers (ΔV) show the amplitude difference, in dB, between both spectra at the frequencies of 19.53 kHz and 488.28 kHz. The second signal was intentionally shifted 20 dB downward for better visibility.
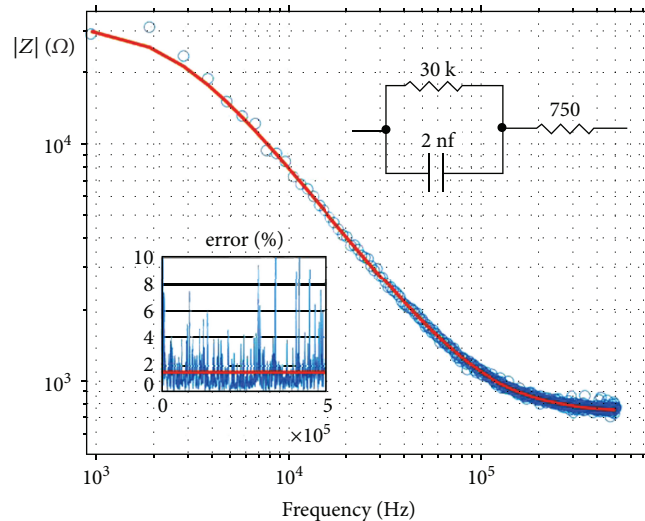

FIGURE 7: Impedance comparison between the model (red) and the estimation from the OMEIS system (blue).

tested as well. Finally, *ex vivo* impedance measurements conducted on inhibited and perfused porcine heart tissue are described, using commercial human PCM probes, for a more realistic condition.

5.1. In Vitro Measurements. These tests focus on the flexibility of the OMEIS system and the estimation of errors during biological sample measurements.

5.1.1. Materials. A commercially available cultureware of Applied BioPhysics Inc. [26], shown in Figure 8, is used during the experimentation. The cultureware consists of an array of 8 wells with 10 electrically interconnected circular gold electrodes ($250 \mu m$ diameter) on each well and one central larger electrode common to all wells. The electrodes are delineated with an insulating film. The cultureware offers a two-electrode setup for EIS measurement: the Working
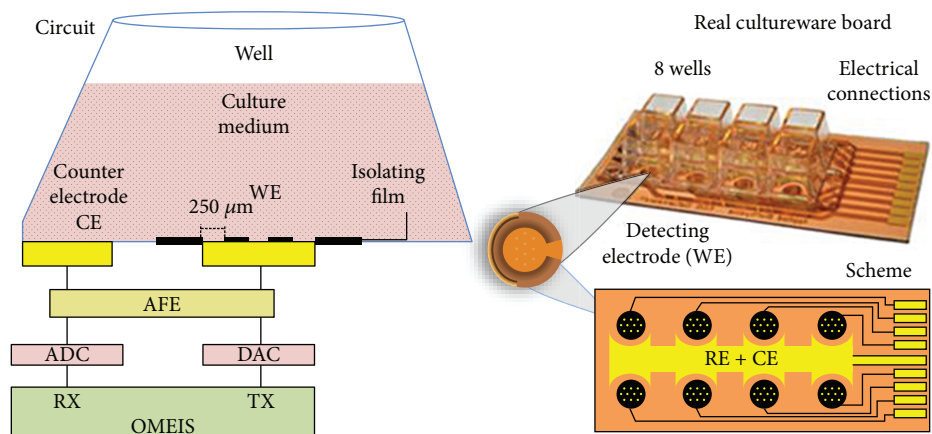
FIGURE 8: The circuit of the electric cell-substrate impedance sensing (ECIS) protocol and the OMEIS system. Also, the picture and the scheme of the ECIS cultureware board (8W10E) with eight miniwells (~0.6 mL) are depicted.

TABLE 2: OMEIS default parameters.

Fs (MHz)	Fm (Hz)	ΔF (Hz)	Ts (ms)
1	1952	976	65.5
0.5	976	488	131
0.25	488	244	262

Electrode (WE) and the Counter Electrode together with the Reference Electrode (CE and RE).

The OMEIS system was calibrated with an IFFT/FFT size of $N = 1024$, a symbol quantity of 32, and 3 values for Fs of 1 MHz, 500 kHz, and 250 kHz. There is a GI at DC and at the first and the last frequencies (Fs/N and Fs/2). The minimum frequency (Fm), the frequency separation (ΔF), and the stimulation time (Ts) for each configuration are shown in Table 2.

5.1.2. Protocol. The in vitro experimentations are performed on an immortalized mouse myoblast cell line (C2C12 cells). Under appropriate conditions, they are cells that produce proteins related to fibrosis [27]. The protocol for in vitro cell-substrate EIS measurements is as follows: at the beginning of the experiment, one well of the cultureware was filled with 7,000 C2C12 myoblasts plus 600 μL of Dulbecco's Modified Eagle's Medium (DMEM) containing 10% Fetal Bovine Serum (FBS), sodium bicarbonate (3.7 g/L), and 1% antibiotics. Another well was filled with only 600 μL of medium and is used as a control well. Cells were cultured in an incubator at 37°C and 5% CO_2 and the medium was changed every 48 hours. Five measurements were taken during the 95 hours of incubation, enough time for the development of a large cell population on the electrode. Visual inspections were performed with a standard inverted microscope.

5.1.3. Results. Figure 9(a) shows the impedance spectrum at five measurement times when Fs = 1 MHz: times 0 h, 23 h, 47 h, 71 h, and 95 h (h stand for hours after the beginning of the experimentation). In the frequency domain, the spectrum shows a negative constant slope, whose magnitude differs depending on the measurement time, from the first frequency up to 20 kHz, when it begins to decrease.

The evolution of the impedance in time could be better evaluated by using Figure 9(b), where the normalized impedance is depicted, taking time 0 h as the reference (measured impedance at point k divided by the impedance of time 0 h at the same point k). As shown, the impedance module increases from 1.5 at time 23 h and frequency 55 kHz to almost 3.5 at time 95 h and frequency 95 kHz, in correspondence with the increase of the cell population in the electrode. This is validated using microscopy photos to visually correlate the state of the culture with the measurements (Figure 9(c)).

For the study of the flexibility of the system, the impedances at 3 sampling frequencies are evaluated together. Here, we are using the sampling frequencies of 1 MHz, 500 kHz, and 250 kHz that give the frequency resolution of 976 Hz, 488 Hz, and 244 Hz, respectively. As expected, the impedance at the same measurement time but at different sampling frequencies overlaps, as shown in Figure 10. This flexibility allows the addition of more frequency points for a better evaluation of the regions of interest. It should be noted that the sampling frequency can be changed by software, either manually or automatically without the need to reconfigure the system.

The results obtained in these experiments show that the frequency band from 30 kHz to 200 kHz is optimal for the observation of the impedance signature corresponding to the growth of the cell population.

5.1.4. In Vitro Experiment Data Modeling. Data presented in Figure 9(a) were used in an impedance model identification algorithm. Due to the bandwidth of the measurements (2 kHz to 500 kHz) and the limited double-layer capacitance associated with the microelectrodes used, the observable behavior is associated with the cell membrane and the intra- and extracellular medium [28]. The electrode impedance is fitted in our case as follows:

$$Z_{\text{elec}}(f) = R \frac{1 + (j(f/f_u))^\gamma}{(j(f/f_u))^\gamma}, \tag{5}$$

where R is the resistance at high frequency, γ is the fractional order of the constant phase element, and f_u is the transition frequency.
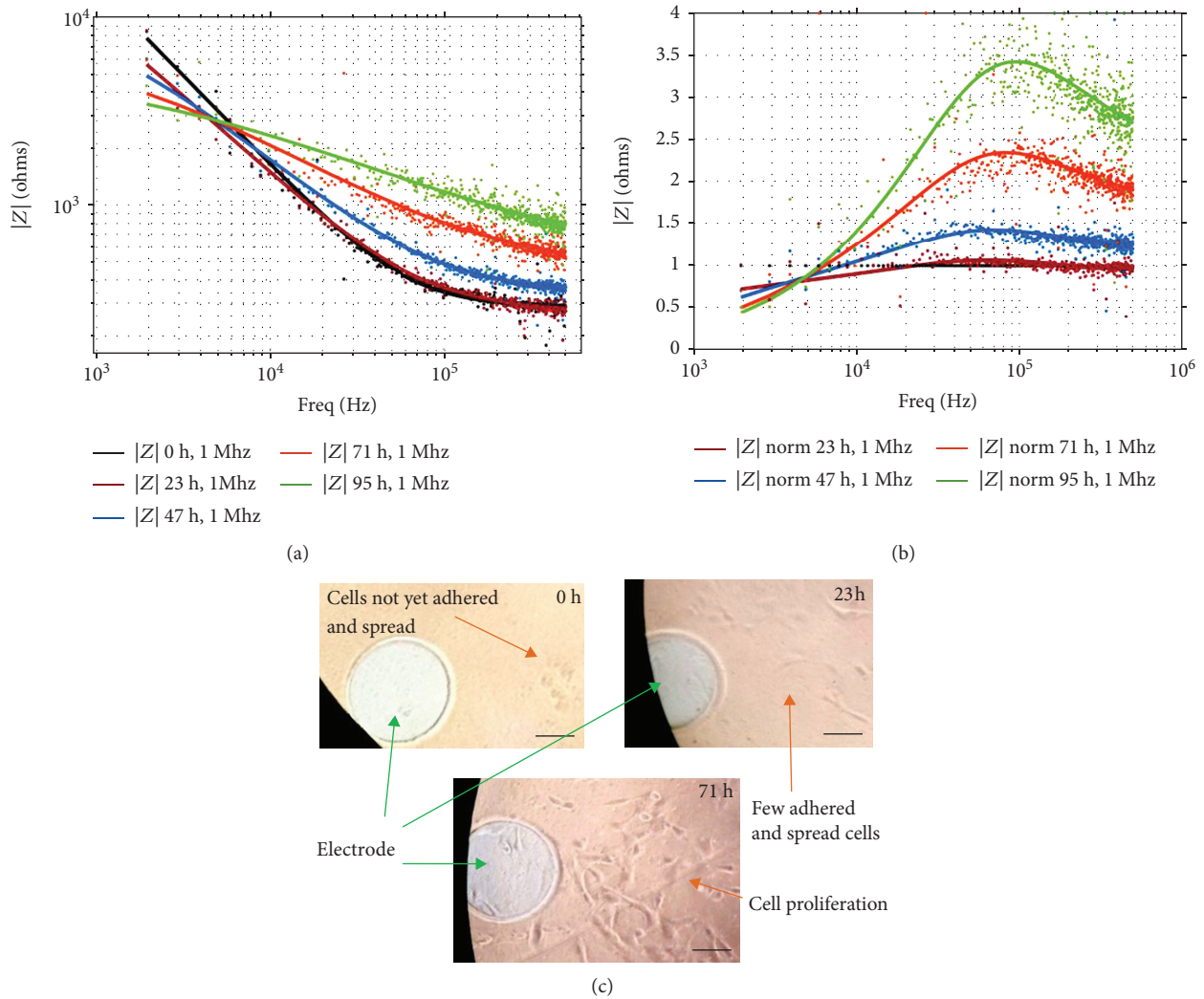
(a)

(b)

(c)

FIGURE 9: Impedance spectrum performed on C2C12 cells cultured *in vitro*. Five measures were taken at 0, 23, 47, 71, and 95 hours. (a) Impedance module. (b) Normalized impedance. (c) Microscopy photos at 0 h, 23 h, and 71 h. The scale bar represents 100 μm.

Data were fit by minimizing the residual function of the distance between the measurement and the modeled data using Powell's method [29]. Results are given in Table 3.

In high frequency, the resistance R shows a slight increase over time. Nevertheless, there is a clear evolution of the Constant Phase Element (CPE) order from values near 1, corresponding to a pure integrator of capacitor, to values around 0.5, corresponding to a Warburg CPE. As the measurements were performed over a single well, no conclusion on the correlation between the model parameters and the biological evolution of the cells can be drawn. However, the measurement method clearly enables observing changes in the electrical impedance over time for the targeted application. Moreover, the measurement data can fit the standard electrode impedance model using conventional optimization algorithms.

5.2. *Ex Vivo Measurements*. The OMEIS flexibility and reliability during impedance measurement have been proven in Section 5.1. The objective now is the evaluation of

OMEIS's ability for in vivo conditions. The following experiments are conducted on cardiac tissues, ex vivo, freshly explanted, using a commercial pacemaker electrode. Two types of characterization are performed on the ventricles of a swine heart: first on a tissue immersed in a cardioplegic solution that inhibits the cardiac contractions and second on perfused tissue that mimics in vivo conditions.

5.2.1. *Materials*. The measurements were performed with the OMEIS system and the commercial lab instrument Solartron 1260 (Ametek Inc., USA), which is an impedance spectrometer commonly used for bioimpedance measurements. A human PCM cardiac lead, Sprint Quattro Secure 6947M (Medtronic, USA), is used as the sensing electrode. This lead has both pacing and defibrillation electrodes, but for this experimentation only the pacing termination was used.

5.2.2. *Animal Model*. This study was carried out in accordance with the recommendations of the Directive 2010/63/EU of the European Parliament on the protection
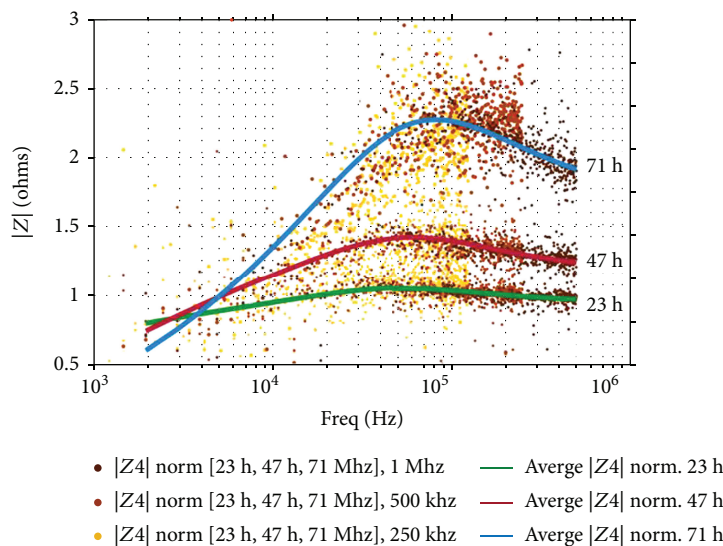
FIGURE 10: Normalized impedance of the C2C12 cells at times 23 h, 47 h, and 71 h (h = cell culture time in hours) when using 3 different sampling frequencies.

TABLE 3: Data fit parameters results.

t (hours)	R (Ω)	γ	f_u (kHz)	NRMSE
0	281	0.93	59.2	0.0138
23	265	0.87	69.2	0.0153
47	321	0.80	79.3	0.0098
71	358	0.54	201.0	0.0386
95	495	0.45	215.0	0.0314

of animals used for scientific purposes and approved by the local ethical committee of Bordeaux CEEA50. The heart was obtained from a young swine (Large White, 40 ± 5 kg). The swine was premedicated with ketamine (20 mg/kg) and acepromazine (Calmivet, 1 mL/50 kg). Anesthesia was induced with the intravenous injection of sodium pentobarbital (10 mg/kg) and maintained under isoflurane, 2%, in 100% O_2. The swine was euthanized by sodium pentobarbital (40 mL, from 50 mg/mL of stock) and the heart rapidly excised, cannulated by the aorta, and rinsed with cold cardioplegic solution containing (in mM) NaCl, 110; CaCl$_2$, 1.2; KCl, 16; MgCl$_2$, 16; NaHCO$_3$, 10; and glucose, 9.01 at 4°C.

5.2.3. Protocol in Cardioplegia. The right ventricle (RV) wall was dissected and placed in the cardioplegic solution (in mM: 110 NaCl, 1,2 CaCl$_2$, 16 KCl, 16 MgCl$_2$, 10 NaHCO$_3$, and 10 glucose) and then chilled with ice during the measurements.

The OMEIS system was configured with an IFFT/FFT size of $N = 1024$, a symbol quantity of 32, and a Fs = 1 MHz. For the Solartron 1260, the measurements were done at a 100 mV peak voltage level (similar to the OMEIS system), with a logarithmic frequency sweep from 1 MHz to 0.1 Hz, with 10 points per decade. Each measure was carried out only once for OMEIS, but they were repeated five times for the Solartron 1260, and the mean of these five measurements was calculated.
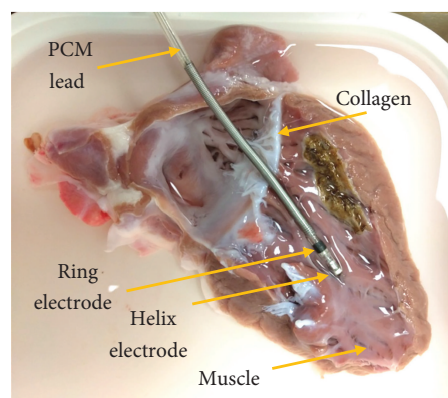

FIGURE 11: *Ex vivo* experimentation on a swine heart. Right ventricle (RV) placed in cardioplegic solution. Pacemaker lead in the endocardial "Muscle" region.

The ex vivo measurements were performed in two different endocardial regions of the ventricle: the healthy lateral wall and a more "collagen-rich" region near the basal area and auriculoventricular ring. From now on, the normal endocardium tissue will be termed "Muscle" and will be compared to the "Collagen" region. The first region is where the lead is placed in Figure 11, and the second one is the region just above the tricuspid valve (white tissue in Figure 11).

5.2.4. Protocol for Perfused Tissue. Figure 12 shows the Langendorff system used for the perfusion protocol in this section. The left ventricle (LV) was dissected and cannulated by the left anterior descending artery. Then, the LV was mounted onto a frame where it was submerged and perfused (20 mL/min) with a warm (37°C) saline solution containing (in mM) NaCl, 130; NaHCO$_3$, 24; NH$_2$PO$_4$, 1.2; MgCl$_2$, 1; glucose, 5.6; KCl, 4; and CaCl$_2$, 1.8 and gassed with 95% O_2/5% CO_2 at 37°C (pH 7.4). A volume-conducted ECG
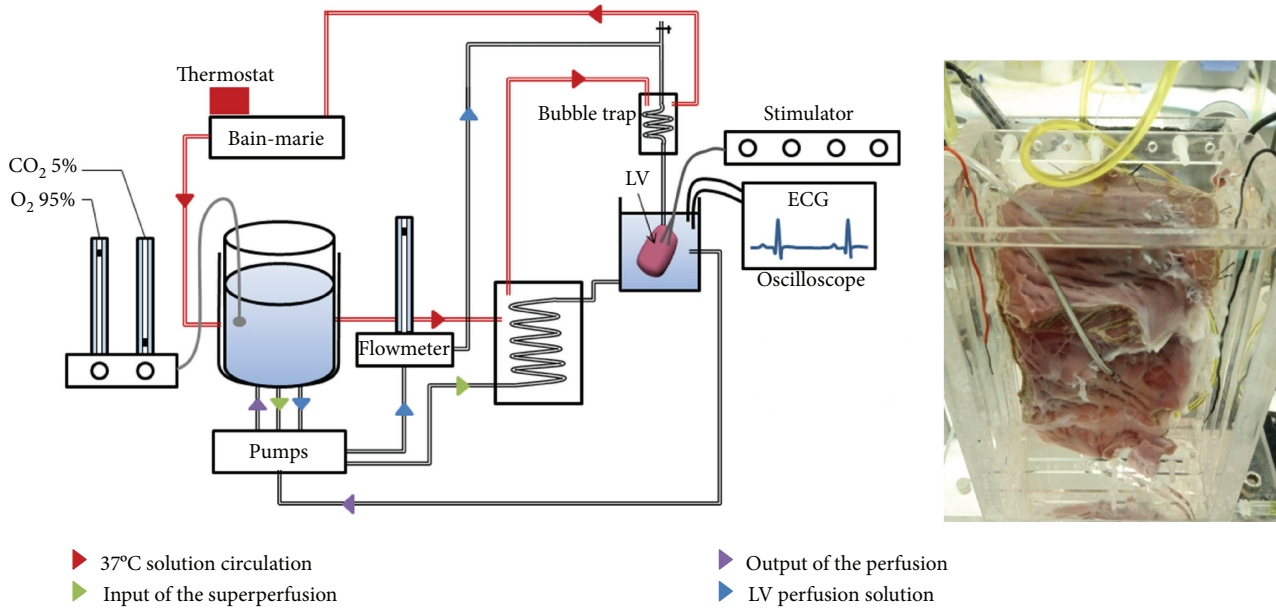
Figure 12: Langendorff system maintaining the ventricle in the in vivo conditions. A picture of the heart inside the perfusion chamber is shown at right.

was measured in the bath to monitor the electrical activity of the tissue preparation.

The ventricle was stimulated from the epicardium at 1 Hz using bipolar tungsten electrodes coupled to a pulse generator and constant current stimulator (DG2A, DS3, Digitimer, UK). The stimulation currents were applied at twice the excitation threshold for a duration of 2 ms.

5.2.5. Results of Inhibited Cardiac Tissue Experiments. In the following experiments, measurements of impedance spectrum were first performed with Solartron and then with OMEIS.

Figure 13 shows the impedance spectrum measured by both instruments in the different heart regions as well as in the cardioplegic solution (CPG). It can be noticed that the "Muscle" has the greatest magnitude of impedance, followed by the "Collagen" region, and lastly the CPG solution that has a much lower impedance of around 190 Ω.

The values of the OMEIS system were noisy due to the fact that a reduced number of symbols ($M = 32$) were used in order to increase measurement speed. However, the averaged version follows very closely the values of the reference instrument with a mean error of about 8% and a standard deviation of 5.8%. This allows a differentiation between the impedance of the tissues.

5.2.6. Results of Cardiac Tissue Perfusion Experiments. During the experimentation with the heart in the perfusion state, the OMEIS system delivered valid results; however, the Solartron yielded meaningless values. We attribute this anomaly, in the reference instrument, to the electrophysiological and mechanical activities of the heart. These activities behave like a time-invariant system that could not be sensed by an instrument that uses the frequency sweep EIS method.

Figure 14 shows the impedance values received from the OMEIS in the perfusion condition for the "Muscle" and "Collagen" regions. It can be noticed that again the "Muscle" tissue has a greater impedance than the "Collagen," although both are lower than the values obtained in the first experience described above. Experimental conditions differ indeed largely, especially in temperature, and also in the fact that both the heart and the electrode were completely submerged here in the saline solution.

Furthermore, the Sprint Quattro Secure 6947M pacing lead has two poles: the proximal electrode (helix electrode) is inserted in the tissue and the distal electrode (larger ring) is used as the returning current path. In the first experiment, cardiac tissue is immobilized and the ring electrode relies simply on the tissue, as can be seen in Figure 11. In the second experiment, the perfused cardiac tissue is immersed and exhibits contractions; the ring electrode is certainly no longer in contact with the tissue but moves in the liquid. However, with the impedance measurement the differentiation between both tissues is possible, even with the dynamics of the heart imposed by the perfusion system.

6. Conclusion and Perspectives

In this article, we propose a novel strategy for the chronic detection of fibrosis induced by the electrodes of cardiac implants. This strategy consists of the application of Electrical Impedance Spectroscopy (EIS) as a technique for sensing fibrosis at short intervals between the pacemaker pulses and the heartbeat. Given the speed and flexibility requirements in the measurement, in addition to the constraint of low hardware cost that this strategy imposes, we have devised, as an innovative solution, the use of orthogonal multitone signals combined with the OFDM implementation method, resulting in the Orthogonal Multitone EIS (OMEIS) approach.
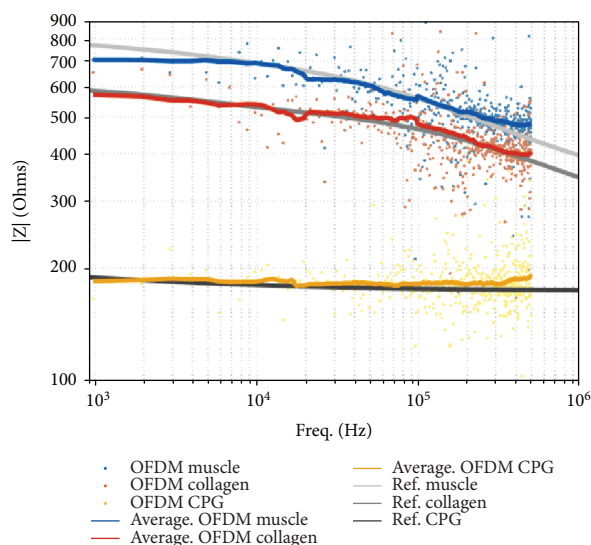
FIGURE 13: Magnitude of impedance measurement for 3 conditions: "Muscle" stands for normal endocardial region, "Collagen" for collagen region, and "CPG" for cardioplegia. OFDM is performed at Fs = 1 MHz. Colored curves represent OMEIS measurements, and grey curves represent Solartron measurements.

This proposed OMEIS system is prototyped on a FPGA-based platform that provides an adjustable sampling frequency and IFFT/FFT size, with a default value of 1 MHz and 1024, respectively. With the default setup, the system offers a maximum OFDM multitone signal bandwidth of 499 MHz with 511 subcarriers separated by 976.5 Hz. This system is validated through experiments with electrical circuits resulting in an impedance spectrum with an average error of 1.39% when using 511 frequencies and an amount of 32 OFDM symbols. In addition, the measurement capacity of biological samples and the flexibility of the OMEIS system were studied by means of measurements of living cells in *in vitro* cultures. It showed a good correlation between the magnitude of the impedance and the cell population at sampling frequencies of 1 MHz, 500 kHz, and 250 kHz, when measuring at the different times when C2C12 cells were cultivated during a period of 95 hours. The adjustment of the sampling frequency can be done manually or automatically, on flight, without the need to reconfigure the system.

Finally, the strategy mentioned at the beginning has been validated by ex vivo measurements of cardiac tissue in inhibited and in perfusion states. In the first case, the OMEIS system showed impedance spectra that, once averaged, were similar to that of the reference instrument, with an 8% average error and 5% standard deviation. In the second case, given the dynamics of the perfusion system, only the OMEIS performed measurements as expected. The acquired values from OMEIS allow us to distinguish between "Muscular" tissue and "Collagen" tissue.

Since the cells used for the *in vitro* experimentation produce collagen in the extracellular matrix, and due to the fact that fibrosis tissue is composed mainly by collagen (with a few cells), we have performed both experimentations (*in vitro* and *ex vivo*) in order to study the OMEIS system in both scenarios. As shown in the *in vitro* results, when
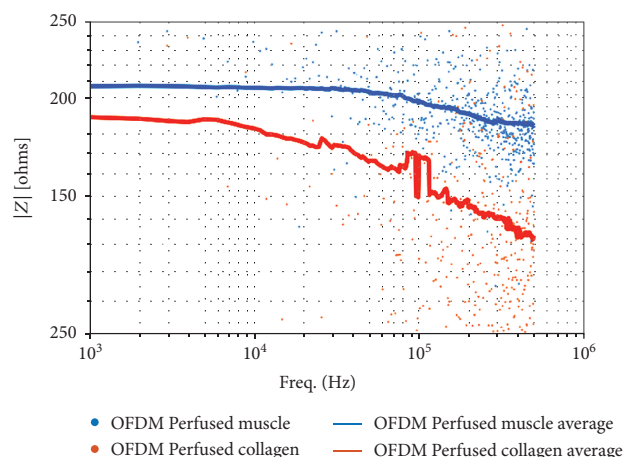

FIGURE 14: Magnitude of impedance of the "Muscle" and "Collagen" regions with the heart in perfusion, measured by the OMEIS system at Fs = 1 MHz.

the cells reproduce, the impedance also increases; therefore, as it is shown in the *ex vivo* experimentation, the "Collagen" region has a lower impedance than the "Muscle" (full of cells) tissue.

The performance in the measurement speed is within the requirements, giving 510 frequency points in a stimulation time of about 64 ms with the following OMEIS parameters: $N = 1024$, $M = 32$, and Fs = 1 MHz.

The tradeoff between noise reduction and symbol quantity is a critical step in the calibration of the system. We were using 32 symbols that showed good results during electrical circuits and *in vitro* experimentations, but that was at the limit for the *ex vivo* experimentation. The increase of the symbol quantity should solve this limitation with the cost of reducing the measurement speed.; however, this solution should be carefully analyzed in order to remain in the time frame required for the proposed strategy. Another solution could be the use of another OFDM code that could better improve the CF with the appropriate modulation scheme. These are topics for future research in our group to further improve the OMEIS system since it is the tool that will allow us to establish an electrical signature of a fibrotic tissue.

Data Availability

All data are provided in full in the Results.

Conflicts of Interest

The authors declare that there is no conflict of interest regarding the publication of this paper.

References

[1] B. Rolfe, J. Mooney, B. Zhang et al., "The fibrotic response to implanted biomaterials: implications for tissue engineering," in *Chapter 3 in Regenerative Medicine and Tissue Engineering—Cells and Biomaterials*, D. Eberli, Ed., Publish. InTech, 2011.

[2] W. M. Grill and J. Thomas Mortimer, "Electrical properties of implant encapsulation tissue," *Annals of Biomedical Engineering*, vol. 22, no. 1, pp. 23–33, 1994.

[3] H. Mase, K. Tamura, A. Hiromoto et al., "Histopathological study of tissue reaction to pacemaker electrodes implanted in the endocardium," *Journal of Nippon Medical School*, vol. 72, no. 1, pp. 52–59, 2005.

[4] S. De Jong, T. A. B. Van Veen, J. M. T. De Bakker, M. A. Vos, and H. V. M. Van Rijen, "Biomarkers of myocardial fibrosis," *Journal of Cardiovascular Pharmacology*, vol. 57, no. 5, pp. 522–535, 2011.

[5] G. C. McConnell, R. J. Butera, and R. V. Bellamkonda, "Bioimpedance modeling to monitor astrocytic response to chronically implanted electrodes," *Journal of Neural Engineering*, vol. 6, no. 5, p. 055005, 2009.

[6] N. Akoum, C. McGann, G. Vergara et al., "Atrial fibrosis quantified using Late Gadolinium Enhancement MRI is associated with sinus node dysfunction requiring pacemaker implant," *Journal of Cardiovascular Electrophysiology*, vol. 23, no. 1, pp. 44–50, 2012.

[7] K. Yokoyama, T. Kariyasu, S. Kuhara, M. Imai, R. Ishimura, and T. Nitatori, "Influence of MRI-conditional cardiac pacemakers on quality and interpretability of images acquiredin 1.5-T cardiac MRI," *International Journal of Clinical Cardiology*, vol. 2, no. 2, 2015.

[8] D. A. Dean, T. Ramanathan, D. Machado, and R. Sundararajan, "Electrical impedance spectroscopy study of biological tissues," *Journal of Electrostatics*, vol. 66, no. 3–4, pp. 165–177, 2008.

[9] G. Amorós-Figueras, E. Jorge, T. García-Sánchez, R. Bragós, J. Rosell-Ferrer, and J. Cinca, "Recognition of fibrotic infarct density by the pattern of local systolic-diastolic myocardial electrical impedance," *Frontiers in Physiology*, vol. 7, p. 389, 2016.

[10] R. Gonzalez-Landaeta, O. Casas, and R. Pallas-Areny, "Heart rate detection from plantar bioimpedance measurements," *IEEE Transactions on Biomedical Engineering*, vol. 55, no. 3, pp. 1163–1167, 2008.

[11] K. Kim, K. Song, K. Bong et al., "A 24 μW 38.51 mΩrms resolution bio-impedance sensor with dual path instrumentation amplifier," in *ESSCIRC 2017 - 43rd IEEE European Solid State Circuits*, pp. 223–226, Leuven, September 2017.

[12] xCELLigence, *Calculation Principles of RTCA Software, Technical Note No. 2*, xCELLigence System, 2010.

[13] S. Gabriel, R. W. Lau, and C. Gabriel, "The dielectric properties of biological tissues: II. Measurements in the frequency range 10 Hz to 20 GHz," *Physics in Medicine and Biology*, vol. 41, no. 11, pp. 2251–2269, 1996.

[14] G. Blanc, I. Epelboin, C. Gabrielli, and M. Keddam, "Measurement of the electrode impedance in a wide frequency range using a pseudo-random noise," *Electrochimica Acta*, vol. 20, no. 8, pp. 599–601, 1975.

[15] M. Cohn and A. Lempel, "On fast M-sequence transforms (Corresp.)," *IEEE Transactions on Information Theory*, vol. 23, no. 1, pp. 135–137, 1977.

[16] I. Schneider, "Broadband signals for electrical impedance measurements of long bone fractures," in *Proceedings of 18th Annual International Conference of the IEEE Engineering in Medicine and Biology Society*, pp. 1934-1935, Amsterdam, Netherlands, 1996.

[17] T. Sun, C. van Berkel, N. G. Green, and H. Morgan, "Digital signal processing methods for impedance microfluidic cytometry," *Microfluidics and Nanofluidics*, vol. 6, no. 2, pp. 179–187, 2009.

[18] R. Bragos, R. Blanco-Enrich, O. Casas, and J. Rosell, "Characterisation of dynamic biologic systems using multisine based impedance spectroscopy," in *IMTC 2001. Proceedings of the 18th IEEE Instrumentation and Measurement Technology Conference. Rediscovering Measurement in the Age of Informatics (Cat. No. 01CH 37188)*, pp. 44–47, Budapest, Hungary, 2001.

[19] T. Breugelmans, E. Tourwé, J. B. Jorcin et al., "Odd random phase multisine EIS for organic coating analysis," *Progress in Organic Coatings*, vol. 69, no. 2, pp. 215–218, 2010.

[20] B. Sanchez, G. Vandersteen, I. Martin et al., "In vivo electrical bioimpedance characterization of human lung tissue during the bronchoscopy procedure. A feasibility study," *Medical Engineering & Physics*, vol. 35, no. 7, pp. 949–957, 2013.

[21] B. Sanchez and R. Bragos, "Fast electrical impedance spectroscopy for moving tissue characterization using bilateral quasilogarithmic multisine bursts signals," in *4th European Conference of the International Federation for Medical and Biological Engineering*, J. Vander Sloten, P. Verdonck, M. Nyssen, and J. Haueisen, Eds., vol. 22 of IFMBE Proceedings, pp. 1084–1087, Springer, Berlin, Heidelberg, 2009.

[22] E. De Roux, M. Terosiet, F. Kolbl et al., "Toward an embedded OFDM-based system for living cells study by electrochemical impedance spectroscopy," in *2018 IEEE 20th International Conference on e-Health Networking, Applications and Services (Healthcom)*, Ostrava, Czech Republic, September 2018.

[23] S. Weinstein and P. Ebert, "Data transmission by frequency-division multiplexing using the discrete Fourier transform," *IEEE Transactions on Communication Technology*, vol. 19, no. 5, pp. 628–634, 1971.

[24] S. Boyd, "Multitone signals with low crest factor," *IEEE Transactions on Circuits and Systems*, vol. 33, no. 10, pp. 1018–1022, 1986.

[25] N. Sood, A. K. Sharma, and M. Uddin, "BER performance of OFDM-BPSK and -QPSK over Nakagami-m fading channels," in *Proceeding of IEEE-IACC'2010*, Patiala, India, February 2010.

[26] Applied BioPhysics, "ECIS: electric cell-substrate impedance sensing," p. 35, 2018, http://www.biophysics.com/cultureware.php.

[27] Y. Li, W. Foster, B. M. Deasy et al., "Transforming growth factor-β1 induces the differentiation of myogenic cells into fibrotic cells in injured skeletal muscle: a key event in muscle fibrogenesis," *The American Journal of Pathology*, vol. 164, no. 3, pp. 1007–1019, 2004.

[28] S. Grimnes, O. Rikshospitalet, and N. Schwan, "Interface phenomena and dielectric properties of biological tissue," *Encyclopedia of Surface and Colloid Science*, vol. 20, pp. 2643–2653, 2002.

[29] M. J. D. Powell, "An efficient method for finding the minimum of a function of several variables without calculating derivatives," *The Computer Journal*, vol. 7, no. 2, pp. 155–162, 1964.

Research Article

Electrical Impedance-Based Methodology for Locating Carcinoma Emulators on Breast Models

Marcos Gutierrez-Lopez [iD],[1] **Juan Prado-Olivarez,**[2] **Javier Diaz-Carmona,**[1,2]
Carlos A. Herrera-Ramírez [iD],[2] **Jose Antonio Gutierrez-Gnecchi** [iD],[3]
and Carlos G. Medina-Sánchez[4]

[1]*Tecnológico Nacional de México, Celaya 38010, Mexico*
[2]*Tecnológico Nacional de México, Departament of Electronics Engineering, Celaya 38010, Mexico*
[3]*Tecnológico Nacional de México, Depatrment of Electronics Engineering, Morelia 58120, Mexico*
[4]*Hospital General de Celaya "ISSSTE", Obstetrics and Gynecology, 38020, Mexico*

Correspondence should be addressed to Carlos A. Herrera-Ramírez; carlos.herrera@itcelaya.edu.mx

There is a worldwide need for new methodologies to prediagnose breast cancer in an early stage, which helps to notably increase the possibility of saving the mammary gland or patient's life. This work describes a new methodology proposal based on electrical impedance for the localization of preclinical carcinoma emulators in agar phantoms of the breast. The impedance is systematically measured through eight Ag/AgCl electrodes uniformly distributed in a ring arrangement placed on the breast agar phantom. The fundamental idea of the proposed location algorithm, named Anomaly Tracking Circle algorithm, is to find the breast agar area defined by straight lines joining the electrode pairs having the minimum difference value of the defined normalized impedance magnitude along the measurement sweep. Such difference is obtained with respect to a breast agar phantom without carcinoma emulator. The proposed methodology was evaluated through seven experimental agar models, six of them having carcinoma lobe emulators with different locations and electrical conductivities. According to the obtained results, the described methodology can obtain the location zone of preclinical-emulated carcinomas with an 83.33% success.

1. Introduction

The highest incidence of breast cancer is presented among women over forty years [1, 2]; a potential reason is the cell genetic alterations accumulated over time, which may cause cancer [3]. Currently, mammography is the most used diagnostic technique worldwide due to its high sensitivity that even microcalcification detection is possible [4]. However, this technique has some disadvantages such as patient pain caused by breast pressing in the X-ray imaging procedure and a low specificity because 80% of cancer-diagnosed cases are negative [5–7]. The second most used technique is ultrasound, useful to differentiate between cystic and noncystic growths with the advantages of being a painless procedure suitable for repetitive explorations [6]. Magnetic resonance imaging, although highly sensitive, is expensive and almost exclusively used for certain clinical circumstances such as breast implants or suspected multifocal carcinoma [6]. These techniques are effective but have some weaknesses such as painful procedures, high-cost equipment, and their unavailability for certain marginalized areas in some developing countries. Therefore, new prebiopsy diagnostic techniques for global use have been developed in the last decades to reduce the number of patients undergoing an unnecessary biopsy procedure [5]. Some examples of these experimental techniques are microwave imaging [8], magnetic resonance elastography [9], thermography [10], and optical mammography [11]. All these techniques are still under study and continuous improvement, due to their limited success [12]. The experimental techniques based on

bioimpedance measurement have been of great interest in the last decades, mainly because of minimally invasive characteristic and low cost in comparison to those mentioned above. Research in this area has generated techniques such as electrical impedance tomography [13], electrical impedance spectroscopy [14], and electrical impedance mammography [15]. The basic of these techniques is the bioimpedance tissue characterization, which has shown by in vitro tests of breast tissues that the conductivity of a carcinoma can be 20 to 40 times greater than that corresponding to a healthy breast tissue [16]. Although very little in vivo work has been done, the existing studies have reported a certain degree of success in the experimentally obtained results, which encourage more bioimpedance research regarding breast carcinoma [6, 13, 17–20]. As the first experimental stage, newly proposed techniques for breast carcinoma detection are evaluated on testing models (phantom) before performing in vivo tests. Biological tissues of interest in the study (normal, benign, and malignant) are emulated within such testing models. Different manufacturing materials and textures for such breast phantoms have been reported [15, 21, 22]. A recent example is the work of Zhou et al. [22], where four silicone testing models are developed to evaluate the elastodigital image tomography technique for breast cancer detection.

Most of the reported works that use electrical impedance for the detection of breast cancer attempt to reconstruct anatomical images of the mammary tissues from bioimpedance measurements to establish the location of a possible cancerous tumor in the preclinical state (diameter less than or equal to 1 cm) [21, 23–27]. All of these works use surface electrodes, which are less invasive than needle electrodes, but their contact area is related to the contact impedance and the current density that is supplied. For example, microelectrodes have a higher contact impedance compared to electrodes of 1 cm in diameter and the current density in both cases is directly proportional to their surface area [28, 29]. The number of electrodes most used in a ring configuration is 16 or 32 [13, 23, 24], but there are also reported cases using 128 [25] or only 4 [26]. A great number of measuring electrodes, improving high resolution, are employed in some of these methodologies [25, 27] and large measuring electrodes, increasing the current density within the tissue, in others [26]. In both cases, an improvement in the detection of mammary carcinomas is sought. The electrical impedance measurements in Ybarra et al. [25] were performed through 128 stainless steel screws placed in a funnel-shaped plastic container with multiple ring arrangements. A solution was used to emulate the electrical properties of the breast and a cylinder (diameter: 1 cm; length: 5 cm) was placed to emulate a carcinoma. After using the reconstruction algorithm based on Distorted Born Iterative Method (DBIM), the resulting images show the location of the carcinoma in two different planes. Sadleir et al. in 2013 [26] designed a computational model for breast cancer detection based on electrical impedance and magnetic resonance imaging. The evaluation of the proposed technique was made using an agar phantom of the thoracic cavity that included the mammary gland and heart. Anatomical images were obtained

from impedance measurements through four large surface electrodes in a ring configuration, where the abnormalities (carcinomas) appear as white spots in a black and white image of the breast. On the other hand, Campisi et al. [27] used a flexible arrangement of 60 microelectrodes to acquire measurements of electrical impedance from agar phantoms emulating the mammary fat tissue. A one cubic centimeter malignant tumor emulator was inserted within these phantoms. The obtained images show the difference between "malignant tumor tissue" and "healthy tissue" but do not show the shape or position of the malignant tumor within the agar phantom. The main drawback in the reconstruction of anatomical images from electrical impedance measurements is the high number of electrodes needed to improve the image resolution and the high computational processing workload required to obtain an image showing the electrical distribution of biological tissues in concordance with mammary anatomy.

This paper describes a new electrical impedance-based methodology to establish the presence and location of an emulated carcinoma within a breast model elaborated in agar. The electrical impedance is measured through a ring arrangement of eight circular Ag/AgCl electrodes installed on a silicone brassiere-shaped mold, which is placed on the agar breast model. The fundamental idea of the proposed location algorithm, named Anomaly Tracking Circle algorithm, is to find the breast agar area defined by straight lines joining the electrode pairs having the minimum difference value of the defined normalized impedance magnitude along a measurement sweep. Such difference is obtained with respect to a breast agar phantom without carcinoma emulator. The proposed methodology is experimentally evaluated through seven breast agar phantoms, six of them having carcinoma lobe emulators with different locations and electrical conductivities.

2. Materials and Methods

In this investigation, surface electrodes were used because they are less invasive than needle electrodes. An arrangement of eight Ag/AgCl electrodes of 1 cm diameter uniformly distributed in a ring configuration was used for the electrical impedance measurement. Such configuration provides a uniform current distribution in the domain of interest with a low contact impedance in the skin-electrode interface, which helps to increase the measurement system sensitivity [28–31].

The electrodes were uniformly distributed in a ring arrangement and placed half height of a silicone mold with the shape of a cup A size brassiere (see Figure 1). The impedance measurement between each electrode pair was done using a bipolar topology because of its implementation simplicity, as well as that this topology is commonly used for in vivo tissue characterization [32, 33]. The electrodes were used dry; no type of gel was placed on the electrodes because the agar models already contain a certain degree of humidity, which reduces the contact impedance. In order to establish a correlation between the fixed electrode position and carcinoma emulator location within the breast-shaped agar
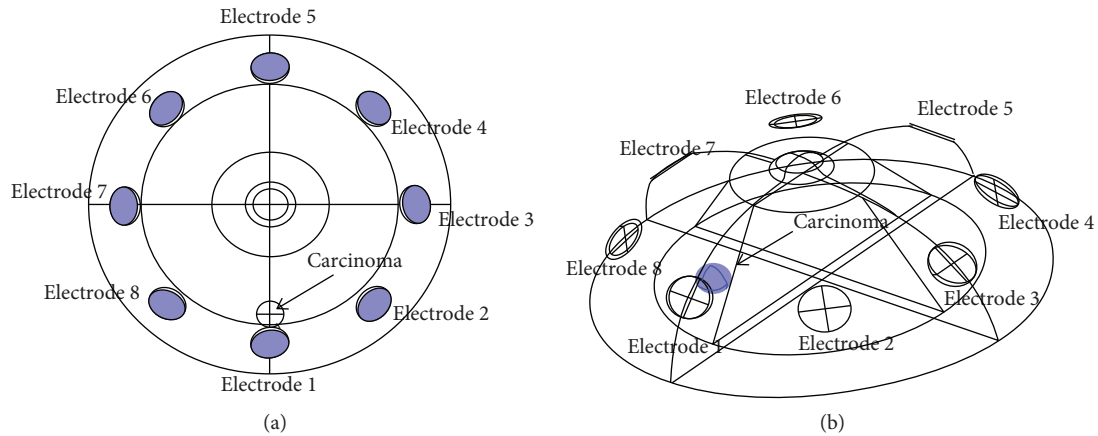
FIGURE 1: Geometric distribution and numbering of electrodes. (a) Front view. (b) 3D view.

phantom, the electrodes were numbered in counterclockwise order according to their position on the silicone mold (see Figure 1).

2.1. Measurement System. A block diagram of the measurement system is shown in Figure 2 consisting of the following components:

(1) Measuring electrodes: arrangement of eight circular Ag/AgCl electrodes of 1 cm diameter uniformly distributed in a ring configuration, which is inserted on a silicone mold with the shape of a cup A size brassiere

(2) Breast model: breast-shaped agar phantom containing the carcinoma emulator

(3) Multiplexer: electronic circuit selecting electrode pairs for synchronizing the impedance bipolar measurements along each measurement sweep

(4) Electrical impedance meter: LCR HiTester analyzer (manufacturer: Hioki; model: 3532-50) for measuring electrical impedance

(5) Data acquisition: computer that configures the electrical impedance meter and acquires the measured electrical impedance values

The multiplexer circuit plays a key role in the acquisition of impedance measurements, since it synchronizes the electrical impedance meter with each of the measuring electrode pairs. The multiplexer circuit was implemented as a microcontroller-embedded board (PIC16f887) and a switching system using sixteen high-frequency relays (HE3621A0510).

A systematized selection of electrodes was used in each measurement sweep. As a first step of each measurement sweep, the electrical impedance is measured between electrode 1 as current source and electrode 2 as current sink (electrical ground), the second electrical impedance measurement is made between electrode 1 as current source and electrode 3 as electrical ground, and so on in a counterclockwise

direction. The measurement sweep finishes when the seventh measurement is made, consisting of electrode 1 as current source and electrode 8 as electrical ground. The same procedure is applied to the following measurement sweeps, where for each one the current source is the counterclockwise next electrode. Hence, at the end, eight measurement sweeps, each one with seven electrical impedance measurements, are carried out. The electrical impedance is measured at four frequency values, then a total of 224 impedance measurement values is obtained for each agar model. The number assigned to the electrical impedance measurement for each electrode pair within a whole measurement set is shown in Table 1. The measurement numbering is helpful in the locating process of the carcinoma emulator.

2.2. Experimentation. Two main breast tissues (adipose and glandular) and carcinoma were considered in this study. The breast tissue and the carcinoma were emulated in the breast phantom by their corresponding reported conductivities. The conductivity values used in the experimentation stage were 0.225 S/m for the mammary gland, 0.023 S/m for subcutaneous fat (adipose tissue), and 1.125 S/m for carcinoma [26]. These values are similar to those used in frequencies ranging from 20 kHz [34] to 500 kHz [35].

The breast phantoms were made from a clinical breast mold, used for educative purposes (see Figure 3(a)). The breast tissues and carcinoma conductivities were emulated by agar and *NaCl* (see Figure 3(b)). The materials used were BD Bioxon agar (manufacturer: Becton Dickinson de México, SA de CV) with 99% purity, distilled water (manufacturer: Laboratorios PISA, SA de CV), and sodium chloride (manufacturer: Productos de Monterrey, SA de CV) with 99.99% purity. The emulators (adipose tissue, mammary gland, and carcinoma) were elaborated according to the Bennet formula [36]. The distribution of the mammary tissue emulators when manufacturing the breast agar phantom is shown in Figure 3(b). The silicone mold with measuring electrodes on the breast agar phantom is depicted in Figure 3(c). Seven different breast phantoms were developed for the experimental evaluation of locating the carcinoma emulators within the breast phantoms. Different locations and electrical
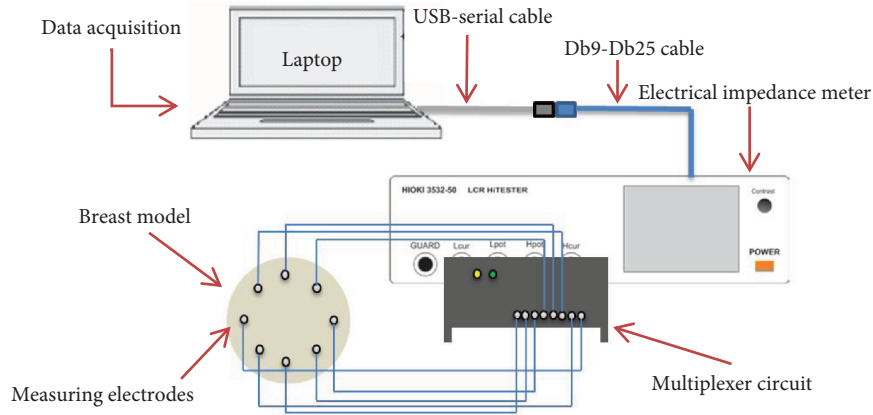
FIGURE 2: Block diagram of the measurement system.

TABLE 1: Assigned measurement number for electrode pairs within a whole measurement set.

Mn	Pe	Mn	Pe	Mn	Pe	Mn	Pe
1	1->2	15	3->4	29	5->6	43	7->8
2	1->3	16	3->5	30	5->7	44	7->1
3	1->4	17	3->6	31	5->8	45	7->2
4	1->5	18	3->7	32	5->1	46	7->3
5	1->6	19	3->8	33	5->2	47	7->4
6	1->7	20	3->1	34	5->3	48	7->5
7	1->8	21	3->2	35	5->4	49	7->6
8	2->3	22	4->5	36	6->7	50	8->1
9	2->4	23	4->6	37	6->8	51	8->2
10	2->5	24	4->7	38	6->1	52	8->3
11	2->6	25	4->8	39	6->2	53	8->4
12	2->7	26	4->1	40	6->3	54	8->5
13	2->8	27	4->2	41	6->4	55	8->6
14	2->1	28	4->3	42	6->5	56	8->7

Mn = measurement number; Pe = pair of electrodes.

conductivities of the carcinoma emulator were implemented in each breast agar phantom.

The manufacturing conditions for the seven breast models were

(1) breast agar phantom without any carcinoma emulator

(2) an amorphous carcinoma emulator with a diameter of approximately 1.2 cm inserted on the breast agar phantom near electrode 1

(3) an amorphous carcinoma emulator with a diameter of approximately 1 cm located on the breast agar phantom near electrode 7

(4) one 1.5 cm diameter carcinoma emulator fragmented (diameter less than 0.3 cm) and placed on the breast agar phantom area between electrodes 5 and 6

(5) one amorphous carcinoma with a maximum diameter of 2 cm inserted in the center of the breast agar phantom, in the same plane as electrode 1

(6) one amorphous carcinoma of approximately 1 cm, maximum diameter, having a conductivity value of 30% of that reported in references [26], placed on the breast agar phantom near electrode 1

(7) one amorphous carcinoma of approximately 1 cm, maximum diameter, with an electrical conductivity of 70% higher than that reported in [26], inserted on the breast agar phantom near electrode 1

In the experimental evaluation, the electrical impedance was measured by injecting a fixed alternating current of $60 \mu A$ peak to peak to the breast model and a maximum variable voltage of 2 volts, which are safe values for measurements on humans according to the IEC/TS 60479-1 standard [37]. The electrical impedance measurements were done at four frequency values (500 Hz, 1 kHz, 5 kHz, and 10 kHz). The measurement time for each frequency was approximately three minutes, and the total time was approximately twelve minutes for the four frequencies in each breast model (224 measurements).
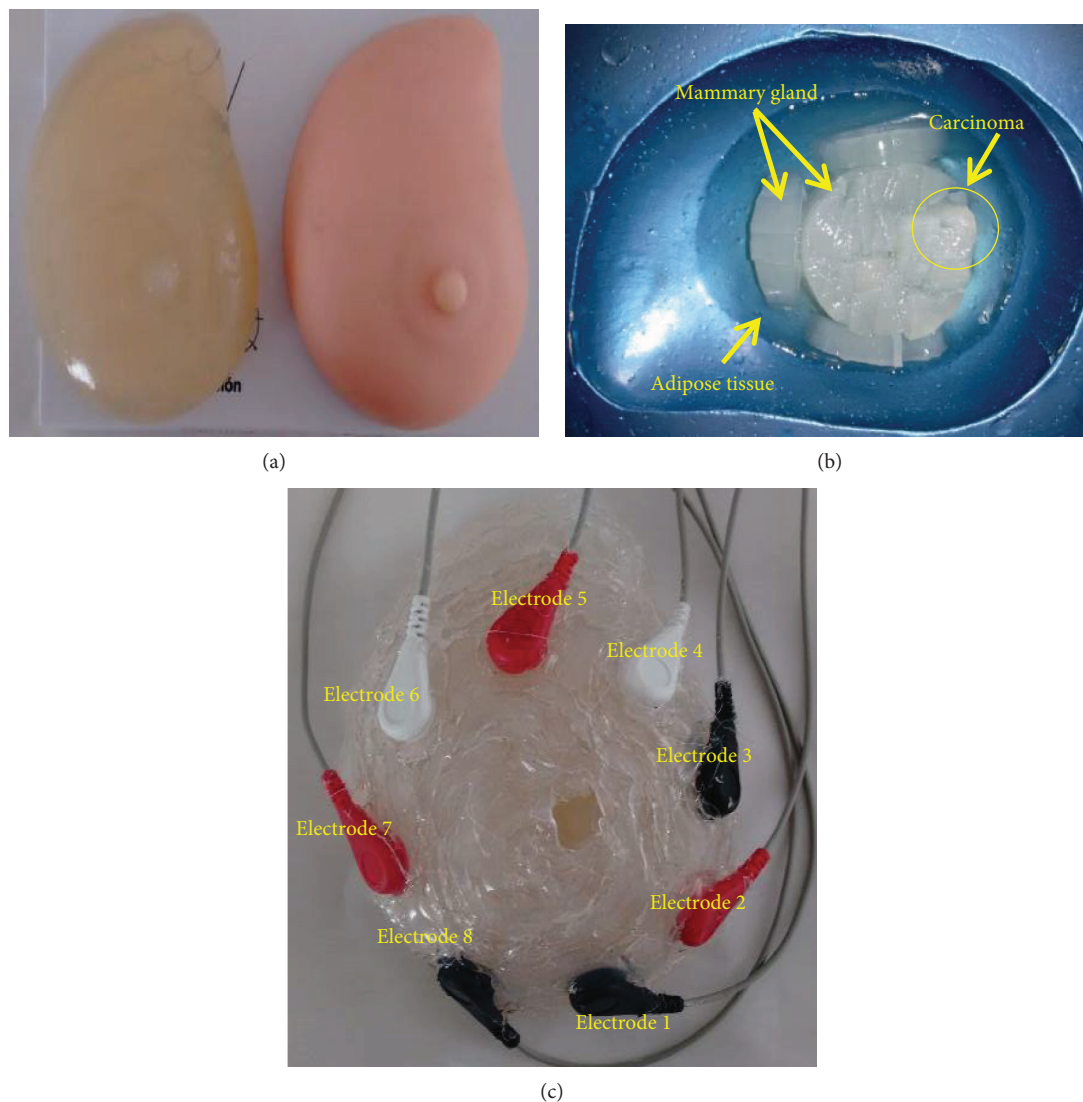
(a)

(b)

(c)

FIGURE 3: Experimental prototypes. (a) Breast-shaped agar phantom containing the carcinoma emulator (left) and clinical breast mold (right). (b) Distribution of breast tissues and carcinoma emulators. (c) Silicone mold with measuring electrodes on the breast agar phantom.
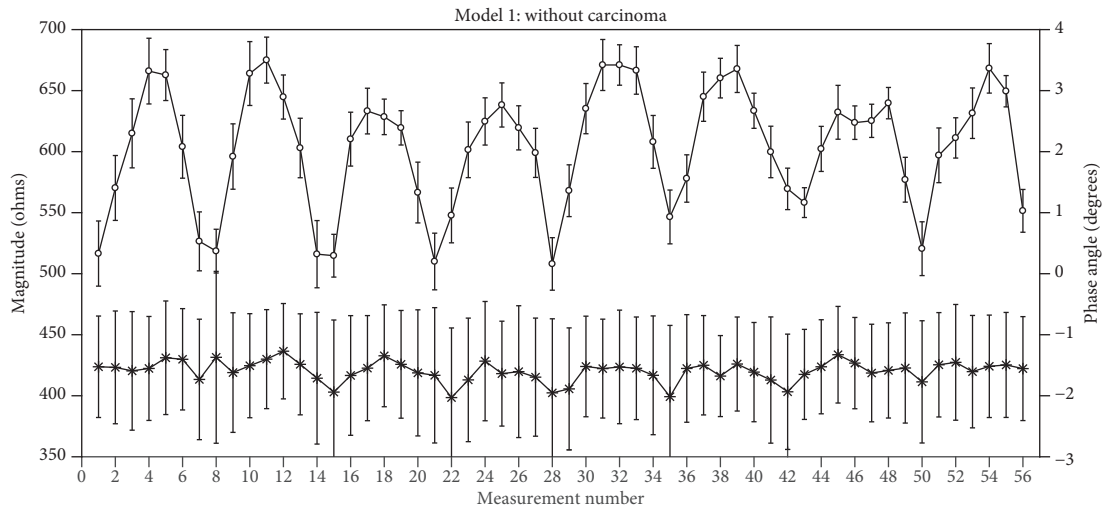
3. Results

From the impedance magnitude values measured at the four defined frequencies, close values were observed for each electrode pair, due to the minimum variation in conductivity with respect to frequency [38]. Then the impedance magnitude average along the frequency values for each electrode pair was considered in the proposed analysis. The average and standard deviations of the impedance magnitude, as well as the phase, obtained along the defined frequency values for each electrode pair are depicted in Figure 4, each corresponding to the analyzed breast models.

In order to find a specific characteristic behavior of the electrical impedance for the considered breast models, an analysis of the average and standard deviations of the obtained impedance magnitude and phase data was done. As can be seen, the average impedance magnitude shows some behavior among the seven breast models, which may be potentially useful to distinguish the condition of the breast agar phantom. On the other hand, average impedance phase does not show any characteristic behavior that may be related to the presence of the carcinoma emulator. Therefore, the carcinoma emulator location research is focused on impedance magnitude analysis. In order to make a dimensionless analysis of the impedance magnitude, a centered and whitened normalization is applied by the following equation:

$$N(x_i) = \frac{x_i - \mu(C_z(x))}{\text{std}(C_z(x))}, \quad 1 \le i \le 56, \quad (1)$$

where $N(x_i)$ is the resulted normalized value of the impedance magnitude measurement x_i, the operator μ represents the mean function, $C_z(x)$ is the set of impedance magnitude measured along the measurement sweep, and the operator std is the standard deviation function. The proposed analysis is based on obtaining the normalized impedance
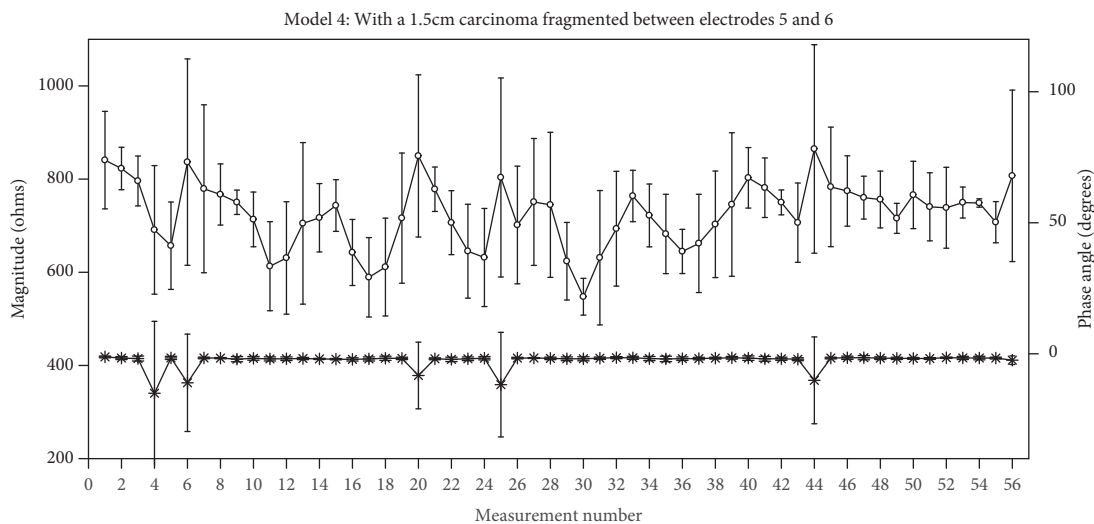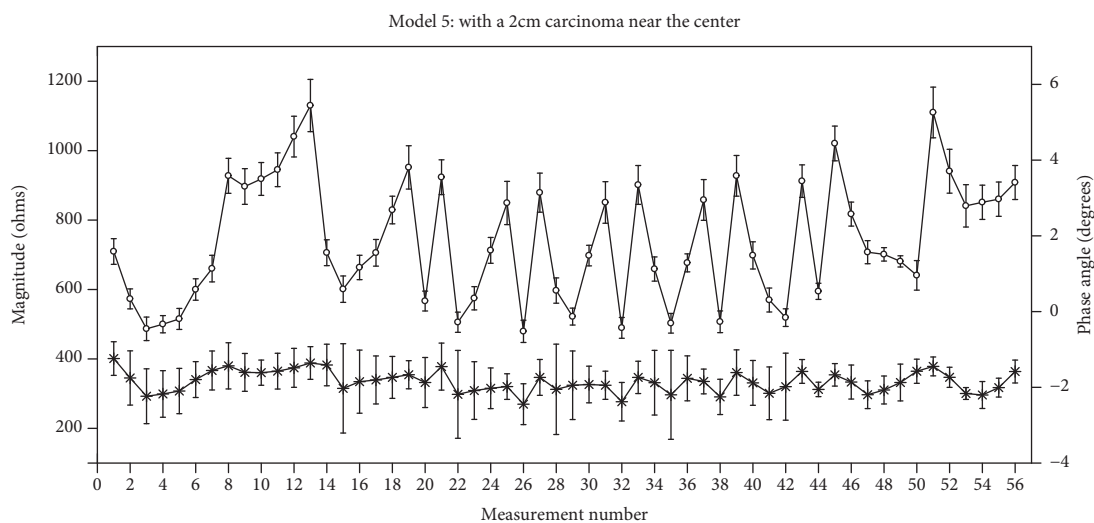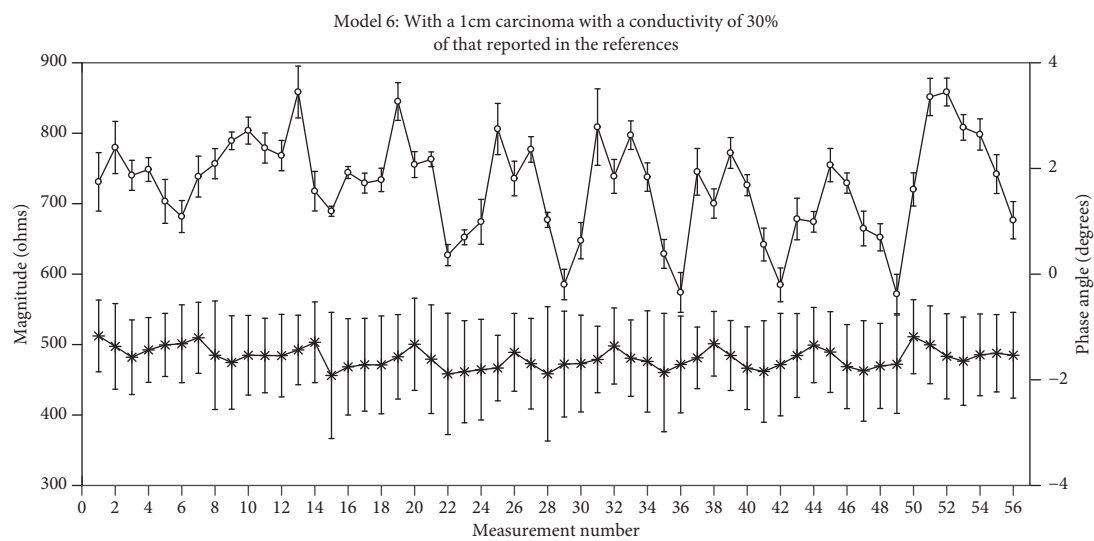
(a)

(b)

(c)

Figure 4: Continued.

Model 4: With a 1.5cm carcinoma fragmented between electrodes 5 and 6

(d)

Model 5: with a 2cm carcinoma near the center

(e)

Model 6: With a 1cm carcinoma with a conductivity of 30%
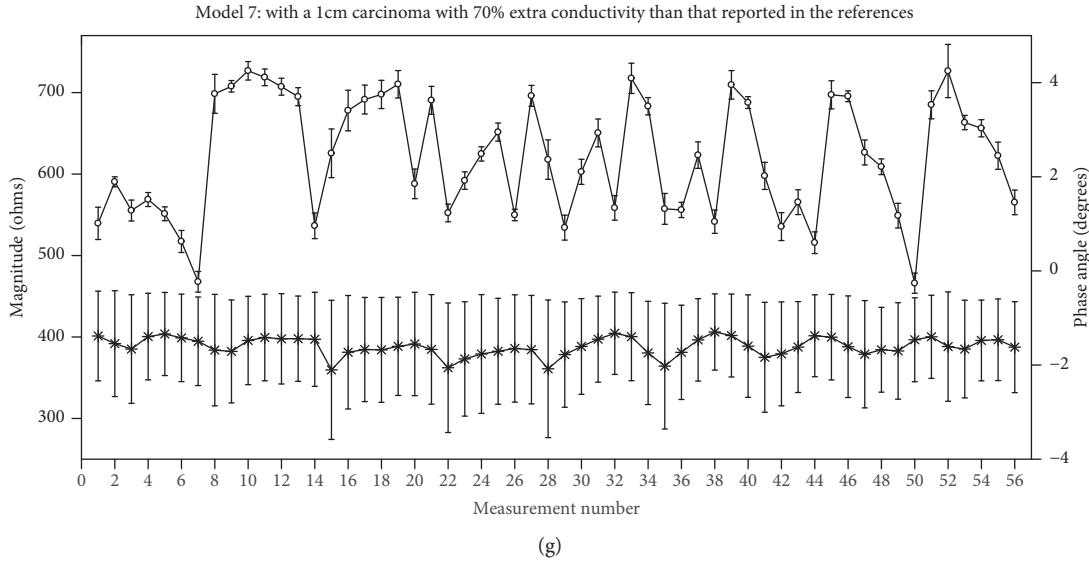of that reported in the references
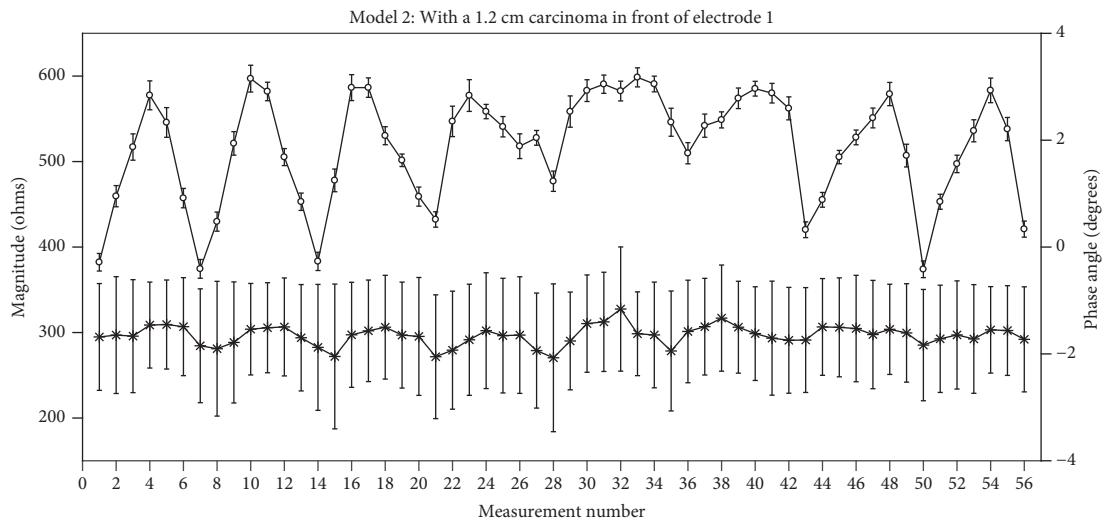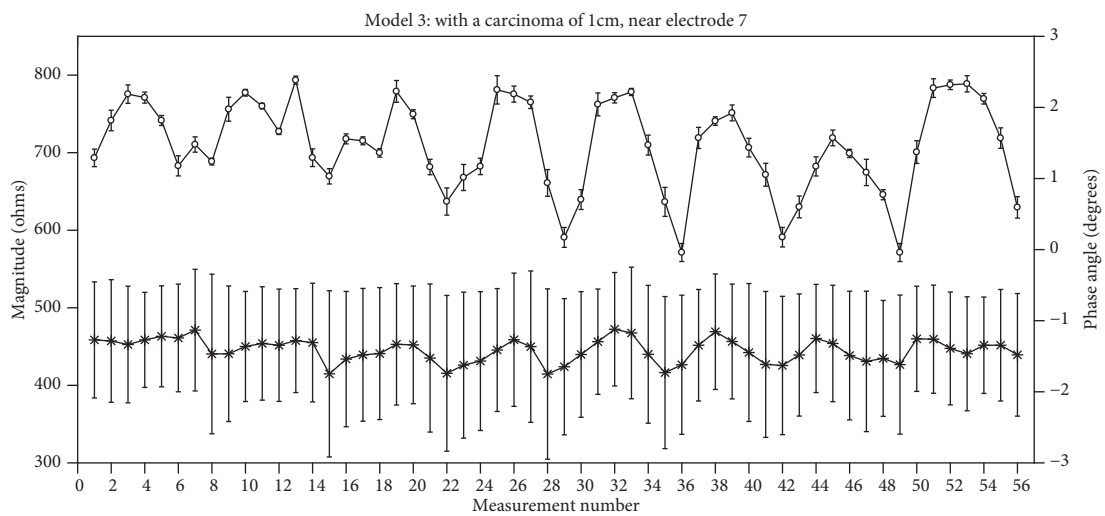
(f)

FIGURE 4: Continued.

Figure 4: Obtained average impedance magnitude (white circles) and phase angle (asterisks) from studied breast models.

magnitude difference between the studied breast model and the breast model without any carcinoma emulator:

$$\mathrm{DN}(x_i) = N_k(x_i) - N_B(x_i), \tag{2}$$

where $\mathrm{DN}(x_i)$ is the algebraic difference, $N_k(x_i)$ is the normalized impedance magnitude corresponding to the kth breast model under study, and $N_B(x_i)$ is the normalized impedance magnitude of the model without carcinoma emulator.

The six breast models containing carcinoma emulator were considered as study cases in the analysis process. The obtained difference of normalized impedance magnitudes for each one of the study cases is depicted in Figure 5. The results labeled as "With carcinoma" in Figure 5 represent the algebraic difference of the normalized impedance magnitude between the measurement corresponding to the breast model under study and the breast model without carcinoma emulator (equation (2)). Hence, such plots show those measurements having a higher or lower normalized impedance magnitude value than the corresponding to the model without the emulator carcinoma. This analysis was proposed as a mean of comparison based on a threshold value defined by the model without carcinoma. In this way, small difference values could indicate the presence of a carcinoma emulator because low impedance is related to the relatively high conductivity of the carcinoma.

The correlation between the obtained normalized impedance magnitude difference and the actual location of the carcinoma emulator on the breast agar phantom was figured out through a developed algorithm, named Anomaly Tracking Circle (ATC). This algorithm obtains for each electrode the electrode pair having the lowest value of normalized impedance magnitude difference within a measurement sweep. This means that for a given electrode the electrode pair with the minimum value of the normalized impedance magnitude difference, with respect to the other seven electrodes, is obtained by the ATC algorithm. For

instance, the resulted electrode pairs for the measurement sweep of electrode 5 in model 3 are composed of the electrode pairs E5-E6, E5-E7, E5-E8, E5-E1, E5-E2, E5-E3, and E5-E4, where the lowest value corresponds to the pair E5-E7. For each electrode, an electrode pair having the minimum value resulted. The total result for each model is eight electrode pairs, which are graphically depicted by straight lines joining the corresponding electrode positions.

The resulted straight lines for model 3 are shown in Figure 6(a), where the actual location of the carcinoma emulator is represented by a dotted circle. In general, the resulted straight lines may cross each other, or two lines may coincide when a double minimum is found in a measurement sweep. The obtained electrode pairs with the minimum values for model 3 are E1-E6, E2-E6, E3-E7, E4-E7, E5-E7, E6-E7, E7-E5, and E7-E6. The pairs of electrodes E7-E5 and E5-E7 are represented by the same straight line because it is an electrodes pair with a minimum value in the two measurements: one from electrode 5 to electrode 7 and another from electrode 7 to electrode 5.

The centroid of the straight line intersections defines a low-impedance area within the breast agar phantom, which is used to determine the presence of a carcinoma emulator and its location with respect to the position of the electrodes. The straight line intersections as well as the obtained centroid for breast model 3 are depicted as asterisks and solid circle, respectively, in Figure 6(b). As the figure shows, the obtained centroid is very near to the actual location of the carcinoma emulator.

The ATC algorithm was applied to the considered breast models; the obtained results for breast models 2, 4, 5, 6, and 7 are presented in Figure 7. According to the obtained results from most of the breast models, a good location approximation to the actual locations of the inserted carcinoma emulators is achieved by the proposed ATC algorithm. The obtained emulator location for breast model 6 is far from the actual one. An explanation for this result is that the
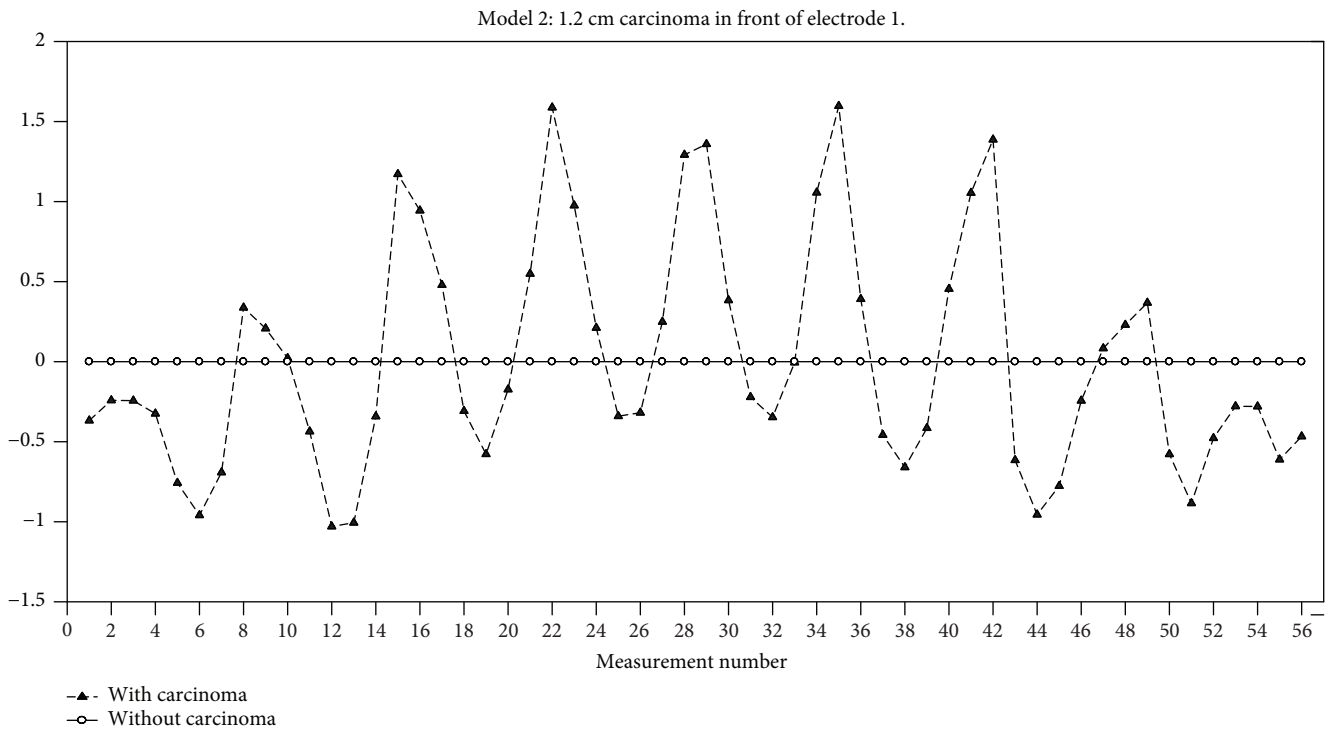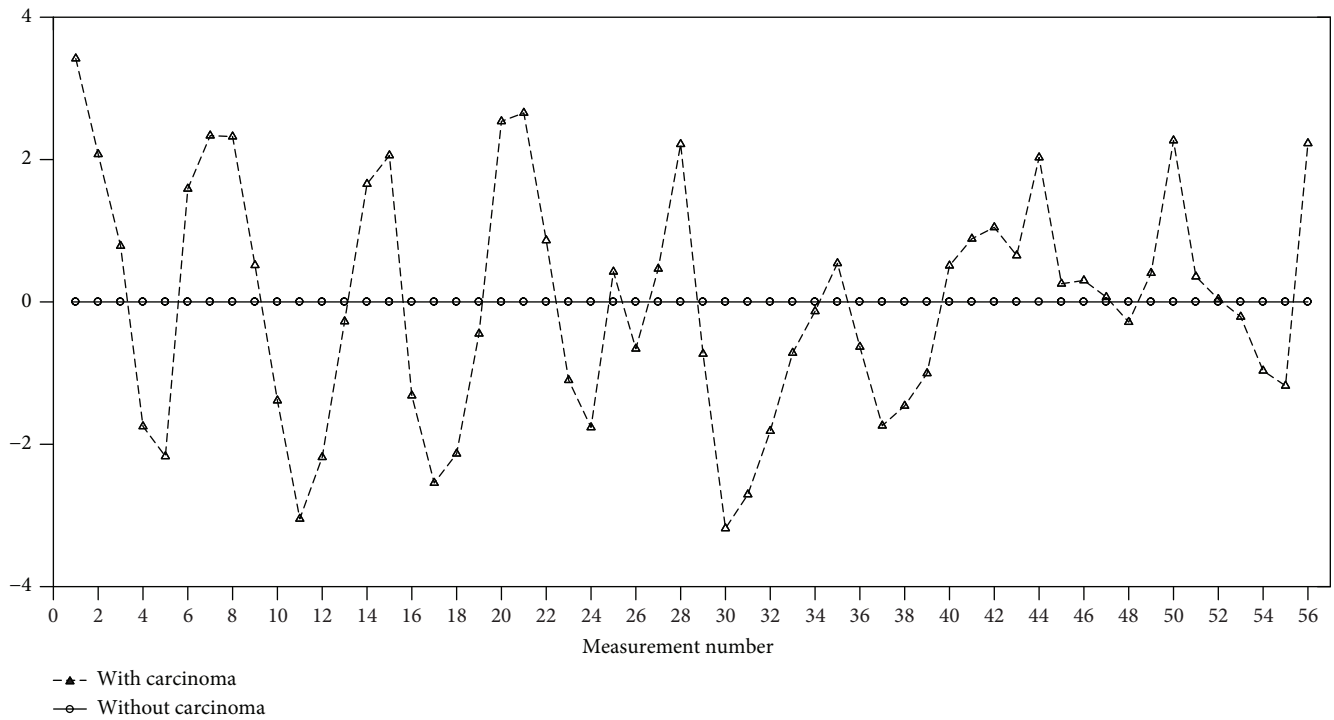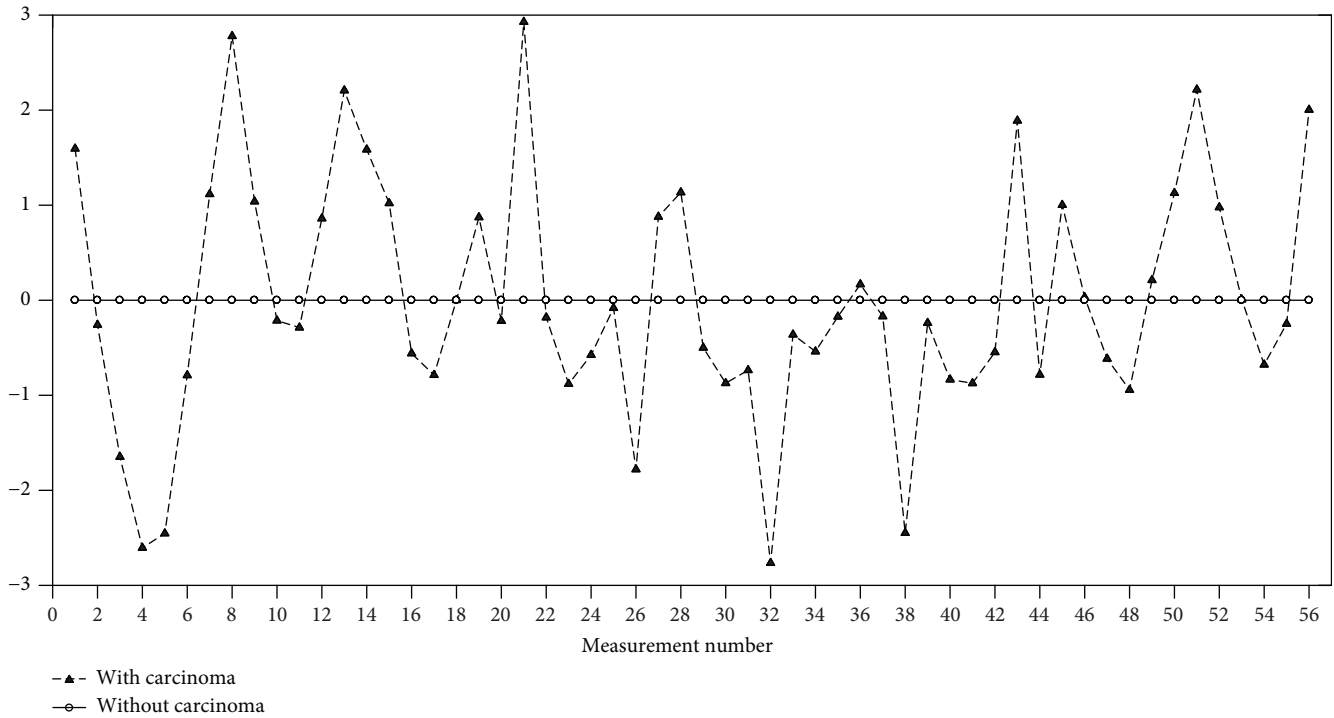
(a)
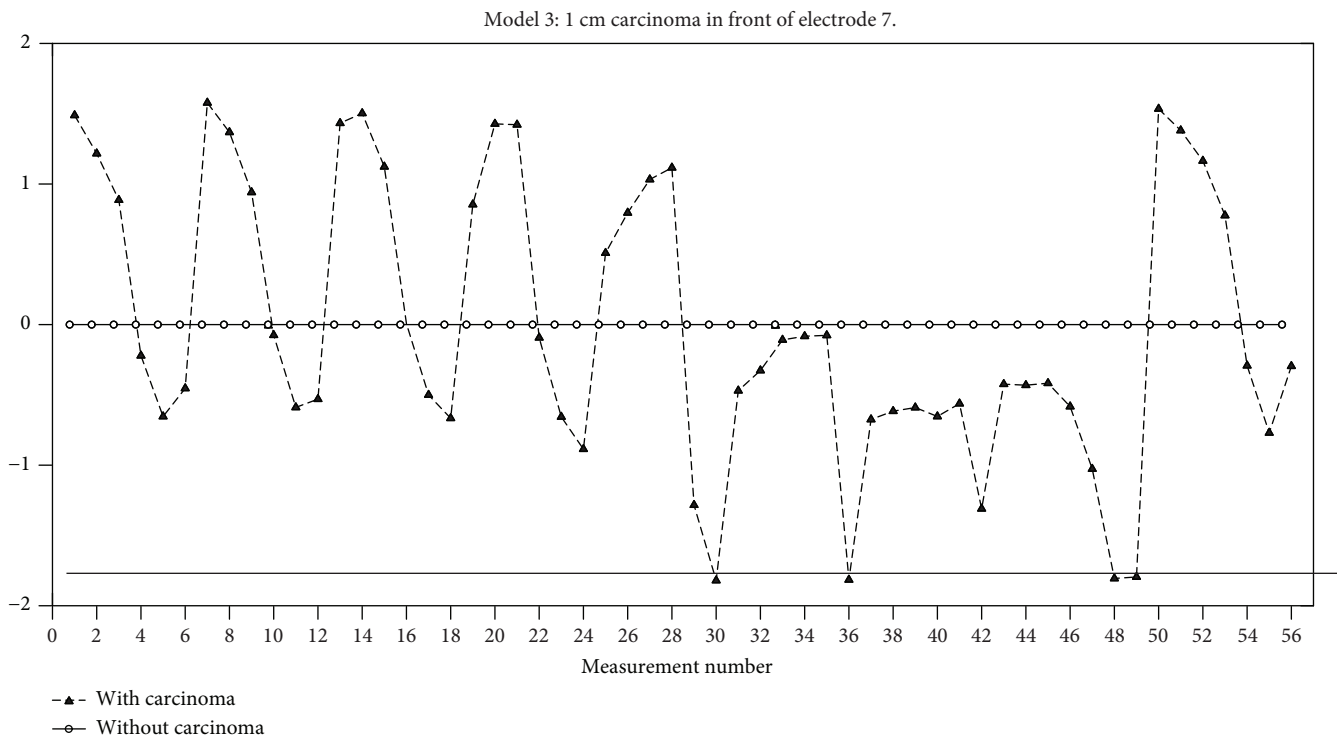
(b)

Figure 5: Continued.

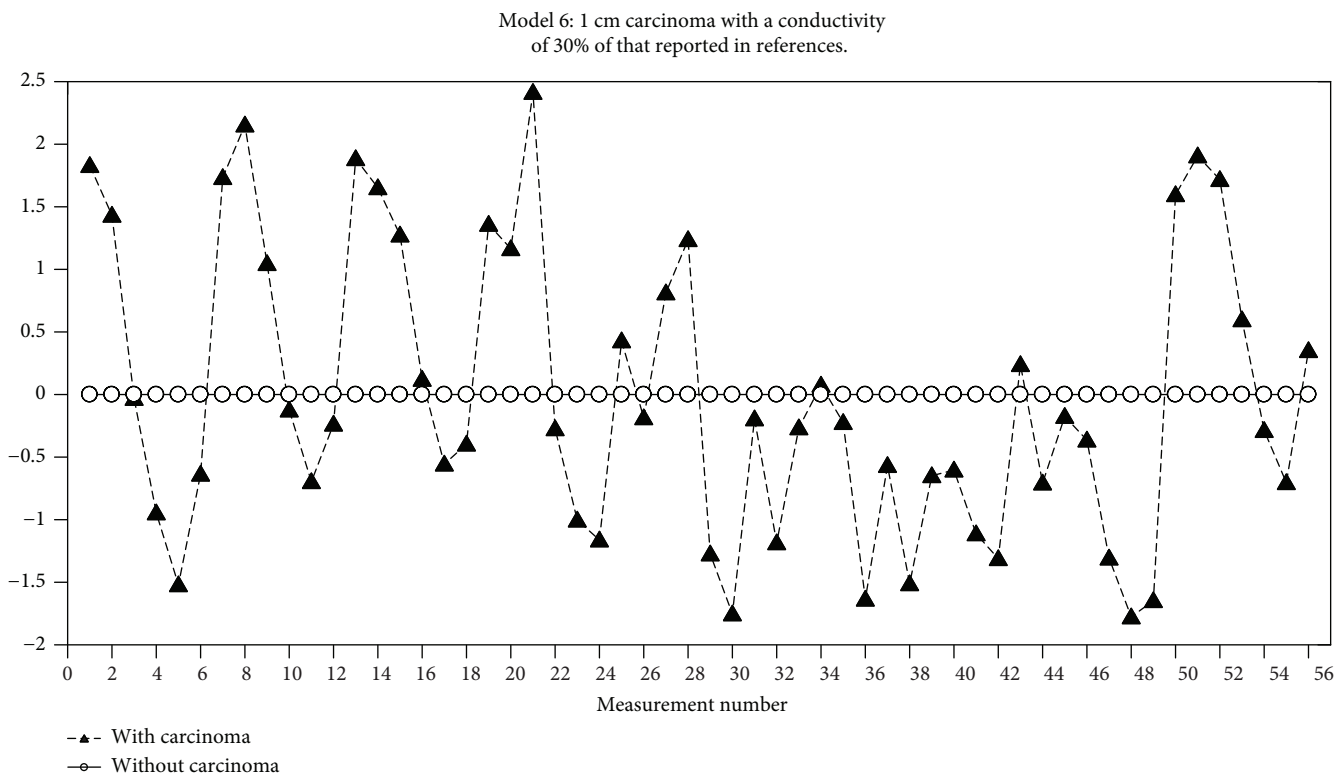Model 4: 1.5 cm carcinoma fragmented between electrodes 5 and 6.

-▲- With carcinoma
-o- Without carcinoma

(c)

Model 5: 2 cm carcinoma close to the center.

-▲- With carcinoma
-o- Without carcinoma

(d)

Figure 5: Continued.

Model 6: 1 cm carcinoma with a conductivity
of 30% of that reported in references.

- ▲ - With carcinoma
- ○ - Without carcinoma

(e)

Model 7: 1 cm carcinoma with 70 % extra conductivty than that reported in the references.

- ▲ - With carcinoma
- ○ - Without carcinoma
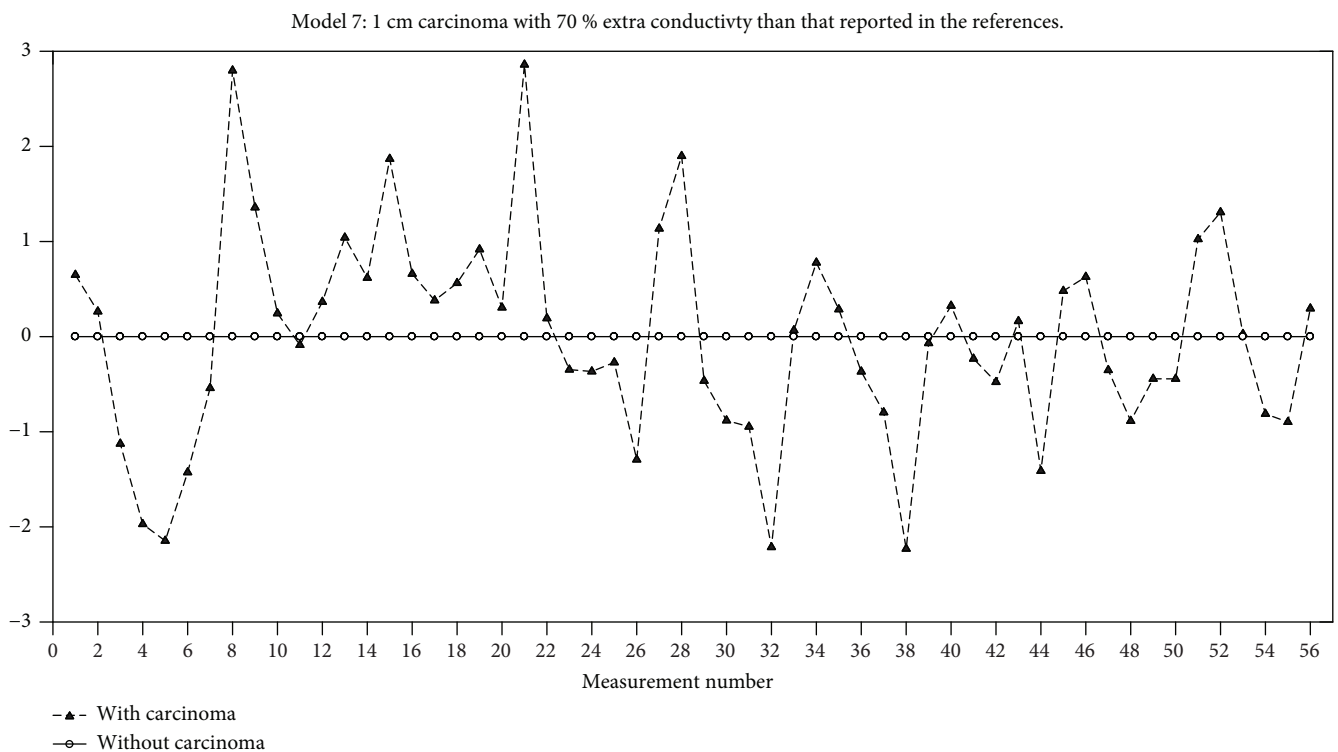
(f)

FIGURE 5: Impedance magnitude normalization for breast models with carcinoma emulators.

chosen emulator conductivity value for this breast model is much smaller than that corresponding to a carcinoma, being close enough to the mammary gland conductivity. This makes the impedance magnitude difference small enough that is not possible to distinguish the carcinoma emulator from the breast agar phantom.

Model 3: 1cm carcinoma in front of electrode 7

Model 3: 1cm carcinoma in front of electrode 7

(a)

(b)
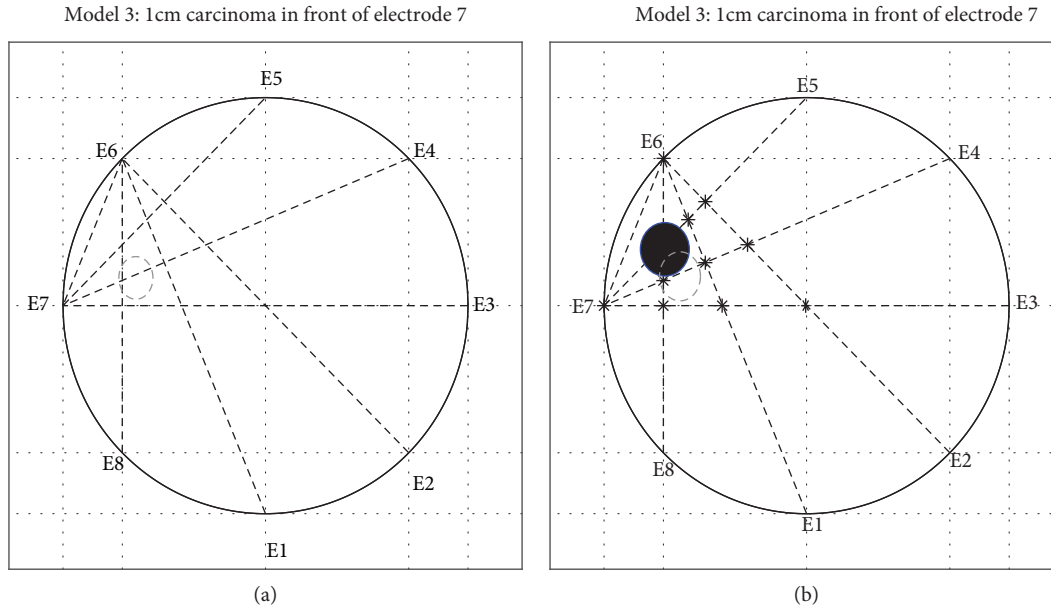
FIGURE 6: ATC algorithm applied to breast model 3. (a) Resulted straight lines joining electrodes with minimum impedance magnitude (dotted lines) and actual location of the carcinoma emulator (dotted circle). (b) Centroid (solid circle) of the straight line intersections (asterisks).

4. Discussion

In the studied cases, the conductivity is controlled by some specific quantity of saline solution in the agar model, where the contact impedance is negligible, and thus, the electrode polarization impedance effect is minimal in the analyzed frequency range [38]. Therefore, the impedance measurements are mainly affected by the distribution of the conductivities of the tissues and carcinoma emulators, as well as by the shape of the breast agar model described in Experimentation.

The carcinoma in breast model 4 was emulated as a fragmentized structure having the largest fragments within the area limited by electrodes 5 and 6, and small ones scattered throughout the agar model. The small fragments caused abrupt changes in the impedance magnitude measurements along the measurements sweeps, meaning large values of the standard deviation for this model (see Figure 4). In this case, the location obtained by the ATC algorithm is given by the largest fragments' position within the agar model.

From the analyzed breast models, the described method can locate preclinical-emulated carcinomas with an 83% success. The breast model 6 is the only case in which the ATC algorithm could not locate the location of the carcinoma emulator. The obtained result for this case may be due to following factors: (1) the chosen conductivity for the carcinoma emulator in this breast model is 0.3375 S/m, which is close enough to the corresponding conductivity of the mammary gland (0.225 S/m). (2) In this case, the location of the carcinoma emulator covers part of the mammary gland. (3) The shape of the breast model is based on an anatomic breast mold, which means a larger agar volume in the lower quadrants of the breast model, increasing in this way the impedance.

There are some limitations in the proposed methodology that must be addressed for future clinical application. The first of these limitations is the definition of a procedure for obtaining a healthy breast reference model (base case), which is required by the ATC algorithm to obtain better results. One of the procedures could be to take the normalized impedance magnitude difference between both breasts of the same patient. Another potential solution, for this limitation, could be the use of a measurement database of healthy participants to define the reference case, where the participant sample meets characteristics affecting the impedance magnitude measurements, such as breast size and subject population.

Another current limitation is the time of 12 minutes for a whole measurement electrode sweep. For this long period, participant's movements are very probable to happen, affecting the impedance measurements due to possible missing electrode contacts. In order to reduce the movement probability, the total time for measuring the whole set of electrodes is planned to be reduced. This can be achieved by increasing the data transfer speed in the device communication and by reducing the measurement time for each measurement sweep, obtaining in this way a more appropriate measurement time for a real clinical scenario. Before the application in a real clinical scenario, several experimental tests must be conducted to define the best reference case and the appropriate measurement time.

No type of gel was placed on the electrodes because the agar models already contain a certain degree of humidity, which reduces the contact impedance. On the other hand, for experimental clinical trials, it is highly recommended to use some conductive gel in order to reduce the impedance effect in the electrode-skin contact [39]. Keeping that in mind, the selected electrodes for experimental clinical trials have a layer of electrolyte on the surface of the conductive metal (Ag/AgCl), which helps to attenuate the electrolytic
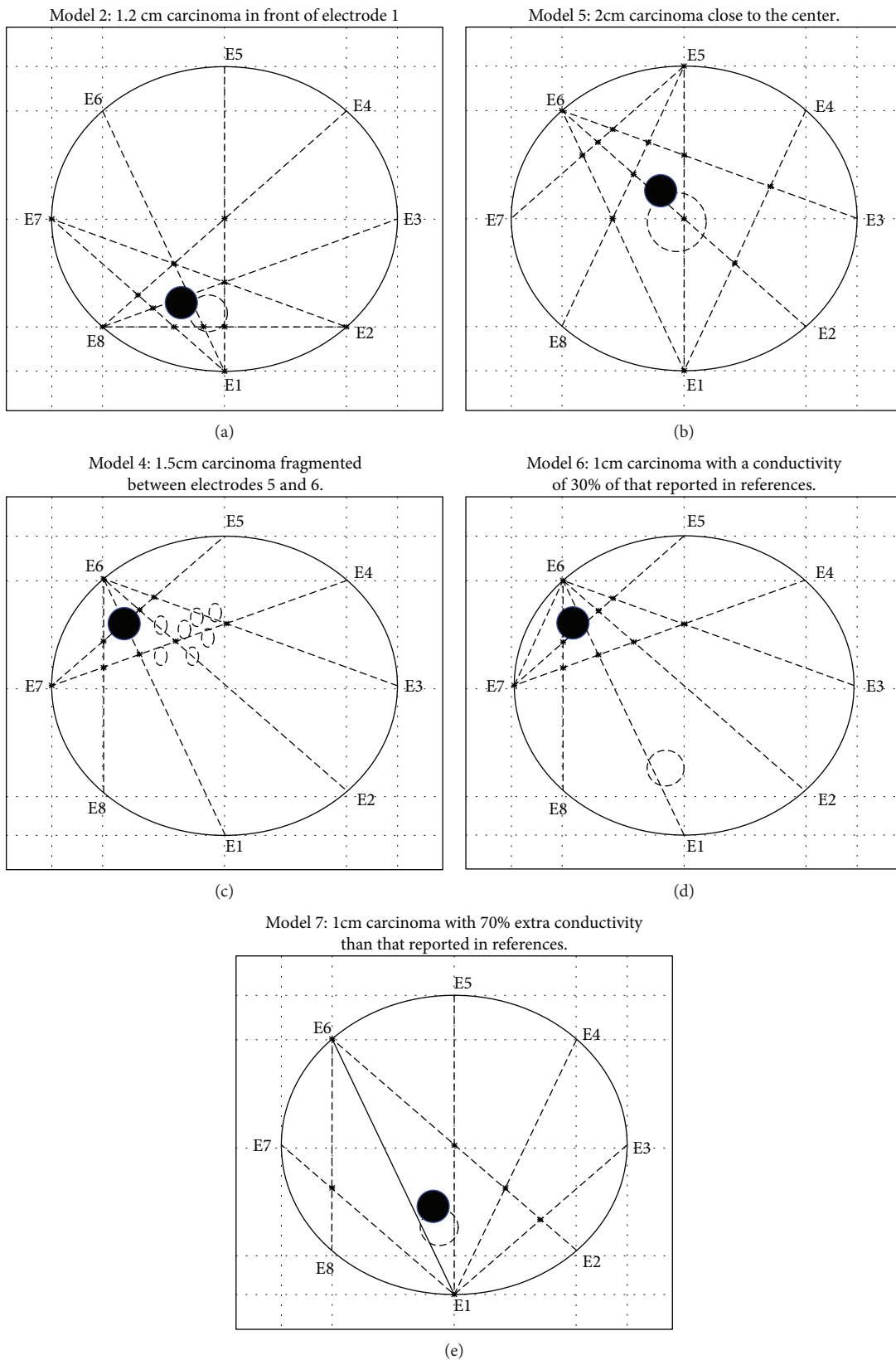
(a)

(b)

(c)

(d)

(e)

Figure 7: ATC algorithm applied to breast models 2, 4, 5, 6, and 7, where solid and dotted circles represent the resulting and actual location, respectively, of the carcinoma emulator.

composition between the outer and inner skin layers [40]. This characteristic is appropriate for the final application in breast tissues, and the selected ring configuration of uniformly distributed electrodes allows a good spatial distribution around circular volumes in the breast carcinoma-locating process [41, 42].

Finally, the definition of specificity and sensitivity of the proposed method is planned to be achieved in a validation stage with real breast tissue results obtained through experimental clinical trials. The validation procedure is planned through result comparison with mammography or ultrasound techniques [43–47].

5. Conclusions

This paper describes a methodology for the location of a carcinoma emulator in preclinical state in breast agar phantoms, which are an approximation of the electrical behavior in real breast tissue [26, 35]. The method is based on measurements of the electrical impedance through eight Ag/AgCl electrodes uniformly distributed in a ring configuration. A proposed Anomaly Tracking Circle algorithm processes the measured impedance magnitude to generate a circular impedance map that indicates the location of a region of lower impedance related to the presence of a carcinoma emulator.

The used normalization of the impedance magnitude allowed an information analysis focused on measurement behavior on a model with carcinoma with respect to the one without carcinoma. Hence, the ATC is a new way to visualize the potential existence of a carcinoma in preclinical state with less computational processing because a complete reconstruction of conductivity distribution within the agar model is avoided.

The proposed ATC algorithm computed the location of carcinoma emulators inserted in six experimental breast models with an 83.33% success. The failure case (breast model 6) was mainly due to the considered low conductivity value of the inserted carcinoma emulator, which was 30% smaller than that reported for real carcinoma.

The implemented measurement system is simple and worked correctly, which allows systematized measurements of the electrical impedance. In addition, it is portable and can be used several times in multiple experimental models. Also, some of the limitations of this methodology can be improved for better performance in clinical trials. On the other hand, the considered values of frequency range and electrical currents are not harmful to tissues [37] and previous work has indicated the possibility of differentiating breast lesions at low frequencies [5]. Therefore, the presented results in this paper suggest that the ATC algorithm may be used as a carcinoma location tool in clinical trials.

In order to use the proposed methodology as a clinical method for locating breast carcinomas, a validation stage through experimental clinical trials is required. Currently, authors are developing a clinical protocol in collaboration with a health center, focused on further research of the proposed methodology to be expanded as a bioimpedance measurement technique for the detection and location of breast carcinomas. Another characteristic of the proposed methodology is that sophisticated instruments are not required in the prediagnosis of breast cancer; in this way, it would reach rural areas without access to other breast evaluation techniques than clinical evaluation by mammary palpation in medical centers or breast self-examination.

Data Availability

The Matlab code of the developed Anomaly Tracking Circle algorithm as well as the measured electrical impedance magnitude and phase data for the seven breast models described in this paper are available in the following link: https://drive.google.com/open?id=1ELpBvs3-C8n-lzpxtxJSzJigaT2Fktei.

Conflicts of Interest

The authors declare that there is no conflict of interest regarding the publication of this paper.

Acknowledgments

References

[1] American Cancer Society, "Cancer treatment and Survivorship facts & figures 2014-2015," *Atlanta: American Cancer Society*, 2014.

[2] M. J. Horner, L. Ries, M. Krapcho et al., *SEER Cancer Statistics Review (1975-2006)*, National Cancer Institute, Bethesda, MD, 2009, https://seer.cancer.gov/csr/1975_2006/.

[3] J. R. Goldblum and S. W. Weiss, *Soft Tissue Tumors*, Mosby, 2008.

[4] A. H. Israyelyan, *The Development of Molecular Diagnostics for Breast Cancer, [LSU Master's Thesis]*, p. 3503, LSU Digital Common, 2003.

[5] Y. Zou and Z. Guo, "A review of electrical impedance techniques for breast cancer detection," *Medical Engineering & Physics*, vol. 25, no. 2, pp. 79–90, 2003.

[6] B. Gowry, A. B. Shahriman, and M. Paulraj, "Electrical bio-impedance as a promising prognostic alternative in detecting breast cancer: a review," in *2015 2nd International Conference on Biomedical Engineering (ICoBE)*, pp. 1–6, Penang, Malaysia, March 2015.

[7] R. P. Burns, "Image-guided breast biopsy," *The American Journal of Surgery*, vol. 173, no. 1, pp. 9–11, 1997.

[8] E. C. Fear, S. C. Hagness, P. M. Meaney, M. Okoniewski, and M. A. Stuchly, "Enhancing breast tumor detection with near-field imaging," *IEEE Microwave Magazine*, vol. 3, no. 1, pp. 48–56, 2002.

[9] E. E. Van Houten, M. M. Doyley, F. E. Kennedy, J. B. Weaver, and K. D. Paulsen, "Initial in vivo experience with steady-state subzone-based MR elastography of the human breast," *Journal of Magnetic Resonance Imaging*, vol. 17, no. 1, pp. 72–85, 2003.

[10] E. Y. K. Ng and S. C. Fok, "A framework for early discovery of breast tumor using thermography with artificial neural

network," *The Breast Journal*, vol. 9, no. 4, pp. 341–343, 2003.

[11] D. Grosenick, K. T. Moesta, H. Wabnitz et al., "Time-domain optical mammography: initial clinical results on detection and characterization of breast tumors," *Applied Optics*, vol. 42, no. 16, pp. 3170–3186, 2003.

[12] E. Y. K. Ng, S. V. Sree, K. H. Ng, and G. Kaw, "The use of tissue electrical characteristics for breast cancer detection: a perspective review," *Technology in Cancer Research & Treatment*, vol. 7, no. 4, pp. 295–308, 2008.

[13] T. E. Kerner, K. D. Paulsen, A. Hartov, S. K. Soho, and S. P. Poplack, "Electrical impedance spectroscopy of the breast: clinical imaging results in 26 subjects," *IEEE Transactions on Medical Imaging*, vol. 21, no. 6, pp. 638–645, 2002.

[14] B. Singh, C. W. Smith, and R. Hughes, "In vivo dielectric spectrometer," *Medical and Biological Engineering and Computing*, vol. 17, no. 1, pp. 45–60, 1979.

[15] A. Zarafshani, T. Bach, C. R. Chatwin, S. Tang, L. Xiang, and B. Zheng, "Conditioning electrical impedance mammography system," *Measurement*, vol. 116, pp. 38–48, 2018.

[16] K. F. Foster and H. P. Schwan, "Electric properties of tissues and biological materials: a critical review," *Critical Reviews in Biomedical Engineering*, vol. 17, pp. 25–104, 1989.

[17] G. S. Sarode, S. C. Sarode, M. Kulkarni, S. Karmarkar, and S. Patil, "Role of bioimpedance in cancer detection: a brief review," *International Journal of Dental Science and Research*, vol. 3, no. 1, pp. 15–21, 2016.

[18] T. Morimoto, Y. Kinouchi, T. Iritani et al., "Measurement of the electrical bio-impedance of breast tumors," *European Surgical Research*, vol. 22, no. 2, pp. 86–92, 1990.

[19] T. Morimoto, S. Kimura, Y. Konishi et al., "A study of the electrical bio-impedance of tumors," *Journal of Investigative Surgery*, vol. 6, no. 1, pp. 25–32, 2009.

[20] A. Stojadinovic, A. Nissan, Z. Gallimidi et al., "Electrical impedance scanning for the early detection of breast cancer in young women: preliminary results of a multicenter prospective clinical trial," *Journal of Clinical Oncology*, vol. 23, no. 12, pp. 2703–2715, 2005.

[21] L. S. Solanki, S. Singh, and D. Singh, "Development and modelling of the dielectric properties of tissue-mimicking phantom materials for ultra-wideband microwave breast cancer detection," *Optik*, vol. 127, no. 4, pp. 2217–2225, 2016.

[22] C. Zhou, J. G. Chase, H. Ismail et al., "Silicone phantom validation of breast cancer tumor detection using nominal stiffness identification in digital imaging elasto-tomography (DIET)," *Biomedical Signal Processing and Control*, vol. 39, pp. 435–447, 2018.

[23] D. Chakraborty, M. Chattopadhyay, and R. Bhar, "Resistivity imaging of a phantom with irregular inhomogeneities with 32 silver electrodes based sensory system in two dimensional electrical impedance tomography," *Procedia Technology*, vol. 10, pp. 191–199, 2013.

[24] R. Kusche, A. Malhotra, M. Ryschka, G. Ardelt, P. Klimach, and S. Kaufmann, "A FPGA-based broadband EIT system for complex bioimpedance measurements—design and performance estimation," *Electronics*, vol. 4, no. 3, pp. 507–525, 2015.

[25] G. A. Ybarra, Q. H. Liu, G. Ye et al., "Breast Imaging Using Electrical Impedance Tomography (EIT)," in *Emerging Technology in Breast Imaging and Mammography, American Scientific Publishers*, pp. 1–16, USA/Canada, 2007.

[26] R. J. Sadleir, S. Z. K. Sajib, H. J. Kim, O. In Kwon, and E. J. Woo, "Simulations and phantom evaluations of magnetic resonance electrical impedance tomography (MREIT) for breast cancer detection," *Journal of Magnetic Resonance*, vol. 230, pp. 40–49, 2013.

[27] M. S. Campisi, C. Barbre, A. Chola, G. Cunningham, V. Woods, and J. Viventi, "Breast cancer detection using high-density flexible electrode arrays and electrical impedance tomography," in *2014 36th Annual International Conference of the IEEE Engineering in Medicine and Biology Society*, pp. 1131–1134, Chicago, Illinois, August 2014.

[28] L. A. Geddes, "Historical evolution of circuit models for the electrode-electrolyte interface," *Annals of Biomedical Engineering*, vol. 25, no. 1, pp. 1–14, 1997.

[29] J. Prado, C. Margo, M. Kouider, and M. Nadi, "Impedance of electrolytes using microelectrodes coplanar," in *Proceeding of COMSOL Multiphysics Conference*, pp. 241–245, Paris, November 2005.

[30] D. G. Gisser, D. Isaacson, and J. C. Newell, "Current topics in impedance imaging," *Clinical Physics and Physiological Measurement*, vol. 8, no. 4A, pp. 39–46, 1987.

[31] K.-S. Cheng, D. Isaacson, J. C. Newell, and D. G. Gisser, "Electrode models for electric current computed tomography," *IEEE Transactions on Biomedical Engineering*, vol. 36, no. 9, pp. 918–924, 1989.

[32] J. A. Padilla-Medina, J. Prado-Olivarez, N. Amador-Licona, L. M. Cardona-Torres, D. Galicia-Resendiz, and J. Diaz-Carmona, "Study on simple reaction and choice times in patients with type I diabetes," *Computers in Biology and Medicine*, vol. 43, no. 4, pp. 368–376, 2013.

[33] T. Uchiyama, S. Ishigame, J. Niitsuma, Y. Aikawa, and Y. Ohta, "Multi-frequency bioelectrical impedance analysis of skin rubor with two-electrode technique," *Journal of Tissue Viability*, vol. 17, no. 4, pp. 110–114, 2008.

[34] A. J. Surowiec, S. S. Stuchly, J. R. Barr, and A. Swarup, "Dielectric properties of breast carcinoma and the surrounding tissues," *IEEE Transactions on Biomedical Engineering*, vol. 35, no. 4, pp. 257–263, 1988.

[35] X. Zhang, C. Chatwin, and D. C. Barber, "A feasibility study of a rotary planar electrode array for electrical impedance mammography using a digital breast phantom," *Physiological Measurement*, vol. 36, no. 6, pp. 1311–1335, 2015.

[36] D. Bennett, "NaCl doping and the conductivity of agar phantoms," *Materials Science and Engineering: C*, vol. 31, no. 2, pp. 494–498, 2011.

[37] International Electrotechnical Commission, "Effects of current on human beings and livestock: part 1–general aspects," International Electrotechnical Commission, Geneva, 2005.

[38] S. Gabriel, R. W. Lau, and C. Gabriel, "The dielectric properties of biological tissues: II. Measurements in the frequency range 10 Hz to 20 GHz," *Physics in Medicine & Biology*, vol. 41, no. 11, pp. 2251–2269, 1996.

[39] M. Lopez-Gordo, D. Sanchez-Morillo, and F. Valle, "Dry EEG electrodes," *Sensors*, vol. 14, no. 7, pp. 12847–12870, 2014.

[40] Y. M. Chi, T. P. Jung, and G. Cauwenberghs, "Dry-contact and noncontact biopotential electrodes: methodological review," *IEEE Reviews in Biomedical Engineering*, vol. 3, pp. 106–119, 2010.

[41] C. C. Barber, B. H. Brown, and I. L. Freeston, "Imaging spatial distributions of resistivity using applied potential tomography," *Electronics Letters*, vol. 19, no. 22, pp. 933–935, 1983.

[42] N. Polydorides and H. McCann, "Electrode configurations for improved spatial resolution in electrical impedance tomography," *Measurement Science and Technology*, vol. 13, no. 12, pp. 1862–1870, 2002.

[43] T. A. Hope and S. E. Iles, "Technology review: the use of electrical impedance scanning in the detection of breast cancer," *Breast Cancer Research*, vol. 6, no. 2, pp. 69–74, 2004.

[44] A. Malich, T. Böhm, M. Facius et al., "Additional value of electrical impedance scanning: experience of 240 histologically-proven breast lesions," *European Journal of Cancer*, vol. 37, no. 18, pp. 2324–2330, 2001.

[45] M. Assenheimer, O. Laver-Moskovitz, D. Malonek et al., "The T-SCAN™ technology: electrical impedance as a diagnostic tool for breast cancer detection," *Physiological Measurement*, vol. 22, no. 1, pp. 1–8, 2001.

[46] A. Malich, T. Fritsch, R. Anderson et al., "Electrical impedance scanning for classifying suspicious breast lesions: first results," *European Radiology*, vol. 10, no. 10, pp. 1555–1561, 2000.

[47] D. D. Pak, N. I. Rozhkova, M. N. Kireeva et al., "Diagnosis of breast cancer using electrical impedance tomography," *Biomedical Engineering*, vol. 46, no. 4, pp. 154–157, 2012.

Research Article

The Influence of Blood Glucose Meter Resistance Variation on the Performance of a Biosensor with a Gold-Coated Circuit Board

Kun-Yong Kim [ID],[1] **Ho Chang** [ID],[1] **Win-Der Lee** [ID],[2] **Yi-Fan Cai**,[2] and **You-Jia Chen**[2]

[1]*Graduate Institute of Manufacturing Technology, National Taipei University of Technology, Taipei 10608, Taiwan*
[2]*Department of Electrical Engineering, Lee-Ming Institute of technology, Taishan, New Taipei 24305, Taiwan*

Correspondence should be addressed to Ho Chang; f10381@ntut.edu.tw and Win-Der Lee; leewd@mail.lit.edu.tw

In this study, a novel gold-coated test strip for blood glucose measurement has been designed. Such gold-coated test strip is feasible for mass production to achieve economies of scale. Cyclic voltammetry was applied to test strips to undergo electrochemical reaction under a potential range of ±0.4 V. Glucose oxidase (GOD) was added into $K_3[Fe(CN)_6]$. When glucose oxidase undergoes electrochemical reaction, the medium, $K_3[Fe(CN)_6]$, will act as an electron acceptor, causing the electrodes on the test strip to generate a pair of clear anodic and reductive peaks. The maximum of the anodic and reductive peaks can be used as reference to adjust the resistance of the blood glucose meter. The experimental results show that by adjusting the resistance of the blood glucose meter, the accuracy of blood glucose meter reading can be tuned and blood glucose reading can be stabilized. Therefore, when the resistance of the blood glucose meter is at 2.4 KΩ, the standard deviation (STD) and coefficient of variation (CV) of the test strip are lower than those of the test strips measured at resistances of 2.2 KΩ and 2.6 KΩ. It has been proved in this study that adjusting the resistance of the blood glucose meter can optimize the chemical reaction on gold-coated test strips as well as its reading. This method can also be applied to tune the accuracy of readings for test strips coated with other materials.

1. Introduction

A blood glucose meter uses blood glucose test strips to measure the blood glucose level of a diabetic patient. The measurement is quick and only requires a small amount of blood. The measured value is recorded in a blood glucose meter which also contains blood glucose data from previous measurements [1–4]. The reaction zone on the electrode of the blood glucose test strip is covered with glucose oxidase, which allows electrons formed in-between the oxidase and electrode surfaces to be transported to the biochemical sensor [5, 6]. The electrode-sensing circuit of the biochemical sensor typically is made from screen-printed carbon paste which acts as the base material for the test strip. Such carbon paste-coated test strip has been widely used in clinical tests for measuring the blood glucose level of diabetic patients [7]. Besides carbon paste, the electrode of test strip can also be made from other base materials such as graphene and gold [8–13]. A gold-coated test strip has the merits of excellent conductivity and a reliable fabrication process. Through

electrochemical reaction of glucose oxidase (GOD), oxidase is catalyzed by electrodes to give the best performance [14]. The working potential of electrodes causes oxidase to undergo electrochemical reaction, creating a set of clear anodic and reductive peaks, which suggests that the reaction between electrodes and oxidase on the test strip is stable [15]. Other types of electrochemical biosensors for the determination of blood glucose levels based on gold structures and glucose oxidase have also been investigated [16]. Therefore, in this study, an effective method was proposed to create an excellent oxidase-based sensing test strip. In this test strip, gold-coated electrode was adopted as the base material since gold has good conductivity and is quite stable. The working principle of the blood glucose meter is based on the electrochemical reaction induced by cyclic voltammetry. By varying the resistance, different electrochemical reactions on the electrode of the test strip will occur. Due to different currents, the oxidase in the reaction zone containing $K_3[Fe(CN)_6]$ will undergo different electrochemical reactions. Such difference in electrochemical reaction will generate different readings

for the test strip. The readings for the test strip were collected, and the accuracy of the readings was determined according to the ISO 15197:2013 standard [17]. Therefore, the aim of this study is to demonstrate the reading accuracy of gold-coated test strips and to investigate the influence of electrochemical resistance on the stability and performance of gold-coated electrodes.

2. Experimental

2.1. GOD Reagent Preparation. 256 U/mg GOD was purchased from Amano Enzyme Inc. (Nagoya, Japan). $K_3[Fe(CN)_6]$ and GOD were well mixed to prepare different solutions. The deionized water used for preparing the solution was purified by various filters to remove impurities. The purpose of using deionized water (18 MΩ·cm resistivity) is to minimize the influence of impurity on the prepared solution.

2.2. Preparation of Test Strips. During the preparation of test strips, the negative film of the desired circuit was laminated on the dry photoresist film which was coated on the copper layer under appropriate temperature and pressure. The substrate with the negative film and dry photoresist was delivered into the UV (ultraviolet) exposure machine to undergo exposure process. After the photoresist under the transparent region of the negative film was exposed to UV light, it underwent polymerization (such region after the developing process will become the protecting material for the etching process) to transform the image of the desired circuit on the dry photoresist. After the etching process of the copper layer, the desired circuit for the working and the reference which was protected by the polymerized photoresist remained. The substrate of the test strip is made of FR4 FRP (glass fiber-reinforced plastic) printed circuit board. The circuit layout of the blood glucose test strip is shown in Figure 1, which clearly shows the copper wire on the test strip substrate. The circuit board containing copper wire was immersed into electroplating solution to coat a layer of nickel with thickness of 120~160 μm, followed by the immersion plating of gold layer with thickness of 1~2 μm. The reaction zone on the test strip contains working electrode and reference electrode. The overall area of the reaction zone is 2 × 2 mm as shown in Figure 2. An ASYMTEK Nordson X-1020 Axiom Semiconductor Jetting Dispenser [18] with an ASYMTEK Nordson DJ-9000 jet dispensing valve [19] was used to carry out the dispensing operation of glucose oxidase (GOD). A droplet of glucose oxidase (GOD) with the volume of 0.45 mg was dispensed onto the reaction zone (2 mm × 2 mm) of each test strip. When the GOD droplet on the reaction zone of the test strip was dried, a hydrophilic layer was added onto the test strip surface.

2.3. Analysis of Electrochemical Measurements. In this study, CHI1221 electrochemical analyzer was used to carry out the electrochemical cyclic voltammetry experiment. The analyzer was equipped with two electrodes: one acting as the working electrode and the other one as the reference electrode. During measurement, potential was applied in-between the working
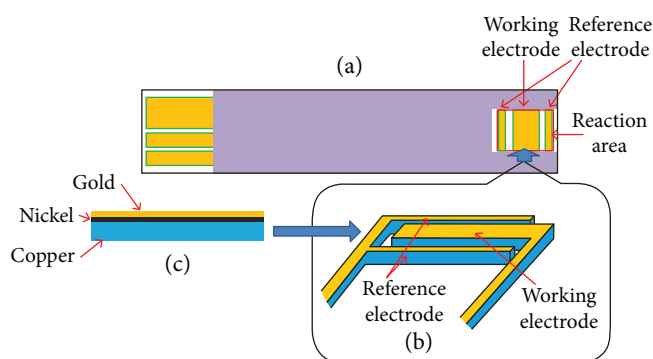

Figure 1: Schematic diagram of the gold-coated blood glucose test strip: (a) reaction zone electrode of the blood glucose test strip, (b) circuit layout of the reaction zone electrode, and (c) layer structure of the conducting material. The purpose of electroplating is to deposit a thin gold film on the copper layer. However, when gold contacts the copper layer directly, the physical phenomenon of electron diffusion will occur (due to difference in potential). Therefore, a layer of nickel must be coated in-between gold and copper, acting as the buffer layer. Such process is called the nickel-gold electroplating process.
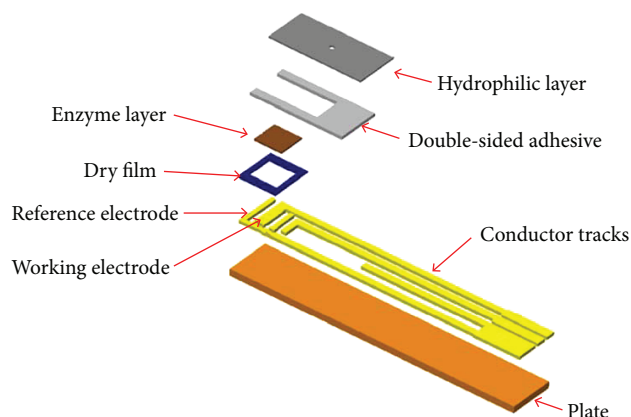

Figure 2: Schematic diagram showing the design of the gold-coated test strip.

electrode and the reference electrode. The experiment was carried out under the temperature of 25 ± 2°C in the laboratory. The test strip used in the experiment underwent cyclic voltammetry electrochemical reaction with potential fixed at ±0.4 V. The electrochemical measurement system used different concentrations of standard solutions to measure the blood glucose test strip through the medium, $K_3[Fe(CN)_6]$, serving as the electron acceptor. The test strip utilized a PET hydrophilic layer on the surface to absorb standard solution. The cyclic voltammetry electrochemical reactions that occurred in the reaction zone of the gold-coated test strip were observed as shown in Figure 3. The glucose oxidase in the reaction zone of the test strip was combined with standard solutions of different concentrations. The medium, $K_3[Fe(CN)_6]$, acting as electron acceptor, in glucose oxidase then triggered the chemical reaction of glucose oxidase to occur in the reaction zone. After the occurrence of
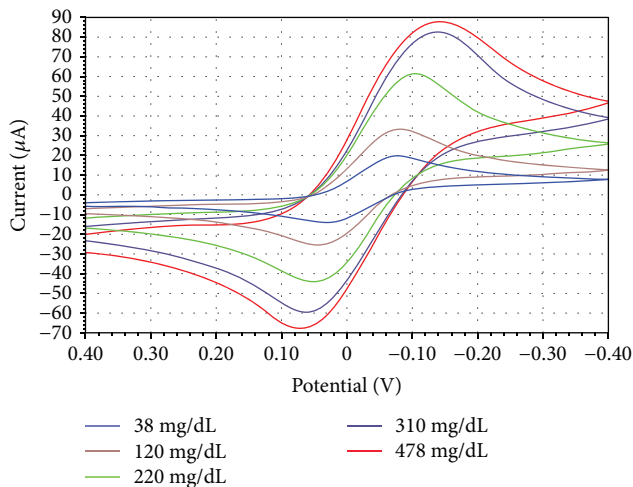
FIGURE 3: The potential for electrochemical reaction was set at the range of ±0.4 V. The result of electrochemical reaction of the test strip containing standard solution of different concentrations was analyzed. The results show that the higher the concentration of standard solution, the greater the current as indicated by the anodic and reductive peaks.

electrochemical reaction in the reaction zone of the test strip, different currents were generated for standard solutions with different concentrations, namely, 38 mg/dL, 119 mg/dL, 220 mg/dL, 310 mg/dL, and 478 mg/dL.

2.4. Blood Glucose Meter Circuit and Measurement. In this study, the internal circuit of the blood glucose meter used for the experiment was adjusted. The blood glucose meter used is a Joinsoon EON L blood glucose meter which has been certified by FDA. The blood glucose meter offered a measurement voltage source, VDD. The voltage source VDD was split by resistors R_1 and R_2 to give Vth (equation 1). The Vth working voltage was then adjusted by resistor R_3. The effect of R_3 on current change is depicted in Figure 4. Based on the current range of the anodic and reductive peaks from the electrochemical reaction, the output current of R_3 was adjusted (equation 2). Four standard solutions with different concentrations were used to carry out test strip measurement. In addition, benchmarking measurements were carried out by YSI-2300 instrument. The standard solution measured by YSI-2300 instrument had a concentration of 38 mg/dL, 120 mg/dL, 220 mg/dL, 310 mg/dL, and 478 mg/dL. The measurement results of the test strip were referred to the requirements of ISO 15197:2013 [16]; when the glucose concentration is lower than 100 mg/dL, STD should be within the range of ±15 mg/dL; when the glucose concentration is higher than 100 mg/dL, CV should be in the range of ±15%. In addition, the error of bias analysis should also be in the range of ±15%. Moreover, linear regression analysis was conducted for data analysis; the closer the correlation coefficient (R^2) is to 1, the more accurate the test strip measurement is. Clarke Error Grid analysis was adopted to assess the significance of test strip measurement on clinical usage. A: clinical accuracy; B: clinically irrelevant deviation (>15%); C: unnecessary

overcorrection possible; D: dangerous failure to detect and treat; E: erroneous treatment.

3. Results and Discussion

3.1. STD (Standard Deviation) and CV (Coefficient of Variation). Blood glucose meter adjusted the resistance of R_3 according to the current change from cyclic voltammetry electrochemical reaction. Blood glucose test strips containing standard solution with concentrations of 38 mg/dL, 120 mg/dL, 220 mg/dL, 310 mg/dL, and 478 mg/dL were measured, and the result was shown in Tables 1 and 2. Table 1 shows the measurement result under different resistance conditions. It is clear that when the resistance is at 2.2 KΩ, the average blood glucose reading is lower. However, when the resistance is at 2.4 KΩ, the average blood glucose reading is closest to that of standard solution. The average blood glucose reading at a resistance of 2.6 KΩ is higher than that of standard solution.

From the above results, it is known that the reading obtained by the blood glucose meter under a resistance of 2.4 KΩ is closer to the reading of standard solution as compared to the readings measured under resistances of 2.2 KΩ and 2.6 KΩ. According to the requirement of ISO 15197:2013 [16], when the glucose concentration is lower than 100 mg/dL, STD should be within the range of ±15 mg/dL and when the glucose concentration is higher than 100 mg/dL, CV should be in the range of ±15%. Therefore, when the glucose concentration of standard solution is lower than 100 mg/dL (i.e., 38 mg/dL), only the STD value is used for reference. On the other hand, when the glucose concentration of standard solution is higher than 100 mg/dL (i.e., 120 mg/dL, 220 mg/dL, 310 mg/dL, and 478 mg/dL), only the CV value is used for reference. This explains why in Table 2, some results only have STD values while others only have CV values.

As shown in Table 2, when the concentration of standard solution is 38 mg/dL, a resistance of 2.4 KΩ gives the lowest STD comparing with resistances of 2.2 KΩ and 2.6 KΩ. CV values are compared for standard solutions with concentrations of 120 mg/dL, 220 mg/dL, 310 mg/dL, and 478 mg/dL. Among them, a resistance of 2.4 KΩ gives the lowest CV values while resistances of 2.2 KΩ and 2.6 KΩ show relatively higher CV values. However, comparing the average reading in Table 2 with STD/CV values in Table 2, the average reading at a resistance of 2.4 KΩ is closest to the standard value of YSI. The STD/CV values at a resistance of 2.4 KΩ are within the scope of ISO 15197:2013.

3.2. Test for the Accuracy of the Control Solution. A total of 250 data were tested for the measurement of test strips under resistances of 2.2 KΩ, 2.4 KΩ, and 2.6 KΩ. The measurement results were summarized in Tables 3 and 4 for standard solutions with glucose concentrations of <100 mg/dL and ≥100 mg/dL, respectively.

For the measurement results with a glucose concentration of <100 mg/dL as shown in Table 3, the measurements under the resistance of 2.4 KΩ with a concentration of 5 mg/dL all (100%) fall within the scope. Comparing to the

$$Vth = \frac{R_2}{R_1 + R_2} \, VDD \qquad (1)$$
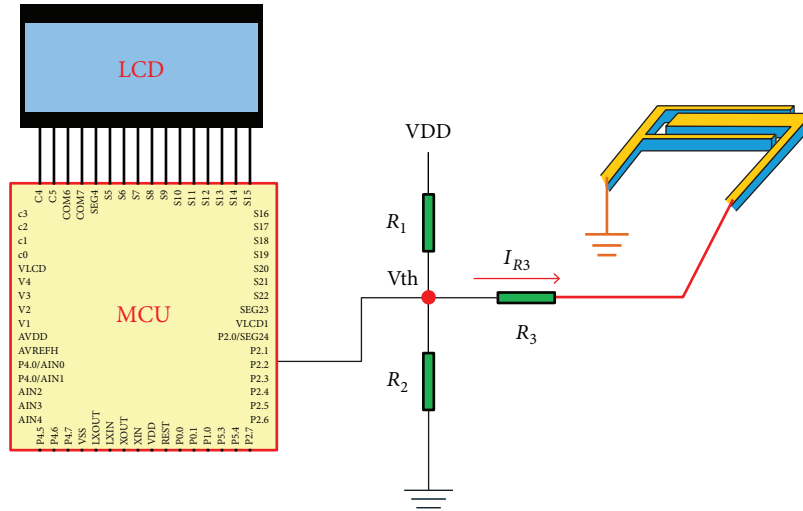
$$I_{R3} = \frac{Vth}{R_3} \qquad (2)$$

FIGURE 4: Circuit diagram of the blood glucose meter—working electrode is connected to R3 while reference electrode is connected to cathode (negative electrode). MCU P2.2 receives the data resulted from electrochemical reaction and the data is shown on LCD display.

TABLE 1: Average reading of test strips measured by a blood glucose meter under different resistance conditions.

YSI reading	R_3 2.2 KΩ (mg/dL)	R_3 2.4 KΩ (mg/dL)	R_3 2.6 KΩ (mg/dL)
38 mg/dL	28.1	38.6	57.8
120 mg/dL	91.9	119.7	155.9
220 mg/dL	187.6	220.0	258.5
310 mg/dL	281.5	315.1	338.5
478 mg/dL	442	472.8	526.8

TABLE 2: Reading of test strips with different concentrations of standard solution obtained by a blood glucose meter under different resistance conditions, showing the influence of resistance on STD and CV.

YSI reading	R_3 2.2 KΩ STD/CV	R_3 2.4 KΩ STD/CV	R_3 2.6 KΩ STD/CV
38 mg/dL	3.7/—	3.0/—	5.8/—
120 mg/dL	—/5.1	—/3.7	—/6.0
220 mg/dL	—/5.3	—/3.7	—/5.0
310 mg/dL	—/5.2	—/3.5	—/5.1
478 mg/dL	—/4.9	—/3.6	—/5.1

TABLE 3: The range of test strip measurements under the resistances of 2.2 KΩ, 2.4 KΩ, and 2.6 KΩ for standard solutions with glucose concentrations of <100 mg/dL.

Resistance	Within 15 mg/dL	Within 10 mg/dL	Within 5 mg/dL
2.2 KΩ	46/50 (92%)	32/50 (64%)	6/50 (12%)
2.4 KΩ	50/50 (100%)	50/50 (100%)	50/50 (100%)
2.6 KΩ	19/50 (38%)	0/50 (0%)	0/50 (0%)

TABLE 4: The range of test strip measurements under the resistances of 2.2 KΩ, 2.4 KΩ, and 2.6 KΩ for standard solutions with glucose concentrations of ≥100 mg/dL.

Resistance	Within 15%	Within 10%	Within 5%
2.2 KΩ	84/200 (42%)	80/200 (40%)	24/200 (12%)
2.4 KΩ	200/200 (100%)	200/200 (100%)	169/200 (85%)
2.6 KΩ	102/200 (51%)	54/200 (27%)	24/200 (12%)

results for the resistances of 2.2 KΩ and 2.6 KΩ, 12% of the measurements under the resistance of 2.2 KΩ with a concentration of 5 mg/dL fall within the scope, 64% of the measurements under the resistance of 2.2 KΩ with a concentration of

10 mg/dL fall within the scope, and 92% of the measurements under the resistance of 2.2 KΩ with a concentration of 5 mg/dL fall within the scope. On the other hand, the measurements under the resistance of 2.6 KΩ with concentrations of 5 mg/dL and 10 mg/dL all fall out of the scope, while 38% of the measurements under the resistance of 2.6 KΩ with a concentration of 15 mg/dL all fall within the scope. The above results suggest that the measurement of the test strip under the resistance of 2.4 KΩ with concentrations < 100 mg/dL will give more accurate reading.

TABLE 5: Linear regression.

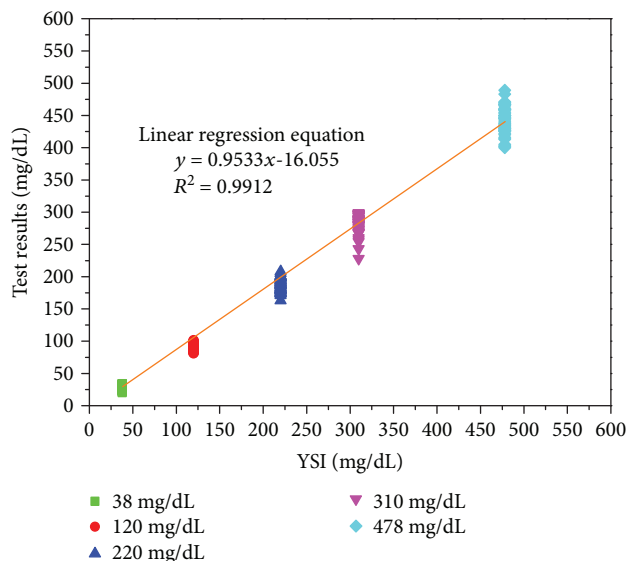| Resistance	N	Slope	Y intercept	Correlation coefficient (R^2)
2.2 KΩ	250	0.9533	-16.055	0.9912
2.4 KΩ	250	0.9918	1.9659	0.9953
2.6 KΩ	250	1.0488	22.917	0.9886

FIGURE 5: Correlation graph between test strip readings measured by the blood glucose meter at a resistance of 2.2 KΩ and measurements of standard solution from YSI.

When the test strip measurements were carried out with concentrations ≥ 100 mg/dL, 200 data were analyzed for each resistance condition, namely, 2.2 KΩ, 2.4 KΩ, and 2.6 KΩ, as shown in Table 4. For the resistance of 2.2 KΩ, 12% of the test strip measurements fall within the 5% range, 40% of the test strip measurements fall within the 10% range, and 42% of the test strip measurements fall within the 15% range. On the other hand, for the resistance of 2.4 KΩ, 85% of the test strip measurements fall within the 5% range and 100% of the test strip measurements fall within the 10% and 15% range. For the resistance of 2.6 KΩ, 12% of the test strip measurements fall within the 5% range, 27% of the test strip measurements fall within the 10% range, and 51% of the test strip measurements fall within the 15% range. From the above results, it is noted that the measurement of the test strip under the resistance of 2.4 KΩ with concentrations ≥ 100 mg/dL will give more stable reading.

3.3. Test Strip Measurement Results Analyzed by Linear Regression. Table 5 shows the linear regression analysis of experimental results for resistances of 2.2 KΩ, 2.4 KΩ, and 2.6 KΩ. A total of 250 reading data were used to perform the analysis for each resistance condition and compared with the results of standard solution from YSI. The correlation graph obtained for resistances of 2.2 KΩ, 2.4 KΩ, and 2.6 KΩ is shown in Figures 5, 6, and 7, respectively. As shown
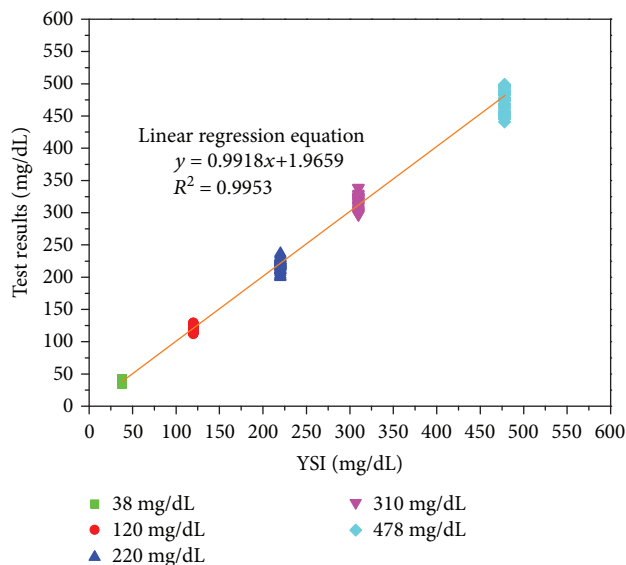
FIGURE 6: Correlation graph between test strip readings measured by the blood glucose meter at a resistance of 2.4 KΩ and measurements of standard solution from YSI.
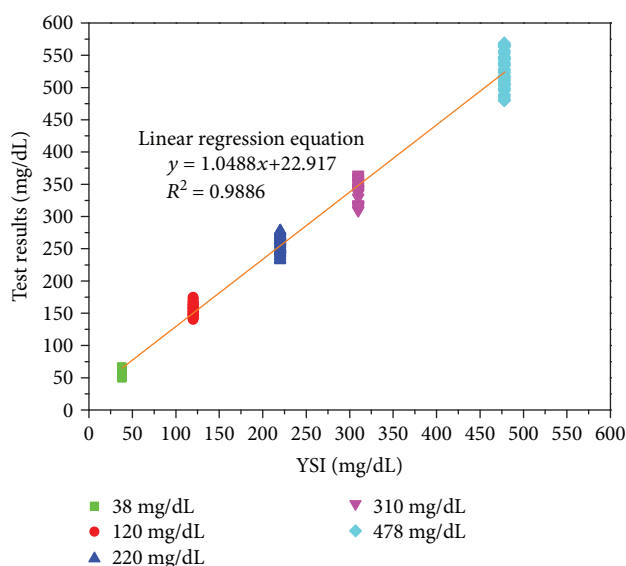

FIGURE 7: Correlation graph between test strip readings measured by the blood glucose meter at a resistance of 2.6 KΩ and measurements of standard solution from YSI.

in Figure 5, when the resistance is at 2.2 KΩ, the distribution of measured readings for standard solution with concentrations of 220 mg/dL and 310 mg/dL is more scattered. The resulting correlation graph has a slope of 0.9533, an Y intercept of -16.055, and a correlation coefficient (R^2) of 0.9912. As shown in Figure 6, when the resistance is at 2.4 KΩ, the distribution of measured readings for glucose standard solution with concentration ranging from low to high is more focused. The resulting correlation graph has a slope of 0.9918, a Y intercept of 1.9659, and a correlation coefficient
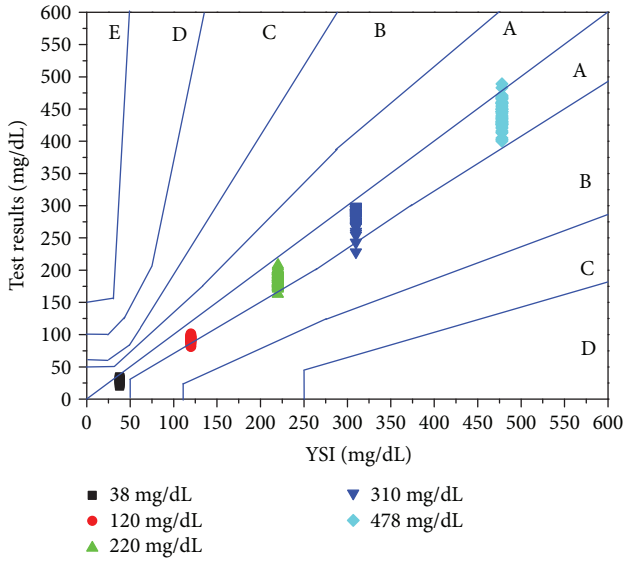
FIGURE 8: Clarke Error Grid analysis for the distribution of test strip readings measured by the blood glucose meter at a resistance of 2.2 KΩ as compared with the measurements of standard solution from YSI; some readings fall in zone B.
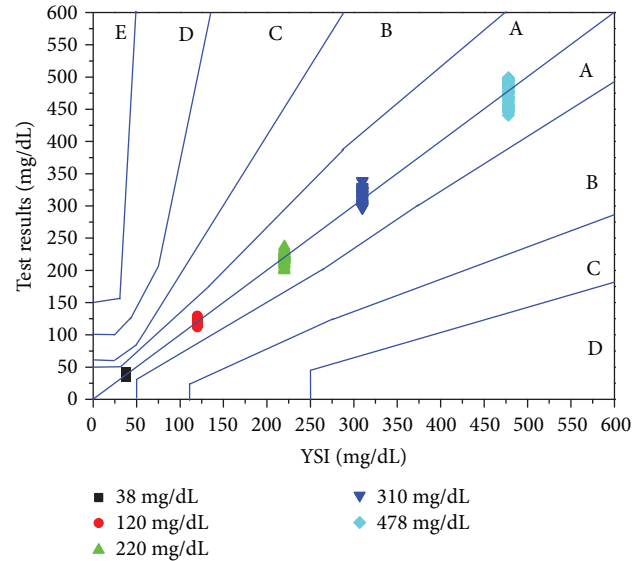
(R^2) of 0.9953. As shown in Figure 7, when the resistance is at 2.6 KΩ, the distribution of measured readings for glucose standard solution with concentration ranging from low to high is more scattered. The resulting correlation graph has a slope of 1.0488, a Y intercept of 22.917, and a correlation coefficient (R^2) of 0.9886. The correlation graph for a resistance of 2.4 KΩ has the smallest Y intercept comparing with that for resistances of 2.2 KΩ and 2.6 KΩ. This suggests that the actual readings for test strips at resistances of 2.2 KΩ and 2.6 KΩ show larger deviation comparing with the standard values of YSI. Therefore, the actual readings for test strips at a resistance of 2.4 KΩ are closer to the standard values of YSI.

3.4. Test Strip Measurement Results Illustrated by the Clarke Error Grid. Figures 8, 9, and 10 show the Clarke Error Grid analysis result for test strip readings as compared with the measurements of standard solution from YSI for resistances of 2.2 KΩ, 2.4 KΩ, and 2.6 KΩ, respectively. As shown in Figure 8, comparing with YSI measurement results, the distribution of readings from 250 measurements at a resistance of 2.2 KΩ is deviated from zone A and moving towards lower zone B. As shown in Figure 9, comparing with YSI measurement results, the distribution of readings from 250 measurements at a resistance of 2.4 KΩ is located in zone A. As shown in Figure 10, comparing with YSI measurement results, the distribution of readings from 250 measurements at a resistance of 2.6 KΩ is deviated from zone A and moving towards upper zone B. The distribution of readings measured for test strips at a resistance of 2.4 KΩ is more crowded together, especially for the readings of standard solution with a concentration of 38 mg/dL. This suggests that the readings for low-concentration standard solution are closer to the readings of YSI, meaning more accurate test strip reading. On the other hand, the distribution of readings measured at a
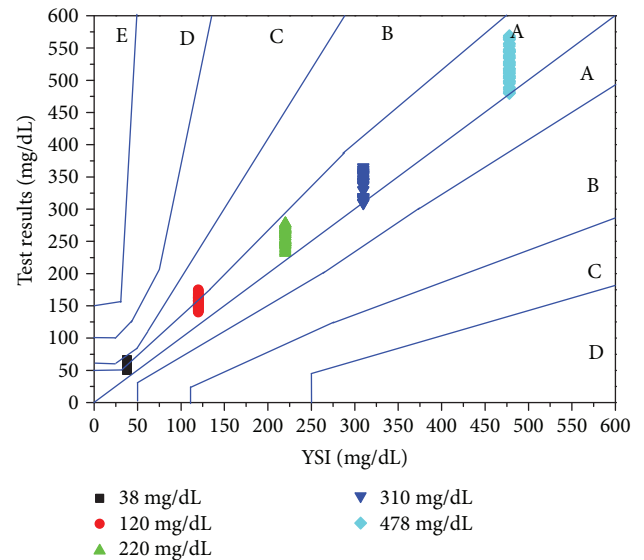

FIGURE 9: Clarke Error Grid analysis for the distribution of test strip readings measured by the blood glucose meter at a resistance of 2.4 KΩ as compared with the measurements of standard solution from YSI; readings are concentrated in zone A; therefore, measurements at resistance of 2.4 KΩ have clinical value.

FIGURE 10: Clarke Error Grid analysis for the distribution of test strip readings measured by the blood glucose meter at a resistance of 2.6 KΩ as compared with the measurements of standard solution from YSI; some readings fall in zone B.

resistance of 2.2 KΩ is located towards lower zone B while the distribution of readings measured at a resistance of 2.6 KΩ is located towards upper zone B, implying that readings of the test strip are deviated from YSI readings.

3.5. Bias Analysis of Test Strip Measurement Results. Figures 11, 12, and 13 show the bias analysis result for test strip readings as compared with the measurements of
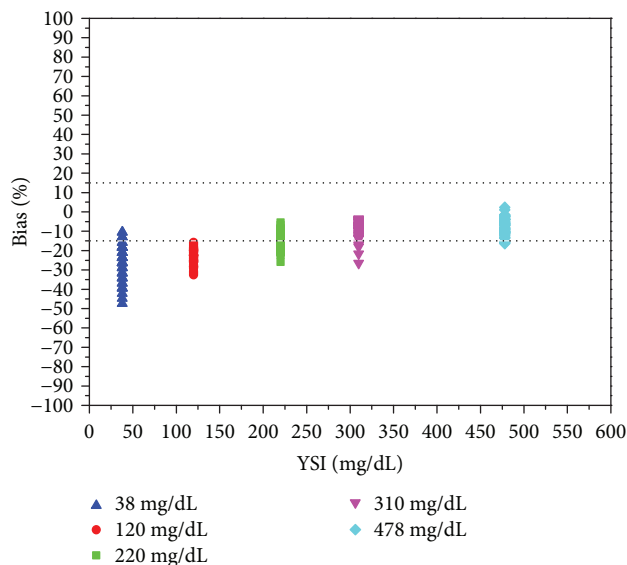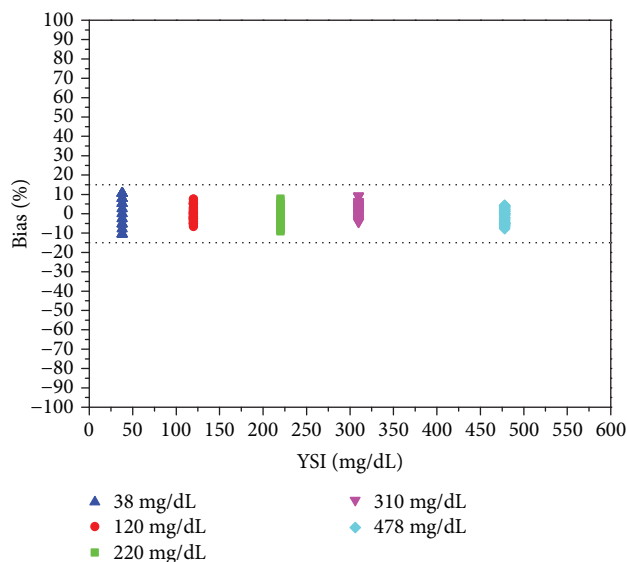
FIGURE 11: Bias analysis result for the distribution of test strip readings measured at a resistance of 2.2 KΩ; the distribution of readings exceeds the ±15% range.

FIGURE 12: Bias analysis result for the distribution of test strip readings measured at a resistance of 2.4 KΩ; the distribution of readings is within the ±15% range, complying with the ISO 15197:2013 standard.

standard solution from YSI for resistances of 2.2 KΩ, 2.4 KΩ and 2.6 KΩ, respectively. As shown in Figure 11, when the resistance is at 2.2 KΩ, the distribution of readings from 250 measurements of the test strip in a bias analysis diagram clearly exceeds the ±15% range, especially for standard solution with a concentration of 38 mg/dL, which shows a bias range of -47.37%. As shown in Figure 12, when the resistance is at 2.4 KΩ, the distribution of readings from 250 measurements of the test strip in a bias analysis diagram is within the ±15% range, suggesting that the readings for all

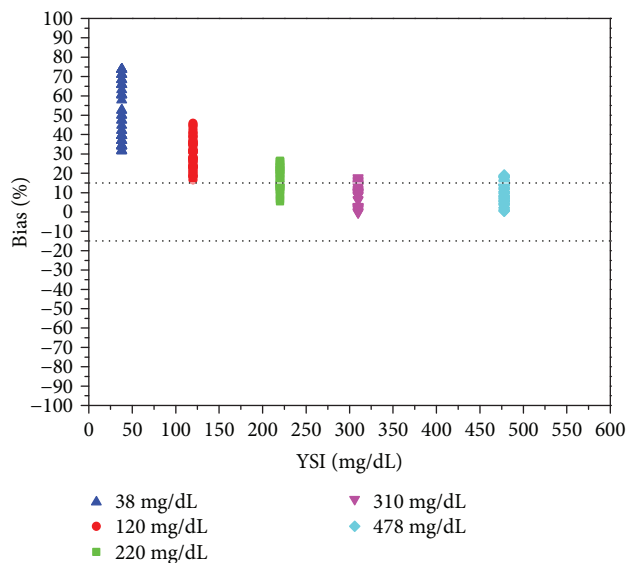FIGURE 13: Bias analysis result for the distribution of test strip readings measured at a resistance of 2.6 KΩ; the distribution of readings exceeds the ±15% range.

concentrations of standard solutions are closer to the readings of from YSI, meaning more accurate test strip reading. As shown in Figure 13, when the resistance is at 2.6 KΩ, the distribution of readings from 250 measurements of the test strip in a bias analysis diagram clearly exceeds the ±15% range, especially for standard solutions with a concentration of 38 mg/dL, both of which have bias reaching as high as 73.68%.

3.6. Deviation Analysis of Test Strip Readings. For STD and CV analysis, the results of test strip measurement carried out under resistances of 2.2 KΩ, 2.4 KΩ, and 2.6 KΩ comply with the ISO 15197:2013 standard. However, this outcome does not apply for linear regression analysis, Clarke Error Grid, and bias analysis. Comparing test strip readings with the measurements of standard solutions from YSI, the readings of the test strip for a resistance of 2.2 KΩ mostly are low, while the readings of the test strip for a resistance of 2.6 KΩ are high. When the resistance of R_3 in the blood glucose meter increases, the current of I_{R3} will gradually decrease, making the reading of the test strip measured by the blood glucose meter to be deviated from the standard value. There are ways to compensate for the shifted blood glucose reading (higher or lower). However, these compensating methods cannot change STD and CV, since different resistances will change blood glucose meter's current supply, creating different electrochemical reactions. The resistance condition of 2.4 KΩ will optimize the electrochemical reaction of the gold-coated electrode test strip, giving lower test strip STD as well as CV and leading to higher accuracy for the gold-coated electrode test strip.

4. Conclusion

In this study, the characteristics of the gold-coated test strip for blood glucose measurement were investigated. The

glucose oxidase (GOD) in the reaction zone of the test strip covering the surface of the gold-coated electrode demonstrated the influence of the resistance of the blood glucose meter on the electrochemical reaction of the blood glucose test strip, which can be utilized to adjust test strip reading and accuracy. It has been proved in this study that by tuning the resistance of the blood glucose meter, the electrochemical reaction of the blood glucose test strip can be varied to improve the accuracy of reading. In this study, the resistance of electrochemical reaction was adjusted. It was found that by adjusting the resistance, the accuracy of test strip reading for blood glucose measurement can be improved. We hope that this finding can also be applied to other blood glucose test strips made from different materials, helping to improve the reading accuracy of these test strips.

Data Availability

The data used to support the findings of this study are included within the article.

Conflicts of Interest

The authors declare that they have no conflicts of interest.

References

[1] A. Soni and S. K. Jha, "A paper strip based non-invasive glucose biosensor for salivary analysis," *Biosensors and Bioelectronics*, vol. 67, pp. 763–768, 2015.

[2] T. Lan, J. Zhang, and Y. Lu, "Transforming the blood glucose meter into a general healthcare meter for in vitro diagnostics in mobile health," *Biotechnology Advances*, vol. 34, no. 3, pp. 331–341, 2016.

[3] A. J. Bandodkar, S. Imani, R. Nuñez-Flores et al., "Re-usable electrochemical glucose sensors integrated into a smartphone platform," *Biosensors and Bioelectronics*, vol. 101, pp. 181–187, 2018.

[4] A. M. Al-Taee, A. Al-Taee, Z. J. Muhsin, M. A. Al-Taee, and W. Al-Nuaimy, "Towards developing online compliance index for self-monitoring of blood glucose in diabetes management," in *2016 9th International Conference on Developments in eSystems Engineering (DeSE)*, August 2016.

[5] B. Liang, X. Guo, L. Fang et al., "Study of direct electron transfer and enzyme activity of glucose oxidase on graphene surface," *Electrochemistry Communications*, vol. 50, no. 1-5, pp. 1–5, 2015.

[6] S. Jawaheer, S. F. White, S. D. D. V. Rughooputh, and D. C. Cullen, "Development of a common biosensor format for an enzyme based biosensor array to monitor fruit quality," *Biosensors and Bioelectronics*, vol. 18, no. 12, pp. 1429–1437, 2003.

[7] D. K. Bishop, J. T. la Belle, S. R. Vossler, D. R. Patel, and C. B. Cook, "A disposable tear glucose biosensor—part 1: design and concept testing," *Journal of Diabetes Science and Technology*, vol. 4, no. 2, pp. 299–306, 2010.

[8] P. Yang, J. Peng, Z. Chu, D. Jiang, and W. Jin, "Facile synthesis of Prussian blue nanocubes/silver nanowires network as a water-based ink for the direct screen-printed flexible biosensor chips," *Biosensors and Bioelectronics*, vol. 92, pp. 709–717, 2017.

[9] V. Mani, B. Devadas, and S.-M. Chen, "Direct electrochemistry of glucose oxidase at electrochemically reduced graphene oxide-multiwalled carbon nanotubes hybrid material modified electrode for glucose biosensor," *Biosensors and Bioelectronics*, vol. 41, pp. 309–315, 2013.

[10] S.-Y. Lu, Y. Lu, M. Jin, S.-J. Bao, W.-Y. Li, and L. Yu, "Design and fabrication of highly sensitive and stable biochip for glucose biosensing," *Applied Surface Science*, vol. 422, pp. 900–904, 2017.

[11] M. Gu, J. Wang, Y. Tu, and J. Di, "Fabrication of reagentless glucose biosensors: a comparison of mono-enzyme GOD and bienzyme GOD–HRP systems," *Sensors and Actuators B: Chemical*, vol. 148, no. 2, pp. 486–491, 2010.

[12] W. Nouira, A. Maaref, H. Elaissari, F. Vocanson, M. Siadat, and N. Jaffrezic-Renault, "Comparative study of conductometric glucose biosensor based on gold and on magnetic nanoparticles," *Materials Science and Engineering C*, vol. 33, no. 1, pp. 298–303, 2013.

[13] C. Gong, Y. Shen, Y. Song, and L. Wang, "On-Off ratiometric electrochemical biosensor for accurate detection of glucose," *Electrochimica Acta*, vol. 235, pp. 488–494, 2017.

[14] C.-T. Hsu, H.-H. Chung, D.-M. Tsai, M.-Y. Fang, H.-C. Hsiao, and J.-M. Zen, "Fabrication of a glucose biosensor based on inserted barrel plating gold electrodes," *Analytical Chemistry*, vol. 81, no. 1, pp. 515–518, 2009.

[15] P. Rafighi, M. Tavahodi, and B. Haghighi, "Fabrication of a third-generation glucose biosensor using graphene-polyethyleneimine-gold nanoparticles hybrid," *Sensors and Actuators B: Chemical*, vol. 232, pp. 454–461, 2016.

[16] A. Ramanavicius, N. German, and A. Ramanaviciene, "Evaluation of electron transfer in electrochemical system based on immobilized gold nanoparticles and glucose oxidase," *Journal of the Electrochemical Society*, vol. 164, no. 4, pp. G45–G49, 2017.

[17] ISO, *In Vitro Diagnostic Test System – Requirements for Blood-Glucosemonitoring Systems for Self-Testing in Managing Diabetes Mellitus*, no. article 15197, 2013International Organization for Standardization, Geneva, 2013.

[18] I. N. C. Nordson Asymtek, *Axiomtm X-1000 Series Dispensing System Operations Manual*, no. article 392888, 2009Nordson Corporation, 2009, Rev. E.

[19] Nordson Asymtek INC, *Dispense Jet Series DJ-9000 Owner's Manual. 2762 Loker Avenue West Carlsbad*, I. N. C. Nordson Asymtek, 2014.

Research Article

Simultaneous Recording of ICG and ECG Using Z-RPI Device with Minimum Number of Electrodes

Abdelakram Hafid [ORCID],[1] **Sara Benouar,**[1] **Malika Kedir-Talha,**[1] **Mokhtar Attari,**[1] **and Fernando Seoane**[2,3,4]

[1]*Laboratory of Instrumentation, University of Sciences and Technology Houari Boumediene, Algiers, Algeria*
[2]*Swedish School of Textiles, University of Borås, 50190 Borås, Sweden*
[3]*The Department for Clinical Science, Intervention and Technology, Karolinska Institutet, 14186 Stockholm, Sweden*
[4]*Department Biomedical Engineering, Karolinska University Hospital, 14186 Stockholm, Sweden*

Correspondence should be addressed to Abdelakram Hafid; abdelakram.hafid@gmail.com

Impedance cardiography (ICG) is a noninvasive method for monitoring mechanical function of the heart with the use of electrical bioimpedance measurements. This paper presents the feasibility of recording an ICG signal simultaneously with electrocardiogram signal (ECG) using the same electrodes for both measurements, for a total of five electrodes rather than eight electrodes. The device used is the Z-RPI. The results present good performance and show waveforms presenting high similarity with the different signals reported using different electrodes for acquisition; the heart rate values were calculated and they present accurate evaluation between the ECG and ICG heart rates. The hemodynamics and cardiac parameter results present similitude with the physiological parameters for healthy people reported in the literature. The possibility of reducing number of electrodes used for ICG measurement is an encouraging step to enabling wearable and personal health monitoring solutions.

1. Introduction

An estimated 17.5 million deaths per year are attributed to cardiac diseases. According to WHO [1], people with cardiovascular diseases (CVDs) require an early and pertinent diagnosis to receive the best treatment [2].

Electrical bioimpedance (EBI) is a sensing technology that has been used for several decades for various applications [3], utilizing different measurement techniques, e.g., segmental and/or total body [4], spectroscopy [5, 6], tomography [7], and impedance plethysmography [8] with its most common application which is impedance cardiography (ICG). Using a single channel with single frequency continuously, the ICG was introduced as a noninvasive method and its waveform has been used for the assessment of certain hemodynamic parameters describing the mechanical function of the heart like the cardiac output (CO), stroke volume (SV), and systolic time intervals, e.g., left ventricular ejection time (LVET noted also ET), preejection period (PEP), and systolic time ratio (STR) [9–11].

An ICG recording is obtained using a specific electrode configuration, the electrodes are placed on the surface of the upper torso, and the EBI is measured across the thorax with the 4-electrode measurement technique from the neck to the abdomen [12]. The measured variation of the impedance (Z) is mainly due to the cardiac activity; it is noted ΔZ; the dZ/dt waveform is obtained from the first derivative of the ΔZ signal, and it is characterized by seven typical characteristic points which are related to cardiodynamics [10, 13].

Electrocardiography (ECG) is a relatively inexpensive technique that allows simple and noninvasive monitoring of the electrical activity of the heart. The action potentials generated during the activity of the heart can be collected by electrodes placed on the surface of the skin. The location of these electrodes is chosen to explore the lead II of the heart electric field.
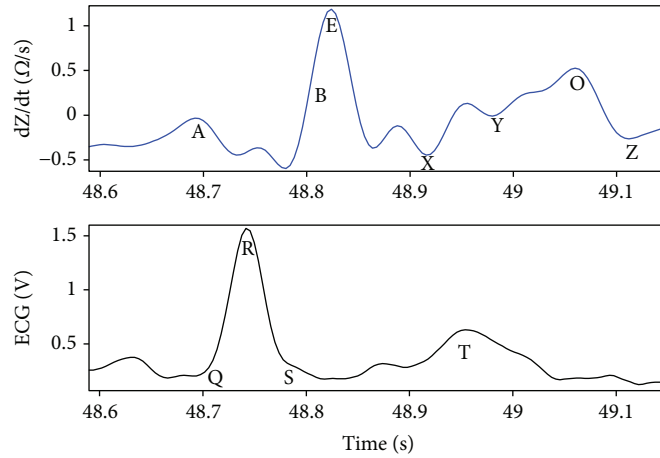
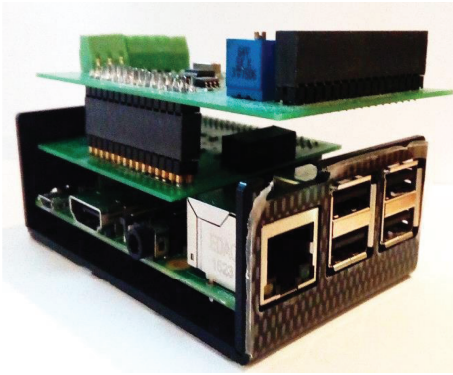Figure 1: Pattern of the ICG and ECG signals simultaneously.

Figure 2: Z-RPI prototype.

Cardiogenic bioelectrical activity is commonly called ECG lead or derivation. Each ECG derivation is defined by a specific label and a precise electrode placement according to [14]; there are different derivations used to measure the ECG signal; each of them has a number and precise electrode locations, such as standard bipolar peripheral derivations, unipolar peripheral derivations, and precipitation unipolar derivations [15].

ECG-based heart rate calculation involves the step of detecting the R wave of the QRS complex. The most common method for detecting the R wave is the Pan-Tompkins algorithm [16–18].

Development of personalized health (p-health) solutions and advances in smart textiles and textile manufacturing has allowed new developments of wearable measurement systems targeting fitness and even home-care but often they have been limited to biopotential recordings [19, 20]. Recent advances in microelectronics have produced system-on-chip (SoC) solutions for biopotential and bioimpedance measurements, and most of them have been successfully tested in several EBI applications [21–25]. Thus, we can confirm that their availability and accessibility have indeed fostered research and development activities targeting p-health monitoring applications based on different embedded

electronic wearable measurement systems and patch technology [23, 26–28].

Thus, for performing ICG and ECG measurements, using two different electrodes' placement to make a simultaneous record is generally the method that is used.

ICG waveforms together with ECG waveforms as presented in Figure 1 are often used to calculate and assess the specific hemodynamic parameters mentioned above [9, 10].

In this paper, we present a measurement system for the acquisition of ICG and one-lead ECG signal simultaneously using the same electrodes for both measurements. The Pan-Thompkins algorithm is used for ECG analysis, and the ensemble average method is applied to assess hemodynamic parameters of the ICG signal.

2. Methods

2.1. Z-RPI Device. The developed ICG recording device used in this work showed in Figure 2 named Z-RPI is a custom-made device that can simultaneously record ECG and ICG. It combines two system-on-chip (SoC) solutions, which are ADAS1000 and AD5933 from Analog Devices combined with additional electronics to have a complete EBI and ECG measurement modules, with the Raspberry PI3 card. It also includes an impedance calibration system, Bluetooth wireless communication, a power management circuit, and a 2500 mAh LiPo battery as power supply with 5 hours of autonomy [24], in its original operation mode, for recording ICG and ECG.

2.2. Experimental Measurement Setup. The regular configuration of the Z-RPI device uses 8 electrodes: 4 electrodes for measuring ICG, in which the electrodes are placed according to the Sramek configuration (two electrodes on the right lateral part of the neck and two on the left side of the thorax) [12]; 3 electrodes for ECG; and 1 electrode for the RLD circuitry, placed in the peripheral extremities (hand and leg) for the ECG [24].

In this work, the configuration of the Z-RPI device has been modified, especially for the ADAS1000 part, which has been moved from a 3-lead ECG recording configuration
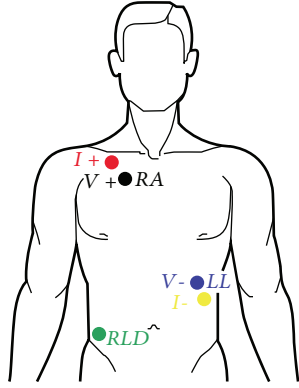
FIGURE 3: Placement of electrodes for ECG/ICG measurement.

TABLE 1: Mean and the SD of anthropomorphic data of volunteers.

Gender	N	Height (cm)	Weight (kg)	Age (years)
Male	7	180 ± 7	81 ± 9	31 ± 13

to a single-lead recording. As we do not have a golden standard for the placement of the ICG electrodes, we chose to place two electrodes on the right lateral part of the upper torso and two electrodes on the left side of the thorax, on the upper abdomen part, and the RLD electrode is placed at the right side of the waist.

As we use a tetrapolar configuration for performing ICG measurement, the placement configuration of the electrodes has been chosen to have the inner ICG electrode (V+ and V−) in the same position as the RA and LL spot for the ECG measurement. In this way, the ECG shielded cables were connected to them (V+ with RA and V− with LL) for performing simultaneously the ICG measurement and ECG lead II measurement.

Figure 3 shows the five spots for the placement of the 3M repositionable Ag/AgCl gel electrodes used for performing the ICG recording [12] and one-lead ECG; the shared voltage-sensing electrodes are marked with V in black and blue, and the current injecting electrodes are the outer ones, indicated with I in red and yellow.

The experimental evaluation was performed at the Laboratory of Instrumentation at the University of Science and Technology Houari Boumediene, Algeria, on seven healthy volunteers (see Table 1). The recordings in the experiment were obtained according to the procedure previously used in [24] and approved by the ethical approval nr 11-274 granted by the regional Ethical Vetting Board in Gothenburg including the use of an informed consent form.

The ICG measurement is obtained using an injecting sinusoidal current of 70 kHz and 133 μA [24], and 280 Hz sampling frequency acquisition was used for both ICG and ECG recording. The measurement sessions lasted for at least 60 seconds while the subjects remained in sitting position keeping a shallow breathing paced at 10 breaths per minute.

2.3. Measurement Data Analysis. The recorded thoracic measurements were processed and analyzed on the PC using a customized program running MATLAB 2015 scripts [24]; high-frequency information is removed applying a low-pass filter with frequency cut at 13 Hz. Since the acquired impedance ΔZ includes both cardiac and respiration components, knowing that the respiration is present in the band of 0.05–0.3 Hz, approximately, a bandpass filter was designed in a 20th-order FIR filter with fc = 0.7–7 Hz, Therefore, the respiration components attenuated a minimum of −6 dB, and the different characterizing parameters and time interval values of the ICG and ECG signal were extracted. More details are present elsewhere in [24].

2.4. Hemodynamic Parameter Calculation. The Pan-Tompkins algorithm [17] was used for detecting the R peak in the ECG recording. Once the R peak is detected, the Q point is extracted from the QRS complex of the ECG signal. The Q point is the minimum before the R peak; it was calculated by subtracting a fixed value of 40 ms from the time of the R wave [29]. Using the R and Q waves, the heart rate (HR) and the PEP are calculated, respectively.

The ΔZ and dZ/dt signals obtained from the ICG recording were analyzed to obtain the different ICG parameters, using the ensemble average method [30, 31]; the $dZ/dt_{\max}$ (E point) is the peak of the first derivative of the transthoracic impedance variation in Ω/s [32]; this later is triggered by the R peaks of the ECG signals. The heart rate of the ICG signal was calculated from the E peaks acquired. The LVET interval is calculated as the distance between B and X point of the ICG signal. Then, SV and CO are calculated according to (1) and (2), respectively, as presented in [24].

$$SV = V_C \sqrt{\frac{dZ(t)/dt_{\max}}{Z_0}} ET,$$ (1)

$$CO = SV \times HR.$$ (2)

3. Results

More than 2700 seconds of recordings were obtained, containing more than 3000 ICG and ECG complexes, similar to the ones plotted in Figure 4. Figure 4(a) shows the ΔZ, Figure 4(b) shows the dZ/dt, and Figure 4(c) shows the ECG.

Figure 5 presents the averaged complexes ICG thin trace in (Ω/s) and ECG coarse trace in (V) obtained from 60 s of recordings of the healthy volunteer HV1.

Table 2 presents the descriptive statistics (mean ± SD) for the characterizing parameters and time interval values, calculated from the ICG/ECG recordings obtained for each volunteer.

Figure 6 presents two averaged ICG complexes produced with the recordings obtained with the 2 different electrode configurations. The recordings obtained with the 5-electrode configuration, continuous trace, show a remarkable minimum between the A and E waves of the ICG complex, minimum significantly more pronounced than the minimum obtained with the 8-electrode configuration.
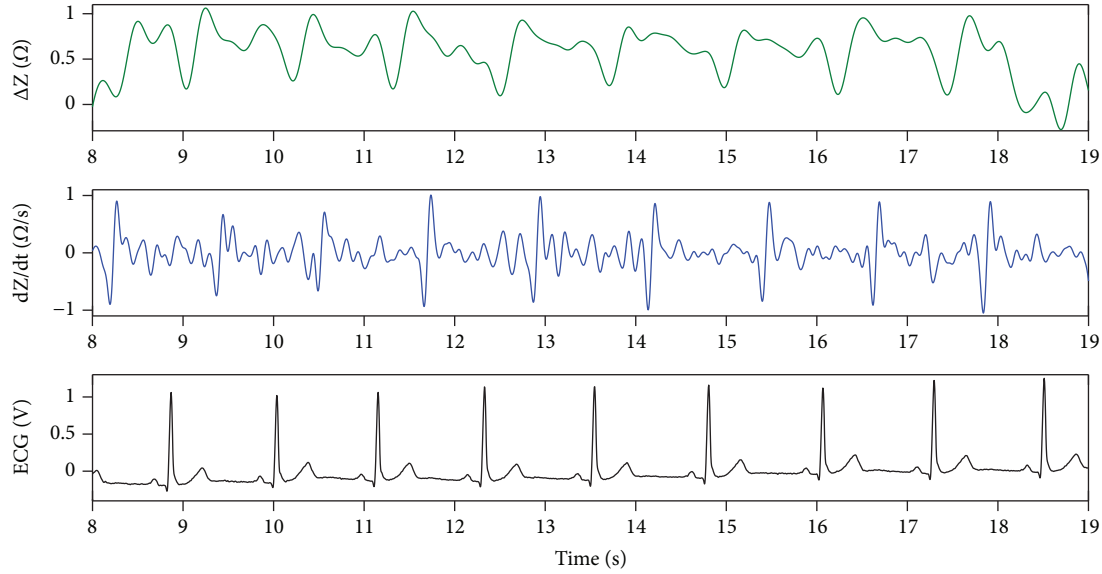
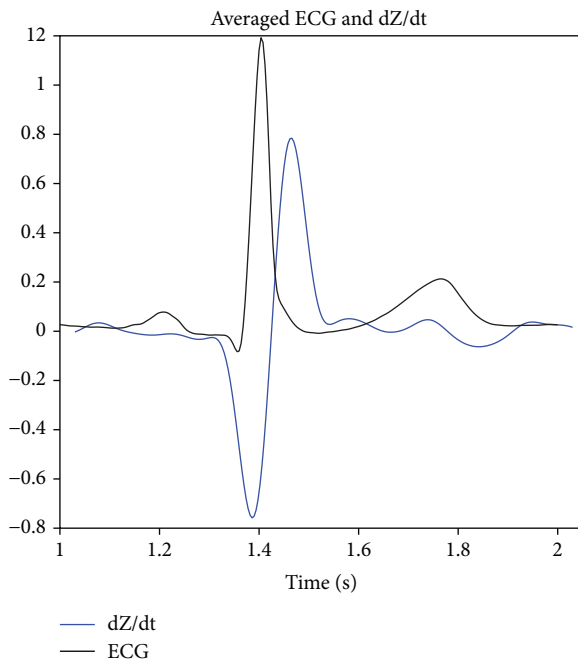Figure 4: ΔZ, dZ/dt, and ECG recorded from one volunteer.

Figure 5: Averaged ICG and ECG signal.

4. Discussion

The purpose of this paper was to evaluate the feasibility of obtaining simultaneously both the ICG and 1-lead ECG, lead II, recordings using the same electrodes for voltage sensing plus one electrode for right leg driven.

The performed measurements sharing the sensing electrodes allowed us to obtain a clean raw ECG, ΔZ, and dZ/dt recordings. However, as showed in Figure 6, the ICG complex obtained with 5 electrodes produces a much denoted minimum than in the recordings obtained with 8

electrodes. Such denoted minimum between the A and E waves appears in all volunteers and can be observed also in the recording showed in Figure 4. This change in the waveform most likely occurs due to the fact that the placement of the electrodes is slightly different between the 5-electrode and 8-electrode configuration [33], where the upper electrode from the neck is placed in the upper section of the torso as shown in Figure 3.

Previously, researchers have raised concerns about problems in experiments, to obtain a straightforward and reliable detection of ICG characteristic points and hemodynamic parameter calculation, especially in automated processing [9, 34–36]. Thus, such denoted minimum is very useful because it allows developing an algorithm for synchronization of ICG complex for the averaging method [30, 31].

Nevertheless, the waveforms obtained using the 5 electrodes as expected exhibit a denoted similarity to other standard ECG and ICG measurements reported elsewhere in the literature [10, 27, 37].

With the exception of the value for HR obtained from ECG, the rest of the hemodynamic and cardiac parameters, SV, CO, and time intervals as the ET and the PEP are obtained from the ICG measurement. The obtained values show certain variability, but such variability can be found between different commercial ICG recorders as reported in [10, 38].

Moreover, given that different electrode configurations as presented in the literature [12, 39–42] yield different results showing also certain dependency to the method use in the analysis [10, 38], we cannot reject the hypothesis that part of the observed variability actually comes from the placement of electrodes. However, the values obtained for the HR and ICG parameters are equivalent and present similar values to hemodynamic parameters obtained from healthy people and reported in the literature [10, 24, 43].

TABLE 2: Cardiac and hemodynamic parameters calculated from the acquired ECG and ICG (mean ± SD).

| Parameters	HV1	HV2	HV3	HV4	HV5	HV6	HV7
Z_0 (Ω)	37.61 ± 6.2	36.84 ± 6.5	37.12 ± 4.7	48.39 ± 6.9	45.94 ± 4.7	27.17 ± 8.7	69.38 ± 1.7
dZ/dt_{max} (Ω/s)	1.03 ± 0.07	1.10 ± 0.14	1.37 ± 0.16	1.36 ± 0.1	1.55 ± 0.11	1.22 ± 0.06	1.42 ± 0.2
ET (ms)	211 ± 13	286 ± 5	319 ± 13	183 ± 1	165 ± 11	210 ± 4	184 ± 7
SV (ml)	54 ± 3	52 ± 3	83 ± 7	43 ± 2	42 ± 1	68 ± 14	46 ± 4
CO (l/min)	4.45 ± 0.26	5.04 ± 0.16	4.29 ± 0.4	3.08 ± 0.15	3.02 ± 0.1	4.67 ± 0.65	2.52 ± 0.06
PEP (ms)	87 ± 19	55 ± 8	90 ± 6	92 ± 33	81 ± 22	81 ± 17	90 ± 4
HR_{ECG} (bpm)	82 ± 1	97 ± 2	51 ± 1	71 ± 2	71 ± 1	68 ± 7	54 ± 4
HR_Z (bpm)	82 ± 1	97 ± 2	50 ± 1	70 ± 2	69 ± 1	67 ± 5	54 ± 5
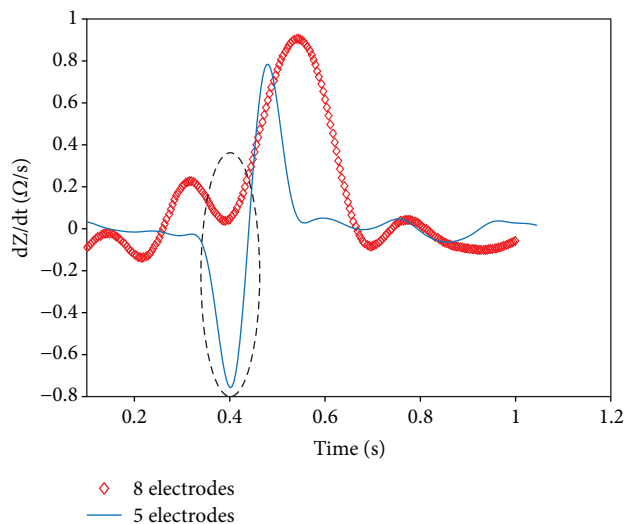
FIGURE 6: Averaged signal for both 5 electrode- vs. 8-electrode configuration.

Thus, this work reinforces the pavement towards wearable applications for engineering, educational, and/or research purposes, in a way that was originally paved by the work done within the HeartCycle project with the wearable impedance cardiographer named IMPACT T-shirt [23] where 8 electrodes where used.

In this paper, one expected confers with such measurement configuration (where the voltage electrodes acquired both the cardiogenic biopotential and the voltage caused by the current injection) would be a certain kind of cross talking of some kind that would create interferences between the different sensing modalities. The close inspection of the recording shows recordings completely free from artifacts caused by interferences between the ICG and the ECG. Consequently, we can assert that the ICG/ECG recordings have been obtained satisfactorily sharing the biopotential electrodes.

Overall, after the evaluation of the obtained recordings, the descriptive statistics of the hemodynamic parameters show a remarkable performance, where the standard deviation is considerably low. In addition, the concordance of the heart rate values between ICG and ECG measurements is obtained.

5. Conclusion

The evaluation results show that the affordable Z-RPI device functions effectively and accurately when performing ECG and ICG simultaneously using only 5 electrodes.

Such successful implementation of the Z-RPI with a reduced number of electrodes facilitates the use of sensorized garments with integrated textile electrodes [27, 43] for wearable and p-health monitoring applications of transthoracic bioimpedance.

Thus, this will also enhance the accuracy of the detection of characteristic points and the calculation of hemodynamic parameters.

With the configuration of electrodes that we presented with the Z-RPI device, we had shown the feasibility of developing an affordable full impedance cardiographer and one-lead electrocardiography device with minimum electrode number. The configuration of electrodes that we are offering in this paper will allow us to go for a comfortable T-shirt that does not have any electrodes or turtleneck around the neck, since the electrodes are placed slightly down to the neck. Thus, we aim to optimize the flexibility and maneuverability and to have greater freedom of action when using a textile garment with a complete affordable device, for the perspective of developing in the future wearable device for p-health or sport effort application.

Data Availability

The data used to support the findings of this study are available from the corresponding author upon request.

Conflicts of Interest

Fernando Seoane is cofounder of Z-Health Technologies AB; neither proprietary technology nor methods of Z-Health Technologies have been used in this work.

Acknowledgments

References

[1] World Health Organization, *Cardiovascular Diseases (CVDs)*, Media centre, 2016.

[2] S. Said and G. T. Hernandez, "The link between chronic kidney disease and cardiovascular disease," *Journal of Nephropathology*, vol. 3, no. 3, pp. 99–104, 2014.

[3] T. K. Bera, "Bioelectrical impedance methods for noninvasive health monitoring: a review," *Journal of Medical Engineering*, vol. 2014, 28 pages, 2014.

[4] U. G. Kyle, I. Bosaeus, A. D. de Lorenzo et al., "Bioelectrical impedance analysis—part I: review of principles and methods," *Clinical Nutrition*, vol. 23, no. 5, pp. 1226–1243, 2004.

[5] J. C. Marquez, F. Seoane, E. Välimäki, and K. Lindecrantz, "Comparison of dry-textile electrodes for electrical bioimpedance spectroscopy measurements," *Journal of Physics: Conference Series*, vol. 224, article 012140, 2010.

[6] F. Seoane, S. Reza Atefi, J. Tomner, K. Kostulas, and K. Lindecrantz, "Electrical bioimpedance spectroscopy on acute unilateral stroke patients: initial observations regarding differences between sides," *BioMed Research International*, vol. 2015, 12 pages, 2015.

[7] R. V. Davalos, D. M. Otten, L. M. Mir, and B. Rubinsky, "Electrical impedance tomography for imaging tissue electroporation," *IEEE Transactions on Biomedical Engineering*, vol. 51, no. 5, pp. 761–767, 2004.

[8] J. Nyboer, M. M. Kreider, and L. Hannapel, "Electrical impedance plethysmography," *Circulation*, vol. 2, no. 6, pp. 811–821, 1950.

[9] A. Sherwood, M. T. Allen, J. Fahrenberg, R. M. Kelsey, W. R. Lovallo, and L. J. P. Doornen, "Methodological guidelines for impedance cardiography," *Psychophysiology*, vol. 27, no. 1, pp. 1–23, 1990.

[10] G. Cybulski, "Ambulatory impedance cardiography," in *Ambulatory Impedance Cardiography. Lecture Notes in Electrical Engineering, vol 76*, pp. 39–56, Springer, Berlin, Heidelberg, 2011.

[11] D. P. Bernstein, I. C. Henry, M. J. Banet, and T. Dittrich, "Stroke volume obtained by electrical interrogation of the brachial artery: transbrachial electrical bioimpedance velocimetry," *Physiological Measurement*, vol. 33, no. 4, pp. 629–649, 2012.

[12] H. H. Woltjer, B. J. M. van der Meer, H. J. Bogaard, and P. M. J. M. de Vries, "Comparison between spot and band electrodes and between two equations for calculations of stroke volume by means of impedance cardiography," *Medical and Biological Engineering and Computing*, vol. 33, no. 3, pp. 330–334, 1995.

[13] Z. Lababidi, D. A. Ehmke, R. E. Durnin, P. E. Leaverton, and R. M. Lauer, "The first derivative thoracic impedance cardiogram," *Circulation*, vol. 41, no. 4, pp. 651–658, 1970.

[14] R. J. Prineas, R. S. Crow, and Z.-M. Zhang, *The Minnesota Code Manual of Electrocardiographic Findings*, Springer Science & Business Media, 2009.

[15] J. D. Dominique Farge, A. Ducros, and C. Neuzillet, "Le livre de sémiologie médicale," 2012, http://www.e-semio.org/Derivation-ECG-frontales.

[16] N. Debbabi, S. El Asmi, and H. Arfa, "Correction of ECG baseline wander application to the Pan & Tompkins QRS detection algorithm," in *2010 5th International Symposium on I/V Communications and Mobile Network (ISVC)*, pp. 1–4, Rabat, Morocco, September-October 2010.

[17] J. Pan and W. J. Tompkins, "A real-time QRS detection algorithm," *IEEE Transactions on Biomedical Engineering*, vol. BME-32, no. 3, pp. 230–236, 1985.

[18] H. Zairi, M. Kedir-Talha, S. Benouar, and A. Ait-Amer, "Intelligent system for detecting cardiac arrhythmia on FPGA," in *2014 5th International Conference on Information and Communication Systems (ICICS)*, pp. 1–5, Irbid, Jordan, April 2014.

[19] N. Meziane, J. G. Webster, M. Attari, and A. J. Nimunkar, "Dry electrodes for electrocardiography," *Physiological Measurement*, vol. 34, no. 9, pp. R47–R69, 2013.

[20] N. Meziane, S. Yang, M. Shokoueinejad, J. G. Webster, M. Attari, and H. Eren, "Simultaneous comparison of 1 gel with 4 dry electrode types for electrocardiography," *Physiological Measurement*, vol. 36, no. 3, pp. 513–529, 2015.

[21] R. Harder, A. Diedrich, J. S. Whitfield, M. S. Buchowski, J. B. Pietsch, and F. J. Baudenbacher, "Smart multi-frequency bioelectrical impedance spectrometer for BIA and BIVA applications," *IEEE Transactions on Biomedical Circuits and Systems*, vol. 10, no. 4, pp. 912–919, 2016.

[22] F. Abtahi, B. Aslamy, I. Boujabir, F. Seoane, and K. Lindecrantz, "An affordable ECG and respiration monitoring system based on Raspberry PI and ADAS1000: first step towards homecare applications," *16th Nordic-Baltic Conference on Biomedical Engineering. IFMBE Proceedings, vol 48*, H. Mindedal and M. Persson, Eds., , pp. 5–8, Springer, Cham, 2015.

[23] M. Ulbrich, J. Mühlsteff, A. Sipilä et al., "The IMPACT shirt: textile integrated and portable impedance cardiography," *Physiological Measurement*, vol. 35, no. 6, pp. 1181–1196, 2014.

[24] A. Hafid, S. Benouar, M. Kedir-Talha, F. Abtahi, M. Attari, and F. Seoane, "Full impedance cardiography measurement device using Raspberry PI3 and system-on-chip biomedical instrumentation solutions," *IEEE Journal of Biomedical and Health Informatics*, vol. 22, no. 6, pp. 1883–1894, 2018.

[25] S. Weyer, T. Menden, L. Leicht, S. Leonhardt, and T. Wartzek, "Development of a wearable multi-frequency impedance cardiography device," *Journal of Medical Engineering & Technology*, vol. 39, no. 2, pp. 131–137, 2015.

[26] J. M. M. Ulbrich, H. Reiter, C. Meyer, and S. Leonhardt, "Wearable solutions using bioimpedance for cardiac monitoring," in *Recent Advances in Ambient Assisted Living-Bridging Assistive Technologies, E-Health and Personalized Health Care, vol. 20*, pp. 30–44, IOS Press, 2015.

[27] J. C. M. Ruiz, M. Rempfler, F. Seoane, and K. Lindecrantz, "Textrode-enabled transthoracic electrical bioimpedance measurements-towards wearable applications of impedance cardiography," *Journal of Electrical Bioimpedance*, vol. 4, no. 1, pp. 45–50, 2013.

[28] M. J. Liebo, R. P. Katra, N. Chakravarthy, I. Libbus, and W. H. W. Tang, "Noninvasive wireless bioimpedance monitoring tracks patients with healthcare utilization following discharge from acute decompensated heart failure: results from the ACUTE pilot study," *Journal of Cardiac Failure*, vol. 19, no. 8, pp. S88–S89, 2013.

[29] R. van Lien, N. M. Schutte, J. H. Meijer, and E. J. C. de Geus, "Estimated preejection period (PEP) based on the detection of the R-wave and dZ/dt-min peaks does not adequately reflect the actual PEP across a wide range of laboratory and ambulatory conditions," *International Journal of Psychophysiology*, vol. 87, no. 1, pp. 60–69, 2013.

[30] R. M. Kelsey and W. Guethlein, "An evaluation of the ensemble averaged impedance cardiogram," *Psychophysiology*, vol. 27, no. 1, pp. 24–33, 1990.

[31] H. Riese, P. F. C. Groot, M. van den Berg et al., "Large-scale ensemble averaging of ambulatory impedance cardiograms," *Behavior Research Methods, Instruments, & Computers*, vol. 35, no. 3, pp. 467–477, 2003.

[32] W. G. Kubicek, J. Kottke, M. U. Ramos et al., "The Minnesota impedance cardiograph-theory and applications," *Bio-Medical Engineering*, vol. 9, no. 9, pp. 410–416, 1974.

[33] K. Sakamoto, K. Muto, H. Kanai, and M. Iizuka, "Problems of impedance cardiography," *Medical and Biological Engineering and Computing*, vol. 17, no. 6, pp. 697–709, 1979.

[34] A. P. DeMarzo and R. M. Lang, "A new algorithm for improved detection of aortic valve opening by impedance cardiography," in *Computers in Cardiology 1996*, pp. 373–376, Indianapolis, IN, USA, September 1996.

[35] D. L. Lozano, G. Norman, D. Knox et al., "Where to B in dZ/dt," *Psychophysiology*, vol. 44, no. 1, pp. 113–119, 2007.

[36] J. H. Meijer, S. Boesveldt, E. Elbertse, and H. W. Berendse, "Method to measure autonomic control of cardiac function using time interval parameters from impedance cardiography," *Physiological Measurement*, vol. 29, no. 6, pp. S383–S391, 2008.

[37] J. Ferreira, F. Seoane, and K. Lindecrantz, "Portable bioimpedance monitor evaluation for continuous impedance measurements. Towards wearable plethysmography applications," in *2013 35th Annual International Conference of the IEEE Engineering in Medicine and Biology Society (EMBC)*, pp. 559–562, Osaka, Japan, July 2013.

[38] P. Carvalho, R. P. Paiva, J. Henriques, M. Antunes, I. Quintal, and J. Muehlsteff, "Robust characteristic points for ICG-definition and comparative analysis," *Proceedings of the International Conference on Bio-inspired Systems and Signal Processing - Volume 1: BIOSIGNALS*, , pp. 161–168, Scienceand Technology Publications, Lda., Rome, Italy, 2011.

[39] A. Ikarashi, M. Nogawa, S. Tanaka, and K.-i. Yamakoshi, "Experimental and numerical study on optimal spot-electrodes arrays in transthoracic electrical impedance cardiography," in *2007 29th Annual International Conference of the IEEE Engineering in Medicine and Biology Society*, pp. 4580–4583, Lyon, France, August 2007.

[40] F. Hoekstra, E. Habers, T. W. J. Janssen, R. M. Verdaasdonk, and J. H. Meijer, "Relationship between the initial systolic time interval and RR-interval during an exercise stimulus measured with impedance cardiography," *Journal of Physics: Conference Series*, vol. 224, article 012117, 2010.

[41] M. Qu, Y. Zhang, J. G. Webster, and W. J. Tompkins, "Motion artifact from spot and band electrodes during impedance cardiography," *IEEE Transactions on Biomedical Engineering*, vol. BME-33, no. 11, pp. 1029–1036, 1986.

[42] E. Raaijmakers, T. J. C. Faes, H. G. Goovaerts, J. H. Meijer, P. M. J. M. de Vries, and R. M. Heethaar, "Thoracic geometry and its relation to electrical current distribution: consequences for electrode placement in electrical impedance cardiography," *Medical and Biological Engineering and Computing*, vol. 36, no. 5, pp. 592–597, 1998.

[43] M. Ulbrich, *Non-Invasive Stroke Volume Assessment Using the Thoracic Electrical Bioimpedance:-Advances in Impedance Cardiography*, Shaker Verlag, 2016.